2015

Novel nanostructured electrocatalysts for fuel cells

Meng Wang
University of Wollongong

NOVEL NANOSTRUCTURED ELECTROCATALYSTS FOR FUEL CELLS

***** A thesis submitted in (partial) fulfilment of the requirements
for the award of the degree

DOCTOR OF PHILOSOPHY

From

University of Wollongong

by

Meng Wang, (BSc. Eng. and M. Eng.)

Faculty of Science, Medicine and Health

May 2015

DECLARATION

I, Meng Wang, declare that this thesis, submitted in partial fulfilment of the requirements for the award of Doctor of Philosophy, in the Faculty of Science, Medicine and Health, University of Wollongong, is wholly my own work unless otherwise referenced or acknowledged. The document has not been submitted for qualification at any other academic institution.

Meng Wang

May 2015

ACKNOWLEDGEMENTS

I would like to express my sincere appreciation to my supervisors, Associate Prof. Jun Chen and Associate Prof. Jiazhao Wang, for their general guidance, financial assistance and constant encouragement throughout my PhD study.

I would also like to acknowledge the general technical support from Dr. Dongqi Shi, Dr. David Wexlar, Dr. Tony Romeo, and Dr. David Mitchell from the University of Wollongong, Mr. Victor Lo from the University of Sydney and Dr. Simon D. Poynton, Prof. Robert C.T. Slade from the University of Surrey, UK.

I am very grateful to all of my colleagues and friends at the Intelligent Polymer Research Institute (IPRI) at the University of Wollongong. In particular, I would like to acknowledge the support and help provided by Dr. Weimin Zhang and Associate Prof. Minyan Wang for their technical advices and discussions during my study. Many thanks also go to Dr. Tania Silver for the critical reading of all my publication and proof reading. In addition, I would like to also thank my dear friends in the IPRI, life would be much more boring without you. They are Mr. Kewei Shu, Mr. Chen Zhao, Mr. Yang Yang, Mr. Yuyang Hou, Mr. Hai Xin, Dr. Wen Zheng, Ms. Jie Zhao, and Ms Yuqing Liu and thanks for their friendliness and kind encouragements.

Finally, I would like to thank my parent and my sister for their love and support. More importantly, I wish to express my gratitude to my wife, Miao Wang for her unfailing love and encouragement, which enable me going through the hard times in my study. Thank you.

The financial assistance from the Australia Research Council and the University of Wollongong is also greatly appreciated.

ABSTRACT

Fuel cells (FCs) are believed to be promising energy conversion systems to satisfy today's increasing energy demand because of their high energy output and zero environmental impact. The cathodic oxygen reduction reaction (ORR) is recognised to be kinetically limited step in fuel cell. As commonly used electrocatalyst, platinum (Pt) has been inhibited from large-scale production because of its high cost, susceptive to fuel poisons and low stability. Therefore, numerous efforts have been devoted in developing novel nanostructured materials with high efficiency, low cost and environmental friendliness for the ORR.

The main goal for this study is to design and develop novel nanostructured electrocatalysts for the ORR to reduce or replace the utilization of Pt, meanwhile with acceptable efficiency, better stability as well as high selectivity to resist the poison from the fuels. Such catalytic materials will would largely reduce the cost of catalysts in FCs and improve the cell performance by facilitating the ORR process and eliminating the by-products. In this study, two analogue FC systems, proton exchange membrane fuel cell (PEMFC) and anion exchange membrane fuel cell (AEMFC) were considered and different types of electrocatalysts were synthesized and examined in these systems respectively.

Pt alloy (Pt-Pd, Pt-Cu) electrocatalysts were firstly synthesized through a facile aqueous based galvanic replacement and their electrocatalytic performance was examined in acidic environment and in PEMFC.

One issue that cause the poor stability of Pt is the aggregation and dissolution of Pt nanoparticle on carbon black during the long term electrochemical process. In this study, using the in-situ localization method, Pt nanoparticles were grown on a palladium shells through a modified galvanic replacement forming a Pt-Pd alloyed nanostructure. This

material showed enhanced ORR performance and better stability under the accelerated durability test (ADT) up to 10,000 cycles. The electrochemical performance of this materials were analysed through the rotating ring disk electrode (RRDE) and single H_2/O_2 proton exchange membrane fuel cell test. The improved electrocatalytic performance and better stability were attributed to the unique structure of Pt/Pd and the strain effects caused by the incorporation of Pd into the lattice of Pt.

A hollow platinum-copper (PtCu) nanoparticle with mesoporous features was prepared through a modified galvanic replacement method using copper nanoparticles as sacrificial templates. The bimetallic PtCu nanoparticle with much lower cost compared with the Pt, showed improved electrocatalytic performance towards the ORR and with extreme stability under the ADT up to 10,000 cycles. The performance of this material was investigated using various electrochemical testing methods including the rotating ring disk electrode (RRDE) and single H_2/O_2 proton exchange membrane fuel cell test. The improved performance of this material was attributed to the geometric and electronic changes of Pt surface due to the alloying of copper, abundant mass transfer channels and the high specific surface area of the mesoporous PtCu.

In the alkaline medium; oxygen could be reduced through a faster reaction kinetic thus offering more choices in selecting electrocatalysts. Moreover, with the development of anion exchange membrane (AEM) in recent decades, the AEMFC has been witnessed as a promising fuel cell system that could provide comparable electrocatalytic performance with the PEMFC. Therefore there is an urgent need for developing novel ORR electrocatalysts in alkaline medium and for AMEFC.

Following the development of this sacrificial template method, a palladium (Pd)-nickel (Ni) hollow nanoparticle using Pd and Ni to replace the utilization of Pt was synthesized and the electrocatalytic performance of this material was examined under

the alkaline medium and in AMEFC. The PdNi alloyed hollow nanoparticles showed porous features on the shells and also exhibited much improved electrocatalytic performance and stability compared with the commercial Pt/C. The electrochemical tests were performed through the rotating disk electrode (RDE) system and AEMFC test. The improved performance of this material was ascribed to the changes of electronic structure and the "strain effect" of Pd when alloying Pd with Ni. In addition, porous structure of this material would also provide large surface area and active sites thus benefiting the reduction of oxygen and mass transfer through the nanoparticles.

Further work includes the synthesis of nitrogen doped graphene nanostructures for the oxygen reduction reaction in the alkaline medium. For this work, the thin polypyrrole (PPy) was deposited onto the graphene aerogel through vapor phase polymerisation (VPP) and the deposited PPy was used as a nitrogen source to provide nitrogen into graphene lattice when thermal treatment. The advantage of this method is that, the deposited PPy could effectively prevent graphene sheets from stacking during the drying and thermal annealing process and the robust crumpled graphene sheets could also be produced during this process. This 3-dimensional (3D) microporous structure could provide the electrocatalysts with ample active site and abundant ion and mass transfer channels thereby facilitating the ORR process. In this process, the nitrogen content and configuration could be well managed through varying the heating temperature thus providing further ways in regulating the ORR performance of the electrocatalysts. The electrochemical properties were tested using the rotating disk electrode (RDE) system and anion exchange membrane fuel cell test revealing the improved catalytic performance of this material compared with the traditional prepared nitrogen doped flat graphene materials. The improved electrocatalytic performance was

suggested to arisen from the optimised nitrogen configuration and the robust 3D porous structure on the electrodes.

In addition, core shell cobalt and cobalt oxide nanostructure supported on nitrogen doped graphene aerogel was also prepared at last and used an comparable electrocatalysts with Pt for the AMEFC. The cobalt oxides coupled on graphene supports have been widely reported with improved catalytic ORR performance, however the relatively low electrical conductivities were thought to inhibit the electron transfer around the nanoparticles. Inspiring the advantage of the core shell nanostructure, a core shell structured consisting of cobalt core and cobalt oxide shell was prepared and anchored onto the graphene sheets through a feasible one-pot hydrothermal process. This material was characterised with scanning electron microscopy, transition electron microscopy and energy X-ray dispersive mapping analysis to confirm the successful synthesis of core shell structure. The electrochemical performance was tested through the rotating disk electrode (RDE) showing improved performance in comparison with the pure cobalt oxide or nitrogen doped graphene aerogel electrocatalysts. The improved electrocatalytic performance was attributed to the well-defined core shell structure and the designed 3D structure of the supporting materials.

TABLE OF CONTENTS

ABBREVIATIONS TABLE

Full Name	Abbreviation
1-electron	1e−
2-electron	2e−
4-electron	4e−
ethylene glycol	EG
zero-dimensional	0D
one-dimensional	1D
two-dimensional	2D
three-dimensional	3D
accelerated durability test	ADT
anion exchange membrane fuel cell	AEMFC
alkaline fuel cell	AFC
silver/silver chloride electrode	Ag/AgCl
Carbon black	CB
carbon nanotubes	CNT
carbon monoxide	CO
bulk concentration of O_2	C_{O2}
Hexadecyltrimethylammonium bromide	CTAB
cyclic voltammetry	CV
density functional theory	DFT
direct methanol fuel cell	DMFC
diffusion coefficient of O_2	D_{O2}
electrochemical active surface area	ECSA
energy dispersive spectroscopy	EDS
Faraday constant	F

Iron(III) p-toluenesulfonate hexahydrate	FeToS
Fourier transform infrared spectroscopy	FTIR
graphene aerogel	GA
gas diffusion layer	GDL
graphene hydrogel	GH
graphene oxide	GO
graphene sheets	GS
hydrogen oxidation reaction	HOR
high resolution transmission electron microscope	HRTEM
Inductively Coupled Plasma - Mass Spectrometry	ICP-MS
L-ascorbic acid	L-AA
Linear Sweep Voltammetry	LSV
molten carbonate fuel cell	MCFC
membrane electrode assembly	MEA
electron transfer number	n
nanocrystal	NC
nitrogen doped graphene aerogel	NGA
oxygen reduction reaction	ORR
phosphoric acid fuel cell	PAFC
palladium	Pd
poly(diallyldimethylammonium chloride)	PDDA
proton exchange membrane fuel cell	PEMFC
platinum	Pt
Poly(tetrafluoroethylene)	PTFE
Poly(vinylbenzyl chloride)	PVBC
rotating disk electrode	RDE

reduced graphene oxide	rGO
reversible hydrogen electrode	RHE
rotating ring disk electrode	RRDE
scanning electron microscope	SEM
scanning transmission electron microscope	STEM
transmission electron microscope	TEM
thine film rotating-disk electrode	TF-RDE
Thermogravimetric Analysis	TGA
N,N,N',N'-Tetramethyl-1,6-hexanediamine	TMDA
underpotentially deposited	UPD
Ultraviolet-visible spectroscopy	UV-Vis
vapor phase polymerisation	VPP
X-ray photoelectron spectroscopy	XPS
X-ray diffractometer	XRD
kinetic viscosity	υ

LIST OF FIGURES AND TABLES

1. FIGURES

2. TABLES

Chapter 1

General Introduction

Chapter 1

1. CONTENTS

Chapter 1

1.1 General Introduction to Fuel Cells

1.1.1 Fuel Cells

The increasing global demands for energy sources and the environmental impacts of traditional forms of energy have raised global awareness on the need to develop clean and sustainable energy sources. The fuel cell, due to its high energy conversion efficiency and low pollution is considered to be one promising solution and thus has received intensive research interest in recent decades.[1] In fuel cells, the chemical energy is continuously converted into electrical power via redox reactions, typically by supplying the fuel (pure hydrogen, hydrogen carbon fuels, or chemical hydrides) on the anode side and the oxidant (oxygen and air) on the cathode side. Also, in contrast to batteries or conventional supercapacitors, the fuel cells are an open system where the active masses undergoing the redox reactions are delivered from the outside of the cell. Therefore, fuel cells are considered to be high-energy systems ideal for various stationary and mobile applications.[2]

Fuel cells can be classified into different types according to the choice of electrolyte and fuel; currently, six major types of fuel cells are available: alkaline fuel cells (AFC), proton exchange membrane fuel cells (PEMFC), direct methanol fuel cells (DMFC), phosphoric acid fuel cells (PAFC), molten carbonate fuel cells (MCFC), and solid oxide fuel cells (SOFC). A simplified illustration of reactions is presented in Figure 1.1. Among these fuel cells, the membrane fuel cells, including the PEMFC and the anion exchange membrane fuel cell (AEMFC or AMFC, with a solid electrolyte (anion exchange membrane) for the AFC developed in the last decade [3]), have been recognised as potential power sources for residential and commercial use because of their relatively low operating temperature, fast start-up,

high efficiency, and low environmental impact.[1] In this study, only these two types of fuel cell will be considered.

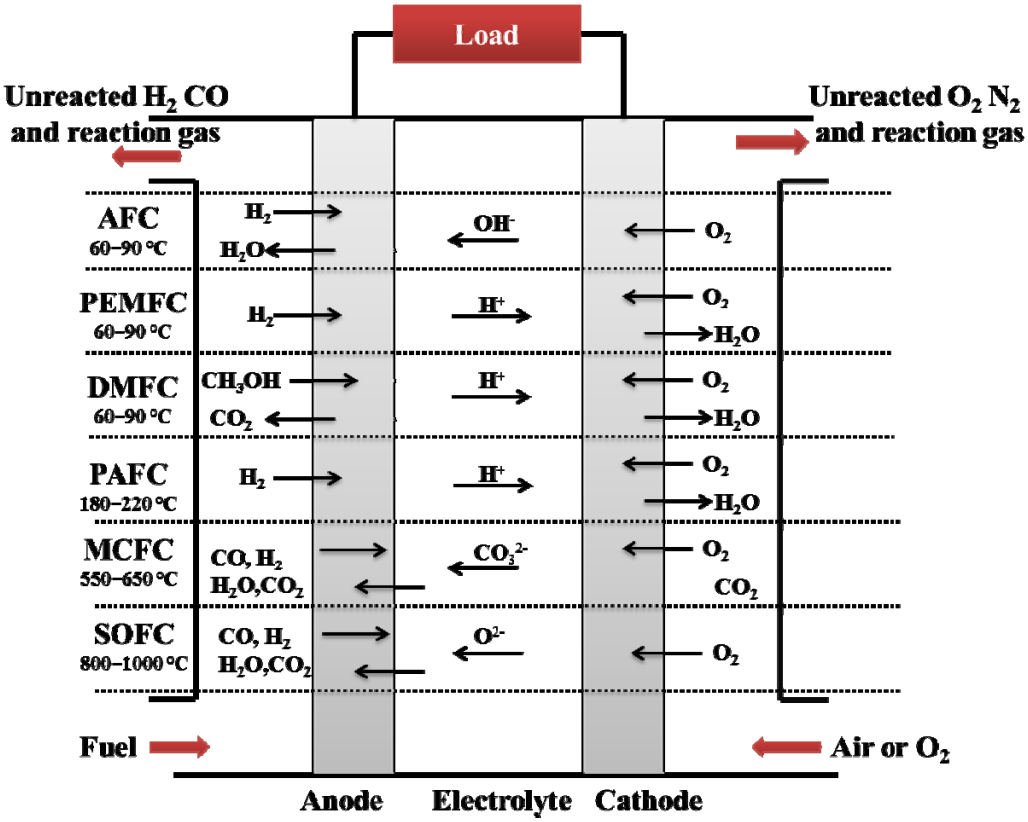

Figure 1.1 Summary of the major types of fuel cells.

1.1.2 Membrane Electrode Assembly

Figure 1.2 illustrates the components of the PEMFC and AEMFC, which both comprise membrane electrode assemblies (MEA), in which hydrogen gas is oxidised on the anode and oxygen gas is reduced at the cathode, all compressed by a bipolar plate with gas flow channels to introduce gaseous reactants and coolants to the MEA and harvest electrical current.[4] In the PEMFC, a Nafion® membrane (a DuPont registered trademark polymer) is used as the proton conducting electrolyte, and the corresponding electrocatalysts are usually dispersed with Nafion® monomer in low boiling point water soluble solvents, such as ethanol and (*n*- or 2-) propanol, and air-

brushed onto gas diffusion layers (GDLs) to fabricate the membrane electrodes. Finally, the two membrane electrodes and the Nafion® membrane are assembled by hot-pressing to form the membrane electrode assembly (MEA). For the AEMFC, the MEA is typically fabricated in the same way except for the different kinds of polymer membranes and monomers used. In the AEMFC, the polymer membrane used is anion conductive rather than proton conductive, and the monomers used are selected to have high anion exchange capabilities.[3] The electrochemical reactions occur at the MEA electrodes, where oxygen reduction reaction (ORR) takes place at the cathode and the hydrogen oxidation reaction (HOR) at the anode. Both reactions take place on the catalyst layer, and water and heat are the only by-products.

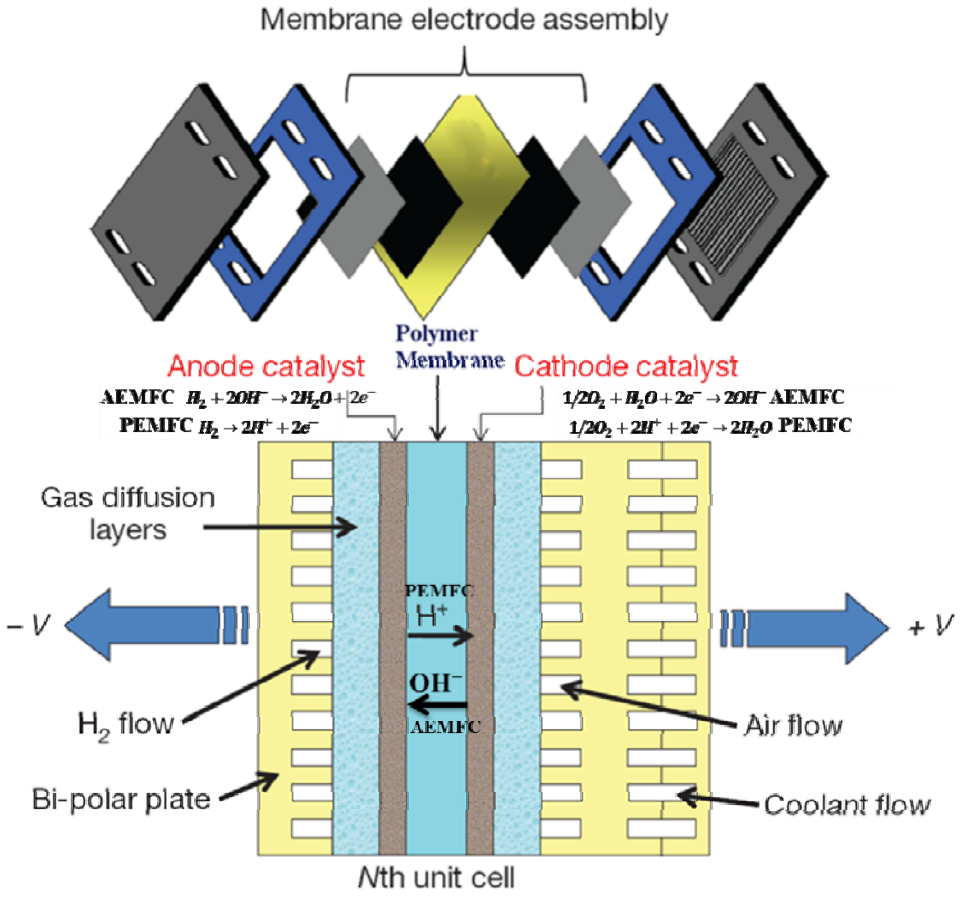

Figure 1.2 Configuration of PEMFC and AEMFC, and the membrane electrode assembly. Note that the catalyst layers and the membrane for the acidic PEMFC are different from those for an AEMFC.[1]

1.1.3 Current Challenges for the PEMFC and AEMFC

Fuel cell MEAs must meet three major criteria before they can be commercialisation: cost, performance, and durability. The cathode ORR is six or more orders of magnitude slower than the anode hydrogen oxidation reaction and thus limits the performance of the fuel cell,[1] so most research and development are focused on improvement of the cathode catalysts and electrodes.[5, 6] Today, in most cathodes, the ORR catalysts used are based on Pt (in the form of Pt nanoparticles dispersed on carbon black supports); however, the scarcity of Pt and its suspect "poison" resistance capability, as well as its poor durability have inhibited it from large-scale production.

In this study, we will consider the synthesis of novel Pt-based porous ORR alloy catalysts with high performance for the PEMFC, where the alloyed nature of the nanoparticles and the abundant electroactive surface area of the electrocatalyst make for catalysts with higher performance, better "poison" resistance, and longer durability compared with the Pt/C electrocatalysts. In addition, for the AEMFC, we will firstly report the development of Pd-based bimetallic electrocatalysts, then the development of non-noble metal based low-cost electrocatalysts, including doped graphene nanostructure and metal-oxide-nitrogen-doped graphene nanostructure electrocatalysts. These pure carbon or non-noble metal catalysts were tested with comparable performance, full tolerance towards the "poison", and much longer durability than the Pt/C because of the high surface area, good mechanical properties,

and superb thermal stability.[5] It is worth noting that the development of novel catalysts require a deep understanding of the ORR mechanism and kinetics, and thus the mechanism of ORR and then recent advances in developing ORR catalysts will be reviewed in the following parts.

1.2 General Introduction to the Oxygen Reduction Reaction

1.2.1 Electrochemical Oxygen Reduction Reaction

As aforementioned, the performance of the PEMFC and AEMFC is kinetically limited by the cathode oxygen (O_2) reduction reaction (ORR), and thus, the ORR is one of the major areas of ongoing research due to its sluggish reaction mechanism.[5, 6] The thermodynamic redox potential E^0 of the ORR for a 4-electtron pathway is 1.229 V at 25 °C. For the state of the art Pt electrocatalysts, the onset potential of the ORR is at about 1 V, indicating a 200 mV high overpotential on the Pt electrode which may be ascribed to the low density of catalytic defect sites on the Pt surface and the sluggish reaction kinetics of the ORR. So, an understanding of the ORR process and mechanism is a necessity for discovering more efficient catalysts for the ORR.

The ORR process is complicated; it generates a number of intermediates, and the mechanism and kinetics for the reaction are dependent on many experimental factors, such as the type of electrode and the electrolyte used. The reaction could proceed by either a four-electron pathway or a two-electron path way in aqueous or organic electrolyte.

In aqueous acid media, the $4e^-$ and $2e^-$ pathways are respectively:

a) Four-electron pathway

$$O_2 + 4H^+ + 4e^- \rightarrow 2H_2O \qquad E^0 = 1.229\,V \qquad (1.1)$$

b) Two-electron pathway

$$O_2 + 2H^+ + 2e^- \rightarrow HOOH \qquad E^0 = 0.607\,V \qquad (1.2)$$

Followed by either

$$HOOH + 2H^+ + 2e^- \rightarrow 2H_2O \qquad E^0 = 0.607\,V \qquad (1.3)$$

Or

$$2HOOH \rightarrow 2H_2O \qquad (1.4)$$

In aqueous alkaline media, the $4e^-$ and $2e^-$ pathways are respectively:

a) Four-electron pathway

$$O_2 + 2H_2O + 4e^- \rightarrow 4OH^- \qquad E^0 = 0.401\,V \qquad (1.5)$$

b) Two-electron pathway

$$O_2 + H_2O + 2e^- \rightarrow HOO^- + OH^- \qquad E^0 = -0.065\,V \qquad (1.6)$$

Followed by either

$$HOO^- + H_2O + 2e^- \rightarrow 3OH^- \qquad E^0 = 0.867\,V \qquad (1.7)$$

Or

$$2HOO^- \rightarrow 2OH^- + O_2 \qquad (1.8)$$

In non-aqueous aprotic solvents,

$$O_2 + e^- \rightarrow O_2^- \qquad (1.9)\ ^{a}$$

$$O_2^- + e^- \rightarrow O_2^{2-} \qquad (1.10)\ ^{b}$$

[a, b]: The thermodynamic potentials (E^0) for the 1-electron reduction reaction to form a superoxide, and its further reduction to O_2^{2-} are not listed because their values are highly dependent on the solvent used.

Depending on the application, the reduction pathways may have unique significance, for example, the 2-electron transfer pathway may be used to generate hydrogen peroxide, the 1-electron transfer pathway is usually the main process in

reversible lithium-air batteries[7, 8], and the 4-electron direct pathway is highly preferred both in PEMFCs and in anion exchange membrane fuel cells (AEMFCs).

1.2.2 Mechanism for Oxygen Reduction Reaction

The mechanism of the ORR has been extensively studied by many researchers, as detailed in several reviews. [4, 9-11] The mechanism is different depending on the kinds of electrodes due to the different physicochemical properties of the materials, such as the crystal structure, interatomic distance, grain size, etc... The reaction steps of the ORR were generally believed, however, to include oxygen gas adsorption, charge transfer, breaking of the O-O bond, and desorption. Herein, only the ORR mechanism on the metal electrodes and carbon electrodes related to this study will be discussed.

1.2.2.1 Mechanism of the Oxygen Reduction Reaction on Pt electrode

As Pt is still the most efficient catalyst for catalysing the ORR both in acidic and basic environments, the mechanism of ORR on a Pt electrode has been widely studied. The ORR usually proceeds through a 4-electron transfer pathway either in acidic or basic solution. The high efficiency of the Pt electrode may be ascribed to the unique geometry of its crystal structure (Pt-Pt bonds) and its electronic structure (*d*-band vacancies).

The simplified mechanism of the ORR on a Pt electrode is shown in Figure 1.3.[12] It can be seen that on a Pt electrode, oxygen can be directly electrochemically reduced to H_2O at a constant rate of k_1 without any formation of intermediate adsorbed $H_2O_{2,ad}$ (direct 4-electron pathway) or to adsorbed H_2O_2 at the rate constant of k_2 (series of 2-electron pathways). The adsorbed peroxide could be reduced to water with the rate of k_3 (series of 4-electron pathways), catalytically

(chemically) decomposed on the electrode surface (k_4), or desorbed into the bulk electrolyte (k_5). All these processes require dissociation of oxygen prior to the transfer of the first electron.[12] The dissociation energy of oxygen is quite large (498.3 kJ mol^{-1}), meaning that dissociation is energetically unfavourable unless the M-O bond, with M a metal, is very strong, e.g., > 250 kJ mol^{-1}. Metals with strong M-O bond strengths, however, usually have strong M-OH bonds, which are unfavourable for the ORR, as mentioned above. The kinetics is rather more complex than usually believed, however, and is affected by many other factors, such as anions in the electrolyte, [13, 14] Pt particle sizes, crystal structures [15-17], etc.

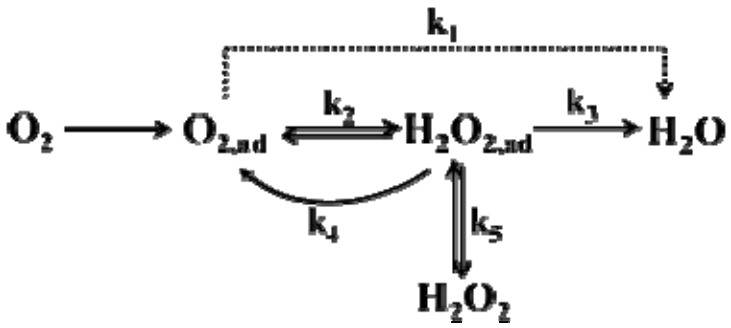

Figure 1.3 Simplified illustration of ORR kinetics on Pt electrode.

1.2.2.2 Mechanism of the oxygen reduction reaction on other precious metal electrodes

The ORR reaction on other precious metal surfaces, such as Au, Ir, Rh, etc., has also been extensively studied, however, these metals show lower catalytic activity towards the ORR than Pt, besides not being electrochemically stable under the ORR testing environment conditions. Nørskov et al. extensively compared the oxygen binding energy and hydroxyl binding energy on various metals and found that Pt or Pd has the greatest catalytic performance towards the ORR (Figure 1.4).[18] Thus,

higher ORR activity requires a smaller ratio of M-OH to M-O bond strengths or a higher activation energy for OH_{ads} compared to oxygen chemisorption.[4]

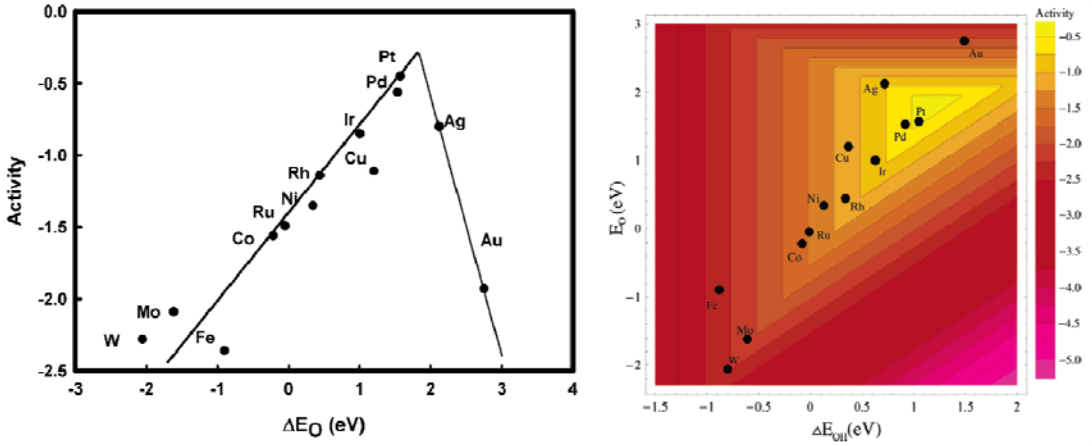

Figure 1.4 Trends in oxygen reduction activity plotted as a function of the oxygen binding energy (left) and as a function of the hydroxyl binding energy (right).[18]

Based on these theories, the major research trends for Pt-based catalysts are focused on (i) shortening of the Pt–Pt interatomic distance, which is favourable for the dissociative adsorption of O_2 (geometric effect), including work on the synthesis of Pt-M alloyed nanostructures and shape-controlled synthesis of Pt nanostructures; (ii) increasing *d*-band vacancies that produce a strong metal–O_2 interaction and a weak M–OH bond (electronic structure), usually involving an of alloy Pt with a second metal; and (iii) surface roughening synthesis of porous Pt based nanostructures. The reports on synthesis of Pt based electrocatalysts will be reviewed later.

1.2.2.3 Mechanism of the oxygen reduction reaction on doped carbon electrode

The ORR kinetics could be greatly enhanced in an alkaline medium because of the improved charge/ion transfer rate in the alkaline electrolyte.[19] It is well known that carbon materials show some electrocatalytic activity towards the ORR in an alkaline medium. The catalytic activities and mechanism involved vary with the type of

carbon used. [12] For example, the ORR on glass carbon electrodes and pyrolytic graphite normally proceeds via a two-electron pathway to yield H_2O_2. The H_2O_2 could be reduced to water at a lower potential. Two mechanisms have been proposed for the carbon-catalysed ORR on glassy carbon electrodes (Equations (1.11)-(1.16)) and on pyrolytic graphite electrodes (Equations (1.17)-(1.18)), respectively.

$$O_2 \rightarrow O_{2(ads)} \quad (1.11)$$

$$O_{2(ads)} + e^- \rightarrow [O_{2(ads)}]^- \quad (1.12)$$

$$[O_{2(ads)}]^- \rightarrow {O_{2(ads)}}^- \quad (1.13)$$

$${O_{2(ads)}}^- + H_2O \longrightarrow HO_{2(ads)} + OH^- \quad (1.14)$$

$$HO_{2(ads)} + e^- \rightarrow HO^-_{2(ads)} \quad (1.15)$$

$$HO^-_{2(ads)} \rightarrow HO^-_2 \quad (1.16)$$

Or

$$[O_{2(ads)}]^- \rightarrow {O_{2(ads)}}^- \quad (1.17)$$

$$2{O_{2(ads)}}^- + H_2O \longrightarrow O_2 + HO^-_2 + OH^- \quad (1.18)$$

The mechanism on doped carbon materials, especially on nitrogen-doped graphene materials, has been studied and reported using the B3LYP density functional theory (DFT).[20] Anderson et al. studied the oxygen reduction reaction on nitrogen-doped graphene using the B3LYP hybrid DFT method [21], and their quantum calculations on cluster models of nitrided and un-nitrided graphite sheets showed that the carbon radical sites formed adjacent to substitutional N in graphite are active for O_2 electroreduction to H_2O_2 via an adsorbed OOH intermediate. The weak catalytic effect of untreated carbon is attributed to the weaker bonding of OOH to the H-atom-terminated graphite edges. Substitutional N atoms that are far from

graphite sheet edges will be active, and those that are close to the edges will be less active. With the same DFT model, Xia et al. proposed a four electron transfer pathway for the ORR on nitrogen doped graphene. The calculations on the electron transformation process show that the ORR is a four-electron pathway on N-graphene, but pure graphene does not take part in such catalytic activities. When H is introduced into the system, the sequential reactions can occur, including the formation of O-C chemical bonds between oxygen and graphene, O-O bond breakage, and the creation of water molecules. For each reaction step, the system energy decreases accordingly, indicating that the four-electron transformation reaction takes place spontaneously. The active catalytic sites on single nitrogen doped graphene are identified, which have either high positive spin density or high positive atomic charge density. The nitrogen doping introduces asymmetry in the spin density and atomic charge density, making it possible for N-graphene to show high electron catalytic activities towards the ORR. (Figure 1.5)

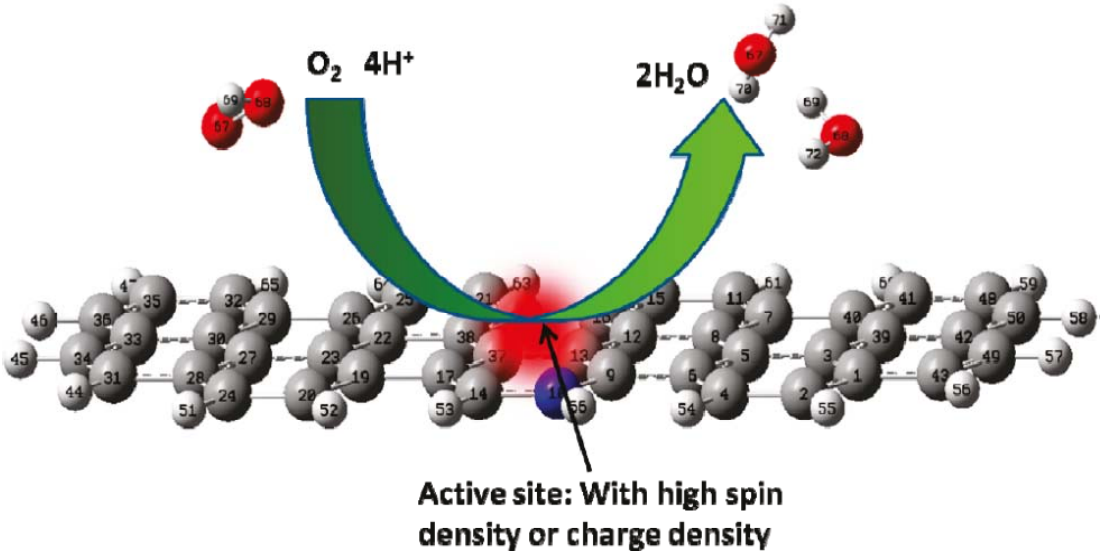

Figure 1.5 Schematic illustration of the active site on nitrogen doped graphene for the ORR process. [20]

1.2.3 Kinetic Parameters for the Oxygen Reduction Reaction

The exchange current density is an important kinetic parameter revealing the electrochemical reaction rate at equilibrium. For the ORR, it is significantly influenced by the electrode surface on which the ORR occurs. For example, on a Pt electrode, the ORR shows a higher exchange current density than an Au electrode. Except for the exchange current density, it is desirable to have the O_2 reduction at a lower overpotential to gain satisfactory current density, which could be expressed as in Equation (1.11).[22]

$$I_c = i_{O2}^0(e^{\frac{n_{a0}a_0F\eta_c}{RT}} - e^{-\frac{n_{a0}(1-a_0)F\eta_c}{RT}}) \quad (1.11)$$

where I_c is the oxygen reduction reaction current density, i_{O2}^0 is the exchange current density, n_{a0} is the number of electrons transferred in the rate determining step, a_0 is the transfer coefficient, η_c is the overpotential of the ORR, *F* is the Faraday constant, *R* is the gas constant, and *T* is the temperature in Kelvin. Therefore, to obtain a high current, the exchange current density i_{O2}^0 should be large and/or $\frac{RT}{n_{a0}a_0F}$ should be small. At the current stage of technology, the Pt electrodes are the most practical catalysts with the highest exchange current density of about 10^{-11} -10^{-9} A cm^{-2} in both acidic and alkaline solutions. In alkaline solution, the reaction is significantly faster than in acidic solution that shows no formation of oxygenated adlayers, and the potential range of M–OH formation on platinum metal in alkaline solutions is considerably wider than in acidic solutions.[23, 24]

If the overpotential is large, Equation (1.11) could be simplified as

$$I_c = i_{O2}^0 e^{\frac{n_{a0}a_0F\eta_c}{RT}} \quad (1.12)$$

The plot of $\eta_c \sim \log(I_C)$ gives a linear relationship, and the slope is $\frac{2.303RT}{n_{a0}a_0F}$, which is called the Tafel slope. For the ORR, usually two Tafel slopes are obtained, 60

mV/dec in the low overpotential region and 120 mV/dec in the high overpotential region. The higher the Tafel slope is, the faster the overpotential increases with the current density, revealing the inferior catalytic performance of the electrocatalyst.

1.3 Electrocatalyst for the Oxygen Reduction Reaction in Acidic Medium for the PEMFC

1.3.1 Pt-based Nanostructures for the Oxygen Reduction Reaction in Acidic Medium for the PEMFC

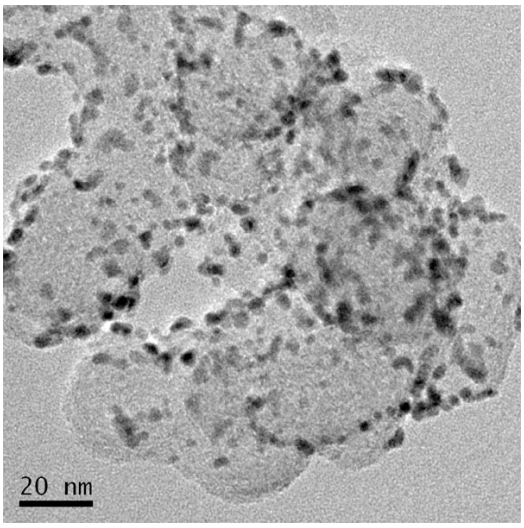

Figure 1.6 Typical TEM image of commercial Pt/C electrocatalyst (40 wt.% loading on Vulcan XR-72C carbon black, Johnson Matthey).

During last several decades, even though numerous efforts have been made to replace platinum with less precious metal,[25] non-noble metals,[26] or organometallic complexes, [27, 28] platinum still seems to be most effective and durable catalyst for PEM fuel cells. In commercially available electrocatalysts, platinum is in the form of nanoparticles with diameters around 2-3 nm, supported on a high surface area carbon support such as Vulcan XR-72C with different loading

amount (typically from 20 -60 wt.%), Figure 1.6 shows a TEM images of a commercially available Pt/C electrocatalyst.

These Pt/C electrocatalysts are expensive, however, and the stability is poor when these catalysts are applied under longer term operation conditions due to carbon corrosion and Pt surface tension; Ostwald ripening; and potential-dependent chemical dissolution of Pt and migration into the proton exchange membrane.[29, 30]. Therefore, almost all efforts on synthesizing Pt based nanostructures are currently devoted to increasing the efficiency and stability of Pt while reducing the cost. To date, these methods include, but are not limited to 1) stabilization of monodisperse Pt nanoparticles on supporting materials to enhance the stability and increase the utilization of Pt, thereby improving ORR performance and reducing the cost; 2) synthesis of well-defined Pt nanostructures that will reduce the surface tension of Pt due to highly active low energy crystalline facets and relatively few defect sites to increase the electrochemical activity; 3) synthesis of alloyed Pt nanostructures (Pt-M, where M maybe is gold, palladium, cobalt, nickel, copper, etc.), which would cause the positive changes to the geometric and electronic structures of Pt, thus giving rise to enhanced performance and stabilization; 4) using other support materials to substitute for carbon support to avoid carbon erosion.

1.3.1.1 Stabilization of Pt Nanoparticles on Carbon Supports for the ORR in PEMFCs

It is well known that the electrocatalytic performance of an electrocatalyst is strongly dependent on the particle size, dispersion, and size distribution. Thus, the synthesis of well-dispersed Pt nanoparticles on carbon supports would significantly increase the stability and the electrocatalytic activity of Pt electrocatalyst because of the

relatively high utilization efficiency and lower aggregation of Pt nanoparticles. Although these different preparation procedures could yield varying sizes of nanocatalytic materials, it is strongly believed that controlled and desired size of the catalytic particles can be achieved by stabilizing the particles either by using surfactants or solvents.[31] Recently Yu et al. reported a simple and efficient solvent approach for the synthesis of carbon-supported Pt nanoparticles (NPs) that combines homogeneous deposition of Pt complex species through a gradual increase in the pH realized by *in situ* hydrolysis of urea and subsequent uniform reduction by ethylene glycol (EG) in a polyol process, giving control over the size and dispersion of Pt NPs. This method has superior advantages in producing uniformly dispersive Pt nanoparticles on carbon supports over some other conventional methods such as borohydride reduction and the polyol process (Figure 1.7), and the results showed that the synthesized Pt/C electrocatalysts manifested improved catalytic performance in PEMFCs compared with the same loading of Pt/C synthesized through other methods.[32]

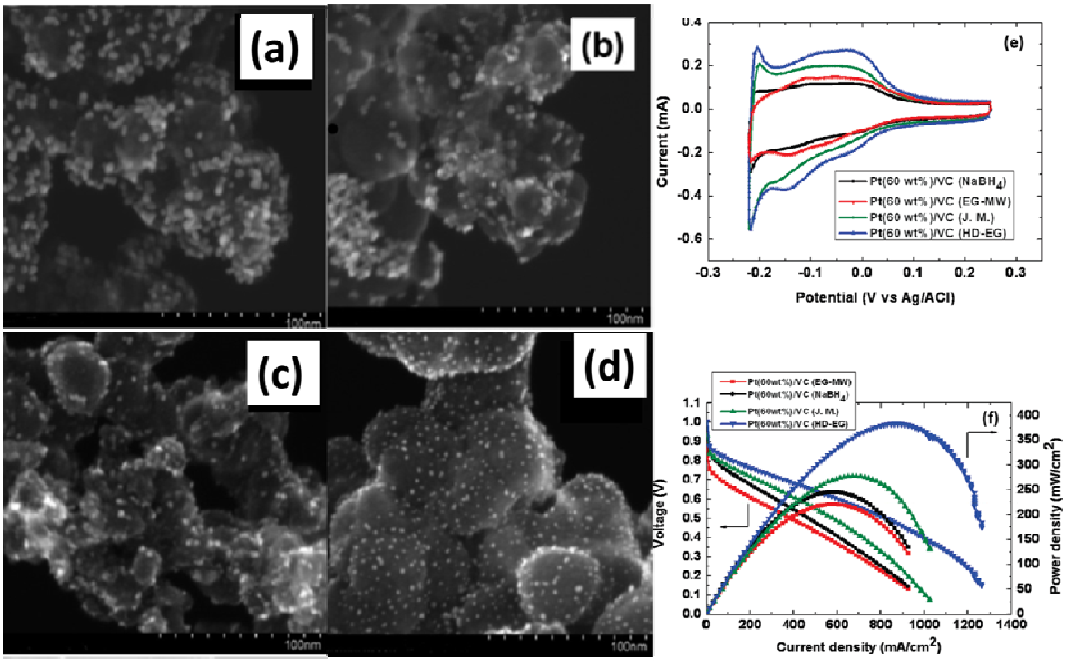

Figure 1.7 HRSEM images for Vulcan Carbon (VC)-supported Pt catalysts with metal loadings of 40 wt % prepared by different methods: borohydride reduction (a), the polyol process (b), Johnson Matthey (c), and homogeneous deposition – ethylene glycol (HD-EG) (d). (e) H-electrosorption profiles in 0.5 M H_2SO_4. Fuel-cell polarization plots at 60 °C (f) for the various Pt /C (60 wt. %) catalysts.[32]

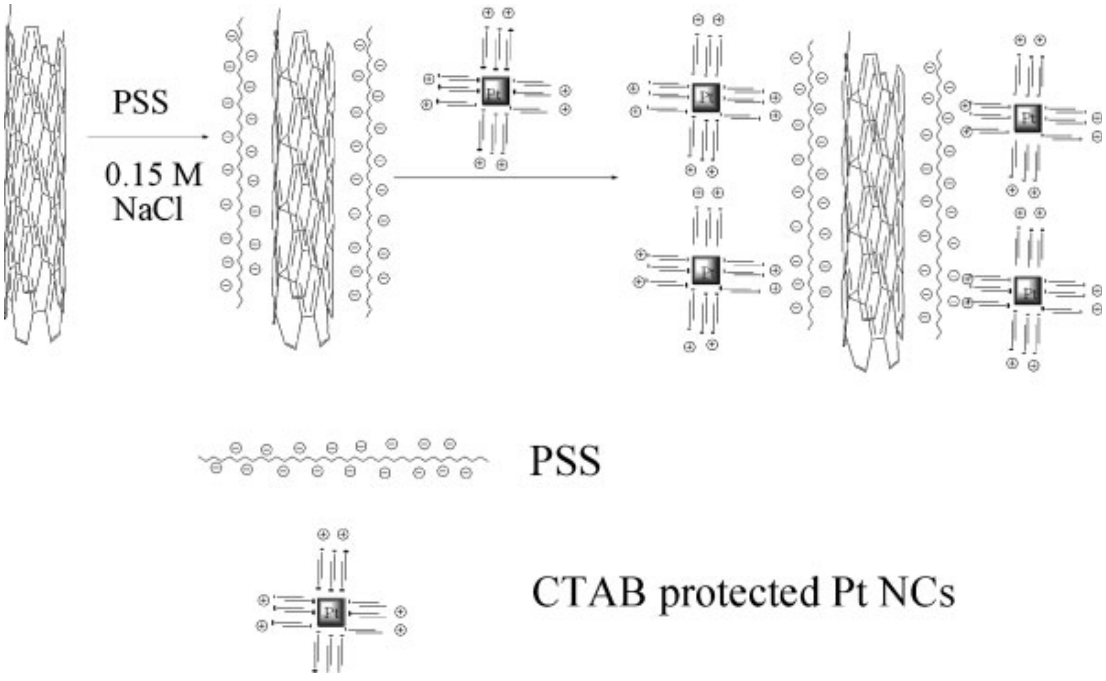

Figure 1.8 Illustration of positively charged Pt nanocrystals assembled on negatively charged poly (sodium 4-styrenesulfonate) (PSS) modified carbon nanotube.[34]

Moreover, the usage of surfactant in the synthesis of Pt nanoparticles has also proposed as an important strategy for stabilization of the Pt nanoparticles on carbon supports because the long-chain polymer surfactant could effectively localize the nanoparticle growth and avoid nanoparticle aggregation when they are supported on carbon supports. For example, the surfactant poly(diallyldimethylammonium chloride) (PDDA) has been reported to produce stabilized Pt/C electrocatalysts because of the interaction between the Pt nanoparticles and the PDDA, which increases the Pt oxidation potential and prevents Pt nanoparticles from migrating/agglomerating on or detaching from the carbon support.[33] Moreover, as the particles are protected with a surfactant layer, charge and electrostatic effects could be realized when the charges of the carbon supports are different from those of the particles, thereby producing mono-disperse nanoparticles self-assembled on carbon supports (Figure 1.8).

1.3.1.2 Stabilization of Pt Nanoparticles on Other Supporting Materials for the ORR in PEMFCs

It is also found that the stability of Pt could be greatly improved when using novel supporting materials for the Pt nanoparticles instead of the conventional carbon black support, to avoid the carbon erosion issue when the electrocatalyst in long-term operation. Adzic et al.[35] found that the Pt nanoparticles could be stabilized when the Pt/C was modified with gold clusters through galvanic displacement by Au of a Cu monolayer on Pt. Using accelerated durability testing, they found that the Pt nanoparticles retain their ORR activity under the oxidizing conditions of the O_2

reduction reaction and potential cycling between 0.6 and 1.1 V in over 30,000 cycles (Figure 1.9).

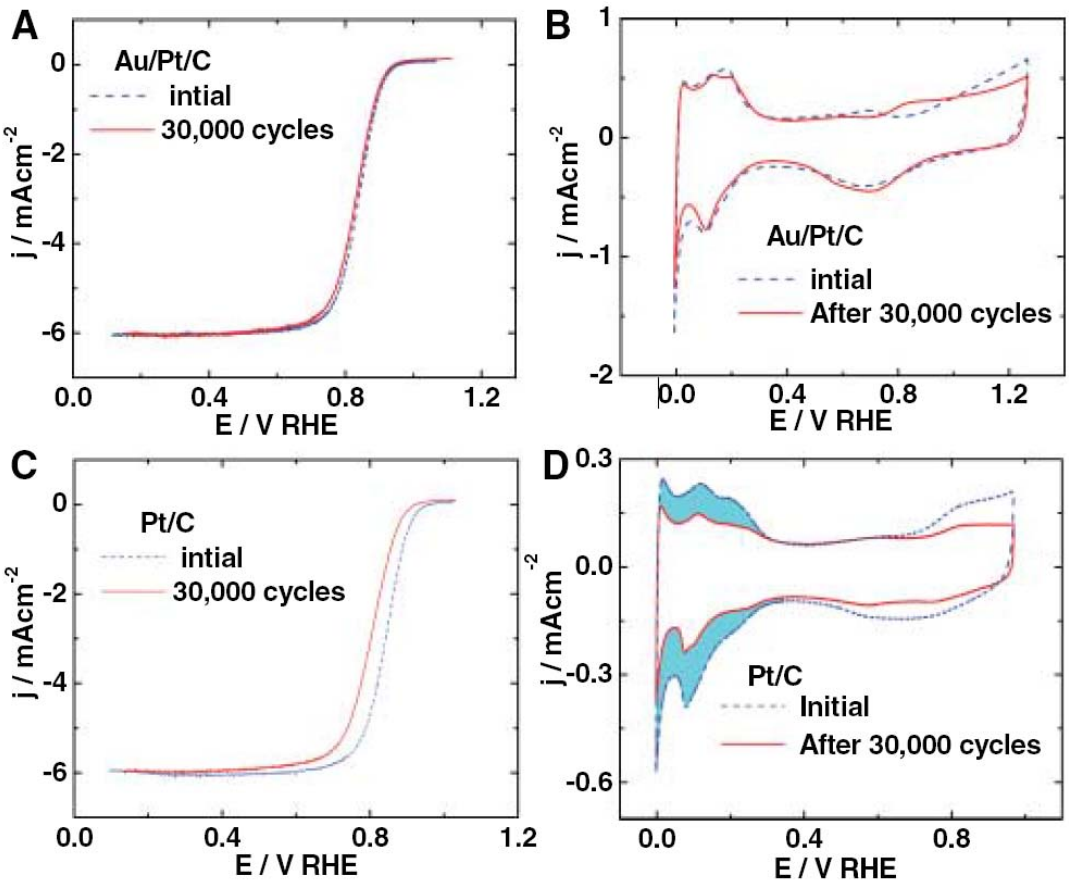

Figure 1.9 Polarization curves for the O_2 reduction reaction on Au/Pt/C (A) and Pt/C (C) catalysts on a rotating disk electrode, before and after 30,000 potential cycles. Sweep rate, 10 mV/s; rotation rate, 1600 rpm. Voltammetry curves for Au/Pt/C (B) and Pt/C (D) catalysts before and after 30,000 cycles; sweep rate, 50 and 20 mV/s, respectively. The potential cycles were from 0.6 to 1.1 V in an O_2-saturated 0.1 M $HClO_4$ solution at room temperature. For all the electrodes, the Pt loading was 1.95 mg (or 10 nmol) of Pt on a 0.164 cm^2 glassy carbon rotating-disk electrode. The shaded area in (D) indicates the lost Pt area [35].

Other supporting materials, such as graphene, [36, 37] doped graphene, [36, 38] nonporous carbon arrays, [39] graphitic carbon [40], TiC,[41] and TiO_2,[42] have

also been reported with improved ORR stability due to the high corrosion resistance of these supporting materials.

1.3.1.3 Shape Controlled Synthesis of Well-defined Pt nanostructures for the ORR in PEMFC

As the zero (0)-dimensional (D) Pt nanoparticles would be easily aggregated, driven by surface tension and the potential-dependent chemical dissolution of Pt, the shape-controlled synthesis of well-defined Pt nanostructures would effectively increase the stability and the ORR performance of Pt, owing to the highly active low energy crystalline facets and relatively few defect sites compared with the 0-D Pt nanoparticles.[43]

Recently, the synthesis of one-dimensional (1D) Pt nanostructures, such as Pt nanotubes or nanowires with long aspect ratios, was reported. Due to the inherent structural characteristics of 1D nanostructures, i.e., high stability, these nanotubes or nanowires were reported to show longer durability compared with the Pt/C. In addition, these nanotubes or nanowires usually have high surface active area, and thus, they were suggested as efficient electrocatalysts for the ORR, even when not supported on carbon supports. For example, Yu et al. discovered that one-dimensional platinum nanotubed with a diameter of only a few nanometers and a very high aspect ratio of 10 000 could be synthesized using ultrathin tellurium (Te) nanowire as both hard template and reducing agent,[44] and with these ultrathin Pt nanotubes, they fabricated a two-dimensional (2D) Pt nanowire (NW) membrane through a simple casting method (Figure 1.10). The free-standing Pt NW membrane could serve as an excellent ORR electrocatalyst with improved catalytic activity and

durability due to the preferential exposure of certain crystal facets and fewer surface defect sites in 1D nanostructures.[45]

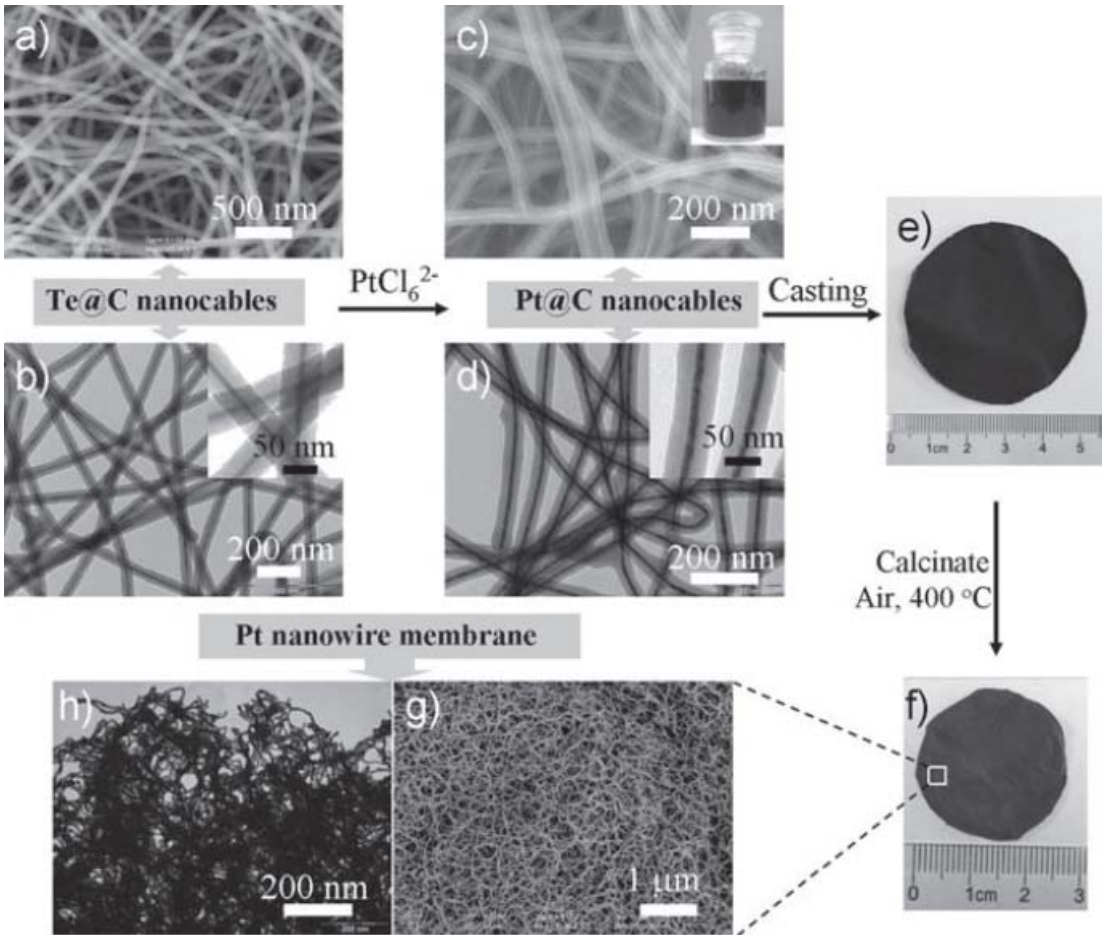

Figure 1.10 Fabrication process of the free-standing Pt NW membrane. a, b) Scanning and transmission electron microscope (SEM and TEM) images of Te@C nanocables. c, d) SEM and TEM images of Pt@C nanocables obtained from Te@C nanocables and H_2PtCl_6. The inset in (c) shows an optical image of a Pt@C nanocable suspension. The insets in (b) and (d) are the corresponding high magnification images. e) Optical image of a Pt@C nanocable membrane that was fabricated by a simple casting process. f) Optical image of free-standing Pt NW membrane obtained by calcination of a Pt@C nanocable membrane at 400 ° C in air for 1 h. g, h) SEM and TEM images of Pt NW membranes.[45]

Similarly, Dodelet et al. found that Pt nanowires could be synthesized using formic acid as a mild reducing agent. Pt single-crystal nanowires could be synthesized, and these nanowires could be assembled into flower-like hierarchical three-dimensional (3D) nanostructures (Figure 1.11a-b) [46]. When carbon supports [47] were used, these nanowire could be grown on the carbon supports (Figure 1.11c-d) giving risie to enhanced performance and much longer durability towards the ORR owing to the enlarged electroactive surface and the unique one-dimensional metallic nanostructures.

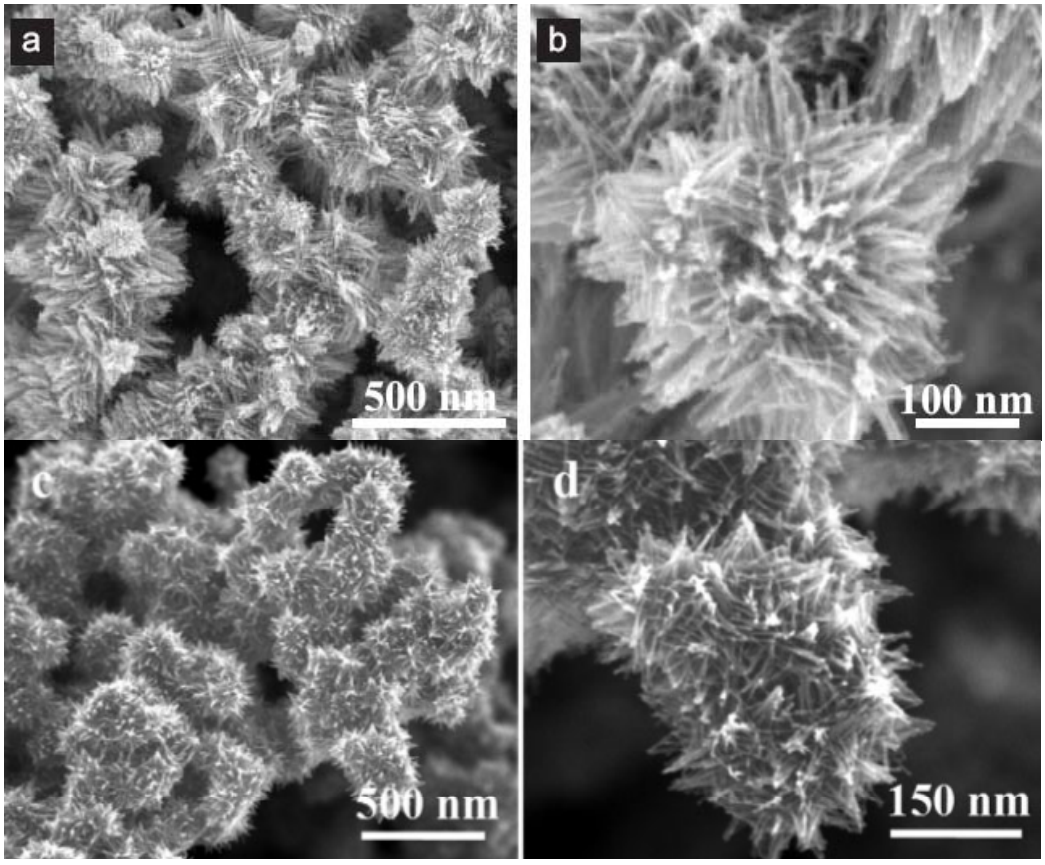

Figure 1.11 SEM images of a, b) Pt nanoflowers composed of nanowires; c, d) Pt nanowires grown on carbon black supports. [47]

Moreover with developments in the synthesis approach, Pt nanostructures in some other shapes, such as nanowires,[16, 46-48] nanotubes,[45, 49, 50] nanocubes,[51, 52] and octahedra,[51] were synthesized through various wet

chemistry methods. The shape of the Pt nanostructure could clearly also play a significant role in determining the performance of the electrocatalysts, i.e., the exposed facets of the Pt nanostructures could have different catalytic activities. Numerous reports have now provided evidence that the catalytic activity of Pt nanoparticles can be drastically enhanced by maximizing the expression of facets of the (100) and (111) planes, which are more active towards the ORR. [16, 44, 45] Specifically, in a H_2SO_4 solution, this activity increases in the order (111) < (100). This difference is caused by the stronger adsorption of sulphate anions on Pt (111) versus on Pt (100). This strong sulphate absorption deactivates the Pt (111) surface, thus limiting its O_2 adsorption and activation capability. When the ORR is tested in a $HClO_4$ solution with only weakly adsorption on Pt (111), the Pt (111) surface becomes more active than the (100) one.[26, 53] For example, Sun et al. [54] reported that the 7 nm Pt nanocubes were much more active than the other Pt NP shapes in catalysing the ORR in H_2SO_4. Figure 1.12 shows the cyclic voltammetry (CV) and ORR curves of Pt NPs with other shapes and the 7 nm Pt nanocubes obtained by scanning from 0 to 1 V. It can be seen that the electrochemical surface area and the ORR current density of the nanocubes is much higher than those of the Pt in other shapes, thus confirming that the ORR activities of the electrocatalysts are dependent on the different shapes of the nanoparticles because of the different ORR activities on different facets.

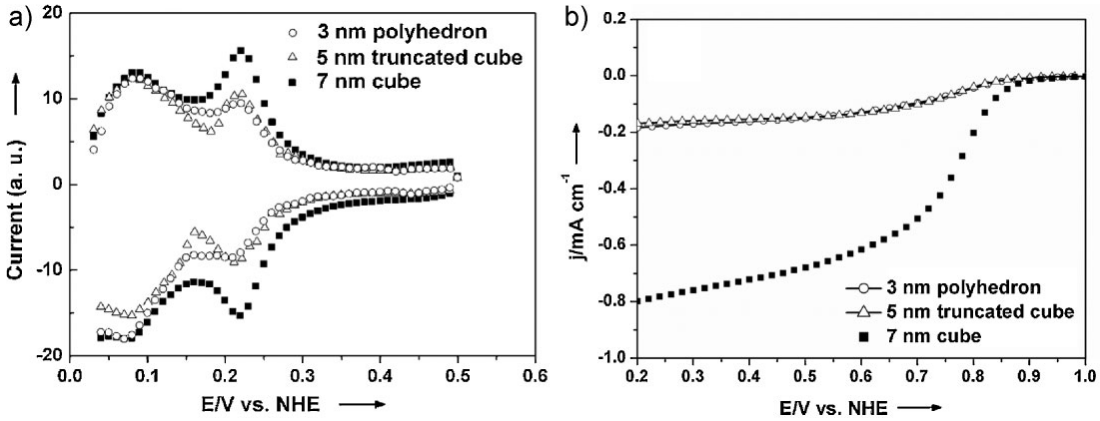

Figure 1.12 a) CVs of Pt NPs in various shapes. The potential was applied with the scanning rate of 10 mV s^{-1}. b) Disk current densities in oxygen saturated 0.5 M H_2SO_4 as a function of potential for different Pt catalysts at the rotation speed of 1600 rpm. [54]

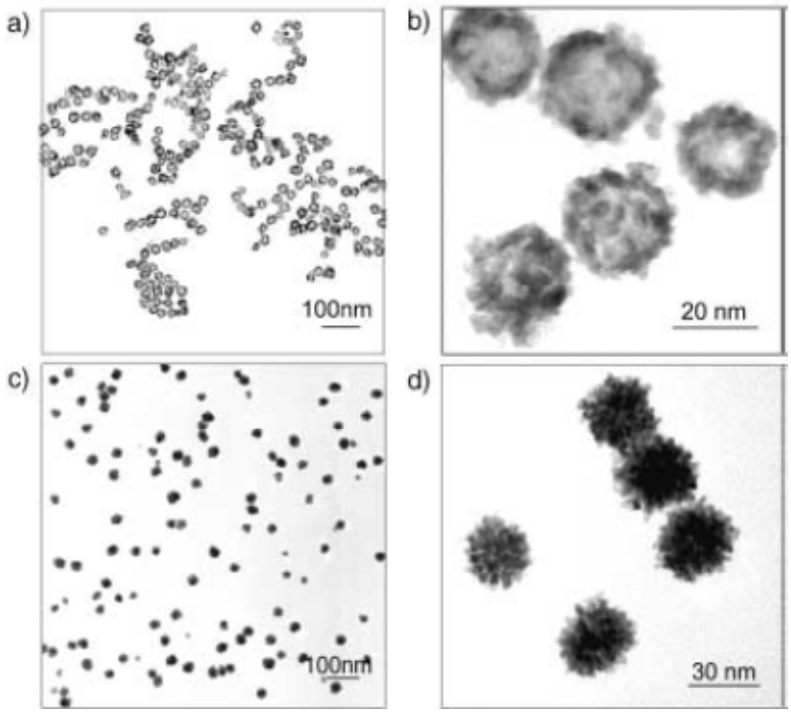

Figure 1.13 TEM images of Pt hollow nanospheres (a) and (b), and solid nanoclusters (c) and (d).[55]

Meanwhile, the development of Pt hollow nanostructures has also received much attention. Compared with their solid counterparts, hollow Pt nanostructured usually have the higher surface area and more active sites, which would be beneficial for

improving the ORR performance of Pt.[55] The hollow Pt nanoparticles are usually synthesized through galvanic replacement by the reaction between Pt ions and metallic nanoparticles with lower standard reduction potential, which was well demonstrated by Xia's group.[56] As the reaction takes place through a more complex pathway than theoretically predicted, some additional features, e.g., porosity, alloyed nanostructures would be also obtained *via* changing certain reaction conditions. For example, by changing the metallic nanoparticles from silver to cobalt, Bai et al. synthesized hollow Pt nanoparticles with porous shells constructed from numerous Pt grains (Figure 1.13).[55] It is also worth noting that by changing the reducing agent in the reaction system, Pt alloyed with other metals to form hollow shapes would be also acquired, and an example of this will be given in the following section.[57]

1.3.1.4 Pt Based Alloyed Nanostructures for the ORR in PEMFC

It was found that when there was alloying with another metal, the electronic and geometric structures of Pt would be changed accordingly, so that many unexpected catalytic activities of Pt could be largely enhanced and the stability of Pt could also be prolonged. In addition, using another cheap metal to substitute partially for Pt could effectively reduce the whole cost of the Pt catalyst, and hence, Pt alloyed with a second noble metal, such as palladium,[6, 57, 58] gold,[35, 59-61] or silver,[62] or with a second non-noble metal, such as one of the relatively cheap transition metal iron,[63-66] cobalt,[67-69] nickel,[70-73] and copper,[74-76] has been extensively studied and reported.

Pd was firstly investigated for alloying with Pt because of their similar intrinsic properties. Xia et al. reported Pd-Pt bimetallic nanodendrites, consisting of a dense

array of Pt branches on a Pd core, by reducing K_2PtCl_4 with L-ascorbic acid in the presence of uniform Pd nanocrystal seeds in an aqueous solution. These nanocrystals exhibited relatively large surface areas and particularly active facets toward the oxygen reduction reaction (ORR). The Pd-Pt nanodendrites were two and a half times more active on the basis of equivalent Pt mass towards the ORR than the state-of-the-art Pt/C catalyst and five times more active than the first-generation supportless Pt-black catalyst, Figure 1.14.[6]

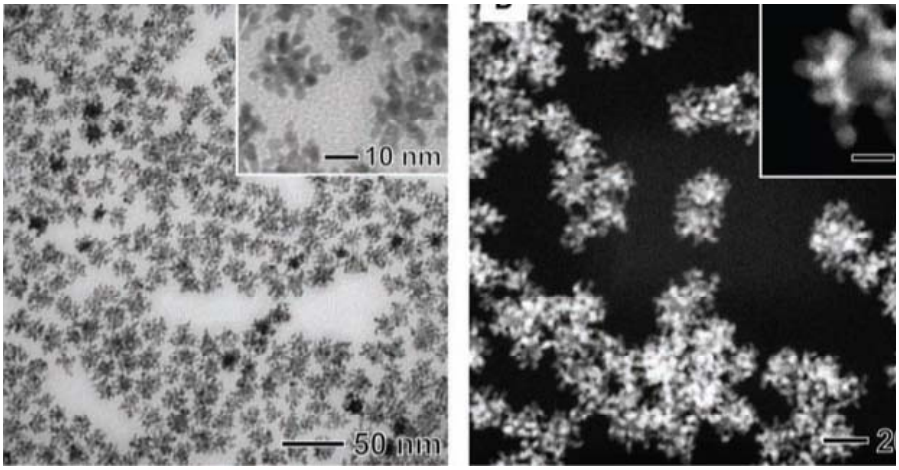

Figure 1.14 TEM images of Pd-Pt bimetallic nanodendrites. [6]

Later on, researcher found when Pt was alloyed with a transition metal, such as nickel, copper, or cobalt, the ORR performance of the alloyed electrocatalyst would be significantly increased due to the so called "strain effect" on the Pt atomic lattice. [77] For example, Huang et al. developed an effective wet-chemical method for the preparation of highly porous Pt_3Ni nanocrystals (Figure 1.15). The branch diameter in the Pt_3Ni was measured to be as thin as only 2.8 nm. More importantly, the obtained porous Pt_3Ni nanocrystals exhibited far better catalytic activity (1.006 mA/cm^2 and 0.757 A/mg_{Pt}) than the commercial Pt carbon black (Aldrich, 0.244 mA/cm^2 and 0.045 A/mg_{Pt}) and commercial Pt/C catalysts (E-TEK, 20 wt.% Pt, 0.177 mA/cm^2 and A/mg_{Pt}) under ORR conditions. The porous Pt_3Ni nanocrystals

were also more stable in the ORR and showed only small changes in ORR activity after 6000 potential sweeps.[70] These findings represented a more practicable way to develop low-cost, efficient ORR electrocatalystd compared with Pt alloyed with Pd, Au, etc.

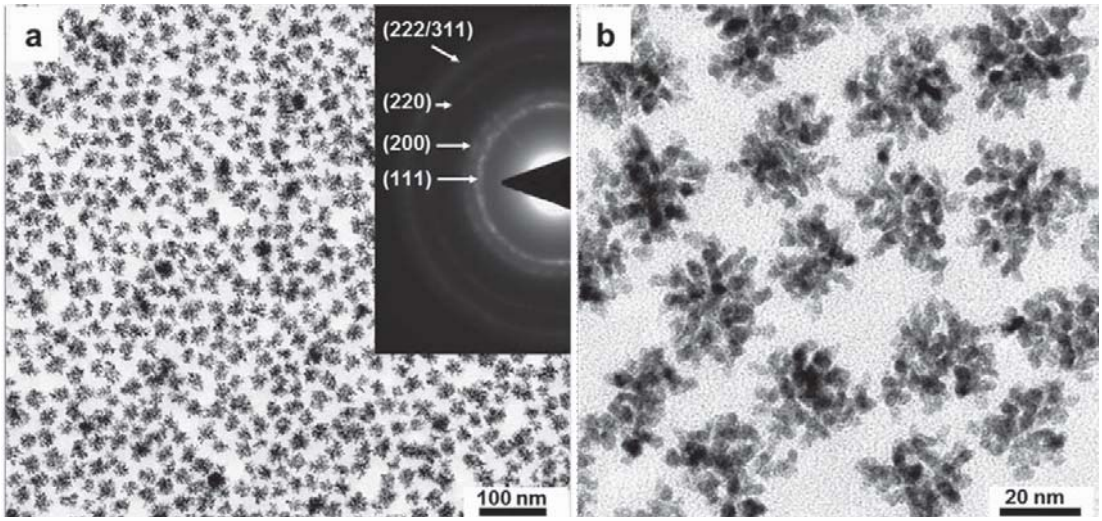

Figure 1.15 Morphology analyses for porous Pt_3Ni nanocrystals. a) Representative low-magnification TEM image, b) high-magnification TEM image. The inset in (a) shows the corresponding selected area electron diffraction (SAED) pattern.[70]

Besides the composition, the shapes of Pt alloyed nanostructures were also extensively investigated, and it was also found that in the alloyed Pt based nanostructures, different compositions and facets of the nanocrystals also showed differences in catalysing oxygen.[78] Moffact et al.[79] systematically studied the influence of the composition of Pt-Ni alloyed nanostructures on the ORR performance of the PtNi electrocatalysts synthesized through an electrodeposition method. Through varying the deposition potential, they synthesized various PtNi alloyed nanostructures with different compositions, and in perchloric acid, the maximum ORR specific activity of 2.8 mA/cm^2 at 0.900 V vs. reversible hydrogen electrode (RHE) was observed for alloys between Pt45Ni55 and Pt55Ni45. A peak

ORR mass activity of 0.78 A/mg_{Pt} at 0.900 V RHE was observed for alloy film compositions between Pt38Ni62 and Pt45Ni55 (Figure 1.16).

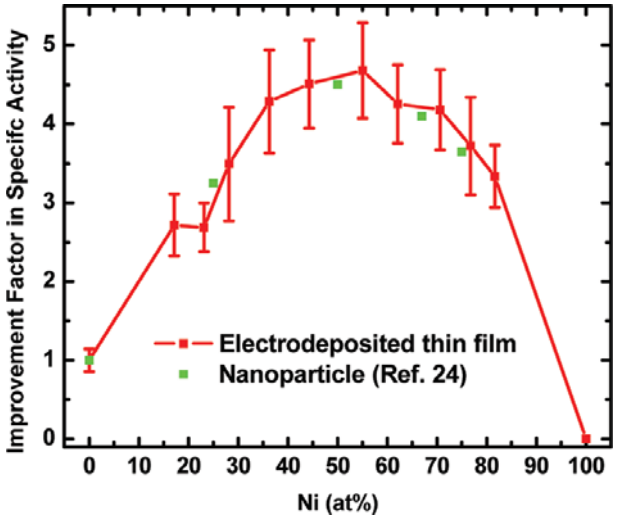

Figure 1.16 Comparison of the composition dependence of the ORR specific activity for two types of $Pt_{100-x}Ni_x$ alloys electrodeposited as thin films vs. nanoparticle ensembles. ORR measurements in these two studies were conducted under very similar experimental conditions. The improvement factor in the specific activity of the $Pt_{100-x}Ni_x$ alloy is relative to that of the elemental Pt counterpart.[79]

Hollow alloyed Pt nanostructures were also extensively studied owing to the superior advantages of the hollow structure and the alloyed material. For example, using palladium nanocrystals (NCs) as sacrificial templates through a modified galvanic replacement method, Han et al. synthesized various hollow shaped Pt-Pd nanocrystals (Figure 1.17), and they found that the type of surface facet plays a crucial role in determining the ORR activities of Pd-Pt NCs. The Pd−Pt nanocages prepared from octahedral Pd NC templates exhibited the largest improvement in ORR performance,[57] and this is a further indication of how the ORR performance is also highly dependent on the facets of the Pt alloyed nanostructures.

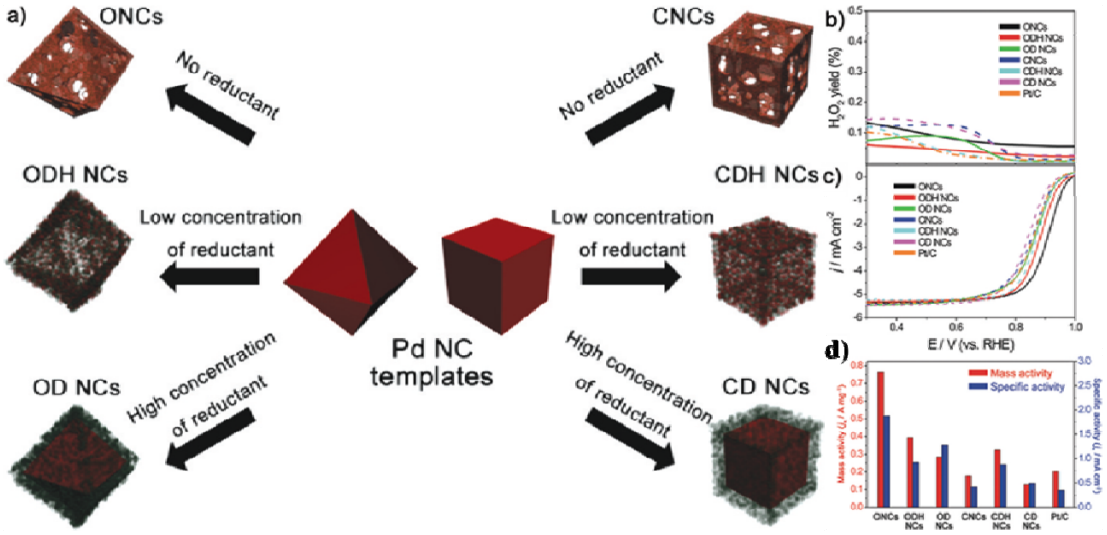

Figure 1.17 a) Schematic illustration of the synthetic parameters to produce various types of Pd-Pt bimetallic NCs from Pd NC templates. (b) H_2O_2 yield plots and (c) ORR polarization curves for the Pd−Pt bimetallic NCs and Pt/C obtained using a rotating ring-disk electrode (RRDE) in O_2-saturated 0.1 M $HClO_4$ at a scan rate of 10 mV s^{-1} and a rotation rate of 1600 rpm. The ring potential was held at 1.2 V vs. RHE. The current densities were normalized to the geometric surface area of the glassy carbon (GC) electrode (0.1256 cm^2). (d) Mass and area-specific activities at 0.85 V vs. RHE for the various catalysts. [57]

Several factors could account for the enhanced catalytic properties. The first hypothesis, as depicted in Figure 1.18, is that it is because of the decreased Pt-OH coverage caused by the lateral repulsion between the OH adsorbed on Pt and the OH or O adsorbed on the neighbouring transition metal atom.[77] As the adsorption of OH mostly occurs on the second metal, the oxygen reduction tends to become a 4e-process, thereby enhancing the performance of the electrocatalyst.

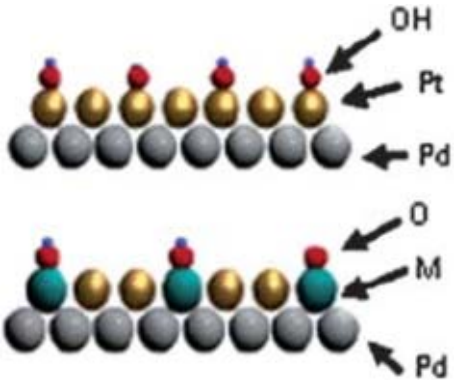

Figure 1.18 Model for the decreased OH coverage on Pt, caused by high OH or O coverage on a second metal M. [77]

Another factor to which the enhancement of the catalytic performance is attributed is the lattice strain effect, as evidenced by experiments reported by Ying et al.[80] On incorporating a metal atom such as Au with a large lattice constant, the lattice constant of Pt would be enlarged, and the performance towards the ORR of Pt-Au would be restrained. On the other hand, if AuCu is chosen as the core, with its smaller lattice parameter than Pt, the ORR performance and the stability of Pt@AuCu would be greatly increased (Figure 1.19). The atomic ensemble and electronic effects of bimetallic structures towards enhanced ORR catalytic performance have also received some limited research.[81]

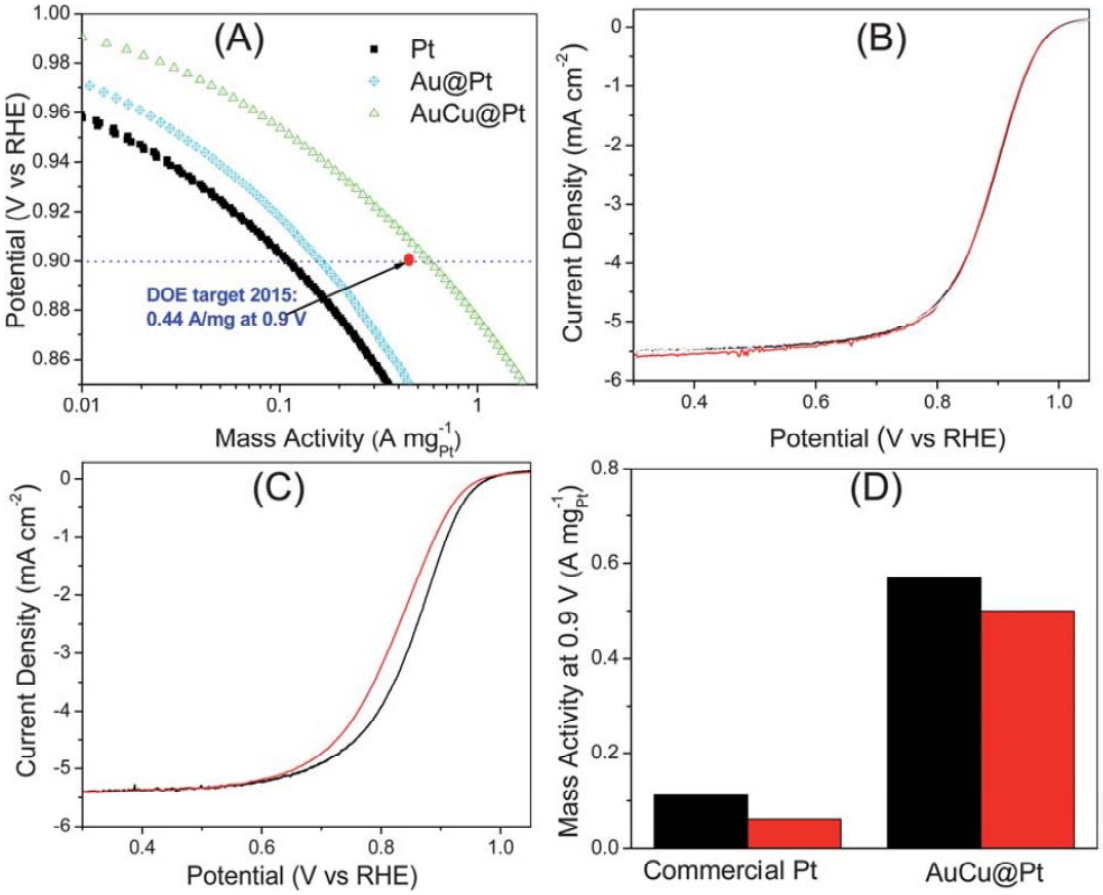

Figure 1.19 (A) Mass-normalized Tafel region of ORR measurements for Pt/C, Au@Pt/C, and AuCu@Pt/C catalysts in oxygen-saturated 0.1 M $HClO_4$, showing the positive-going scans. Sweep rate: 20 mV s^{-1}; 1600 rpm; room temperature. Pt loading was 15 µg cm^{-2} for Pt/C and Au@Pt/C, and7 .5 µg cm^{-2} for AuCu@Pt/C. Linear sweep voltammograms of (B) AuCu@Pt/C and (C) Pt/C catalysts before (—) and after (—) 30 000 cycles of stability testing. (D) Kinetic mass activities towards the ORR of commercial Pt/C and AuCu@Pt/C before (■) and after (■) 30 000 cycles of stability testing.[80]

1.3.2 Non-Pt Based Metal Nanostructures for the Oxygen Reduction Reaction in Acidic Medium for the PEMFC

1.3.2.1 Pd Based Nanostructures for the Oxygen Reduction Reaction in Acidic Medium for the PEMFC

Palladium (Pd), with some intrinsic electrocatalytic performance towards the ORR, is less expensive and more abundant than Pt and has received considerable attention recently. In comparison to Pt, Pd has a greater résistance to methanol in DMFCs and to CO in PEMFCs, and all these advantages have made Pd a substitute candidate for the ORR in PEMFCs.[82] The ORR exchange current density for Pd is only 10^{-10} A/cm^2, however, and its intrinsic ORR activity (i.e., at 0.9 V vs. reversible hydrogen electrode (RHE)) is nearly an order of magnitude lower than that of Pt in acidic medium. Furthermore, the stability is still a big problem for Pd-based electrocatalysts in PEMFCs.[24] Thus, to enhance the catalytic performance and stability of Pd, various methods have been reported including as shape-controlled synthesis of well-defined Pd nanocrystals,[43, 83] alloying Pd with another metal such as gold,[84] iron,[25, 85] nickel[86], copper [87, 88] or cobalt[89, 90], etc. Many of these outcomes have indicated the possibility of using Pd-based catalysts as more efficient and stable catalysts for the ORR than Pt/C. The mechanism for improved catalytic performance is very similar to that for Pt and thus is not described here in detail.

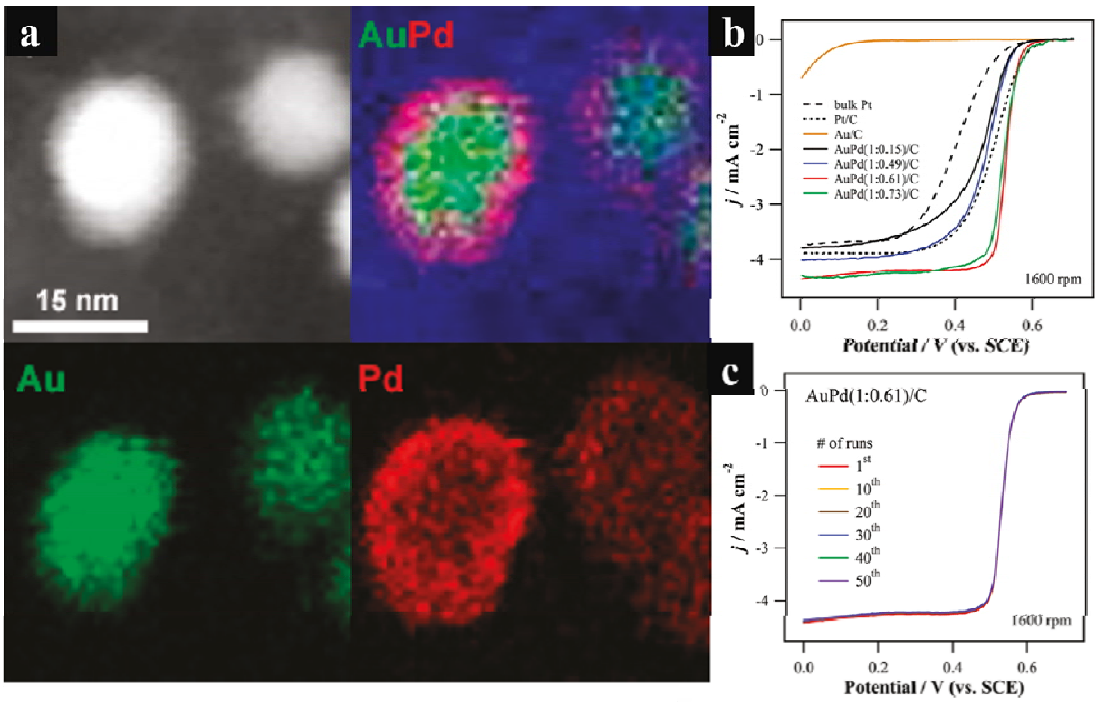

Figure 1.20 a) High angle annular dark field – scanning TEM (HAADF-STEM) image (top left panel) of AuPd(1:0.61)/C and its corresponding Pd (red) and Au (green) elemental mapping images. The blue colour of the top right panel corresponds to the carbon support of the AuPd(1:0.61)/C. b) Rotating disk electrode (RDE) voltammograms for oxygen reduction in O_2-saturated 0.5 M H_2SO_4 for bulk Pt, Pt/C, Au/C, AuPd(1:0.15)/C, AuPd(1:0.49)/C, AuPd(1:0.61)/C, and AuPd(1:0.73)/C electrodes at a scan rate of 10 mV s^{-1} with a rotation speed of 1600 rpm. The current density was obtained by normalization to the electrode geometric surface area (GSA). c) RDE voltammograms for the ORR obtained repetitively for 50 runs in an O_2-saturated 0.5M H_2SO_4 solution using an AuPd(1:0.61)/C loaded GC electrode (scan rate of 10 mV s^{-1}).[84]

Lee et al.[84] synthesized a series of carbon-supported Pd shell coated Au NPs for varying Pd precursor concentrations using a rather straightforward method. A porous Pd layer formed spontaneously without any reducing agent and completely encapsulated the Au NP core completely. RDE voltammetry results confirmed that

some of the AuPd/C exhibited better ORR activity than the commercial Pt/C in terms of the positive ORR onset and $E_{1/2}$ potentials, greater limiting current density, higher n value (~4), and steeper RDE curve slope in the mixed kinetic-diffusion controlled region, and the AuPd/C also showed good stability in the RDE tests (Figure 1.20). Pd alloyed with transition metals could also produce highly efficient catalysts towards the ORR, mainly because of the so-called strain effects and relatively smaller coverage of Pd-OH on the Pd atoms. For example Adzic et al. reported the synthesis of PdFe nanoparticles on carbon and they found that these nanoparticles exhibited higher ORR catalytic performance compared with the Pt/C, indicating the possibility of devising non-Pt efficient ORR catalysts.[25]

1.3.2.2 Other Precious Metal (Au, Ag, Ir, Rh, etc.) Based Nanostructures for the Oxygen Reduction Reaction in Acidic Medium for the PEMFC

Gold and silver were also reported to have some catalytic performance towards the ORR, however, their catalytic performance were relatively poor,[81, 91] while it should be mentioned that the synthesis of well-defined gold or silver nanoparticles in different shapes was relatively easier that that of Pt or Pd, mainly because of their higher standard reduction potential. Thus, Au and Ag were extensively studied and used as seeds to synthesize advanced nanostructures to mediate the properties of Pt or Pd.[92-97] Other metals such as tin[98, 99] and iridium[100] have also been reported to have relatively poor ORR activties due to the strong affinity for OH and O species, leading to the formation of surface oxide coverage, although the ORR activity of Ir could be increased by alloying with the first row of transition metals (TMs), and a high methanol tolerance could also be obtained by addition of metal chalcogenides to Ir.[98-101]

1.3.3 Other Catalysts for the Oxygen Reduction Reaction in Acidic Medium for the PEMFC

1.3.3.1 Macrocyclic Transition Metal Complexes for the Oxygen Reduction Reaction in Acidic Medium for the PEMFC

A large variety of transition metal (e.g., Fe, Co, Mn, etc.) macrocyclic complexes, such as N4-, N_2O_2-, N_2S_2--, O4-, and S4- systems showed a certain level of catalytic activity towards oxygen reduction [27, 28]. Among these macrocyclic transition metal complexes, the N4-chelate of a transition metal, such as iron- and cobalt-porphyrins, phthalocyanines, and teteraazannulenes, are the most popular active catalysts for the ORR, which is possibly because of the inductive and mesomeric effects of the ligands on the central ion [2, 27].

Normally transition metal macrocyclic complexes do not have long-term stability in concentrated acid or alkaline solution. It has been found that a thermal treatment at high temperature (typically above 800 °C) is necessary to obtain a stable catalyst [102, 103]. Even though the heat treatment could destroy the macrocyclic ring, the N4 ring structure in porphyrin and similar macrocycles is still retained. After heat treatment, not only would their stability be increased, but their ORR catalytic activity would also be increased, even though the enhancement mechanism is still not fully understood [104].

1.3.3.2 Transition Metal Nitrogen Containing Carbon Complexes (M-N-C) for the Oxygen Reduction Reaction in Acidic Medium for the PEMFC

Since the discovery that heat treatment could significantly increase the ORR activity as well as stability of catalysts in the 1970s [103], heat treatment has come to be used in many other non-N4-macrocycles, and furthermore it was pointed out that

highly catalytic sites could also be created even when the metallic centre was not chemically attached to the macrocycle [105]. Soon afterwards, many other catalysts were prepared in a similar manner, using much cheaper and more common inorganic salts and carbon as starting materials and a wide range of N-containing chemicals as the nitrogen source[103, 106-113]. Recently, Asefa et al.[111] used mesoporous silica as template, and iron salts and polyaniline as the Fe, C, N sources to synthesize mesoporous Fe-N-C catalysts showing comparable catalytic performance towards the ORR with Pt/C. With the same concept, Müllen et al.[114] reported the synthesis of Co-N-C and Fe-N-C using vitamin B12 and polyaniline-Fe as the metal, carbon, and nitrogen sources. Their catalysts showed remarkable ORR activity in acidic medium (half-wave potential of 0.79 V, only ~58 mV deviation from Pt/C), high selectivity (electron-transfer number > 3.95), and excellent electrochemical stability (only 9 mV negative shift of half-wave potential after 10 000 potential cycles). It has been shown that the content of metal species plays a pivotal role in determining the ORR catalytic performance of a catalyst, and thus, the optimal metal content has been studied in many research groups. It was found that ORR activity increases as the iron content increases from 1 to 10 wt.%, but the addition of more iron results in no significant change to the activity [115].

1.3.3.3 Other Catalysts for the Oxygen Reduction Reaction in Acidic Medium for the PEMFC

Other groups of materials such as transition metal chalcogenides and transition metal carbides also show catalytic activity towards the ORR. Chalcogenides can catalyse either 2-electron or 4-electron O_2 reduction, depending on the catalyst used. For example, $Mo_4Ru_2Se_8$, $Ru_{1.92}Mo_{0.08}SeO_4$, $Ru_xS_y(CO)_n$, Ru_xSe_y, etc. catalyze 4-electron

transfer, while W-Co-Se catalyzes a 2-electron O_2 reduction reaction.[22] The transition metal carbides, especially tungsten carbide, represent another type of non-noble-metal catalyst showing activity towards the oxygen reduction reaction. For example, Trassatti et al. reported[116] that WC, TaC, TiC, and TiN showed catalytic activity towards the ORR in acid solutions, although these materials are not stable either in acid or in alkaline solution.

1.4 Electrocatalysts for the Oxygen Reduction Reaction in Alkaline Medium for the AEMFC

The kinetics of the ORR could be greatly enhanced, and the overpotential of ORR could be significantly decreased in alkaline medium, and therefore, a wider selection of electrocatalysts could be realized than in the acidic medium. Typically, Pt is still the most efficient electrocatalyst for the ORR in alkaline medium, however, as the kinetics of the ORR proceeds through a faster pathway, low-cost and more efficient metal catalysts such as palladium[23, 24, 81, 117, 118] and much cheaper electrocatalysts such as doped carbon[5, 103, 109, 119-121] and metal oxides on doped carbon[122-124] were also developed with comparable electrocatalysts in the last decade and are still attracting significant interests as a current research area. With the development of novel solid alkaline membrane with high anion exchange conductivities and the development of the anion exchange ionomer, [3, 125-129] the performance of the AEMFC has been greatly increased to the same magnitude as that of the PEMFC.[3, 126, 128, 130] All these advantages and developments have added further incentives towards developing lower cost but highly efficient electrocatalysts for the ORR in the AEMFC.

1.4.1 Pd-based Electrocatalysts for the Oxygen Reduction Reaction in Alkaline Medium for the AEMFC

Palladium (Pd), with poorer intrinsic electrocatalytic performance towards the ORR compared to Pt in acidic medium, is competitive with Pd in catalysing the ORR in alkaline medium due to the faster reaction kinetics of the ORR in alkaline medium. The abundance of Pd is 200 times greater than that of Pt, and the price of Pd is only 20%-25% of that of Pt, which makes Pd a realistic alternative as a fuel cell catalyst in alkaline medium. To further decrease the cost of Pd, Pd-based alloyed nanostructures were synthesized and showed enhanced ORR performance over that of Pt/C due to the lattice shrinkage or electronic changes.[24, 81, 117, 131]

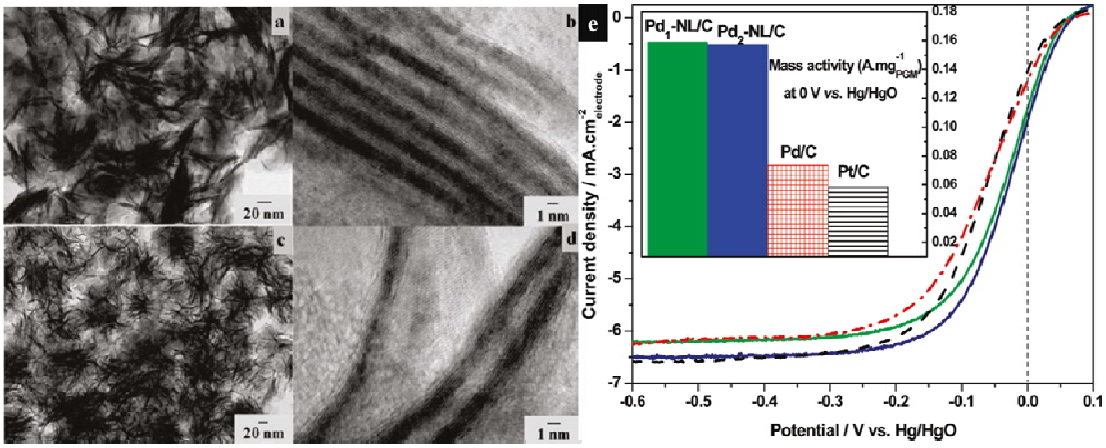

Figure 1.21 a-d) TEM images of the synthesized PdFe nanoleaves, and e) the ORR polarization curves of commercial Pt/C, Pd/C (self-prepared by the EG method), Pd_1-NL/C, and Pd_2-NL/C in 0.1 M NaOH, with bubbling O_2 (conditions: 10 mV/s, 2500 rpm, room temperature). [24]

For example, Li et.al [24] reported novel PdFe nanoleaves (NLs) with a diameter of ~2 nm and a large surface are of > 50m^2/g prepared through a wet-chemistry-based solution phase reduction synthesis route. They found that the PdFe NLs exhibited a high reactivity towards electrocatalytic reduction of oxygen in 0.1 M

NaOH electrolyte and exhibited a 3.0× increase in specific activity and a 2.7× increase in mass activity, compared to those of a commercial Pt/C catalyst (at 0 V vs. Hg/HgO). The electrocatalytic activity enhancement can be attributed to the unique nanoleaf structure, i.e., extensive Pd (111) facets, large surface area, and more resistance to Pd oxide formation. In addition, Pd alloyed with other metals such as silver,[81, 117] nickel,[86, 131] etc. were also reported and showed competitive ORR performance compared with the Pt/C. These findings have clearly provided a promising strategy for producing highly efficient and low-cost electrocatalysts for the ORR in alkaline medium for the AEMFC.

1.4.2 Doped Nano-Carbon Materials for the Oxygen Reduction Reaction in AEMFCs

Following the discovery that N-doped vertically aligned carbon nanotubes could be used as a metal-free efficient ORR catalyst [5], various new metal-free nitrogen doped carbon catalysts have been developed for the ORR for fuel cell applications. These discoveries have raised the possibility of using heteroatom (N[106, 132], B[121, 133, 134], S[120, 135-137], P[138, 139]) doped carbon materials to substitute for the commonly used high cost Pt electrocatalysts as low cost, “poison”-resistant, and highly stable catalysts for the ORR process. Carbon black (CB) [140-142], carbon nanotubes (CNTs) [5, 143-148], reduced graphene oxide (rGO) [5, 121, 149-154], and graphene sheets (GS) [120] have all been proven to be promising efficient catalysts upon doping. Among the various dopant atoms, N-doping is the most widely available and thus the most widely used. N-doping could effectively alter the spin density and the charge distribution of neighbouring atoms, which would induce the activation of the carbon region on the surface of the nitrogen-doped carbons.[155,

156] Through extensive research, it has been found that controllable doping (nitrogen configuration) and the doped carbon material play a pivotal role in determining the catalytic performance.

1.4.2.1 Approaches to Synthesizing Doped Carbon Materials

Various methods have been developed to doping foreign atoms into the graphene lattice, including chemical vapor deposition,[119] thermal annealing with nitrogen-containing precursors at high temperatures[111, 120, 121, 132, 135, 157, 158], chemical reactions at relatively low temperatures[124, 137, 156, 159], and nitrogen plasma treatment.[151, 160] These methods have all proved to be effective ways to produce nitrogen doped carbon materials with various advantages and disadvantages.

Thermal annealing of the nitrogen source, such as ammonia or N-containing polymers, is the most widely used method, and the nitrogen content and nitrogen configuration can be well tuned *via* controlling the annealing conditions. Dai et al. first reported that nitrogen doped carbon nanotube arrays produced through annealing under ammonia atmosphere could be used as a metal-free ORR catalyst with full methanol tolerance and better stability.[5] Their findings opened up an exciting approach to explore efficient catalysts towards the ORR with low cost and environmental friendliness. Following their research, many other N-containing polymers such as urea,[161, 162] melamine,[107, 151, 157] and polypyrrole[158, 163] were reported as dopants in carbon materials with good ORR catalytic performance [21, 150, 164-177].

When nitrogen atoms are introduced into graphene (G), three different types of N-functional groups can be formed: pyridinic, pyrrolic, and graphitic N, as shown in Figure 1.22. Pyridinic N refers to N atoms at the edges or defects of the G-plane,

pyrrolic N atoms are incorporated into five-membered heterocyclic rings, and graphitic N refers to N atoms that incorporate into and substitute for carbon atoms within the G-plane. It has been well documented that with increasing temperature, the nitrogen content would be reduced, possibly because the pyrrolic N is not stable at high temperature [119]. The quaternary (graphitic) N and pyridinic N components could be greatly increased through increasing the annealing temperature, however. From comparing with the performances of different samples, it is believed that the quaternary N and pyridinic N, rather than the pyrrolic N, serve as catalytically active sites for the ORR, and this will be discussed in detail later on [106, 119, 156, 158].

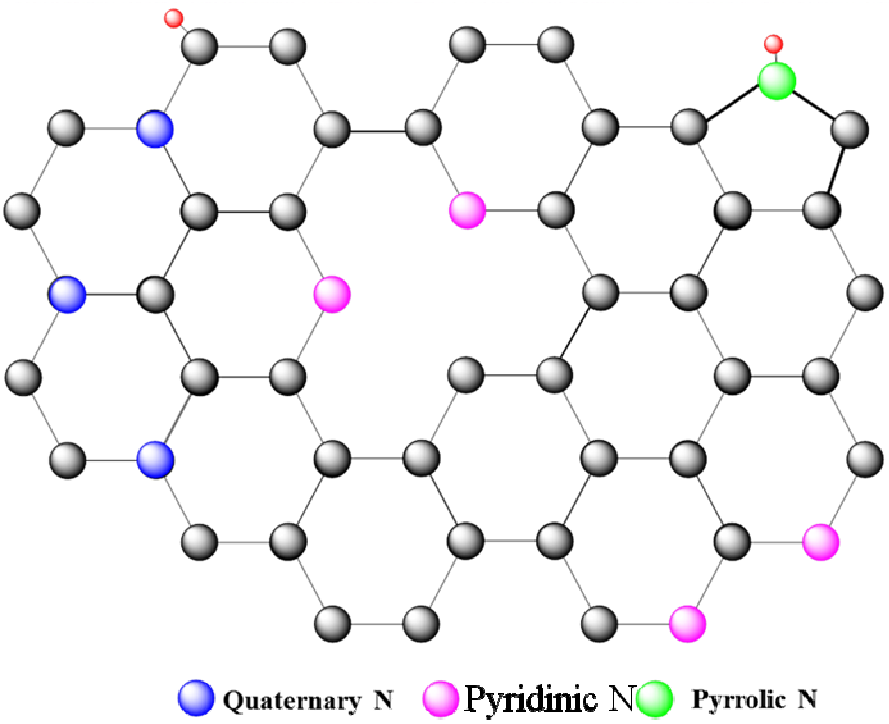

Figure 1.22 Schematic representation of N-doped graphene (grey balls for carbon atoms, different coloured balls for different types of nitrogen atoms; a possible defect structure is shown in the middle of the ball-stick model)

The solvent thermal method was also proposed to be an efficient way to produce N-doped carbon materials. The oxygen-containing functionalities could reacted with nitrogen-containing salts, such as ammonia,[124] urea,[178], ammonium thiocyanate

(NH_3SCN),[137] and ammonia boron trifluoride (NH_3BF_3)[159] at elevated temperatures and be incorporated into the carbon lattice through cyclization/rearrangement. Unfortunately, the nitrogen configuration cannot be well controlled during the doping process. Recently Dai et al. [124] reported the synthesis of nitrogen doped graphene through hydrothermal reaction with ammonia, and they then explored the application of cobalt oxide and nitrogen doped graphene as a synergistic catalyst for the ORR. Even though the cobalt oxide showed limited ORR performance, their composite exhibited remarkably high catalytic performance towards the ORR, which is comparable to that of Pt/C, but with excellent methanol tolerance and longer term stability. (Figure 1.27) They ascribed the high performance to the strong synergistic effect between nitrogen doped graphene and the cobalt oxide.

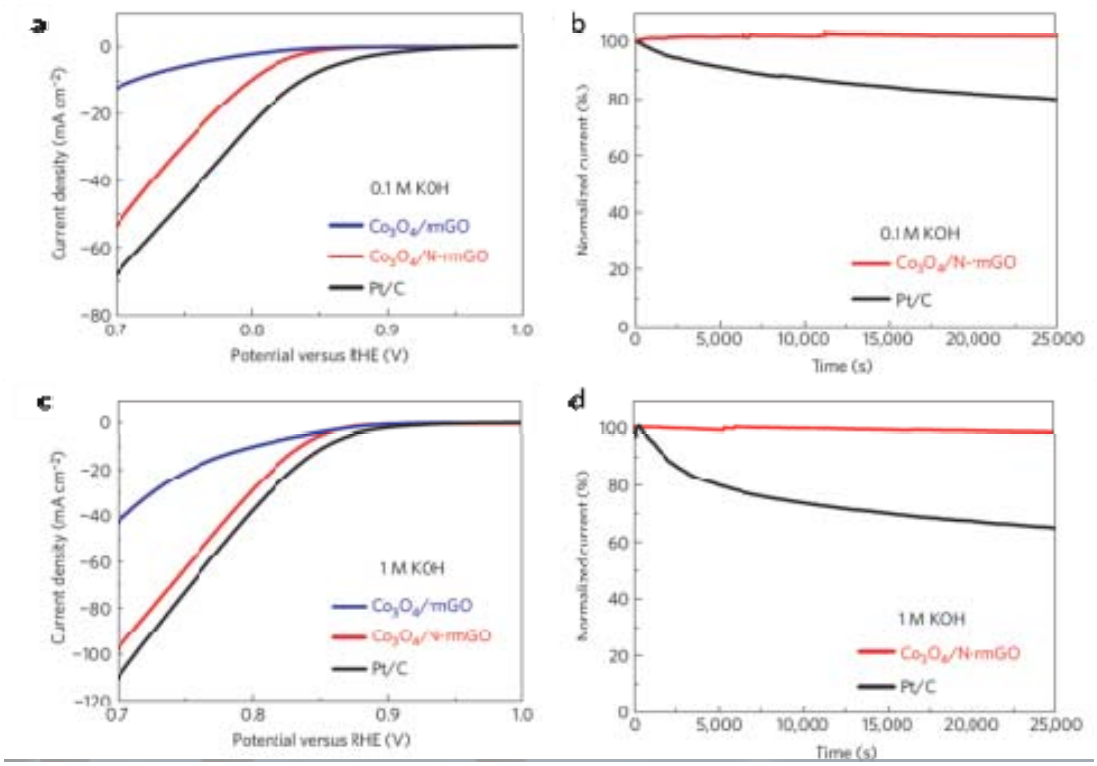

Figure 1.23 ORR performance and stability of catalysts. a) Oxygen reduction polarization curves and b) chronoamperometric responses (percentage of current retained versus operation time) of Co_3O_4/rmGO, Co_3O_4/N-rmGO, and a high quality

commercial Pt/C catalyst in 0.1 M KOH electrolyte. c–d) Oxygen reduction polarization curves (c) and chronoamperometric responses (d) after the electrolyte is changed to 1 M KOH.[124]

Plasma treatment is a simple approach to material surface modification and can be used for the introduction of foreign atoms, groups, or structures onto bulk scaffold surfaces. N-doped carbon materials could also be fabricated through exposure to nitrogen plasma treatment for a certain time. The N-content could be well regulated by varying exposure time, although again, the nitrogen configuration is beyond control with this method.[151]

1.4.2.2 Nitrogen Doped Graphene Based Materials for the Oxygen Reduction Reaction in AEMFCs

Carbon materials also play an important role in determining the electrocatalytic performance of the doped carbon electrocatalyst. Beginning with Dai's research on nitrogen doped vertically aligned carbon nanotubes,[5] various carbon materials, including carbon black,[179] carbon nanotubes,[5, 146, 180-183] mesoporous carbon,[111, 135, 184, 185] and other novel carbon architectures[161] were synthesized and utilized for doping with nitrogen, and their electrocatalytic performance towards the ORR was studied. They showed appreciable catalytic performance with better poison resistance.

Among the various nano-carbon materials, chemically derived graphene oxide [186-188] has been extensively used for doping owing to its easy preparation, high surface area, and good thermal and electricity conductivity [156]. The introduction of foreign atoms into the graphene lattice could effectively alter the spin density and charge distribution of the neighbouring inert carbon atoms and thus provide

reasonable catalytic activity [20, 135]. Müllen et al.[119] reported the synthesis of nitrogen-doped ultrathin graphene using graphene oxide as precursor, based on annealing under ammonia atmosphere at different temperatures. Through carefully control of the annealing conditions and comparison of the corresponding X-ray photoelectron spectra (XPS), they found that the nitrogen configuration could be well tuned by varying the annealing temperature. Their results showed that an outstanding ORR performance of the N-doped ultrathin graphene oxide could be obtained with annealing at 900 °C. Combined with the XPS results, they concluded that the electrocatalytic activity of nitrogen-doped graphene (NG) prepared between 600 and 900 °C could be ascribed to the enhancement of both the pyridinic and the graphitic N contents, while the lower activity of NG1000 with respect to NG900 should be due to the reduced pyridinic N in the matrix. Given that the two types of nitrogen atoms with strong electron-accepting capability can create a net positive charge on the adjacent carbon atoms in the resulting NG sheets, they assist with the adsorption of oxygen and can readily attract electrons from the anode, thus facilitating the ORR (Figure 1.24).

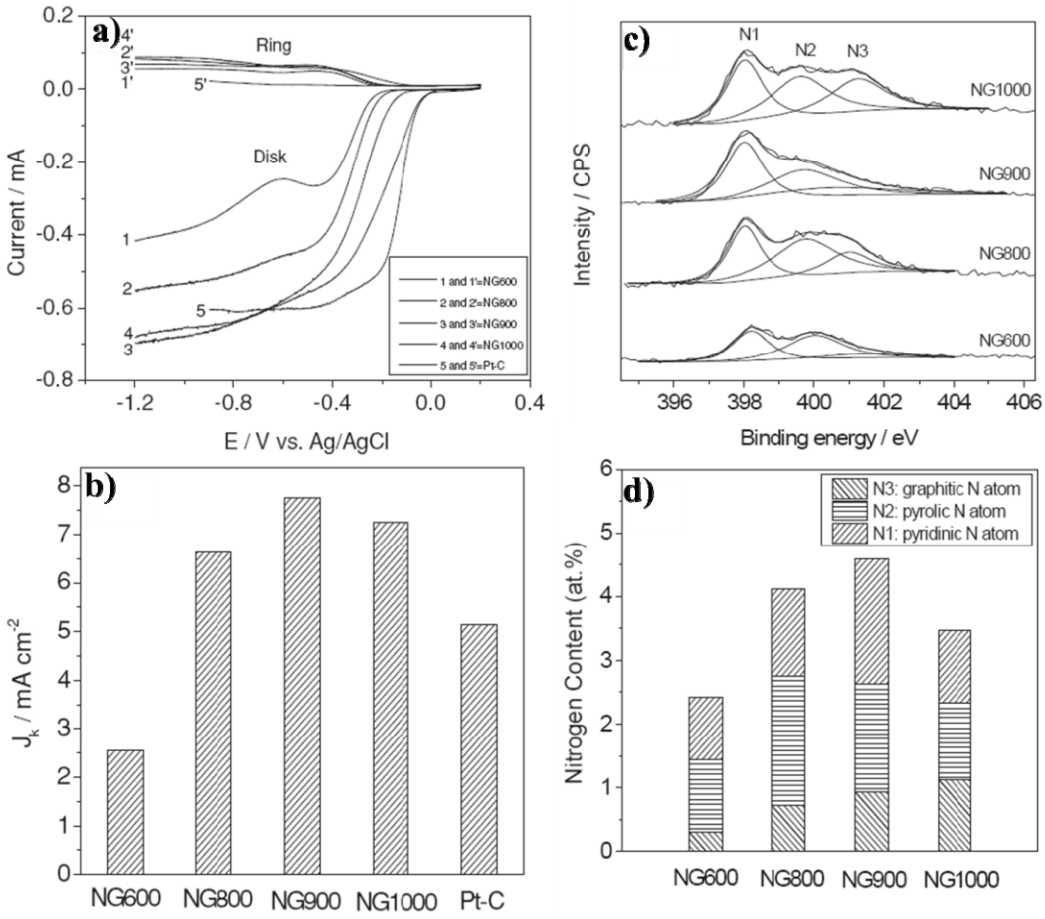

Figure 1.24 (a, b) Electrocatalytic activity of N-doped graphene towards the ORR. a) Rotating ring disk electrode (RRDE) linear sweep voltammograms (LSVs) of NG600, NG800, NG900, NG1000, and Pt/C at a rotation rate of 1600 rpm. b) Electrochemical activity represented by the kinetic limiting current density (J_k) at – 0.50 V for all NG and Pt-C samples. (c) High resolution N 1s XPS spectra of NG samples. The peaks are fitted to three energy components centred at around 398.0, 400.0, and 401.3 eV, corresponding to pyridinic-N (N1), pyrrolic-N (N2), and graphitic-N (N3), respectively. d) The contents of the three nitrogen species (N1, N2, and N3) in NG sheets.[119]

It should be noted that the porosity of the doped carbon materials is very important for providing large surface area and ample active sites for catalysing oxygen and allowing mass transport. The chemically derived graphene sheets are

vulnerable to stacking and aggregation, however, during the thermal treatment processes, especially at high temperature when doping, due to the strong van der Waals and hydrogen bonding between the water molecules and graphene sheets[189, 190], which would decrease the specific surface area, cause losses of active sites and further hamper uniform doping, thereby compromising the overall properties of the electrocatalyst.[157, 188-202] Thus, to further increase the ORR activity of the N-doped graphene, graphene architectures such as mesoporous graphene and graphene aerogel were synthesized and doped. Qiao et al.[135] used silicon nanoparticles as hard templates for synthesizing N, S co-doped mesoporous graphene, and this novel porous materials shows excellent catalytic activity, including a highly positive onset potential and very high kinetic limiting current comparable with those of the commercial Pt/C (Figure 1.25).

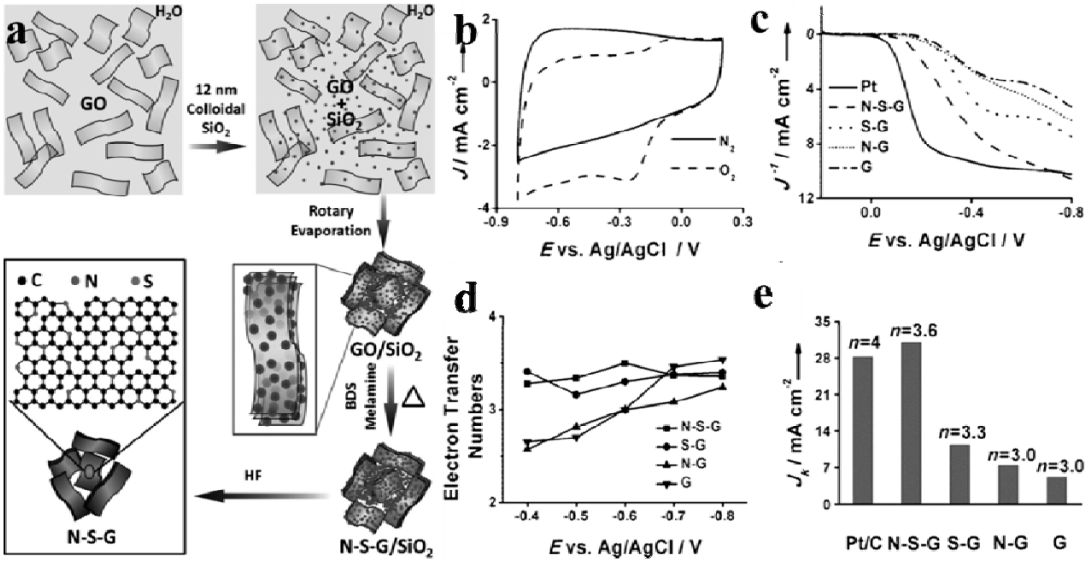

Figure 1.25 a) Fabrication of N and S dual-doped mesoporous graphene (N-S-G) nanosheets from graphene oxide. b-e) Electrochemical characterisation of the N-S-G, N-G, S-G, G, and the Pt/C. b) CV curves of the N-S-G in O_2- or N_2-saturated electrolyte. b) LSVs of different samples at 1600 rpm. d) Koutecky-Levich (K-L)

plots of different samples at − 0.6 V. e) Kinetic limiting current of different samples, as well as the corresponding electron-transfer numbers at − 0.6 V. [135]

Graphene aerogel, which is synthesized *via* a feasible self-assembly hydrothermal method, represents a novel class of 3D macroporous graphene architectures with good mechanical properties.[158, 159, 196, 197, 203] The 3D interconnected macropores can offer more active sites, multiple electron and ion transport pathways, and easy access to the oxygen and electrolyte, thus minimizing the transfer resistance of ions and electrons between the bulk electrode and the electrolyte.[137, 158, 159, 195, 197, 203-206]. These excellent features suggest that graphene aerogel could work as an outstanding ORR catalyst after doping. Müllen et.al demonstrated the synthesis of Fe_3O_4 supported on nitrogen doped graphene aerogels (N-GAs, Figure 1.26).[158] The graphene hybrids show an interconnected macroporous framework of graphene sheets with uniform deposition of Fe_3O_4 NPs. In studying the effects of the carbon support on the Fe_3O_4 NP ORR catalyst, we found that Fe_3O_4/N-GAs exhibits a more positive onset potential, higher cathodic density, lower H_2O_2 yield, and higher electron transfer number for the ORR in alkaline media than Fe_3O_4 NPs supported on N-doped carbon black (Fe_3O_4/N-CB) or N-doped graphene sheets (Fe_3O_4/N-GSs), which reveals the significance of the porous structure in catalysing oxygen reduction.

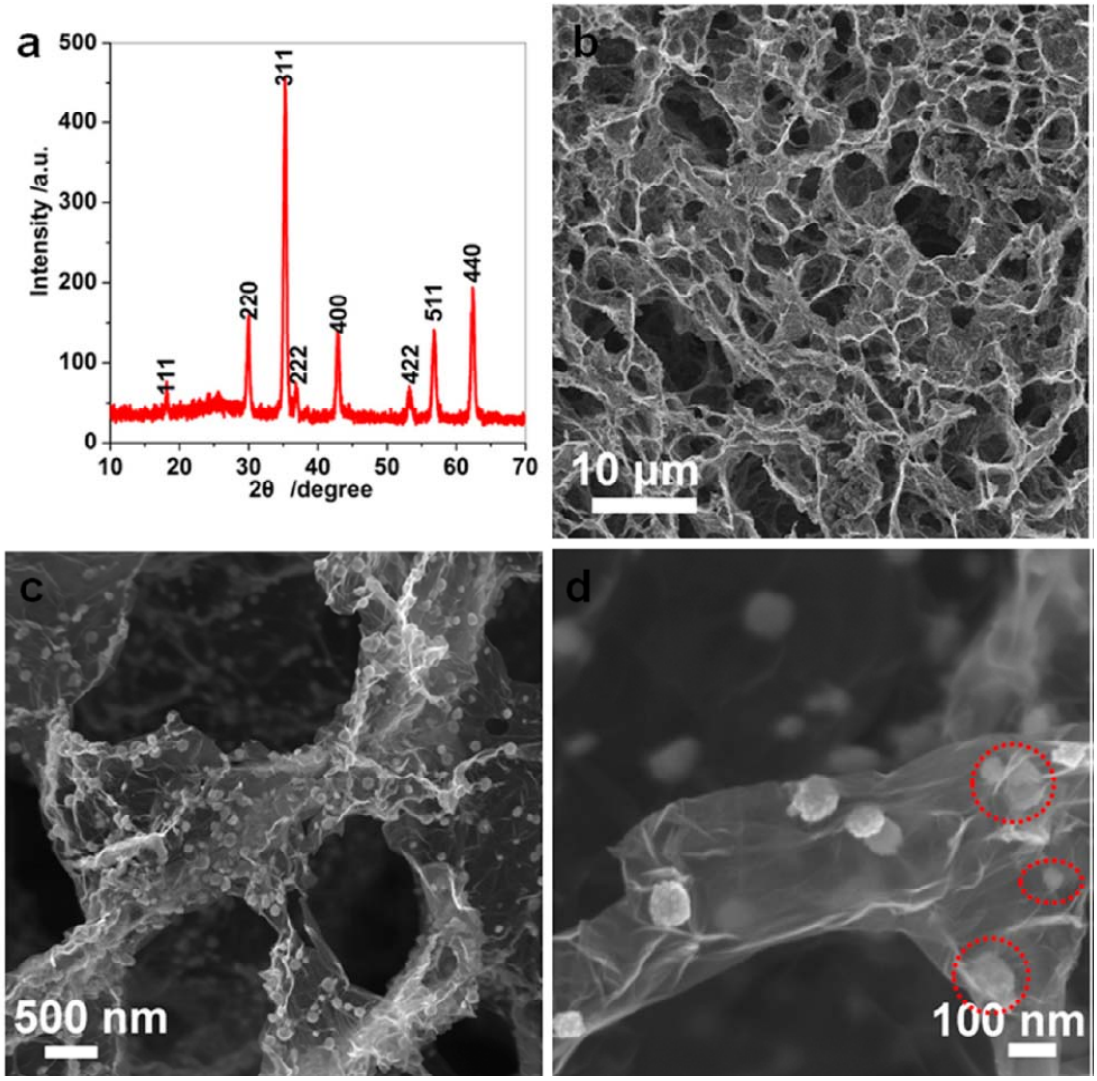

Figure 1.26 Structure and morphology of Fe_3O_4/N-GAs catalyst. (a) XRD pattern and (b−d) typical SEM images of Fe_3O_4/N-Gas, revealing the 3D macroporous structure and the uniform distribution of Fe_3O_4 NPs in the GAs. The red rings in (d) indicate Fe_3O_4 NPs encapsulated in thin graphene layers.[158]

1.4.3 Metal Oxides Supported on Nitrogen Doped Carbon as Enhanced Electrocatalysts for the ORR in AEMFCs

Metal oxide crystals, such as Fe_xO_y,[158] Co_xO_y,[122-124, 207-209] Cu_xO_y,[210] Mn_xO_y[211, 212], which show poor ORR catalytic performance themselves, could be used as efficient catalysts for the ORR in alkaline medium if they were supported

with some kind of nitrogen doped or un-doped carbon support [123, 124, 207, 209, 210]. Moreover, in a promising development, when nitrogen doped graphene was used as the carbon support, the unique charge transfer between the graphene-metal interface [207] and the "synergistic effects" between nitrogen, carbon, and cobalt atoms could effectively alternate the local electronic structure of the electrocatalyst thus promoting the electrocatalytic activity towards the ORR. [122, 124]

Dai et al. [124] first explored the application of cobalt oxide and nitrogen doped graphene as a synergistic catalysts for the ORR. Even though both graphene oxide and cobalt oxide showed limited ORR performance on their own, their composite showed remarkably high catalytic performance towards the ORR, which is comparable with that of Pt/C, but with excellent methanol tolerance and longer term stability (Figure 1.23). They ascribed the high performance to the strong synergistic effect between the nitrogen-doped graphene and cobalt oxide. Following their research, the novel metal oxides $NiCo_2O_4$ [122] and $NiCo_2S_4$ [136] coupled with graphene were also reported to have good electrocatalytic performance.

When alloying with a second atom in the oxide, the ORR catalytic performance would also be enhanced [122, 212], which provides a new route to explore the range of ORR catalysts based on metal oxides. With respect to this, Dai et al. [213] synthesized a novel $MnCo_2O_4$/N-doped reduced graphene oxide (N-rGO) nanosheet hybrid as a highly efficient electrocatalyst for the ORR in KOH aqueous solution by taking advantage of the high electrocatalytic activity of $MnCo_2O_4$ compared to pure Co_3O_4 and the strong coupling with N-rGO. The nucleation and growth method results in covalent interaction between the $MnCo_2O_4$ NPs and N-rGO nanosheets, giving rise to much higher activity and durability than a simple physical mixture of $MnCo_2O_4$ NPs and N-rGO (Figure 1.28). Moreover, the Mn substitution mediates the

size and phase of $MnCo_2O_4$ and increases the activity of the catalytic sites of the hybrid material, which eventually boosts the ORR activity compared with the pure Co_3O_4/N-rGO hybrid. Similarly, $NiCo_2O_4$-rGO [122] and $NiCo_2S$-grahene composites[136] were also reported with improved ORR catalytic activities and better methanol tolerance.

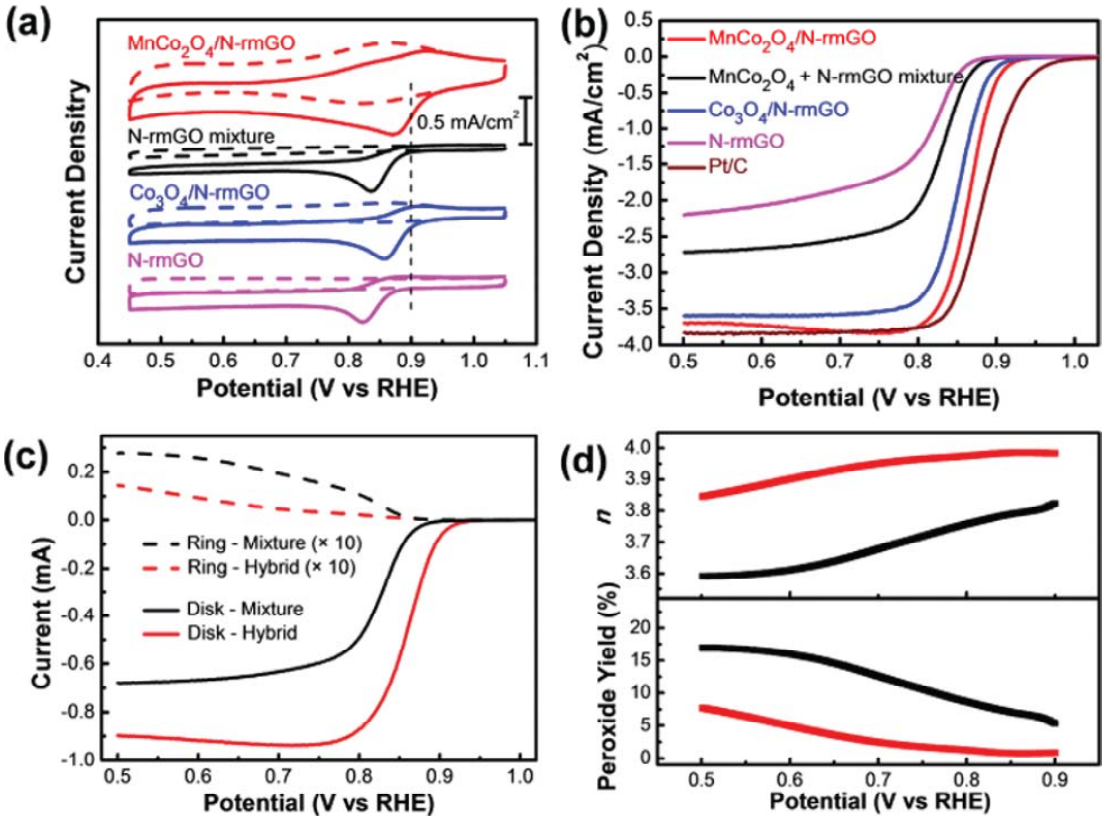

Figure 1.27 (a) CV curves of $MnCo_2O_4$/N-rmGO hybrid, $MnCo_2O_4$ + N-rmGO mixture, Co_3O_4/N-rmGO hybrid, and N-rmGO on glassy carbon electrodes in O_2-saturated (solid line) or N_2-saturated (dash line) 1 M KOH. The peak position of Pt/C is shown as a dashed line for comparison. (b) Rotating-disk electrode voltammograms of $MnCo_2O_4$/N-rmGO hybrid, $MnCo_2O_4$ + N-rmGO mixture, Co_3O_4/N-rmGO hybrid, N-rmGO, and Pt/C in O_2-saturated 1 M KOH at a sweep rate of 5 mV/s at 1600 rpm. (c) Rotating ring−disk electrode voltammograms of $MnCo_2O_4$/N-rmGO hybrid and $MnCo_2O_4$ + N-rmGO physical mixture in O_2-

saturated 1 M KOH at 1600 rpm. The disk potential was scanned at 5 mV/s, and the ring potential was constant at 1.3 V vs RHE. (d) Percentage of peroxide (bottom) with respect to the total oxygen reduction products and the electron transfer number (n) (top) of $MnCo_2O_4$/N-rmGO hybrid and$MnCo_2O_4$ + N-rmGO mixture at various potentials based on the corresponding RRDE data in panel (c). Catalyst loading was 0.10 mg/cm^2 for all samples. [213]

1.5 Research Goals and Outline

As discussed above, the commercialization of fuel cells (either PEMFC or AEMFC) relies on the development of novel, efficient catalysts with low cost and environmental friendliness. The main objective of this study is to develop a novel electrocatalyst with high catalytic activity towards the ORR and better stability to replace or lower the utilization of Pt in the cathode catalyst of fuel cells. The major contents of this study include the synthesis high performance electrocatalysts based on Pt alloyed nanoparticles (with noble metal or non-noble metal) for catalysing the ORR in acidic environment for PEMFCs, and non-Pt electrocatalysts, nanostructured metal oxides, and metal-free catalysts based on doped graphene materials for catalysing the ORR in a basic environment for the AEMFC. Such a study will provide a fundamental understanding of the catalytic performance of different kinds of catalyst towards the ORR and will have benefits for the development of novel electrocatalysts for the PEMFC or AEMFC with good efficiency, better stability, and low cost compared with the state-of-the-art Pt/C electrocatalysts.

In Chapter 3, the synthesis of low-Pt-content electrocatalysts is investigated by stabilization of Pt on hollow palladium surfaces. Such a unique structure would effectively prevent Pt nanoparticle aggregation under long term testing conditions,

thereby increasing the stability of the Pt. Furthermore the strong interactopm between Pt and Pd would further decrease Pt-OH formation during the ORR process, thus providing enhanced performance. As a result, this catalyst exhibits better catalytic performance as well as better stability towards the ORR than the commercially available E-Tek Pt/C catalysts.

In Chapter 4, the synthesis of a high surface area electrocatalyst is reported − mesoporous PtCu alloyed hollow nanostructures. The incorporation of copper into Pt the lattice would significantly reduce the cost of the electrocatalyst as a whole, and the "strain effects" between Pt lattice and the Cu, as well as the novel hollow porous structure, would provide large surface area and abundant active sites for oxygen adsorption and desorption. This electrocatalyst showed several orders of magnitude higher specific area activity compared with that of the Pt/C at operating potential of 0.510 V (vs. Ag/AgCl), and it showed very good stability in the accelerating durability tests.

In Chapter 5, with the method developed for synthesizing mesoporous PtCu, a non-Pt Pd-based alloy with Ni is reported as an electrocatalyst with porous and hollow features and uses it as more an efficient electrocatalyst compared with Pt in alkaline medium for the AEMFC. We alloyed Pd with the cheap metal nickel to significantly further reduce the cost of Pd and enhance the performance of the Pd. The resultant electrocatalysts showed better electrocatalytic performance and durability.

In Chapter 6, a new method associated with vapour phase polymerisation was developed for fabricating nitrogen-doped crumpled graphene, in which the nitrogen configuration and content could be well tuned. In contrast to other reported N-doped graphene aerogels, the fabricated N-graphene aerogel showed microporous crumpled features. Even the macroporous 3D structure was destroyed for the purpose of

preparing ORR electrodes or Mesa This unique microporous structure could offer higher surface area and a more open structure. The electrochemical tests, as well as the AEMFC testing, provided more convincing evidence that non-metal electrocatalysts could work as efficient catalysts in the AEMFC, as well as useful information for developing metal-free electrocatalysts.

In Chapter 7, cobalt oxide core-shell nanostructures were used to enhance the ORR performance of nitrogen doped graphene aerogel in alkaline medium. Through careful comparison, it was concluded that the well-defined core-shell structures of the cobalt/cobalt oxide as well as the porous structure of the nitrogen graphene supports result in catalysts with much better catalytic performance compared with the nitrogen-doped graphene aerogel or cobalt oxide/nitrogen doped graphene aerogel. In addition, the catalysts showed comparable catalytic performance to Pt/C towards the ORR, which was also examined in the AEMFC tests.

1.6 References

1. Debe, M.K., Nature, 2012. **486**(7401): 43-51.
2. Zhou, X., J. Qiao, L. Yang, and J. Zhang, Advanced Energy Materials, 2014. **4**(8): DOI: 10.1002/aenm.201301523.
3. Deavin, O.I., S. Murphy, A.L. Ong, S.D. Poynton, R. Zeng, H. Herman, and J.R. Varcoe, Energy & Environmental Science, 2012. **5**(9): 8584-8597.
4. Morozan, A., B. Jousselme, and S. Palacin, Energy & Environmental Science, 2011. **4**(4): 1238-1254.
5. Gong, K., F. Du, Z. Xia, M. Durstock, and L. Dai, Science, 2009. **323**(5915): 760-764.

6. Lim, B., M. Jiang, P.H.C. Camargo, E.C. Cho, J. Tao, X. Lu, Y. Zhu, and Y. Xia, Science, 2009. **324**(5932): 1302-1305.

7. Black, R., B. Adams, and L.F. Nazar, Advanced Energy Materials, 2012. **2**(7): 801-815.

8. Ogasawara, T., A. Débart, M. Holzapfel, P. Novák, and P.G. Bruce, Journal of the American Chemical Society, 2006. **128**(4): 1390-1393.

9. Markovic, N.M., H.A. Gasteiger, and P.N. Ross, The Journal of Physical Chemistry, 1995. **99**(11): 3411-3415.

10. Jalan, V. and E.J. Taylor, Journal of the Electrochemical Society, 1983. **130**(11): 2299-2302.

11. Kunz, H.R. and G.A. Gruver, Journal of the Electrochemical Society, 1975. **122**(10): 1279-1287.

12. Wolf Vielstich, H.A.G., Arnold Lamm and Harumi Yokokawa., ed. *Handbook of Fuel Cells– Fundamentals, Technology and Applications*. Vol. 2. 2010, John Wiley & Sons, Ltd. 1136.

13. Marković, N.M., H.A. Gasteiger, B.N. Grgur, and P.N. Ross, Journal of Electroanalytical Chemistry, 1999. **467**(1–2): 157-163.

14. Schmidt, T.J., U.A. Paulus, H.A. Gasteiger, and R.J. Behm, Journal of Electroanalytical Chemistry, 2001. **508**(1–2): 41-47.

15. Stamenkovic, V., N. M. Markovic, and P.N. Ross Jr, Journal of Electroanalytical Chemistry, 2001. **500**(1–2): 44-51.

16. Sun, S., G. Zhang, D. Geng, Y. Chen, R. Li, M. Cai, and X. Sun, Angewandte Chemie International Edition, 2011. **50**(2): 422-426.

17. Marković, N.M., T.J. Schmidt, V. Stamenković, and P.N. Ross, Fuel Cells, 2001. **1**(2): 105-116.

18. Nørskov, J.K., J. Rossmeisl, A. Logadottir, L. Lindqvist, J.R. Kitchin, T. Bligaard, and H. Jónsson, Journal of Physical Chemistry B, 2004. **108**(46): 17886-17892.

19. Meadowcroft, D.B., Nature, 1970. **226**(5248): 847-848.

20. Zhang, L. and Z. Xia, Journal of Physical Chemistry C, 2011. **115**(22): 11170-11176.

21. Sidik, R.A., A.B. Anderson, N.P. Subramanian, S.P. Kumaraguru, and B.N. Popov, The Journal of Physical Chemistry B, 2006. **110**(4): 1787-1793.

22. Zhang, J., ed. *PEM Fuel Cell Electrocatalysts and Catalyst Layers*. Fundamentals and Applications Vol. 2. 2008, Springer: Vancouver, BC. 1119.

23. Sekol, R.C., X. Li, P. Cohen, G. Doubek, M. Carmo, and A.D. Taylor, Applied Catalysis, B: Environmental, 2013. **138–139**(0): 285-293.

24. Zhang, Z., K.L. More, K. Sun, Z. Wu, and W. Li, Chemistry of Materials, 2011. **23**(6): 1570-1577.

25. Shao, M.-H., K. Sasaki, and R.R. Adzic, Journal of the American Chemical Society, 2006. **128**(11): 3526-3527.

26. Mazumder, V., Y. Lee, and S. Sun, Advanced Functional Materials, 2010. **20**(8): 1224-1231.

27. Zhang, L., J. Zhang, D.P. Wilkinson, and H. Wang, Journal of Power Sources, 2006. **156**(2): 171-182.

28. Zagal J, B.P., Yeager E., Journal of the electrochemical Society. **127**: 1506-1517.

29. Alia, S.M., G. Zhang, D. Kisailus, D. Li, S. Gu, K. Jensen, and Y. Yan, Advanced Functional Materials, 2010. **20**(21): 3742-3746.

30. Zhang, S., X.-Z. Yuan, J.N.C. Hin, H. Wang, K.A. Friedrich, and M. Schulze, Journal of Power Sources, 2009. **194**(2): 588-600.

31. Prabhuram, J., X. Wang, C.L. Hui, and I.M. Hsing, The Journal of Physical Chemistry B, 2003. **107**(40): 11057-11064.

32. Fang, B., N.K. Chaudhari, M.-S. Kim, J.H. Kim, and J.-S. Yu, Journal of the American Chemical Society, 2009. **131**(42): 15330-15338.

33. Zhang, S., Y. Shao, G. Yin, and Y. Lin, Journal of Materials Chemistry, 2009. **19**(42).

34. Yang, W., X. Wang, F. Yang, C. Yang, and X. Yang, Advanced Materials, 2008. **20**(13): 2579-2587.

35. Zhang, J., K. Sasaki, E. Sutter, and R.R. Adzic, Science, 2007. **315**(5809): 220-222.

36. Zhao, Y., Y. Zhou, B. Xiong, J. Wang, X. Chen, R. O'Hayre, and Z. Shao, Journal of Solid State Electrochemistry, 2012: 1-10.

37. Li, Y., E. Zhu, T. McLouth, C.Y. Chiu, X. Huang, and Y. Huang, Journal of the American Chemical Society, 2012. **134**(30): 12326-12329.

38. Zhang, L.S., X.Q. Liang, W.G. Song, and Z.Y. Wu, Physical Chemistry Chemical Physics, 2010. **12**(38): 12055-12059.

39. Joo, S.H., S.J. Choi, I. Oh, J. Kwak, Z. Liu, O. Terasaki, and R. Ryoo, Nature, 2001. **412**(6843): 169-172.

40. Wu, Z., Y. Lv, Y. Xia, P.A. Webley, and D. Zhao, Journal of the American Chemical Society, 2012. **134**(4): 2236-2245.

41. Xie, X., S. Chen, W. Ding, Y. Nie, and Z. Wei, Chemical Communications (Cambridge, United Kingdom), 2013. **49**(86): 10112-10114.

42. Akalework, N.G., C.J. Pan, W.N. Su, J. Rick, M.C. Tsai, J.F. Lee, J.M. Lin, L.D. Tsai, and B.J. Hwang, Journal of Materials Chemistry, 2012. **22**(39): 20977-20985.

43. Koenigsmann, C., A.C. Santulli, E. Sutter, and S.S. Wong, ACS Nano, 2011. **5**(9): 7471-7487.

44. Liang, H.-W., S. Liu, J.-Y. Gong, S.-B. Wang, L. Wang, and S.-H. Yu, Adv. Mater. (Weinheim, Ger.), 2009. **21**(18): 1850-1854.

45. Liang, H.-W., X. Cao, F. Zhou, C.-H. Cui, W.-J. Zhang, and S.-H. Yu, Advanced Materials, 2010. **23**(12): 1467-1471.

46. Sun, S.H., D.Q. Yang, D. Villers, G.X. Zhang, E. Sacher, and J.P. Dodelet, Advanced Materials, 2008. **20**(3): 571-574.

47. Sun, S., F. Jaouen, and J.-P. Dodelet, Advanced Materials, 2008. **20**(20): 3900-3904.

48. Sun, S., G. Zhang, D. Geng, Y. Chen, M.N. Banis, R. Li, M. Cai, and X. Sun, Chemistry - A European Journal, 2010. **16**(3): 829-835.

49. Ci, S., J. Zou, G. Zeng, S. Luo, and Z. Wen, Journal of Materials Chemistry, 2012. **22**(33): 16732-16737.

50. Yang, S., F. Hong, L. Wang, S. Guo, X. Song, B. Ding, and Z. Yang, The Journal of Physical Chemistry C, 2009. **114**(1): 203-207.

51. Lee, H., S.E. Habas, S. Kweskin, D. Butcher, G.A. Somorjai, and P. Yang, Angewandte Chemie International Edition, 2006. **45**(46): 7824-7828.

52. Ren, J. and R.D. Tilley, Journal of the American Chemical Society, 2007. **129**(11): 3287-3291.

53. Guo, S., S. Zhang, and S. Sun, Angewandte Chemie International Edition, 2013. **52**(33): 8526-8544.

54. Wang, C., H. Daimon, T. Onodera, T. Koda, and S. Sun, Angewandte Chemie International Edition, 2008. **47**(19): 3588-3591.

55. Liang, H.-P., H.-M. Zhang, J.-S. Hu, Y.-G. Guo, L.-J. Wan, and C.-L. Bai, Angewandte Chemie, International Edition, 2004. **43**(12): 1540-1543.

56. Sun, Y. and Y. Xia, Journal of the American Chemical Society, 2004. **126**(12): 3892-3901.

57. Hong, J.W., S.W. Kang, B.S. Choi, D. Kim, S.B. Lee, and S.W. Han, ACS Nano, 2012. **6**(3): 2410-2419.

58. Zhang, H., M. Jin, H. Liu, J. Wang, M.J. Kim, D. Yang, Z. Xie, J. Liu, and Y. Xia, ACS Nano, 2011. **5**(10): 8212-8222.

59. Ye, F., H. Liu, W. Hu, J. Zhong, Y. Chen, H. Cao, and J. Yang, Dalton Transactions, 2012. **41**(10): 2898-2903.

60. Cherevko, S., N. Kulyk, and C.H. Chung, Langmuir, 2012. **28**(6): 3306-3315.

61. Zhang, M. and L. Dai, Nano Energy, 2012. **1**(4): 514-517.

62. He, W., X. Wu, J. Liu, K. Zhang, W. Chu, L. Feng, X. Hu, W. Zhou, and S. Xie, Langmuir, 2010. **26**(6): 4443-4448.

63. Di Noto, V. and E. Negro, Fuel Cells, 2010. **10**(2): 234-244.

64. Guo, S. and S. Sun, Journal of the American Chemical Society, 2012. **134**(5): 2492-2495.

65. Guo, S., S. Zhang, X. Sun, and S. Sun, Journal of the American Chemical Society, 2011. **133**(39): 15354-15357.

66. Kim, J., Y. Lee, and S. Sun, Journal of the American Chemical Society, 2010. **132**(14): 4996-4997.

67. Chen, G., D. Xia, Z. Nie, Z. Wang, L. Wang, L. Zhang, and J. Zhang, Chemistry of Materials, 2007. **19**(7): 1840-1844.

68. Tzitzios, V., D. Niarchos, M. Gjoka, N. Boukos, and D. Petridis, J. Am. Chem. Soc., 2005. **127**(40): 13756-13757.

69. Yu, Z., J. Zhang, Z. Liu, J.M. Ziegelbauer, H. Xin, I. Dutta, D.A. Muller, and F.T. Wagner, The Journal of Physical Chemistry C, 2012. **116**(37): 19877-19885.

70. Huang, X., E. Zhu, Y. Chen, Y. Li, C.-Y. Chiu, Y. Xu, Z. Lin, X. Duan, and Y. Huang, Adv. Mater. (Weinheim, Ger.), 2013. **25**: 2974-2979.

71. Carpenter, M.K., T.E. Moylan, R.S. Kukreja, M.H. Atwan, and M.M. Tessema, Journal of the American Chemical Society, 2012. **134**(20): 8535-8542.

72. Cui, C., L. Gan, H.H. Li, S.H. Yu, M. Heggen, and P. Strasser, Nano Letters, 2012. **12**(11): 5885-5889.

73. Gan, L., M. Heggen, S. Rudi, and P. Strasser, Nano Letters, 2012. **12**(10): 5423-5430.

74. Yu, X., D. Wang, Q. Peng, and Y. Li, Chemical Communications, 2011. **47**(28): 8094-8096.

75. Wang, M., W. Zhang, J. Wang, A. Minett, V. Lo, H. Liu, and J. Chen, Journal of Materials Chemistry A, 2013. **1**(7): 2391-2394.

76. Mani, P., R. Srivastava, and P. Strasser, The Journal of Physical Chemistry C, 2008. **112**(7): 2770-2778.

77. Zhang, J., M.B. Vukmirovic, K. Sasaki, A.U. Nilekar, M. Mavrikakis, and R.R. Adzic, Journal of the American Chemical Society, 2005. **127**(36): 12480-12481.

78. Xu, D., Z. Liu, H. Yang, Q. Liu, J. Zhang, J. Fang, S. Zou, and K. Sun, Angewandte Chemie International Edition, 2009. **48**(23): 4217-4221.

79. Liu, Y., C.M. Hangarter, U. Bertocci, and T.P. Moffat, Journal of Physical Chemistry C, 2012. **116**(14): 7848-7862.

80. Yang, J., X. Chen, X. Yang, and J.Y. Ying, Energy & Environmental Science, 2012. **5**(10): 8976-8981.

81. Slanac, D.A., W.G. Hardin, K.P. Johnston, and K.J. Stevenson, Journal of the American Chemical Society, 2012. **134**(23): 9812-9819.

82. Chen, X., G. Wu, J. Chen, X. Chen, Z. Xie, and X. Wang, Journal of the American Chemical Society, 2011. **133**(11): 3693-3695.

83. Koenigsmann, C., E. Sutter, T.A. Chiesa, R.R. Adzic, and S.S. Wong, Nano Letters, 2012. **12**(4): 2013-2020.

84. Shim, J.H., J. Kim, C. Lee, and Y. Lee, Chem. Mater., 2011. **23**: 4694-4700.

85. Neergat, M., V. Gunasekar, and R. Rahul, Journal of Electroanalytical Chemistry, 2011. **658**(1-2): 25-32.

86. Chen, L., H. Guo, T. Fujita, A. Hirata, W. Zhang, A. Inoue, and M. Chen, Advanced Functional Materials, 2011. **21**(22): 4364-4370.

87. Zhang, L., F. Hou, and Y. Tan, Chemical Communications (Cambridge, United Kingdom), 2012. **48**(57): 7152-7154.

88. Caixia, X., Z. Yan, X. Liqiang, B. Xiufang, M. Houyi, and D. Yi, Chemistry of Materials, 2009. **21**(14): 3110-3116.

89. Wang, D., H.L. Xin, H. Wang, Y. Yu, E. Rus, D.A. Muller, F.J. Disalvo, and H.D. Abruña, Chemistry of Materials, 2012. **24**(12): 2274-2281.

90. Fernández, J.L., V. Raghuveer, A. Manthiram, and A.J. Bard, Journal of the American Chemical Society, 2005. **127**(38): 13100-13101.

91. Giovanni, M., H.L. Poh, A. Ambrosi, G. Zhao, Z. Sofer, F. Šaněk, B. Khezri, R.D. Webster, and M. Pumera, Nanoscale, 2012. **4**(16): 5002-5008.

92. Huang, M.H. and P.H. Lin, Advanced Functional Materials, 2012. **22**(1): 14-24.

93. Au, L., X. Lu, and Y. Xia, Advanced Materials, 2008. **20**(13): 2517-2522.

94. Mallin, M.P. and C.J. Murphy, Nano Letters, 2002. **2**(11): 1235-1237.

95. Wiley, B., T. Herricks, Y. Sun, and Y. Xia, Nano Letters, 2004. **4**(9): 1733-1739.

96. Sun, Y. and Y. Xia, Science, 2002. **298**(5601): 2176-2179.

97. Abecassis, B., F. Testard, and T. Zemb, Soft Matter, 2009. **5**(5): 974-978.

98. Chen, J., K. Takanabe, R. Ohnishi, D. Lu, S. Okada, H. Hatasawa, H. Morioka, M. Antonietti, J. Kubota, and K. Domen, Chemical Communications, 2010. **46**(40): 7492-7494.

99. Du, W., Q. Wang, D. Saxner, N.A. Deskins, D. Su, J.E. Krzanowski, A.I. Frenkel, and X. Teng, Journal of the American Chemical Society, 2011. **133**(38): 15172-15183.

100. Antolini, E., ACS Catalysis, 2014. **4**(5): 1426-1440.

101. Xu, T., H. Zhang, Y. Zhang, H. Zhong, H. Jin, and Y. Tang, Journal of Power Sources, 2011. **196**(14): 5849-5852.

102. Bagotzky, V.S., M.R. Tarasevich, K.A. Radyushkina, O.A. Levina, and S.I. Andrusyova, Journal of Power Sources, 1978. **2**(3): 233-240.

103. Bezerra, C.W.B., L. Zhang, K. Lee, H. Liu, A.L.B. Marques, E.P. Marques, H. Wang, and J. Zhang, Electrochimica Acta, 2008. **53**(15): 4937-4951.

104. Zheng, S. and Z. Jiujun, Journal of Physical Chemistry C, 2007. **111**(19): 7084-7090.

105. Gupta, S., D. Tryk, I. Bae, W. Aldred, and E. Yeager, Journal of Applied Electrochemistry, 1989. **19**(1): 19-27.

106. Parvez, K., S. Yang, Y. Hernandez, A. Winter, A. Turchanin, X. Feng, and K. Müllen, ACS Nano, 2012. **6**(11): 9541-9550.

107. Lee, J.-S., G.S. Park, S.T. Kim, M. Liu, and J. Cho, Angewandte Chemie, International Edition, 2013. **52**: 1026-1030.

108. Xiao, H., Z.-G. Shao, G. Zhang, Y. Gao, W. Lu, and B. Yi, Carbon, 2013. **57**(0): 443-451.

109. Choi, J.-Y., R. Hsu, and Z. Chen, ECS Transactions, 2010. **28**: 101-112.

110. Liu, G., X. Li, P. Ganesan, and B.N. Popov, Electrochimica Acta, 2010. **55**(8): 2853-2858.

111. Silva, R., D. Voiry, M. Chhowalla, and T. Asefa, Journal of the American Chemical Society, 2013. **135**(21): 7823-7826.

112. Proietti, E., F. Jaouen, M. Lefèvre, N. Larouche, J. Tian, J. Herranz, and J.-P. Dodelet, Nat Commun, 2011. **2**: 416.

113. Lefèvre, M., E. Proietti, F. Jaouen, and J.-P. Dodelet, Science, 2009. **324**(5923): 71-74.

114. Liang, H.-W., W. Wei, Z.-S. Wu, X. Feng, and K. Müllen, Journal of the American Chemical Society, 2013. **135**(43): 16002-16005.

115. Kramm, U.I., M. Lefèvre, N. Larouche, D. Schmeisser, and J.-P. Dodelet, Journal of the American Chemical Society, 2013. **136**(3): 978-985.

116. Mazza, F. and S. Trassatti, Journal of the Electrochemical Society, 1963. **110**(7): 847-849.

117. Liu, M., Y. Lu, and W. Chen, Advanced Functional Materials, 2013. **23**(10): 1289-1296.

118. Wang, M., W. Zhang, J.-Z. Wang, D. Wexler, S.D. Poynton, R.C.T. Slade, H. Kun-Liu, B. Winther-Jenson, R. Kerr, D. Shi, and J. Chen, ACS Applied Materials & Interfaces, 2013. **5**(23): 12708-12715.

119. Yang, S., L. Zhi, K. Tang, X. Feng, J. Maier, and K. Muellen, Advanced Functional Materials, 2012. **22**: 3634-3640.

120. Xu, J., G. Dong, C. Jin, M. Huang, and L. Guan, ChemSusChem, 2013. **6**(3): 493-499.

121. Wang, S., L. Zhang, Z. Xia, A. Roy, D.W. Chang, J.B. Baek, and L. Dai, Angewandte Chemie, International Edition, 2012. **51**(17): 4209-4212.

122. Zhang, G., B.Y. Xia, X. Wang, and X.W. Lou, Advanced Materials, 2013: 2408-2412.

123. Liang, Y., H. Wang, P. Diao, W. Chang, G. Hong, Y. Li, M. Gong, L. Xie, J. Zhou, J. Wang, T.Z. Regier, F. Wei, and H. Dai, Journal of the American Chemical Society, 2012. **134**(38): 15849-15857.

124. Liang, Y., Y. Li, H. Wang, J. Zhou, J. Wang, T. Regier, and H. Dai, Nature Materials, 2011. **10**(10): 780-786.

125. Gu, S., R. Cai, T. Luo, Z. Chen, M. Sun, Y. Liu, G. He, and Y. Yan, Angewandte Chemie, International Edition, 2009. **48**(35): 6499-6502.

126. Varcoe, J.R., R.C.T. Slade, and E. Lam How Yee, Chemical Communications (Cambridge, United Kingdom), 2006(13): 1428-1429.

127. Varcoe, J.R. and R.C.T. Slade, Electrochemistry Communications, 2006. **8**(5): 839-843.

128. Li, X., B.N. Popov, T. Kawahara, and H. Yanagi, Journal of Power Sources, 2011. **196**(4): 1717-1722.

129. Sun, W., A. Hsu, and R. Chen, Journal of Power Sources, 2011. **196**(10): 4491-4498.

130. He, Q., Q. Li, S. Khene, X. Ren, F.E. López-Suárez, D. Lozano-Castelló, A. Bueno-López, and G. Wu, Journal of Physical Chemistry C, 2013. **117**(17): 8697-8707.

131. Li, B. and J. Prakash, Electrochemistry Communications, 2009. **11**(6): 1162-1165.

132. Liang, J., Y. Zheng, J. Chen, J. Liu, D. Hulicova-Jurcakova, M. Jaroniec, and S.Z. Qiao, Angewandte Chemie, International Edition, 2012. **51**(16): 3892-3896.

133. Zheng, Y., Y. Jiao, L. Ge, M. Jaroniec, and S.Z. Qiao, Angewandte Chemie, International Edition, 2013. **52**(11): 3110-3116.

134. Zhu, J., C. He, Y. Li, S. Kang, and P.K. Shen, Journal of Materials Chemistry A, 2013. **1**(46): 14700-14705.

135. Liang, J., Y. Jiao, M. Jaroniec, and S.Z. Qiao, Angewandte Chemie, International Edition, 2012. **51**(46): 11496-11500.

136. Liu, Q., J. Jin, and J. Zhang, ACS Applied Materials & Interfaces, 2013. **5**(11): 5002-5008.

137. Su, Y., Y. Zhang, X. Zhuang, S. Li, D. Wu, F. Zhang, and X. Feng, Carbon, 2013. **62**: 296-301.

138. Zhang, C., N. Mahmood, H. Yin, F. Liu, and Y. Hou, Advanced Materials, 2013. **25**(35): 4932-4937.

139. Latorre-Sánchez, M., A. Primo, and H. García, Angewandte Chemie, International Edition, 2013. **52**(45): 11813-11816.

140. Zahoor, A., M. Christy, Y.J. Hwang, Y.R. Lim, P. Kim, and K.S. Nahm, Applied Catalysis B: Environmental, 2014. **147**: 633-641.

141. Ma, Y., H. Wang, S. Ji, J. Goh, H. Feng, and R. Wang, Electrochimica Acta, 2014. **133**: 391-398.

142. Jeyabharathi, C., P. Venkateshkumar, M.S. Rao, J. Mathiyarasu, and K.L.N. Phani, Electrochimica Acta, 2012. **74**: 171-175.

143. Al-Aqtash, N. and I. Vasiliev, Journal of Physical Chemistry C, 2011. **115**(38): 18500-18510.

144. Zheng, B., P. Hermet, and L. Henrard, ACS Nano, 2010. **4**(7): 4165-4173.

145. Yu, S.S. and W.T. Zheng, Nanoscale, 2010. **2**(7): 1069-1082.

146. Panchakarla, L.S., A. Govindaraj, and C.N.R. Rao, Inorganica Chimica Acta, 2010. **363**(15): 4163-4174.

147. Srivastava, D., M. Menon, C. Daraio, S. Jin, B. Sadanadan, and A.M. Rao, Physical Review B - Condensed Matter and Materials Physics, 2004. **69**(15): 153414-1-153414-4.

148. Choi, C.H., M.W. Chung, Y.J. Jun, and S.I. Woo, RSC Advances, 2013. **3**(30): 12417-12422.

149. Romero-Aburto, R., T.N. Narayanan, Y. Nagaoka, T. Hasumura, T.M. Mitcham, T. Fukuda, P.J. Cox, R.R. Bouchard, T. Maekawa, D.S. Kumar, S.V. Torti, S.A. Mani, and P.M. Ajayan, Advanced Materials, 2013. **25**(39): 5632-5637.

150. Qu, L., Y. Liu, J.-B. Baek, and L. Dai, ACS Nano, 2010. **4**(3): 1321-1326.

151. Wang, Y., Y. Shao, D.W. Matson, J. Li, and Y. Lin, ACS Nano, 2010. **4**(4): 1790-1798.

152. Dai, J., J. Yuan, and P. Giannozzi, Applied Physics Letters, 2009. **95**(23): DOI:10.1063/1.3272008.

153. Yang, Z., Z. Yao, G. Li, G. Fang, H. Nie, Z. Liu, X. Zhou, X. Chen, and S. Huang, ACS Nano, 2012. **6**(1): 205-211.

154. Park, J.E., Y.J. Jang, Y.J. Kim, M.S. Song, S. Yoon, D.H. Kim, and S.J. Kim, Physical Chemistry Chemical Physics, 2014. **16**(1): 103-109.

155. Xue, Y., J. Liu, H. Chen, R. Wang, D. Li, J. Qu, and L. Dai, Angewandte Chemie International Edition, 2012. **51**(48): 12124-12127.

156. Wang, H., M. Xie, L. Thia, A. Fisher, and X. Wang, Journal of Physical Chemistry Letters, 2013. **5**(1): 119-125.

157. Wen, Z., X. Wang, S. Mao, Z. Bo, H. Kim, S. Cui, G. Lu, X. Feng, and J. Chen, Advanced Materials, 2012. **24**: 5610-5616.

158. Wu, Z.-S., S. Yang, Y. Sun, K. Parvez, X. Feng, and K. Müllen, Journal of the American Chemical Society, 2012. **134**(22): 9082-9085.

159. Wu, Z.S., A. Winter, L. Chen, Y. Sun, A. Turchanin, X. Feng, and K. Müllen, Advanced Materials, 2012. **24**(37): 5130-5135.

160. Moon, J., J. An, U. Sim, S.-P. Cho, J.H. Kang, C. Chung, J.-H. Seo, J. Lee, K.T. Nam, and B.H. Hong, Advanced Materials, 2014: 3501-3505.

161. Ye, T.N., L.B. Lv, X.H. Li, M. Xu, and J.S. Chen, Angewandte Chemie - International Edition, 2014. **53**(27): 6905-6909.

162. Juanjuan, Z., L. Ruiyi, L. Zaijun, L. Junkang, G. Zhiguo, and W. Guangli, Nanoscale, 2014. **6**(10): 5458-5466.

163. Lin, Z., G.H. Waller, Y. Liu, M. Liu, and C.P. Wong, Nano Energy, 2013. **2**(2): 241-248.

164. Chan, L.H., K.H. Hong, D.Q. Xiao, T.C. Lin, S.H. Lai, W.J. Hsieh, and H.C. Shih, Physical Review B - Condensed Matter and Materials Physics, 2004. **70**(12): 125408-1-125408-7.

165. Nieto-Márquez, A., J.C. Lazo, A. Romero, and J.L. Valverde, Chemical Engineering Journal (Lausanne), 2008. **144**(3): 518-530.

166. Shao, Y., J. Sui, G. Yin, and Y. Gao, Applied Catalysis B: Environmental, 2008. **79**(1): 89-99.

167. Stoyanov, S.R., A.V. Titov, and P. Král, Coordination Chemistry Reviews, 2009. **253**(23-24): 2852-2871.

168. Yu, S.S., W.T. Zheng, and Q. Jiang, IEEE Transactions on Nanotechnology, 2010. **9**(1): 78-81.

169. Shao, Y., S. Zhang, M.H. Engelhard, G. Li, G. Shao, Y. Wang, J. Liu, I.A. Aksay, and Y. Lin, Journal of Materials Chemistry, 2010. **20**(35): 7491-7496.

170. Reddy, A.L.M., A. Srivastava, S.R. Gowda, H. Gullapalli, M. Dubey, and P.M. Ajayan, ACS Nano, 2010. **4**(11): 6337-6342.

171. Kan-Nari, N., S. Okamura, S.I. Fujita, J.I. Ozaki, and M. Arai, Advanced Synthesis and Catalysis, 2010. **352**(9): 1476-1484.

172. Cho, Y.J., H.S. Kim, H. Im, Y. Myung, G.B. Jung, C.W. Lee, J. Park, M.H. Park, J. Cho, and H.S. Kang, Journal of Physical Chemistry C, 2011. **115**(19): 9451-9457.

173. Zhang, C., L. Fu, N. Liu, M. Liu, Y. Wang, and Z. Liu, Advanced Materials, 2011. **23**(8): 1020-1024.

174. Wu, P., Z. Cai, Y. Gao, H. Zhang, and C. Cai, Chemical Communications (Cambridge, United Kingdom), 2011. **47**(40): 11327-11329.

175. Mou, Z., X. Chen, Y. Du, X. Wang, P. Yang, and S. Wang, Applied Surface Science, 2011. **258**(5): 1704-1710.

176. Li, X., D. Geng, Y. Zhang, X. Meng, R. Li, and X. Sun, Electrochemistry Communications, 2011. **13**(8): 822-825.

177. Yen, M.Y., C.K. Hsieh, C.C. Teng, M.C. Hsiao, P.I. Liu, C.C.M. Ma, M.C. Tsai, C.H. Tsai, Y.R. Lin, and T.Y. Chou, RSC Advances, 2012. **2**(7): 2725-2728.

178. Zheng, B., J. Wang, F.-B. Wang, and X.-H. Xia, Journal of Materials Chemistry A, 2014. **2**(24): 9079-9084.

179. Sun, X., P. Song, Y. Zhang, C. Liu, W. Xu, and W. Xing, Sci. Rep., 2013. **3**: DOI:10.1038/srep02505.

180. Chen, P., T.-Y. Xiao, Y.-H. Qian, S.-S. Li, and S.-H. Yu, Adv Mater, 2013. **25**: 3192-6.

181. Ma, Y., L. Sun, W. Huang, L. Zhang, J. Zhao, and Q. Fan, Journal of Physical Chemistry C, 2011. **115**(50): 24592-24597.

182. Tang, Y., B.L. Allen, D.R. Kauffman, and A. Star, Journal of the American Chemical Society, 2009. **131**(37): 13200-13201.

183. Krstić, V., M. Glerup, S. Hansel, and M. Lafkioti, Physica Status Solidi - Rapid Research Letters, 2009. **3**(6): 187-189.

184. Tan, Y., C. Xu, G. Chen, X. Fang, N. Zheng, and Q. Xie, Advanced Functional Materials, 2012. **22**(21): 4584-4591.

185. Groenewolt, M. and M. Antonietti, Advanced Materials, 2005. **17**(14): 1789-1792.

186. Hummers, W.S. and R.E. Offeman, Journal of the American Chemical Society, 1958. **80**(6): 1339-1339.

187. Chen, Z., W. Ren, L. Gao, B. Liu, S. Pei, and H.-M. Cheng, Nature Materials, 2011. **10**(6): 424-428.

188. Bai, H., C. Li, and G. Shi, Advanced Materials, 2011. **23**(9): 1089-1115.

189. Lee, J.H., N. Park, B.G. Kim, D.S. Jung, K. Im, J. Hur, and J.W. Choi, ACS Nano, 2013. **7**(10): 9366–9374.

190. Mao, S., Z. Wen, H. Kim, G. Lu, P. Hurley, and J. Chen, ACS Nano, 2012. **6**: 7505-7513.

191. Luo, J., H.D. Jang, and J. Huang, ACS Nano, 2013. **7**: 1464-1471.

192. Ma, X., M.R. Zachariah, and C.D. Zangmeister, Nano Letters, 2012. **12**: 486-489.

193. Tao, Y., X. Xie, W. Lv, D.-M. Tang, D. Kong, Z. Huang, H. Nishihara, T. Ishii, B. Li, D. Golberg, F. Kang, T. Kyotani, and Q.-H. Yang, Sci. Rep., 2013. **3**: DOI: 10.1038/srep02975.

194. Xu, Y., Z. Lin, X. Huang, Y. Liu, Y. Huang, and X. Duan, ACS Nano, 2013. **7**(5): 4042-4049.

195. Xu, Y., K. Sheng, C. Li, and G. Shi, ACS Nano, 2010. **4**(7): 4324-4330.

196. Xu, Y., Q. Wu, Y. Sun, H. Bai, and G. Shi, ACS Nano, 2010. **4**(12): 7358-7362.

197. Hu, H., Z. Zhao, W. Wan, Y. Gogotsi, and J. Qiu, Advanced Materials, 2013. **25**(15): 2219-2223.

198. Niu, Z., J. Chen, H.H. Hng, J. Ma, and X. Chen, Advanced Materials, 2012. **24**(30): 4144-4150.

199. Chen, J., K. Sheng, P. Luo, C. Li, and G. Shi, Advanced Materials, 2012. **24**(33): 4569-4573.

200. Lee, S.H., H.W. Kim, J.O. Hwang, W.J. Lee, J. Kwon, C.W. Bielawski, R.S. Ruoff, and S.O. Kim, Angewandte Chemie, International Edition, 2010. **49**(52): 10084-10088.

201. Yoon, Y., K. Lee, C. Baik, H. Yoo, M. Min, Y. Park, S.M. Lee, and H. Lee, Advanced Materials, 2013. **25**(32): 4437-4444.

202. Compton, O.C., S. Kim, C. Pierre, J.M. Torkelson, and S.B.T. Nguyen, Advanced Materials 2010. **22**: 4759-4763.

203. Zhang, X., Z. Sui, B. Xu, S. Yue, Y. Luo, W. Zhan, and B. Liu, Journal of Materials Chemistry, 2011. **21**: 6494-6497.

204. Chen, W. and L. Yan, Nanoscale, 2011. **3**: 3132-3137.

205. Ren, L., K.S. Hui, and K.N. Hui, J. Mater. Chem. A, 2013. **1**: 5689-5694.

206. Chen, L., X. Wang, X. Zhang, and H. Zhang, Journal of Materials Chemistry, 2012. **22**: 22090-22096.

207. Guo, S., S. Zhang, L. Wu, and S. Sun, Angewandte Chemie, International Edition, 2012. **51**(47): 11770-11773.

208. Wang, M., J. Huang, M. Wang, D. Zhang, W. Zhang, W. Li, and J. Chen, Electrochemistry Communications, 2013. **34**(0): 299-303.

209. Li, Y., M. Gong, Y. Liang, J. Feng, J.-E. Kim, H. Wang, G. Hong, B. Zhang, and H. Dai, Nat Commun, 2013. **4**: 1805.

210. Zhou, R., Y. Zheng, D. Hulicova-Jurcakova, and S.Z. Qiao, Journal of Materials Chemistry A, 2013. **1**(42): 13179-13185.

211. Duan, J., Y. Zheng, S. Chen, Y. Tang, M. Jaroniec, and S. Qiao, Chem. Commun. (Cambridge, U. K.), 2013. **49**: 7705-7707.

212. Zhu, H., S. Zhang, Y.-X. Huang, L. Wu, and S. Sun, Nano Letters, 2013. **13**(6): 2947-2951.

213. Liang, Y., H. Wang, J. Zhou, Y. Li, J. Wang, T. Regier, and H. Dai, Journal of the American Chemical Society, 2012. **134**(7): 3517-3523.

Chapter 2

General Research Techniques

Chapter 2

2. CONTENTS

2.1 Reagents and Materials

Chemicals	*Grade*	*Supplier*
1-Butanol ($C_4H_{10}O$)	A.R.	Sigma-Aldrich
Acetone	A.R.	Ajax Finechem
Ammonium solution (28 wt%, NH_3OH)	A.R.	Sigma-Aldrich
Carbon black (Vulcan XC 72R)	-	CABOT
Chloroplatinic acid solution (8 wt% H_2PtCl_6)	A.R.	Sigma-Aldrich
Citric Acid ($C_6H_8O_7$)	A.R.	Sigma-Aldrich
Cobalt chloride ($CoCl_2$)	A.R.	Sigma-Aldrich
Copper chloride dihydrate ($CuCl_2 \cdot 2H_2O$)	A.R.	Sigma-Aldrich
Ethanol (CH_3OH)	A.R.	Ajax FineChem
Graphite	A.R.	Sigma-Aldrich
Hexadecyltrimethylammonium bromide (CTAB)	A.R.	Fluka
Hydrazine Solution (30 wt.%, N_2H_4)	A.R.	Sigma-Aldrich
Hydrochloride Acid (35 wt.% HCl)		
Iron(III) p-toluenesulfonate hexahydrate (FeToS)	A.R.	Sigma-Aldrich
Isopropanol ($C_3H_8O_2$)	A.R.	Ajax FineChem
L-ascorbic acid (L-AA)	A.R.	Sigma-Aldrich
N,N,N',N'-Tetramethyl-1,6-hexanediamine (TMDA)	A.R.	Sigma-Aldrich
Nafion® 117 Membrane	-	Sigma-Aldrich
Nafion® 117 solution (~5% in a mixture of lower aliphatic alcohols and water)	A.R.	Sigma-Aldrich
Nickel chloride hexahydrate ($NiCl_2 \cdot 6H_2O$)	A.R.	Sigma-Aldrich
Palladium(II) chloride ($PdCl_2$)	A.R.	Sigma-Aldrich
Perchloric Acid (70wt%, $HClO_4$)	A.R.	Sigma-Aldrich

Phosphoric acid solution (85 wt%, H_3PO_4)	A.R.	Sigma-Aldrich
Poly(tetrafluoroethylene) (PTFE)	A.R.	Sigma-Aldrich
Poly(vinylbenzyl chloride) (PVBC)	A.R.	Sigma-Aldrich
Potassium Hydroxide (KOH)	A.R.	Sigma-Aldrich
Potassium permanganate ($KMnO_4$)	A.R.	Sigma-Aldrich
Pt/C (20wt.% Pt on Vulcan XC72R)	-	E-Tek
Pyrrole (distilled)	A.R.	Sigma-Aldrich
Sodium borohydride ($NaBH_4$)	A.R.	Sigma-Aldrich
Sodium Hydroxide (NaOH)	A.R.	Sigma-Aldrich
Sulphuric Acid (98wt.%, H_2SO_4)	A.R.	Ajax FineChem
Urea (CN_2H_4O)	A.R.	Sigma-Aldrich
VBC-grafted-ETFE Membrane	-	University of Surrey

2.2 Physical Characterization

2.2.1 X-ray Diffractometer (XRD)

X-ray Diffractometer (XRD) is a non-destructive technique that could be used to determine the chemical structural properties and crystallinity of metal or metal alloy nanocrystals. In this study, a GBC MMA diffraction metal (GBC Scientific Equipment Pty Ltd, Australia) with a monochromatic Cu-Kα radiation source was utilized to confirm the structural properties and particle size of metal or bimetallic catalysts. The XRD equipment and a typical XRD pattern of the commercial Pt/C (20 wt. % Pt on Vulcan XR 72C, E-Tek) was shown in Figure 2.1.

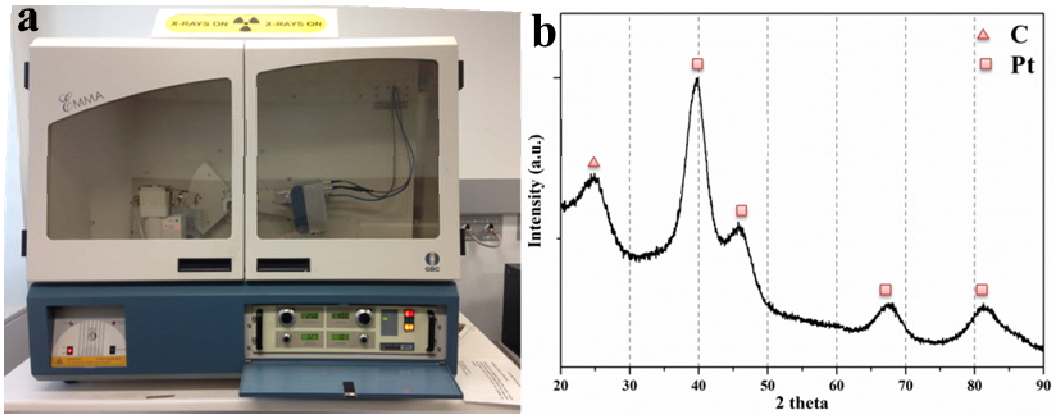

Figure 2.1a) Digital image of the X-ray diffractometer and b) the typical XRD curves of the commercial E-Tek Pt/C (20 wt. % on Vulcan XR 72C) recorded at a scan rate of 2°/min.

2.2.2 Raman Spectroscopy

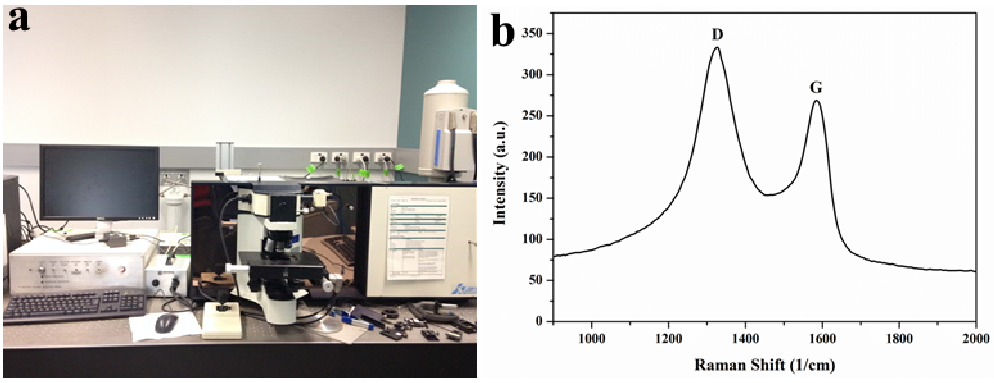

Figure 2.2 a) The digital photo of the JOBIN YVON HR800 confocal Raman Spectrometer and b) a typical Raman Spectrum of graphene oxide at the excitation laser of 632.81 nm.

Raman spectroscopy is a spectroscopic technique to observe vibration, rotational and other low-frequency mode in a system. In this study, a JOBIN YVON HR800 confocal Raman Spectrometer (HORIBA, Pty Ltd., France) with the laser beam of 632.81nm at room temperature was select to determine the surface functionality of graphene oxide, reduced graphene oxide, graphene aerogel, nitrogen doped graphene, and cobalt oxide-

graphene composite etc. The corresponding used Raman equipment and a typical Raman spectrum of graphene oxide is shown in Figure 2.2.

2.2.3 Fourier Transform Infrared Spectroscopy (FTIR)

Fourier transform infrared spectroscopy (FTIR) is a technique which is used to obtain an infrared spectrum of one sample. Such infrared spectrum represents a fingerprint of a sample with absorption peaks which correspond to the frequencies of vibrations between the bonds of the atoms making up the material and thus could be used to identify the chemical composition of samples. In this study, we used Shimadzu FTIR Prestige-21(Shimadzu Scientific Instruments, Australia) to analyse the chemical bonding of graphene, graphene polypyrrole (PPy) samples. Figure 2.3 shows the corresponding used FTIR instrument and a typical FTIR spectrum of PPy.

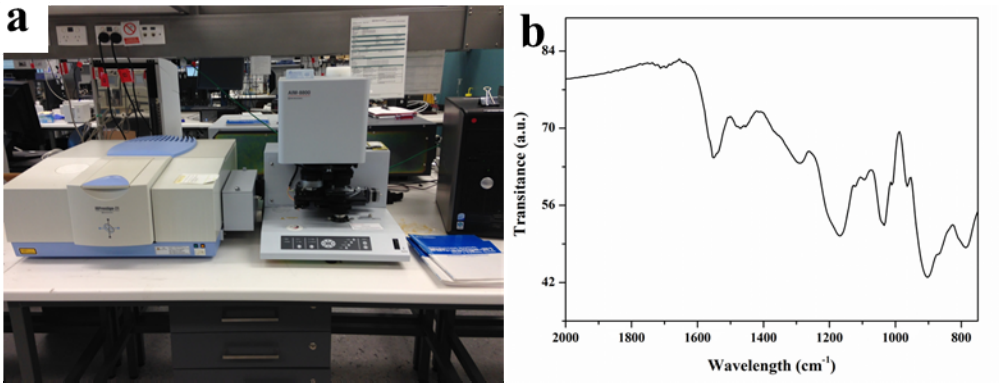

Figure 2.3 a) Digital image of the Shimadzu Prestige-21Fourier transform infrared spectrometry and b) the typical FTIR spectrum of PPy

2.2.4 UV-visible Spectroscopy

UV-Visible (UV−vis) spectroscopy is routinely used in analytical chemistry for the quantitative determination of different analyses, such as transition metal ions, highly conjugated organic compounds, and biological macromolecules. In this study, we carried out the in-situ UV-Vis spectroscopy (Shimadzu UV 1800 spectrophotometer) to

monitor the formation and sacrifice of copper nanoparticle in the colloids (Chapter 4) and to identify the formation of graphene oxide from a chemical oxidation method (Chapter 6). The corresponding used UV-Vis equipment and an example of UV-vis spectrum of copper nanoparticle colloids were shown in Figure 2.4.

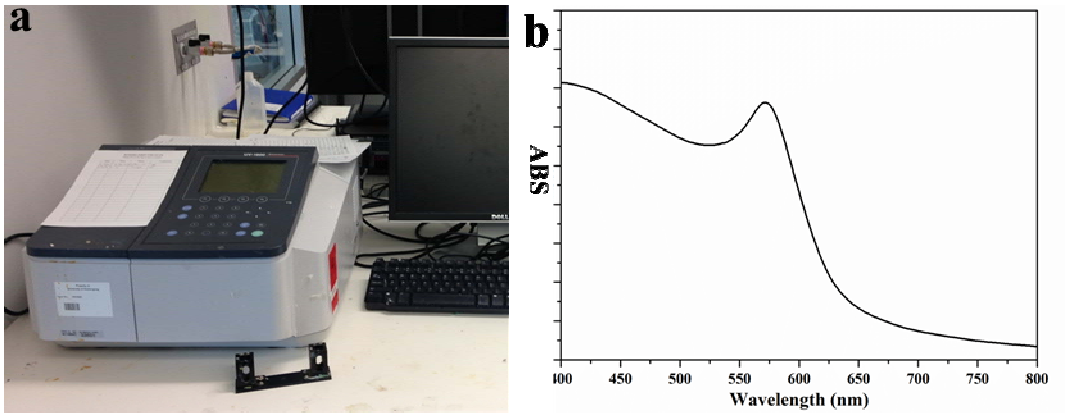

Figure 2.4 a) Digital image of the Shimadzu UV 1800 spectrophotometer and b) a typical spectrum of the copper nanoparticle dispersed in de-oxygen water.

2.2.5 X-ray Photoelectron Spectroscopy (XPS)

X-ray photoelectron spectroscopy (XPS) is a surface-sensitive quantitative spectroscopic technique that measures the elemental composition at the parts per thousand range, empirical formula, chemical state and electronic state of the elements that exist within a material. In this study, we use XPS to study the electronic structure and element composition of various samples, which would be further discussed in later chapter. The used XPS equipment was shown in Figure 2.5

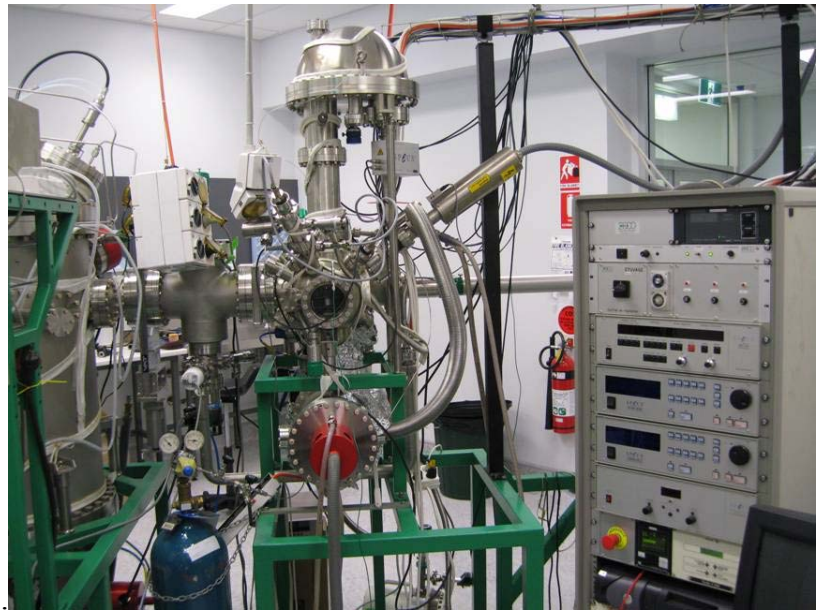

Figure 2.5 The digital image of the X-ray photoelectron spectrometer

2.2.6 Thermogravimetric Analysis (TGA)

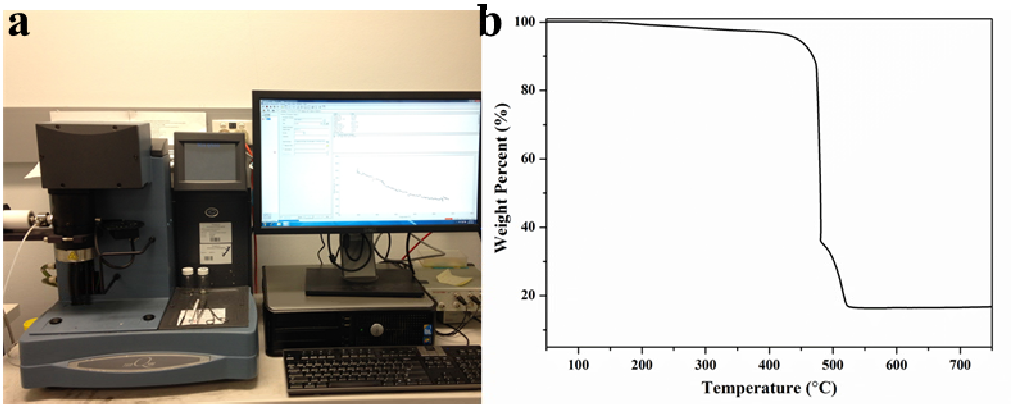

Figure 2.6 a) The digital photo of the Q500 TGA analyser and b) TGA curves of the commercial E-Tek Pt/C under air environment at a ramp heating rate of 10 °C min^{-1} from room temperature to 750°C

Thermogravimetric analysis (TGA) is a method of thermal analysis in which changes in physical and chemical properties of materials are measured as a function of increasing temperature (with constant heating rate), or as a function of time (with constant temperature and/or constant mass loss). In this study, a Q500 TGA analyser (TA

Instruments, UK) was used to determine the loading amount of metal, metal alloys on carbon support. Figure 2.6 shows the TGA equipment and the typical TGA curves of the commercial Pt/C (20 wt.% Pt loading on the Vulcan XR 72C, E-Tek). Determined from the curves, the Pt loading is about 20.5 wt.% for the commercial E-Tek Pt/C.

2.2.7 Inductively Coupled Plasma−Mass Spectrometry (ICP-MS)

Inductively coupled plasma−mass spectrometry (ICP-MS) is a type of mass spectrometry which is capable of detecting metals and several non-metals at concentrations as low as one part in 1012 (part per trillion) by ionizing the sample with inductively coupled plasma and then using a mass spectrometer to separate and quantify those ions. In this study, we use the ICP-MS (Thermo Scientific, Australia) to determine the metal compositions of the bimetallic catalysts.

2.3 Electrochemical Methods

2.3.1 Cyclic Voltammetry

Cyclic Voltammetry (CV) is the most useful technique in electrochemistry. It can quickly provide qualitative information about catalysts and electrochemical reactions, such as the electrochemical response of the catalysts and the catalytic activity of the catalysts with respect to some electrochemical reactions. In a classic cycle of CV triangle waveform, the potential is swept from an Initial E, to vertex E and back to Final E. Repeating this waveform for multi-times will perform multi-cycles of CVs.

In this study, CV was performed using a CHI 720C bipotentiostat (CH instruments, USA) was mainly used to determine the electrochemical active surface area (ECSA), which is a crucial index figure in Pt or Pd contained electrocatalyst. Through this index, we can get how much ratio of Pt was activated when it was use to oxygen reduction and

hence to characterize the dispersion of Pt in its support materials and also whether the micro-structure of Pt is suitable towards ORR. Besides CV was also used to preliminarily study the oxygen reduction reaction (ORR) responses on the non-noble metal based electrocatalysts.

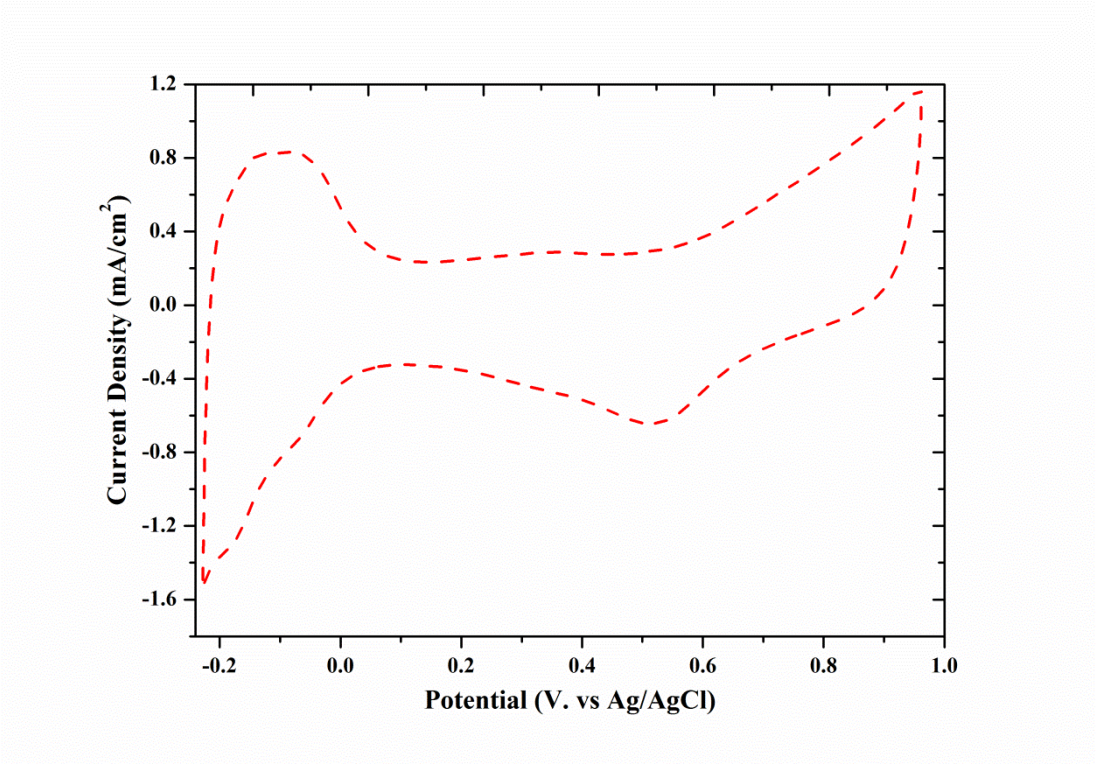

Figure 2.7 Typical CV curves of commercial E-Tek Pt/C at a scan rate of 50 mV/s in 0.1 M HClO4 solution saturated with high purity N_2 at room temperature.

For the ECSA measurements on noble catalysts, the CV was recorded in high purity N_2 saturated 0.1 M $HClO_4$ electrolyte (Figure 2.7).[1] The calculation of ECSA (S_{act}) can be obtained by following equation

$$S_{act} = Q_h \,/\, Q_{h0} \qquad \text{Equation 2-1}$$

Where Q_h refers to specific charge transfer due to hydrogen adsorption and desorption, Q_{h0} refers to the theoretically adsorption of hydrogen per real cm^2 of Pt with monolayer, Q_{h0}=210 μC/cm^2. The Q_h could be obtained from the following equation:

$$Q_h = \frac{1}{2}\,(Q_t - Q_{DL}) \qquad \text{Equation 2-2}$$

Where Q_t is the total specific charge transfer in the hydrogen adsorption/desorption potential region and Q_{DL} is the specific capacitive charge in the double layer of both Pt and the carbon supports. Q_t could be obtained by integration of the CV curves in the relevant potential region:

$$Q_t = \frac{1}{\upsilon}\int_a^b (I_d - I_a)\, dE \qquad \text{Equation 2-3}$$

Where υ is the scanning rate, I_d and I_a are the specific current of desportion and adsorption, respectively, and E is the potential. Q_{DL} can be similarly obtained by integrating the double layer charging region.

2.3.2 Linear Sweep Voltammetry

Linear Sweep Voltammetry (LSV) is a simpler subset of cyclic voltammetry, consisting of a single unidirectional voltage sweep. In our study, the LSV technique was used to obtain the steady state polarization curves of the electrocatalysts towards the ORR. Typically, the LSV was recorder in either 0.1 M $HClO_4$ or KOH electrolyte at a scan rate of 5 mV s^{-1} for noble metal based electrocatalysts modified electrode and 10 mv s^{-1} for non-noble metal based electrocatalysts modified electrode since further decrease of scan rate result in no change in the LSV curves.

2.3.3 Rotating (Ring) Disk Electrode Technique

The rotating ring-disk electrode (RRDE) is double working electrode used in hydrodynamic voltammetry in a three electrode system, it could be used as a rotating disk electrode if the ring is left inactive during the experiment. In this study, we use RDE or RRDE to study the mechanism of the ORR on various catalysts modified electrodes (Figure 2.8a).

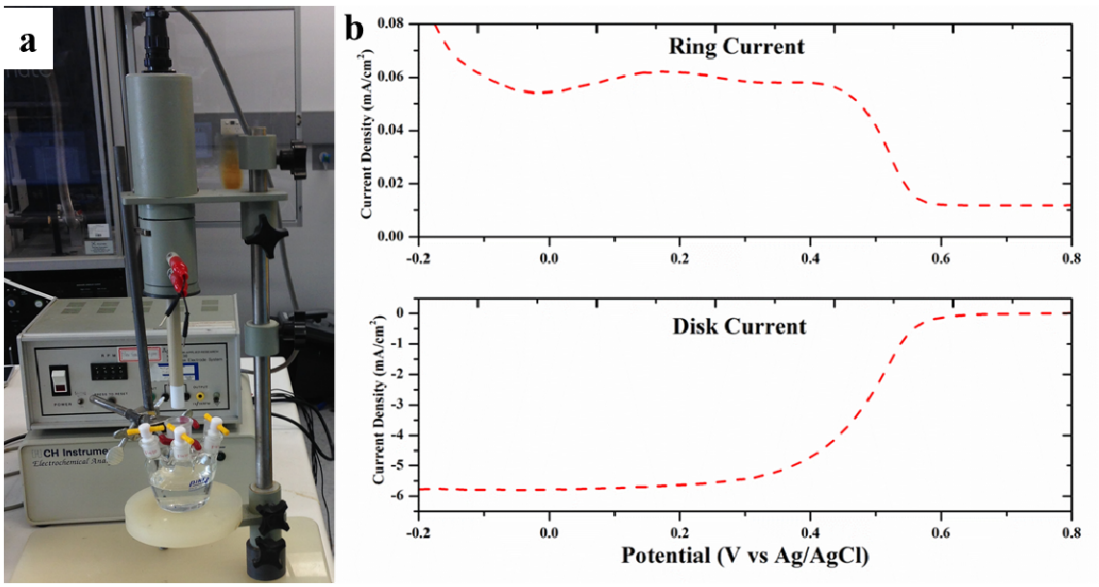

Figure 2.8 a) Digital photo of the rotating ring disk electrode (RRDE) used in the experiments and b) the RRDE curves obtained on a Pt/C modified electrode at a scan rate of 5 mV s^{-1} in 0.1M O_2 saturated $HClO_4$ electrolyte, the applied potential on the ring is 1V.

The electron transfer number during the ORR could be exactly calculated through the well-known Levich-Koutechy equation as below: [2]

$$\frac{1}{j} = \frac{1}{j_k} + \frac{1}{B\varpi^{0.5}} \qquad \text{Equation 2-4}$$

$$B = 0.2nF(D_{O2})^{2/3}(v)^{-1/6}C_{O2} \qquad \text{Equation 2-5}$$

Where j_k is the kinetic current and ω is the electrode rotating rate. F is the Faraday constant (F = 96485 C mol-1), D_{O2} is the diffusion coefficient of O_2, υ is the kinetic viscosity, and C_{O2} is the bulk concentration of O_2. The constant 0.2 is adopted when the rotation speed is expressed in rpm. For the RDE data analysis, three non-electrochemical kinetic parameters, such as the diffusion coefficient of O_2, the kinematic viscosity of the electrolyte solution, and the solubility of O_2 must be known accurately. These parameters are all temperature dependent. Their values are also

slightly dependent on the electrolyte used lists these parameters at various conditions. Table 2.1 shows the non-electrochemical kinetic parameters for the RDE data analysis.

Table 2.1 Non-electrochemical kinetic parameters for the RDE data analysis

Experimental Conditions (T, electrolyte)	***Diffusion coefficient of O_2, $cm^2\ s^{-1}$***	***Kinematic viscosity of the electrolyte solution, $cm^2\ s^{-1}$***	***Solubility of O_2, mol cm^{-3}***	***Ref***
0.1 M $HClO_4$, 20°C	1.67×10^{-5}	0.01	1.38×10^{-6}	[3]
0.5 M H_2SO_4, 25°C	1.4×10^{-5}	0.01	1.1×10^{-6}	[4]
0.1 M KOH, 25°C	1.9×10^{-5}	0.011	1.2×10^{-6}	[5, 6]
0.1 M NaOH, 25°C	1.65×10^{-5}	0.011	8.4×10^{-7}	[7]

The intermediates produced on the disk electrode in the ORR process could be detected on the ring and be further used to deduce the ORR mechanism in the RRDE method. In this study, we conduct the RRDE measurement on the PtCu electrocatalysts to study the mechanism of the ORR occurred on the PtCu modified electrode by determination of the generation of H_2O_2. Figure 2.8b shows the RRDE polarization curves obtained on the commercial Pt/C modified electrode with the constant ring potential at 1V. The number of electrons exchanged in the ORR (n) and the percentage of hydrogen peroxide (% H_2O_2) can be obtained using the following equations.

$$n = \frac{4I_D}{I_D + \left(\frac{I_R}{N}\right)} \qquad \text{Equation 2-6}$$

$$\%H_2O_2 = \frac{100(4-n)}{2} \qquad \text{Equation 2-7}$$

Where I_D is the disk current, I_R is the ring current and N is the collection efficiency of the RRDE apparatus used in this study which is 0.37 determined using the Fe^{II}/Fe^{III} redox system in a solution containing 1 mM $K_3Fe(CN)_6$ and 0.1 M $NaNO_3$.

2.3.4 Specific Area Activity and Mass Activity

To detailed study the electroactivities of the electrocatalyst, the kinetic current is calculated from ORR polarization curves by considering the mass-transport correction using the Levich-Koutecky equation:

$$\frac{1}{i} = \frac{1}{i_k} + \frac{1}{i_d}, \qquad \text{Equation 2-8}$$

where i_k is the kinetic current and i_d is the diffusion limiting current) and normalized against to ECSA and mass of electrocatalysts to compare the specific area activity and mass activity.[8]

2.3.5 Single Fuel Cell Test

The hydrogen oxygen fed proton exchange membrane and anion exchange membrane fuel cell tests were conducted to obtain the real performance of the catalysts in a real operating environment. The cell configuration is as depicted in Figure 2.9. As could been seen, the cell was constructed with two graphite plate sandwiched with the core part of fuel cell – membrane electrode assembly (MEA). The MEA was prepared through sandwiched using gas diffusion layer (GDL) loaded with catalysts and a membrane (either proton or anion exchanged). Although the preparation method of GDL is different for PEMFC or AEMFC, the assembly configuration is exactly the same except the different membrane used.

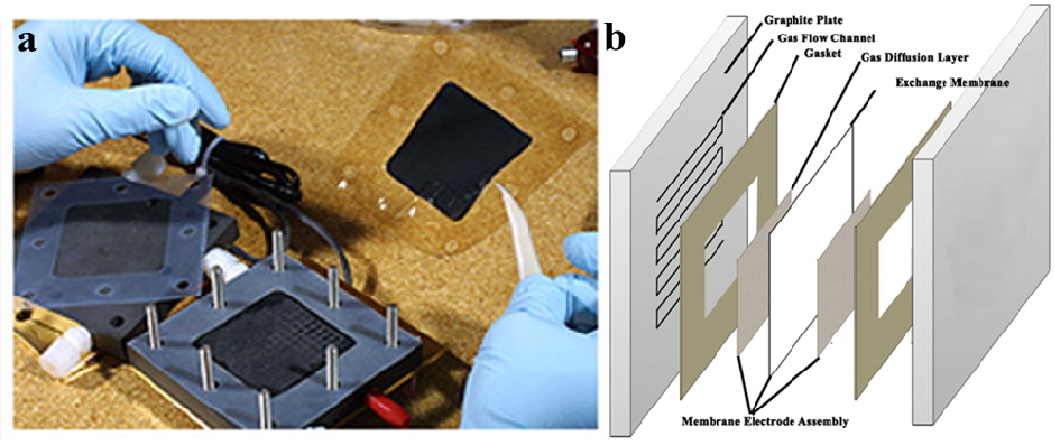

Figure 2.9 a) Digital figure of the single fuel cell hardware and b) schematic illustration of cell configuration

To test the single cell performance, an 850e fuel cell test system (Fuel Cell Technologies, Inc., USA, Figure 2.10) fed with humidified hydrogen and oxygen respectively was used. In a typical testing procedure, polarization curves were recorded using a current scan method by holding the cell at each current for 60s in order to get the steady-state potential value with a scan rate of 10 dec/pt from 0A to a certain current or using a potential scan method by holding the cell at each potential for 60s in order to get the steady-state current value with a scan rate of 25 mV s^{-1} from 0.95 V to a certain potential. For PEMFC, the cell temperature was maintained at 80 °C with back pressure of 15 psi and the gas flow was controlled at 0.08 mL min^{-1} with humidifier temperature at 80 °C. For AEMFC, the cell temperature was maintained at 60 °C without back pressure and the gas flow was controlled at 0.6 mL min^{-1} with humidifier temperature at 60 °C. Figure 2.10b gives the steady-state polarization curves of PEMFC using E-Tek Pt/C (20 wt.%) as cathode catalysts with loading of 0.4 $mg_{pt}.cm^{-2}$ at 80 °C using a scan current technique.

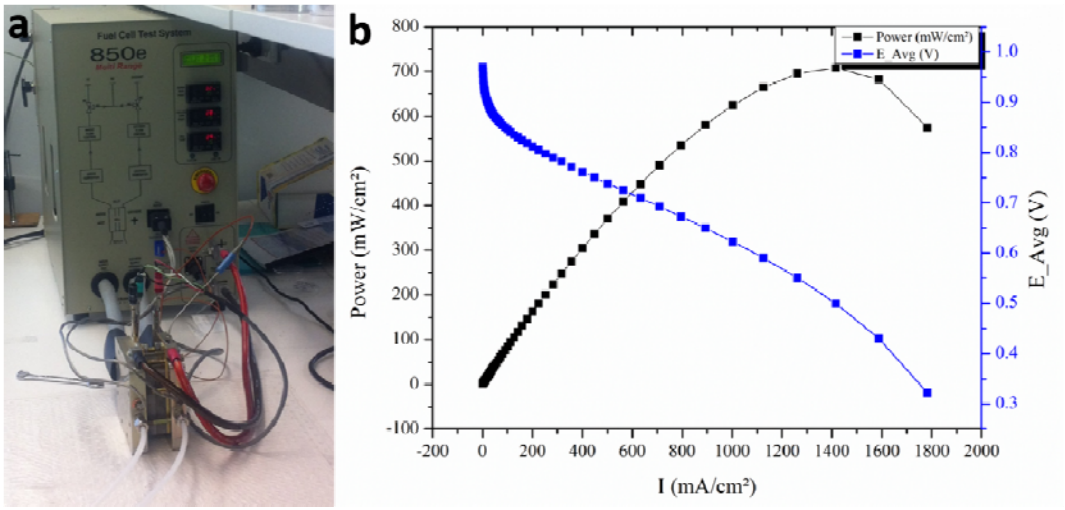

Figure 2.10 a) The single fuel cell testing system and b) the steady-state polarisation curves of the commercial E-Tek Pt/C electrocatalysts. Pt loading amount are 0.4 mg cm^{-2} at the cathode, 0.2 mg cm^{-2} at the anode. Operating conditions: Humidifier temperatures are 80°C for anode, 75°C for the cathode, cell temperature is 80°C and the back pressure is 1.5 atm.

2.4 Synthesis of Nanostructured Electrocatalysts

2.4.1 Sacrificial Template Method in Preparing Hollow Nanostructures

In this study, the sacrificial template method was employed to synthesize various Pt or Pd based nanostructures with hollow features, which have larger specific area and thus having great advantageous in producing high electroactive electrocatalysts for the ORR. [9, 10] The scheme for synthesis of gold-silver nanocages using a sacrificial template is illustrated in Figure 2.11. [11]

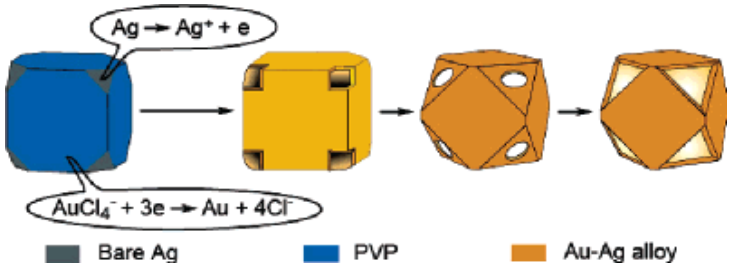

Figure 2.11 Schematic illustration detailing all major steps involved in the formation of Au-Ag nanocages with well-controlled pores at the corners.[11]

In our experiment, metal nanoparticle with relatively lower standard reduction potential was firstly synthesized thorough borohydride or hydrazine reduction method, then the later added metal ions with higher standard reduction potential, the galvanic replacement would occur immediately, the second ions would be reduced and deposited on the surface of first metal surface and diffused into first metal atoms and hollow bimetallic nanostructure would therefore be formed.

2.4.2 Synthesis of Graphene Oxide through an Improved Hummers Method

The chemical derived graphene oxide was extensively used in research because of its ease preparation. In this study, we used the improved method to synthesize graphene oxide, which is reported by Tour et.al.[12] In a typical synthesis procedure, a 9:1 mixture of concentrated H_2SO_4/H_3PO_4 (360:40 mL) was added to a mixture of graphite flakes (3.0 g) and KMnO4 (18.0 g), producing a slight exothermal to 35-40 °C. The reaction was then heated to 50 °C and stirred for 12 h. The reaction was cooled to RT and poured onto ice (400 mL) with 30% H_2O_2 (13 mL). The mixture was washed with HCl acid (10 wt. %) and centrifuged (4000 rpm for several times), the supernatant was decanted away. The remaining solid material was filtered over a PTFE membrane with a 0.45 m pore size. The solid obtained on the filter was vacuum-dried overnight at room

temperature, obtaining 5.8 g of product. Dialysis was finally used for 2 weeks with exchanging water several times to complete remove acid and metal ions.

2.4.3 Synthesis of Graphene Hydrogel and Aerogel

In this study, we utilize the graphene aerogel as supporting materials and catalysts for the ORR in alkaline medium because of its open structure could provide ample ion transfer channels and mass diffusion channels. The conventional synthesis procedure involves in a hydrothermal method.[13] In the procedure, the graphene oxide with a concentration of 2 mg/mL h was sealed in a 16-mL Teflon-lined autoclave and maintained at 180 °C for 12 h. Then the autoclave was naturally cooled to room temperature and the as-prepared graphene hydrogel were taken out with tweezers and to synthesize graphene aerogel, the hydrogel was freeze drying for 12 hours. The process could also been simplified by adding weak reducing agent, such as ascorbic acid and keeping in mild temperature for less hours. In our process, a 20 mL GO (4 mg mL^{-1}) with 320 mg L^{-1} ascorbic acid solution were mixed and sonicated for 10 min before placing in a water bath at 70 °C for 4 hours. After reduction, the graphene hydrogels were carefully taken out and purified by distilled water for one week.

2.4.4 Vapor Phase Polymerization Method

Vapor phase polymerization is a well-developed method in our group in producing inherent conducting polymer films with high conductivities, uniformities at the nanoscale on certain substrates.[14] In this study, it was employed to produce uniform PPy films on the graphene hydrogel to fabricate uniformly nitrogen doped graphene sheets. In a typical synthesis procedure, hydrogels were firstly converted to alcogels by exchanging with ethanol for several times and then submerged into Iron (III) p-toluenesulfonate (FeToS) butanol solution. After that alcogels were dried in a

conventional oven at 100 °C for 30 minutes to prepare FeToS films on the graphene aerogel sheets. To synthesize PPy on graphene alcogels, these alcogels were placed in sealed flasks saturated with pyrrole (Figure 2.12) monomer for 1 hour in an oven at 60 °C to polymerized polypyrrole on the graphene sheets. After vapor phase polymerization, the PPy- alcogels were washed with copious amount of ethanol and water several times to completely removed unreacted oxidizing agent, pyrrole and butanol.

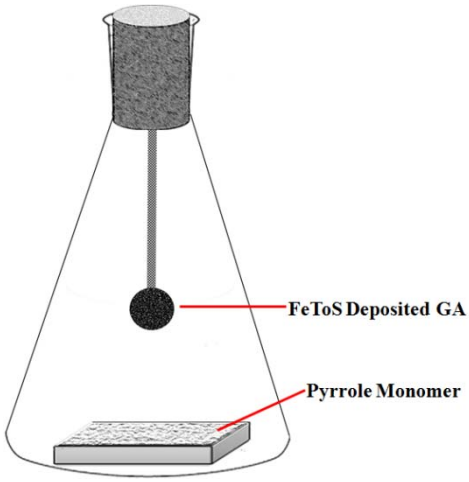

Figure 2.12 Schematic illustration of the vapour phase polymerisation chamber

2.4.5 Fabrication of Membrane Electrode Assembly

The fabrication process of gas diffusion electrodes (GDEs) and membrane electrode assembly (MEA) are shown in Figure 2.13. The process for PEMFC and AEMFC was almost the same except the use of different membrane and ionomer. For the GDE preparation, ink slurry containing catalysts and ionomer (approximate 30 wt. % of the catalysts) dispersed in isopropanol (PEMFC) or ethyl acetate (AEMFC) was sonicated for 1 hour to obtain the well dispersion. Then this dispersion was spray coated onto the gas diffusion layer (GDL) using an air brush technique (Sonotek Spray Coating System) and dried in a vacuum oven at 60°C (AEMFC) or 100 °C (PEMFC) for 6 hours. For

PEMFC, the MEA was directly assembled by sandwiching a piece of Nafion membrane between two GDEs and the cell is tightening to 4 N with a torque wrench. For AEMFC, the anion exchange membrane, in this case an electron-beam-grafted ETFE as alkaline anion-exchange membrane [15] and the GDEs were submerge t in 1.0 mol dm^{-3} KOH for 1 hour and washed extensively with water. The MEA is constructed within the fuel cell by placing the electrode against the membrane without hot pressing. The cell is tightening to 5.5 N with a torque wrench.

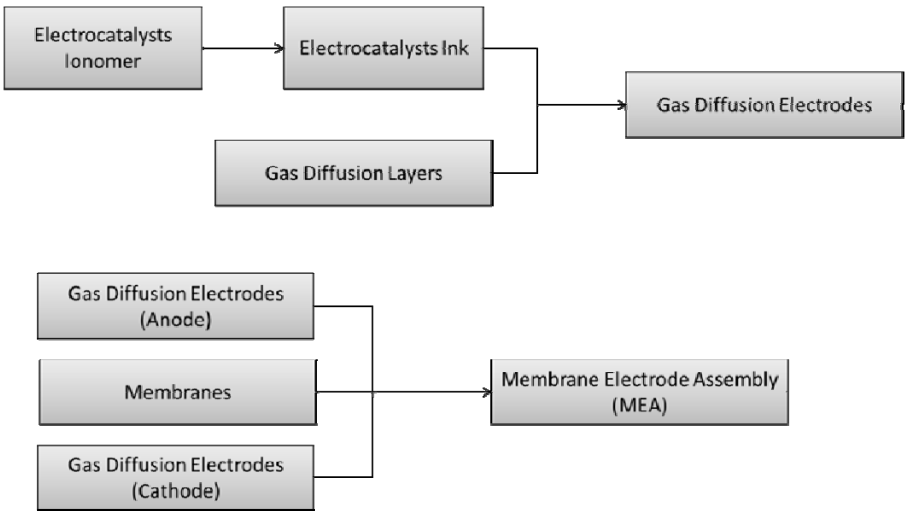

Figure 2.13 Fabrication process for the gas diffusion electrodes and membrane electrode assembly

2.5 References

1. Xing, Y., The Journal of Physical Chemistry B, 2004. **108**(50): 19255-19259.
2. Wang, S., D. Yu, and L. Dai, Journal of the American Chemical Society, 2011. **133**(14): 5182-5185.
3. Wakabayashi, N., M. Takeichi, M. Itagaki, H. Uchida, and M. Watanabe, Journal of Electroanalytical Chemistry, 2005. **574**(2): 339-346.
4. Gochi-Ponce, Y., G. Alonso-Nuñez, and N. Alonso-Vante, Electrochemistry Communications, 2006. **8**(9): 1487-1491.

5. Parthasarathy, A., S. Srinivasan, A.J. Appleby, and C.R. Martin, Journal of the Electrochemical Society, 1992. **139**(9): 2530-2537.

6. Jahan, M., Q. Bao, and K.P. Loh, Journal of the American Chemical Society, 2012. **134**(15): 6707-6713.

7. Paliteiro, C., A. Hamnett, and J.B. Goodenough, Journal of Electroanalytical Chemistry and Interfacial Electrochemistry, 1987. **233**(1–2): 147-159.

8. Lim, B., M. Jiang, P.H.C. Camargo, E.C. Cho, J. Tao, X. Lu, Y. Zhu, and Y. Xia, Science, 2009. **324**(5932): 1302-1305.

9. Zhou, X., Y. Gan, J. Du, D. Tian, R. Zhang, C. Yang, and Z. Dai, Journal of Power Sources, 2013. **232**: 310-322.

10. Lou, X.W., L.A. Archer, and Z. Yang, Advanced Materials, 2008. **20**(21): 3987-4019.

11. Chen, J., J.M. McLellan, A. Siekkinen, Y. Xiong, Z.Y. Li, and Y. Xia, Journal of the American Chemical Society, 2006. **128**(46): 14776-14777.

12. Marcano, D.C., D.V. Kosynkin, J.M. Berlin, A. Sinitskii, Z. Sun, A. Slesarev, L.B. Alemany, W. Lu, and J.M. Tour, ACS Nano, 2010. **4**(8): 4806-4814.

13. Xu, Y., K. Sheng, C. Li, and G. Shi, ACS Nano, 2010. **4**(7): 4324-4330.

14. Winther-Jensen, B., J. Chen, K. West, and G. Wallace, Macromolecules, 2004. **37**(16): 5930-5935.

15. Chen, J., J.Z. Wang, A.I. Minett, Y. Liu, C. Lynam, H. Liu, and G.G. Wallace, Energy & Environmental Science, 2009. **2**(4): 393-396.

16. Winther-Jensen, B., O. Winther-Jensen, M. Forsyth, and D.R. MacFarlane, Science, 2008. **321**(5889): 671-674.

17. Varcoe, J.R. and R.C.T. Slade, Electrochemistry Communications, 2006. **8**(5): 839-843.

Chapter 3

Stabilization of Pt on Pd as a Bimetallic Electrocatalyst with Enhanced Catalytic Activity and Durability for Proton Exchange Membrane Fuel Cell

3. **CONTENTS**

Chapter 3

3.1 Introduction

Fuel cells have recently attracted a great number of concern owing to its fast start-up, high energy density and low environmental impact and thus are believed to be promising solution for today's increasing demand on energy.[1, 2] It is generally believed that the performance of fuel cells is kinetically limited at the cathodic oxygen reduction reaction (ORR) step because of its relatively sluggish reaction mechanism.[1-3] Although many non-metal or non-precious metal electrocatalysts have been developed in order to lower the catalyst cost,[4-7] currently platinum (Pt) nanoparticles (with size from 2-3 nm) on carbon supports is considered to be the most efficient catalysts for the ORR process, however, the high cost, low utilization and poor stability issues are the major challenges hindering wide-spread commercialisation of fuel cell technology.[8] The question here becomes one of finding practical ways to reduce the cost and at the meantime to increase the catalytic efficiency and stability of Pt catalysts.

In order to reduce the cost and enhance its catalytic efficiency and stability, alloying of Pt with noble elements such as Pd,[3] Au,[9] Ir,[10] etc. has been extensively investigated and proved to be effective due to the change on the electronic and geometric structure of Pt.[11-13] Among these Pt-based alloy electrocatalysts, Pt-Pd systems have attracted particular attention because the less expensive Pd has similar intrinsic ORR catalytic activity as Pt, and is stable in acidic solutions, therefore the combination of Pt with Pd would not only reduce the cost of Pt but also enhance the catalytic performance of the Pt-based catalysts. Moreover, the stability of Pt-Pd electrocatalysts was also seen to be improved due to the changes on the geometric structure of Pt.[3, 13, 14] With this respect, many strategies have been developed for the synthesis of Pt-Pd catalysts with different structures such as alloys, dendrites, core-shells, multiple-shells, and monolayer.[3, 11, 15-19] However, conventionally, Pt on Pd

nanoparticles were often synthesized by using Pd as sacrificial template or Pd seed-mediated reduction method, resulting in additional cost from Pd or random nucleation problem of Pt in reductive media[11, 18, 19]. More effort is still needed to explore the methods for the controllable synthesis of Pt on Pd in a large scale.

In this chapter, we demonstrate a simple approach based on modified galvanic replacement reaction that is capable of stabilized growing Pt on the surface of Pd hollow particles directly, which produced excellent bimetallic electrocatalysts Pt-Pd with longer term durability and higher catalytic activities. The sacrificial template (galvanic replacement), which was firstly well demonstrated by Xia's group[20], has been widely applied to synthesise nanocrystals with hollow features[21]. In this study, the utilization of the hollow shaped Pd nanoparticle would increase the specific area, provide more active sites and mass transfer channels for the electrocatalysts. When the Pt precursor was reduced by accepting the electrons transported from the sacrificial template beneath Pd layer, Pt nanoparticles would be nucleated onto the surface of the Pd hollow nanostructure forming the Pt-Pd alloyed nanostructures. The as-synthesized Pt-Pd has been physically characterized showing their alloyed nature and the hollow shaped morphologies. In addition, the electrochemical tests also revealed the synthesized Pt-Pd electrocatalysts with much improved catalytic activities and stabilities compared with the commercial E-Tek Pt/C (20 wt.%).

3.2 Experimental

3.2.1 Reagents

Sodium citrate (Sigma-Aldrich, 99%), Sodium borohydride ($NaBH_4$, Sigma-Aldrich, 98.5%), Cobalt chloride ($CoCl_2$, Sigma-Aldrich, 98%), Palladium chloride($PdCl_2$, Sigma-Aldrich, 99.9%), Chloroplatinic acid (K_2PtCl_4, Sigma-Aldrich, 99.9%), Pt/C (20

wt, E-TEK) and Nafion 117 solution (Sigma, ~5%), carbon fibre paper (GDL, 5 cm^2), acetone (Sigma), perchloric acid (ACS reagent, 70%, HClO4, Sigma-Aldrich)were used as received.

3.2.2 Synthesis of Pt-Pd Bimetallic Hollow Nanoparticles

The Pt-Pd bimetallic nanoparticles were synthesised as the follows. Firstly, cobalt nanoparticles was firstly synthesized and used as a sacrificial template Pd nanoparticles growth. In Brief, 2.6 mg $CoCl_2$ and 15 mg sodium citrate were dissolved in 50 mL Milli-Q water under vigorous stirring and purged with high purity N_2 for 30 minutes. An ice-cold solution of $NaBH_4$ (3.8 mg in 2 mL of H_2O) was added dropwise to the solution with stirring and N_2 bubbling. After 60 min, 0.71 mg $PdCl_2$ was dissolved in 10 mL deoxygenated HCl solution and then added dropwisely to the Co solution with stirring. Upon the completion of the galvanic replacement reaction of Co nanoparticles with $PdCl_4^{2-}$, 10 mL deoxygenated aqueous solution containing 4.98 mg K_2PtCl_4 was added and kept stirring for 60 min. For electrochemical measurements, the Pt-Pd nanoparticles were supported on carbon black to a loading amount of 20 wt% by mixing the above colloids and functionalised CB water dispersion and stirring overnight. Before filtration, an aliquot amount of acetone was added with stirring for another 2 hours, then the products were rinsed with water for several times to remove any unreacted substrate or surfactants and dried at 80 °C overnight and collected. To make a comparison of different Pt/Pd ratio on the ORR performance, different ratio of Pt/Pd were also prepared with Pt/Pd equalled 3:1, 2:1, 1:1, 1:2 and 1:3 respectively.

3.2.3 Preparation of Pt Hollow Nanoparticles

To make comparisons, the hollow shaped Pt nanoparticles on carbon supports was also synthesized and the preparation process was under identical conditions as that of the Pt-

Pd except only K_2PtCl_4 (5.8 mg in 10 mL H_2O) was added dropwise to the synthesized Co nanoparticles solution.

3.2.4 Physical Characterisations

The transmission electron microscope (TEM) images of samples were taken using a JEOL JEM-2200 FS transmission electron microscope operated at 200 kV. Energy dispersive X-ray spectroscopy (EDS) in the scanning transition electron microscopy STEM mode was employed for elemental composition and distribution of the catalyst particles. Samples for TEM were prepared through placing one drop of the cleaned nanoparticles ethanol dispersion on gold grid (200 mesh). The powder X-ray diffraction (XRD) patterns were recorded with a PANalytical X'Pert Pro MRD.

3.2.5 Electrochemical Characterisations

Electrochemical measurements were performed using a glassy carbon rotating ring disk electrode (RRDE, Pine Research Instrumentation, disk area=0.196 cm^2) connected to a CHI 720c potentiostat (CHI instrument) in a standard three-electrode cell with a Pt wire as the counter electrode and a 3 M KCl saturated Ag/AgCl electrode as the reference electrode. An electrochemical cell (Pine Instrument) was filled with about 100 ml 0.1M perchloride acid and covered with a Teflon cap. The eletrocatalysts ink was prepared by dispersing the electrocatalysts in 5% Nifion/H_2O/isopropanol (m/m/m/=0.5/10/50) to reach a 1mg/ml dispersion with an ultrasonicator (Brandson). 30 μL of the ink was dropped on the RRDE electrode and let it air-dry for 2 hours before the electrochemical tests. The electrode film was cycled 200 times between 0 and 1.2 V at 0.5 V/s to a stable current-voltage curves in nitrogen saturated electrolyte.

The additional CV curves were recorded in 0.1 M perchloride acid with a sweeping rate of 50 mV/s, and the Pt electrochemical surface area (ECSA) was estimated from the

charge of the underpotentially deposited (UPD) hydrogen, assuming 210 $\mu C/cm^2_{Pt}$.Oxygen reduction reaction (ORR) curves were recorded in oxygen saturated 0.1 M perchloride acid with a sweeping rate of 5 mV/s at successive rotation speed of 100, 400, 900, and 1600 rpm from −0.2- 1V.

To evaluate the electrochemical performances, electrochemical surface areas (ECSAs) were calculated by measuring the charge collected in the Hupd adsorption/desorption region after double-layer correction and assuming a value of 210 mC/cm2 for the adsorption of a hydrogen monolayer.

To determine the relative durability of the catalysts, the ORR activity of a catalyst thin film was measured before and after being subjected to 10,000 voltage cycles from 0.6 V to 1.0 V (vs. RHE) in oxygen saturated electrolyte at a rate of 50 mV/s.

3.2.6 Proton Exchange Membrane Fuel Cell Tests

The as-synthesised Pt-Pd/C or Pt/C electrode was used as the cathode to prepare the membrane electrode assembly (MEA), whereas the anode was a gas diffusion electrode with a commercial Pt/C (20 wt%, E-TEK) as an electrocatalyst. The metal loadings of the anode and the cathode were 0.25 and 0.2 mg cm^{-2}, respectively. For comparison, a reference MEA using E-TEK Pt/C for both sides with an equal amount of metal loadings as the Pt-Pd/C MEA was prepared. The prepared MEAs were tested using a 850e fuel cell test system (Fuel Cell Technologies, Inc., USA) fed with humidified hydrogen and oxygen respectively. The gas flow was controlled at 0.08 mL min^{-1}. The fuel cell measurements were carried out at 80°C under 15 psi (103.42 kPa) back pressure.. The polarization curves were recorded using a current scan method by holding the cell at each current for 60s in order to get the steady-state current value with a scan rate of 10 pt/dec from 0 A to 4.5 A.

3.3 Result and Discussion

3.3.1 Synthesis

The formation of Pt-Pd nanoparticles is similar to an electrochemical corrosion process as illustrated in Figure 3.1. Co nanoparticles were firstly synthesised using $NaBH_4$ as reducing agent and citric acid as surfactants. After the addition of H_2PdCl_4 solution, due to the redox potential of $PdCl_4^{2-}$/Pd (0.591 V vs. SHE) being higher than that of Co^{2+}/Co (-0.28 V vs. SHE), the surface of Co nanoparticle will be replaced by Pd and lead to the formation of a thin, incomplete layer of Pd. This is a typical electrochemical corrosion cell structure where Pd layer severs as cathode and the underneath Co as anode. With the Co being oxidized at the anode into Co^{2+}, the released electrons will migrate to the surface of Pd layer and could be used to reduce the subsequently added $PtCl_4^{2-}$ into zero-state Pt which leads to a Pd core Pt shell structure. As the released electrons were well be localized on the surface of Pd, the zero-state Pt would only be formed on the surface of Pd without any other random nucleation in the solution, which could be used to well controlled growth of Pt nanoparticles without any aggregation. And since Pt nanoparticles were formed on the surface of Pd, the aggregation of Pt due to carbon supports erosion on the long term fuel cell tests would be largely minimised generating longer durability electrocatalysts.

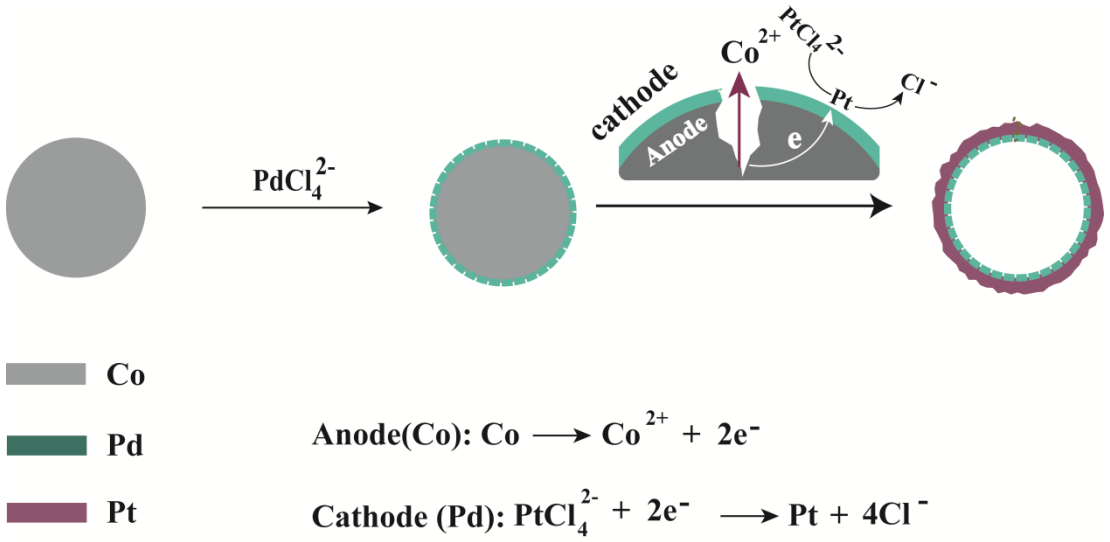

Figure 3.1 Schematic illustration for the synthesis procedures of the Pt-Pd hollow nanoparticles

3.3.2 Influence of the Pd/Pt ratio on the ORR Performance

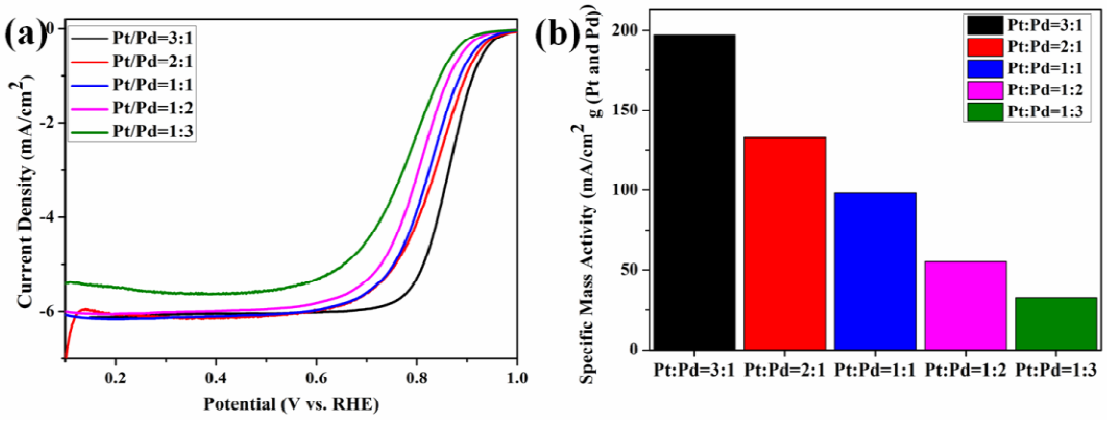

Figure 3.2 (a) ORR polarization curves and (b) Mass activities of the synthesized PtPd hollow nanoparticles with different precursor molar ratio at 0.9V.

To qualify the electroactivities of the PtPd/C ssynthesized with different precursor molar ratio, the solid state ORR polarisation curves and the kinetic mass current density were obtained. (Figure 3.2) The onset potential and half-wave potential of the Pt_3Pd_1/C (synthesized from the precursor molar ratio of Pt/Pd=3/1) is obviously positive than other three products synthesized from different precursor molar ratios indicating the

Pt_3Pd_1/C had a higher ORR catalytic activity than the other three products.(Figure 3.2a) The mass activity also revealed the similar trends on the ORR activities of the various products, the mass activity the Pt_3Pd_1/C is 197.3 mA cm^{-2} g^{-1}_{PtPd}, which is significantly higher than those of the other products activities (132.7, 98.2, 55.1 and 32.5 mA cm^{-2} g^{-1}_{PtPd} for Pt_2Pd_1/C, Pt_1Pd_1/C, Pt_1Pd_2/C and Pt_1Pd3/C respectively at 0.9 V (vs. RHE)). The enhanced ORR activity of the Pt_3Pd_1/C could possibly because a completed Pt shell could be only formed with this ratio. Thus in this chapter, the Pt_3Pd_1 nanoparticles was further characterized in detail and made comparisons with the commercial E-Tek Pt/C and homemade Pd/C electrocatalysts to study the differences of the electrocatalytic ORR abilities.

3.3.3 Morphology and Structure Analysis

The as-produced Pt-Pd nanoparticles were characterized with the TEM to investigate its morphological and structural information, which are shown in Figure 3.2. It could be seen the nanoparticles were well dispersed and displayed a hollow structure with size arranging around 15 nm and a shell thickness of 1-2 nm. Besides no random nucleation of Pt nanoparticles could be seen revealing all the Pt ions were nucleated on the Pd shell which maybe because the lattice of Pd is much closer to that of Pt thus facilitating the alloying process. More interestingly, the shell of the nanoparticles was covered with numerous grains with particle size of 2 nm forming a porous dendrite structure, which were possibly caused by the lattice mismatch(~0.77%) between the Pd and Pt during the formation process,[11] where the growth of Pt on Pd leads to the formation of a dense array of Pt branches on the Pd instead of a uniform Pt layer shell. High-resolution TEM (HRTEM) images (Figure 3.2c and d) gives more detailed information on the nanostructures. As could been seen, the outside grains were strong bonded with the

hollow core indicating the as-formed Pt shell were well regulated on the core of the Pd hollow nanoparticles during the formation process which would be beneficial in the longer term application for the ORR process because the nature of this structures. The lattice parameter was calculated to be 0.210 nm, which is smaller than that of Pt or Pd [11] lattice contraction of Pt on Pd.[22]

To make a comparison, Pt hollow nanoparticles without the Pd interior was also synthesized accordingly and Figure 3.2 e-f showed the structure of the formed Pt hollow nanoparticles. It could also be seen the Pt hollow particles was formed with size from 10-20 nm and a shell thickness about 1 nm. However distinct differences could be seen compared with Pt-Pd nanoparticles: many random nucleated Pt nanoparticles were formed unexpectedly which mostly possible because the lattice parameter mismatch between Pt and Co (3.920Å and 2.510Å) are too large resulting the difficulty in localizing the growth on the Co. The HR-TEM showed lattice spacing of the as-formed shell was about 0.22 nm which is corresponding to the (111) plane of Pt.

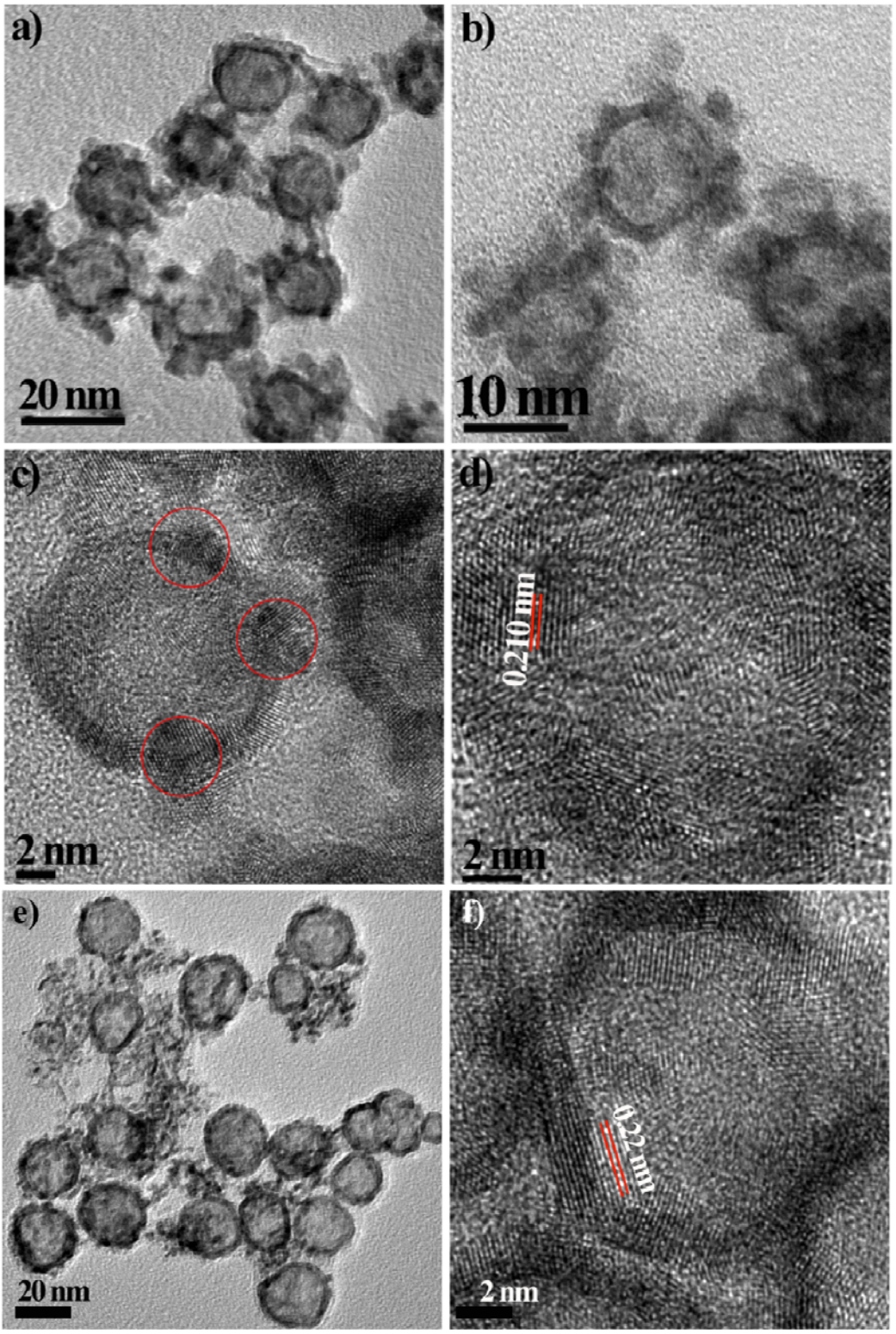

Figure 3.3 Morphology characterisation of the resultant product. Typical (a-b) TEM images and (c-d) HR-TEM images of the Pt-Pd hollow nanoparticles, red circles in c) shows the Pt-Pd nanoparticles on the shell, (e-f) Morphology characterisation of Pt

hollow nanoparticle. Typical (e) TEM images and (f) HR-TEM images of the Pt hollow nanoparticles

3.3.4 STEM and EDS Analysis

The STEM-EDS was employed to further investigate the element distribution of the hollow nanoparticles, as is shown in Figure 3.3. The STEM also confirmed the as formed Pt-Pd is hollow shaped with multiply porous Pt grown on the hollow core (Figure 3.3a). Further EDS analysis (Figure 3.3b) confirmed both Pt and Pd element were distributed in the nanoparticles homogenously with much more on the shell of the particle indicating a hollow featured distribution. More importantly, it could be seen, the intensity of Pt is higher than that of Pd revealing a Pt shell covering of the Pd interior, which would benefit the ORR process as Pt is more active than Pd in acidic medium.

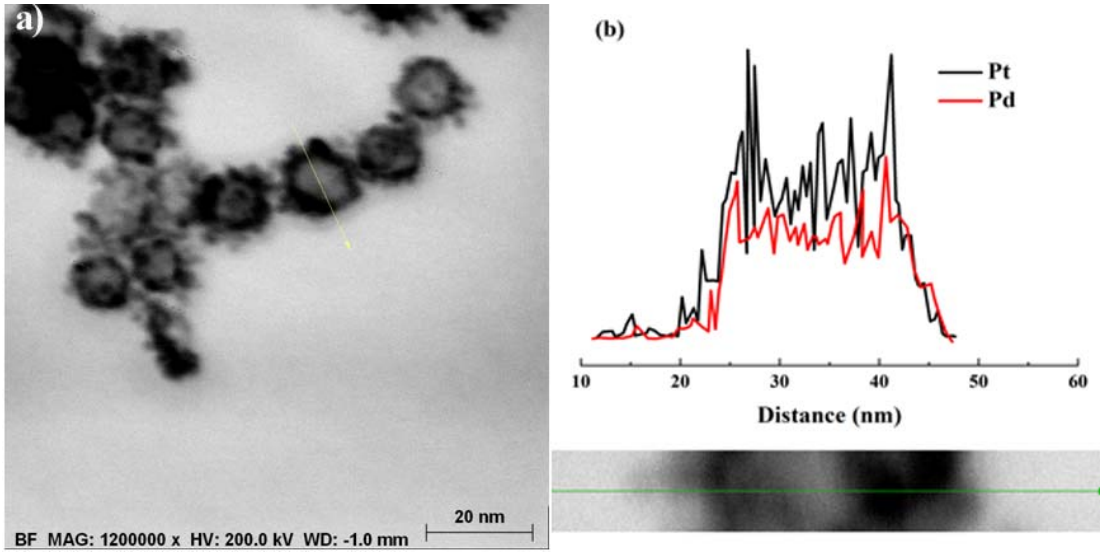

Figure 3.4 STEM-EDS analysis of the as-synthesized Pt-Pd hollow nanoparticles. a) Typical STEM image, yellow line indicates where the EDS line scan was performed, b) EDS line scanning profile.

3.3.5 XRD analysis

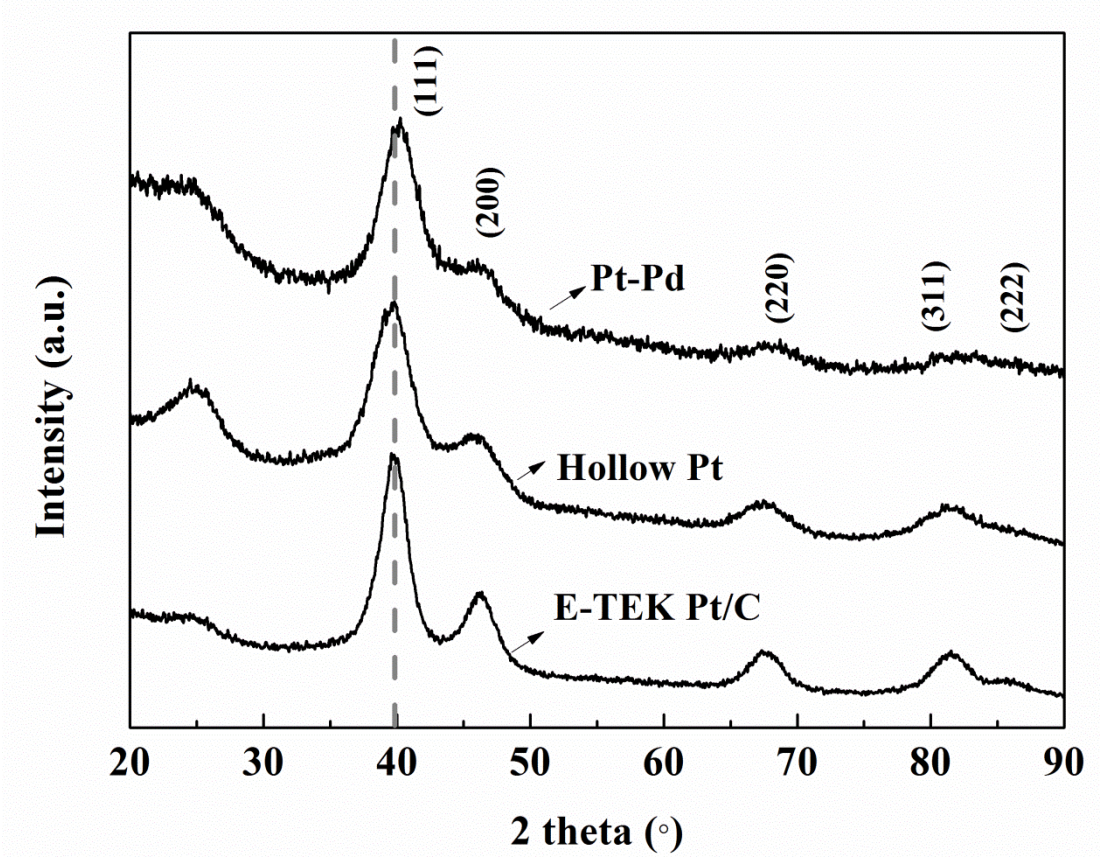

Figure 3.5 The XRD patterns of the Pt-Pd hollow particle, Pt hollow particle and the E-tek Pt/C catalysts.

XRD was conducted in order to acquire the crystal structure of the products, as shown in Figure 3.4.All the products show five characteristic peaks, which could be corresponded to the (111), (200), (220), (311), and (222) planes, indicating the crystal structure are the face-centre-cubic (*fcc*) metal phase.[12, 23] In addition, it could be noted that all the peaks of Pt-Pd are slightly up-shifted to higher 2θ, which is a typical phenomenon that Pd is incorporated into the Pt lattice.[13]. Moreover, no single Pd or Pd peaks was detected in the products indicated that all the Pd was alloyed into the lattice of Pt. The results were fitted with a mixture of Gaussian and Lorentzian profiles (50% Gaussian) as suggested by Sarkar at al. to obtain the lattice parameters.[24] The fixed lattice parameter of the Pt-Pd is 0.3876 Å which is smaller than both of the E-TEK

Pt/C (0.3922 Å) and hollow Pt (0.3914 Å), indicating a lattice contraction of Pt on Pd.[19, 25]. This lattice strain effect, due to the changes on the geometric structures on the surface of Pt when alloying with a second metal, Pd, has already been reported with the possibilities to increase the electrocatalytic activities as well as the stability of the Pt-based electrocatalysts.[26] Together with the formation of the hollow shaped nanostructures, which could largely increase the specific area and electroactive sites of the electrocatalysts, the ORR catalytic ability of the as-synthesized products were believed to be improved, which were further confirmed by the electrochemical measurements.

3.3.6 Cyclic Voltametric Measurement

CV curves were firstly acquired and used for a preliminary study of the electrochemical performance of the hollow Pt-Pd, the hollow Pt nanoparticles, the commercial available E-Tek Pt/C was chosen as a control experiment to study the electrochemical surface area of the three products (Figure 3.5). It could be seen that all the CVs are consistent with typical characterized CV regimes of Pt: typical hydrogen underpotential adsorption/desorption peaks in the potential range of 0 to 0.3V; a double-layer capacitance region from 0.3 to 0.75 V; and Pt oxidation/reduction peaks in the range between 0.75 and 1.15 V revealing the Pt-Pd hollow nanoparticles exhibited a Pt-like behavior, which also suggested the nano Pt shell is covered on the Pd hollow interior. The electrochemical surface active area (ECSA) was calculated based on the charge transfer in the hydrogen adsopriton/desoprtion region at around 0 to 0.3V (vs. RHE), subtracting the double layer correction and assuming 0.210 mC cm^{-2} for the adsoprtion of a monolayer of hydrogen on the Pt monolayer surface.[24]. The calculated ECSA of Pt-Pd/C is 108 m^2 g^{-1} metal and much higher than that of hollow Pt/C (75 m^2 g^{-1} metal)

or the Pt/C (62 m^2 g^{-1} metal) , indicating that the hollow interior as well as the surface roughness of the Pt shell leads to higher electrochemical accessibility than conventional nanoparticles. The enlarged ECSA of the Pt-Pd electrocatalysts could increase the electroactive sites of the electrocatalysts thus facilitating the ORR process.[7]

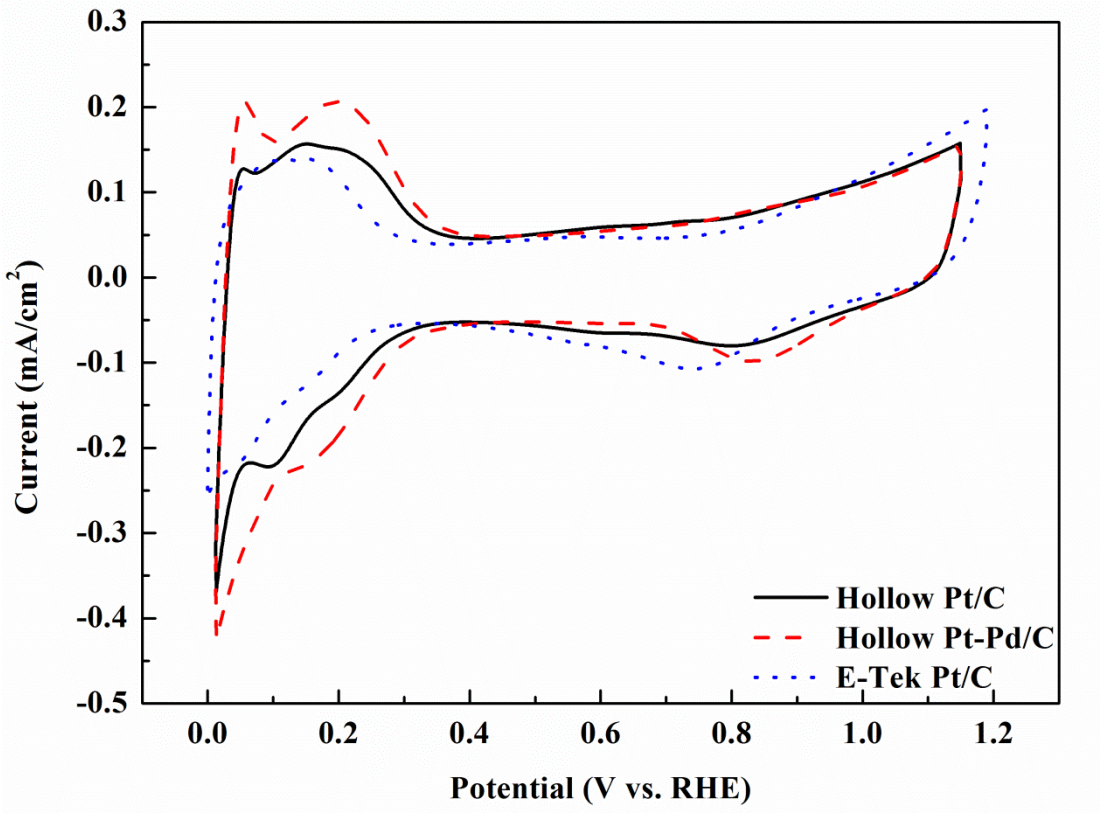

Figure 3.6 CV curves of the hollow Pt/C, hollow Pt-Pd/C and the E-Tek Pt/C. Recorded in a N_2 saturated 0.1 M $HClO_4$ solution with a scan rate of 50 mV s^{-1}.

3.3.7 The Oxygen Reduction Reaction Polarisation Curves

To gain insight of the activities of the synthesized Pt-Pd/C, the ORR polarisation curves were obtained with these electrocatalysts using the rotating disk electrode (RDE) at 1600 rpm, as shown in Figure 3.6a. All the polarization curves display a well-defined diffusion-limiting current region from 0.1 V – 0.7 V and a mixed kinetic-diffusion control region from 0.7 V – 0.9 V suggesting their comparable electrochemical performance. It is obvious that the Pt-Pd/C showed a much positive onset potential (at

which the oxygen began to reduce) compared with the E-Tek Pt/C or hollow Pt/C suggesting its superior electrocatalytic performance. To qualify the electrochemical performance of the three electrocatalysts, the half-wave potential ($E_{1/2}$, at which the half diffusion limiting current was reached) was calculated. Remarkably, the $E_{1/2}$ for the Pt-Pd/C catalyst is 0.855V, which is about 55 mV positive than that of the E-Tek Pt/C (0.800V) or hollow Pt/C (0.810) in the RDE curve. These comparisons clearly suggested the significant improvement in the ORR activities when stabilization of Pt nanoparticles on the Pd hollow interior which may be ascribed to the lattice contraction as well as the optimised porous structures of Pt shell.

In order to obtain the kinetics of the ORR, ORR polarization curves were collected at various rotation speeds (Figure 3.6c) and corresponding Koutecky-Levich (K-L) plots (Figure 3.6d)were drafted from the ORR polarization curves at different potentials. The number of electrons involved per O_2-molecule reduction can be determined using the Koutecky-Levich (K-L) equation

$$j = 1/j_k + 1/B\omega^{0.5};$$

$$[B = 0.2n\mathrm{F}(D_{O2})^{2/3}(v)^{-1/6}C_{O2}]$$

where, j_k is the kinetic current, ω is the electrode rotation rate, n is the transferred electron number, F is the Faraday constant (F = 96485 C mol^{-1}), D_{O2} is the diffusion coefficient of O_2 = 1.9×10^{-5} cm^2 s^{-1}, υ is the kinetic viscosity (0.01 cm^2 s^{-1}), and C_{O2} is the bulk concentration of O_2 (1.2×10^{-6} mol cm^{-3}). The constant 0.2 is adopted when the rotation speed is expressed in rpm. The transferred electron number was calculated to be 3.90-4.0 at around 0.4 – 0.7 V, revealing that the ORR from0.4 – 0.7 V is dominated by a four-electron (4e) pathway and that O_2 is reduced to H_2O during the reaction.

To further investigate the electrochemical performance of the three electrocatalysts, the specific activities kinetic current of the three catalysts which were calculated using the mass-transport correction for RDE[3]:

$$i_k = \frac{i_d i}{i_d - i} \quad (1)$$

where i_k is the mass-transport free kinetic current, i_d is the diffusion limited current, and i the experimentally recorded current in Figure 3.6c. Specific current was normalized with the total metal loading on the electrodes. As shown in Figure 3.6d, the Pt-Pd/C electrode exhibits a specific mass activity of 197.3 mA mg^{-1} metal based on the total loading of Pt and Pd at 0.9 V (vs. RHE). The value is 2.1 times and 2.3 times higher than that of the hollow Pt/C (94.5 mA mg^{-1} metal) and the commercial Pt/C (87.1 mA mg^{-1} metal). Normalized with the Pt loading, the specific activity of Pt-Pd is 2.5 and 2.8 times greater than that of the hollow Pt/C and the commercial Pt/C. The specific area activities were also calculated by normalising the kinetic current to the specific area. The Pt-Pd/C showed a specific area activity of 532.5 mA/cm^2_{Pt}, which was about 1.65 and 2.7 times higher than those of the hollow Pt/C (322.3 mA/cm^2_{Pt}) and the commercial E-Tek Pt/C (194.2 mA/cm^2_{Pt}). The enhancement of catalytic activity could be attributed to the lattice contraction and ECSA increase of Pt on Pd and again confirmed that the controlled growth of Pt on the Pd could significantly improve the electrochemical activities of Pt by increasing the Pt utilization thus reduce the overall cost of the electrocatalyst.

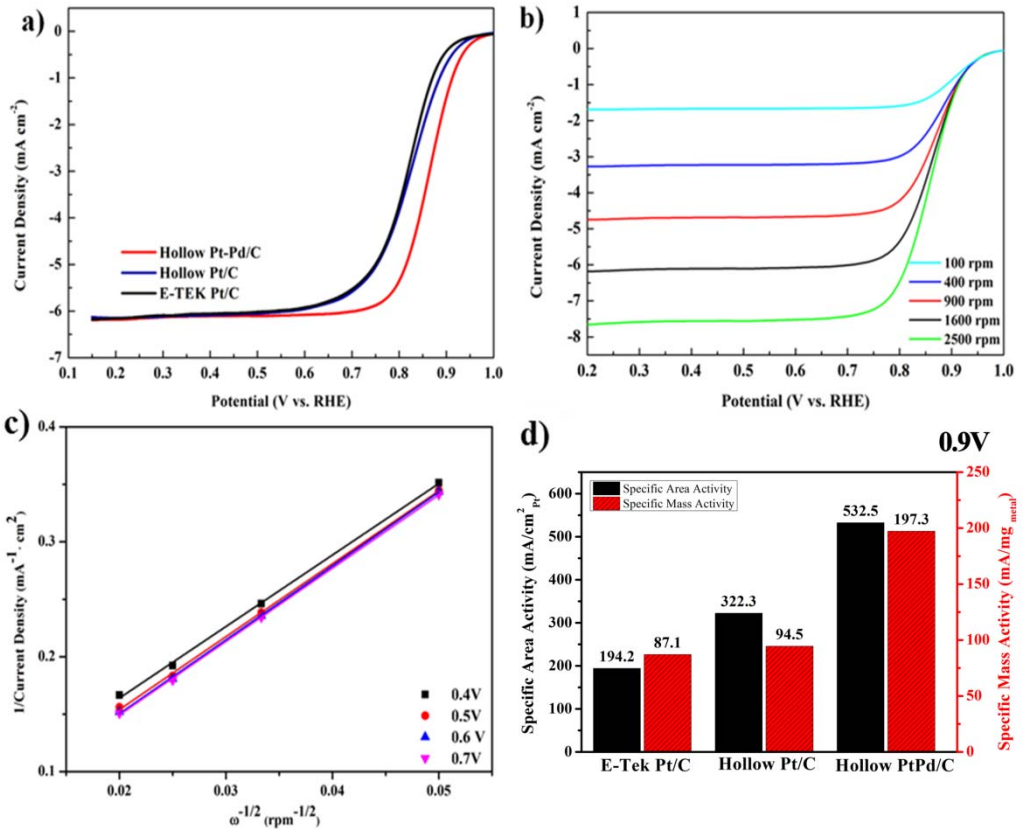

Figure 3.7 a) The RDE polarisation curves of the hollow Pt-Pd/C, hollow Pt/C and E-Tek Pt/C in O_2 saturated 0.1 M $HClO_4$ electrolyte with a scan rate of 5 mv s^{-1} b) The RDE polarisation curves of the Pt-Pd/C collected at various speed from 2500 rpm to 100 rpm. c) K-L plots derived from b). d) The specific mass activities and area activities of the hollow Pt-Pd/C, hollow Pt/C and E-Tek Pt/C at 0.9 V derived from the RDE results.

3.3.8 Stabilities Test

The stabilities issue of the PGM group electrocatalysts is still one problem needed to be addressed before commercialising the electrocatalysts, to this end, the durability test were conducted using the accelerate durability test (ADT) method by cycling the electrocatalysts in O_2 saturated electrocatalysts for hundred thousand times to study the change on the ORR performance.[3, 27] The ORR polarisation curves for the Pt-Pd/C,

hollow Pt/C and the E-Tek Pt/C were recorded before and after subjecting them into the O_2 saturated electrocatalysts for 10 000 voltage cycles between 0.6-1.0V, which is shown in Figure 3.7. As could be seen, after 10 000 continuous cycles, the half-wave potential $E_{1/2}$ underwent only a small negative shift of ~ 5 mV, while ~ 16 mV and ~29 mV negative shift was observed on the hollow Pt/C and commercial Pt/C electrode. These observations suggested the stability of the Pt-Pd was largely improved compared with the hollow Pt/C or the E-Tek Pt/C due to the well-controlled growth of Pt nanoparticle on the Pd shell and the alloyed nature of the synthesized products, which would significantly inhibit the Pt nanoparticles or dissolving from aggregation during the long-term electrochemical cycling process. And these results also suggested that the alloying of Pd into the Pt lattice would not only reduce the cost but also the increase the electrocatalytic activities as well as the stability of the electrocatalysts, which proved the effectiveness of this method in fabricating improved electrocatalytic ORR electrocatalyst with lower cost.

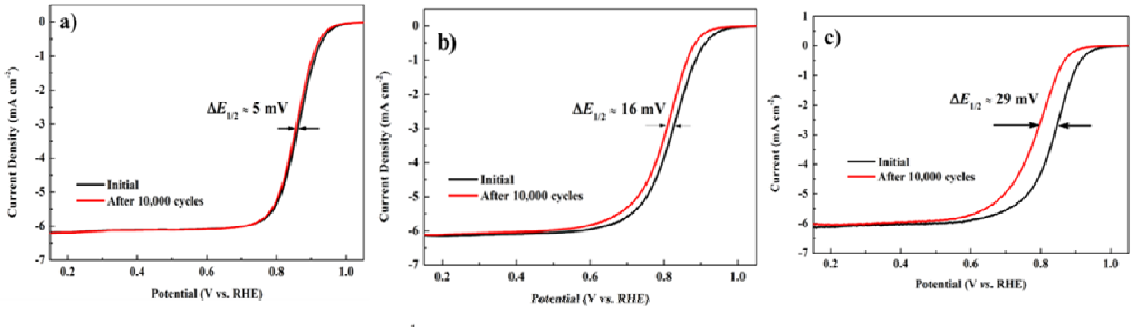

Figure 3.8 The ORR polarisation curves of a) Pt-Pd/C and b) hollow Pt/C and c) E-Tek Pt/C before and after 10,000 cycles potential scan

3.3.9 Single Fuel Cell Test

The RDE system is ideal in identifying the candidates for the ORR, however for practical applications, the testing of electrocatalysts in a real device is needed. [28] At

last, to acquire the real performance of the electrocatalysts under practicable fuel cell device, proton exchange membrane fuel cell tests were conducted and the polarisation curves for the Pt-Pd/C, hollow Pt/C, and commercial Pt/C were recorded as shown in Figure 3.8. Evidently, the single-cell results are in good accordance with the RDE data illustrated above. A remarkable improvement in the whole polarization region was observed from the Pt-Pd/C electrode. At practicable operating potential (≈ 0.6V),[29] the Pt-Pd/C showed a current density of 563 mA cm^{-2} , in comparison, the hollow Pt/C and E-Tek Pt/C showed current densities of 399 and 317 mA cm^{-2}. The maximum power density based on the geometric area is 395.9 mW cm^{-2} for the Pt-Pd/C electrode, which is about 1.3 times and 1.7 times higher than that of the hollow Pt/C electrode(295.5 mW cm^{-2})for the and the commercial E-Tek Pt/C electrode(231.4 mW cm^{-2}). These comparisons once again indicate that the superior electrocatalytic activities of the Pt-Pd/C and also evident the Pt-Pd/C could work as more efficient electrocatalysts than the commercial E-Tek Pt/C under real practicable environment. The improved performance may again be ascribed to the "constrain effects" due to the alloying of Pd-Pt nature and hollow and porous structure of the Pt-Pd electrocatalysts which could provide large specific area, more electroactive sites and sufficient mass transport channels on the gas diffusion electrode.[30]

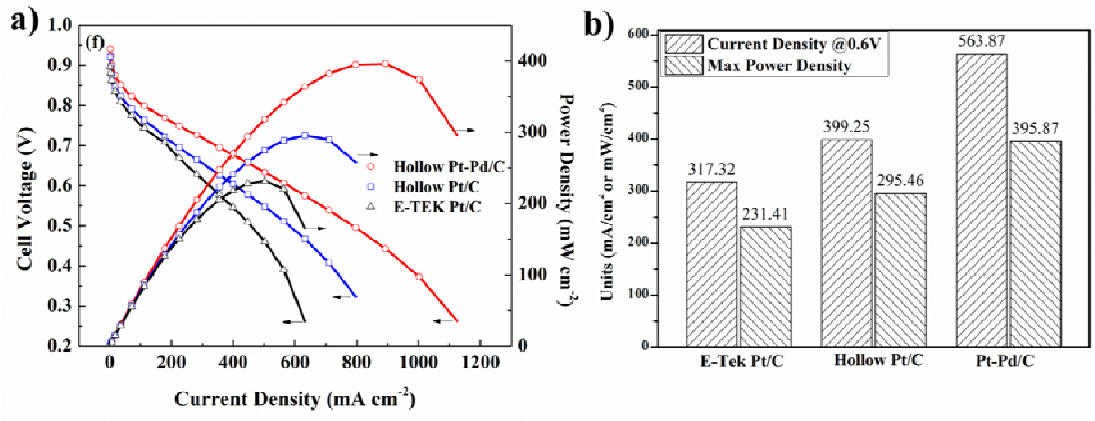

Figure 3.9 a) Polarisation curves obtained in single fuel cell test using the hollow Pt-Pd/C, hollow Pt/C and E-Tek Pt/C as cathodes catalysts and b) comparisons of the current density at 0.6V and power density derived from a).

3.4 Conclusion

In this chapter, we have demonstrated using a modified galvanic replacement to stabilize Pt nanoparticles on the Pd hollow interior and used as ORR electrocatalysts with higher electrochemical and superior stability for the PEMFC. The lattice constrain effects and the porous structure generated by lattice mismatch between the Pt and Pd are believed to be the important factor that accounts for the improved performance of this electrocatalysts. Besides as the Pt nanoparticles were stabilized on the Pd interior, the conventional carbon erosion problems would be resolved thus prolonging the stability of Pt compared with the Pt/C electrocatalysts.

It is believed that the open and porous structure could provide the electrocatalysts with higher utilization efficiency of Pt *via* producing more active sites and abundant mass transfer channels thus facilitating the ORR process thereby reducing the relative cost of the electrocatalyst, which was confirmed by the ECSA and RDE measurements. In the ADT tests, we have evidenced the Pt-Pd/C could work as more endurable electrocatalyst in longer term operating conditions with minor performance drop during up to 10,000 potential cycles compared with the hollow Pt/C or E-Tek Pt/C. At last, we conduct the PEMFC tests with the synthesized Pt-Pd electrocatalysts confirming the Pt-Pd/C electrocatalysts could work as practicable electrocatalyst under real-world devices.

To conclude, this chapter discussed the possibility of using a Pd hollow interior to increase the utilization of the Pt nanoparticles and increase the stability of Pt, whereas it should be noted that not all the Pd atoms were alloyed into the Pt lattice due to the

preparation method, thus it is considered that the electrocatalytic activity of the Pt nanoparticles would be further increased by alloying Pt with another metal. In the next chapter, to further reduce the cost and improve the electrocatalytic performance of the electrocatalysts, we will discuss the alloying Pt with transition metal Cu forming a PtCu bimetallic electrocatalysts which possess significant improvement in the electrocatalytic performance towards the ORR.

3.5 Reference

1. Joo, S.H., S.J. Choi, I. Oh, J. Kwak, Z. Liu, O. Terasaki, and R. Ryoo, Nature, 2001. **412**(6843): p. 169-172.
2. Debe, M.K., Nature, 2012. **486**(7401): p. 43-51.
3. Lim, B., M. Jiang, P.H.C. Camargo, E.C. Cho, J. Tao, X. Lu, Y. Zhu, and Y. Xia, Science, 2009. **324**(5932): p. 1302-1305.
4. Shao, Y., J. Sui, G. Yin, and Y. Gao, Applied Catalysis B: Environmental, 2008. **79**(1): p. 89-99.
5. Zhang, S., Y. Shao, G. Yin, and Y. Lin, Journal of Materials Chemistry A, 2013. **1**(15): p. 4631-4641.
6. Morozan, A., B. Jousselme, and S. Palacin, Energy & Environmental Science, 2011. **4**(4): p. 1238-1254.
7. Guo, S. and S. Sun, Journal of the American Chemical Society, 2012. **134**(5): p. 2492-2495.
8. Li, Y., E. Zhu, T. McLouth, C.Y. Chiu, X. Huang, and Y. Huang, Journal of the American Chemical Society, 2012. **134**(30): p. 12326-12329.
9. Gu, X., X. Cong, and Y. Ding, ChemPhysChem, 2010. **11**(4): p. 841-846.

10. Tayal, J., B. Rawat, and S. Basu, International Journal of Hydrogen Energy, 2011. **36**(22): p. 14884-14897.

11. Hong, J.W., S.W. Kang, B.S. Choi, D. Kim, S.B. Lee, and S.W. Han, ACS Nano, 2012. **6**(3): p. 2410-2419.

12. Wang, D., H.L. Xin, Y. Yu, H. Wang, E. Rus, D.A. Muller, and H.D. Abruña, Journal of the American Chemical Society, 2010. **132**(50): p. 17664-17666.

13. Yin, A.X., X.Q. Min, Y.W. Zhang, and C.H. Yan, Journal of the American Chemical Society, 2011. **133**(11): p. 3816-3819.

14. Koenigsmann, C., A.C. Santulli, K. Gong, M.B. Vukmirovic, W.-p. Zhou, E. Sutter, S.S. Wong, and R.R. Adzic, Journal of the American Chemical Society, 2011. **133**(25): p. 9783-9795.

15. Zhang, W., R. Wang, H. Wang, and Z. Lei, Fuel Cells, 2010. **10**(4): p. 734-739.

16. Wang, L. and Y. Yamauchi, Journal of the American Chemical Society, 2010. **132**(39): p. 13636-13638.

17. Lebon, A., A. García-Fuente, A. Vega, and F. Aguilera-Granja, Physical Review B, 2011. **83**(12): p. 125427.

18. Yang, J., J. Yang, and J.Y. Ying, ACS Nano, 2012. **6**(11): p. 9373-9382.

19. Marković, N.M., T.J. Schmidt, V. Stamenković, and P.N. Ross, Fuel Cells, 2001. **1**(2): p. 105-116.

20. Sun, Y. and Y. Xia, Journal of the American Chemical Society, 2004. **126**(12): p. 3892-3901.

21. Mayers, B., X. Jiang, D. Sunderland, B. Cattle, and Y. Xia, J. Am. Chem. Soc., 2003. **125**: p. 13364-13365.

22. Zhang, W., M. Wang, J. Chen, T. Romeo, A.T. Harris, and A.I. Minett, Electrochemistry Communications, 2013. **34**(0): p. 73-76.

23. Shao, M., K. Shoemaker, A. Peles, K. Kaneko, and L. Protsailo, Journal of the American Chemical Society, 2010. **132**(27): p. 9253-9255.

24. Carpenter, M.K., T.E. Moylan, R.S. Kukreja, M.H. Atwan, and M.M. Tessema, Journal of the American Chemical Society, 2012. **134**(20): p. 8535-8542.

25. Chen, Z., M. Waje, W. Li, and Y. Yan, Angewandte Chemie International Edition, 2007. **46**(22): p. 4060-4063.

26. Yang, J., X. Chen, X. Yang, and J.Y. Ying, Energy & Environmental Science, 2012. **5**(10): p. 8976-8981.

27. Zhang, S., X.-Z. Yuan, J.N.C. Hin, H. Wang, K.A. Friedrich, and M. Schulze, Journal of Power Sources, 2009. **194**(2): p. 588-600.

28. Fernández, J.L., V. Raghuveer, A. Manthiram, and A.J. Bard, Journal of the American Chemical Society, 2005. **127**(38): p. 13100-13101.

29. Wagner, H.A.G.S.S.K.B.S.F.T., Applied Catalysis B: Environmental, 2005. **56**: p. 9-35.

30. Dumitrescu, I. and R.M. Crooks, Proceedings of the National Academy of Sciences, 2012. **109**(29): p. 11493-11497.

Chapter 4

Mesoporous PtCu Hollow Nanoparticles for the Oxygen Reduction Reaction in Proton Exchange Membrane Fuel Cells

4. **CONTENTS**

Chapter 4

4.1 Introduction

The performances of proton exchange membrane fuel cell (PEMFC) is believed to be kinetically limited at cathodes because of the sluggish reaction schematics of oxygen reduction reaction(ORR).[1, 2] As a commonly used and high effective catalysts towards ORR, Platinum (Pt) has been extensively studied, however it is inhibited from large scaled commercialisation due to its high cost and poor stability[1, 2]. Previous chapter demonstrated that the stability as well as the electrocatalytic performance of Pt nanoparticles towards the ORR could be improved by stabilization growth of the 2-3 nm Pt nanoparticles on the hollow Pd interior. The enhance performance is attributed to the well-defined porous structure and the lattice constrain effect generated between Pt and Pd. However it is aware during the preparation process, not all the Pd atoms were alloyed into Pt lattice (some of Pd was beneath Pt skin in the form of metallic Pd) and Pd is still expensive compared with the transition metals, thus to further reduce the cost of the Pt electrocatalysts, it is desirable and interesting to develop cheap transition metals alloyed Pt electrocatalysts with improved electrocatalytic performance. It is well documented that the ORR performance of Pt could be effective improved when alloying with early transition metals such as Ni[3], Fe[4, 5], Cu[6] and Co[7, 8] due to changes of the geometric (Pt-Pt bond distance and coordination numbers) and electronic structures of Pt[4, 9]. Therefore, compared alloying with the noble metals (such as Pd[2], Au[10], Ag[11]), platinum alloying with transition metals (much less expensive) provides a more practical pathway in preparing electrocatalysts for oxygen reduction reaction (ORR) in fuel cells.

Recently, many efforts have been devoted into the synthesis of Pt-Cu in order to investigate the origin of the high ORR activity and designe dealloyed Pt−M catalysts with superior activity and durability.[12-15] For example,, PtCu hollow nanocrystalls

with better electrocatalytic activities have been synthesised in organic solutions[12], however the organic solvent based process raised an environmental issue on post-treatment of samples compared with the approach using aqueous solution. Also PtCu or PdCu hollow nanotublar structures were also reported [13, 14], however, the synthesis of copper nanostructures templates was difficult and multiply steps were needed to prepare final products. More importantly, without excess reductants, copper contents would be rather low (2.9 wt.%) due to the large sacrifice of copper[14]. Thus there is still an urgent need in developing green and facile synthetic procedure of Pt-Cu bimetallic nanostructured electrocatalysts for the ORR, moreover, as the ORR is believed to be a surface-based catalytic process, [9] the synthesis of porous surface would be an advantage for the electrocatalysts because of the enlarged electrochemical surface area and abundant active sites on the electrocatalysts.[2, 15, 16]

In the last chapter, we have well demonstrate the unique properties of hollow nanostructure, including their high surface area, low density, and catalysts utilization efficiency[13], and it was aware that the so called sacrificial template (galvanic replacement) [17], could also been applied in fabricating bimetallic nanostructure with hollow features[18]. Inspired by this, in this chapter, we report the successful synthesis of porous PtCu hollow nanostructures in aqueous environment using copper nanoparticles as sacrificial templates via a modified galvanic replacement approach. Physical characterisation confirmed the copper was alloyed into the Pt lattice with a maximum atomic percentage of 57% revealing the expense of the electrocatalysts would be largely reduced. In addition, the electrochemical tests towards ORR revealed that the as-synthesised porous PtCu hollow NPs had a significant high specific activity of 1286 $\mu A/cm^2$ (when the precursors molar ratio of Pt/Cu =0.5/1, which was further denoted as $Pt_{0.5}Cu_1$ in this chapter), which is seven times higher than that of commercial available

Pt/C (192 μA/cm^2) at 0.510V under identical conditions. Moreover, the accelerated durability test displayed the prepared porous PtCu hollow NPs had an excellent electrochemical stability over potential cycling from 0.5 to 1V (*vs.* SHE) up to ten thousands cycles. Combined with the single cell tests, it has proved that the synthesized porous hollow PtCu electrocatalysts could potentially be a much more efficient and durable low-cost catalysts for ORR than commercial available Pt/C catalysts.

4.2 Experimental

4.2.1 Reagents

Cetyltrimethylammonium bromide (CTAB, 99.9+%, Fluka), cupric chloride (BDH Anala R), ammonia solution (Ajax Finechem), hydrazine (35% wt in water, Sigma Aldrich), $H_2PtCl_6 \cdot xH_2O$ (Sigma-Aldrich), carbon black (CB, Vulcan XC-72 R, Cabot Corp.), carbon fibre paper (GDL, 5 cm^2), acetone (Sigma), perchloric acid (ACS reagent, 70%, HClO4, Sigma-Aldrich)

4.2.2 Synthesis

Copper nanoparticles were synthesized according to the procedures elaborated earlier [19]. In a typical experiment, two solution of 37 mg CTAB dissolved in 20 ml water solutions, one containing 100 μL 0.1 M cupric chloride and with PH=10 adjusting by ammonia solution and the other containing 60 ul hydrazine were mixed together with vigorous stirring for 3 hours until a red wine colour appeared. Once copper nanoparticles were formed, 50 μL 0.1 M $H_2PtCl_6 \cdot xH_2O$ in 20 ml degased water was added dropwisely and let it react for another 3 hours. To avoid particle aggregation, the alloyed PtCu nanoparticles were supported on carbon black to a loading amount of 20wt% by mixing the above colloids and functionalised CB water dispersion and stirring

overnight. Before filtration, an aliquot amount of acetone was added with stirring for another 2 hours, then the products were rinsed with water for several times to remove any unreacted hydrazine or surfactants and dried at 80 °C overnight and collected. This sample was denoted as $Pt_{0.5}Cu_1/C$. To find a better molar ratio of Pt/Cu as electrocatalysts, several molar ratio of Pt/Cu were prepared with 1, 0.75, and 0.25:1 by adding different amount of $H_2PtCl_6 \cdot xH_2O$ and these samples were denoted as Pt_1Cu_1, $Pt_{0.75}Cu_1$, $Pt_{0.25}Cu_1$respectively.

4.2.3 Physical Characterisation

The transmission electron microscope (TEM) images of samples were taken using a JEOL JEM-2100 F transmission electron microscope operated at 200 kV. Energy dispersive spectroscopy (EDS) in the STEM mode was employed for elemental composition and distribution of the catalyst particles. HRTEM were conducted at a JEOL JEM-3000F transmission microscope operated at 300 kV. Samples for TEM were prepared through placing one drop of the cleaned nanoparticles ethanol dispersion on gold grid (200 mesh). The powder X-ray diffraction (XRD) patterns were recorded with a Bruker D8-advance X-ray powder diffracto-meter with Cu Kα radiation (λ= 1.5406 Å)(XRD instrument details).Energy dispersive spectroscopy (EDS, Bruker) in the SEM was used to determine the elemental composition and distributions of the catalysts. Inductively coupled plasma mass spectrometry (ICP-MS 7500CS, Agilent Technologies) were used to determine the metal contents of the products.

4.2.4 Electrochemical measurements

Electrochemical measurements were performed using a glassy carbon rotating ring disk electrode (RRDE, Pine Research Instrumentation, disk area=0.2475 cm^2) connected to a CHI 720c potentiostat (CHI instrument) in a standard three-electrode cell with a Pt mess

as the counter electrode and a 3 M KCl saturated Ag/AgCl electrode as the reference electrode. An electrochemical cell (Pine Instrument) was filled with about 100 ml 0.1M perchloride acid and covered with a Teflon cap. The eletrocatalysts ink was prepared by dispersing the electrocatalysts in 5% Nifion/H_2O/isopropanol (m/m/m/=0.5/10/50) to reach a 1mg/ml dispersion with an ultrasonicator (Brandson). 30 µL of the ink was dropped on the RRDE electrode and let it air-dry for 2 hours before the electrochemical tests. Assuming that copper were not stable during electrochemical test, the electrode film was cycled 200 times between -0.28 and 0.962 V at 0.5 V/s to a stable current-voltage curves in nitrogen saturated electrolyte.

The additional CV curves were recorded in 0.1 M perchloride acid with a sweeping rate of 50 mV/s, and the Pt electrochemical surface area (ECSA) was estimated from the charge of the underpotentially deposited (UPD) hydrogen, assuming 210 $\mu C/cm^2_{Pt}$.Oxygen reduction reaction (ORR) curves were recorded in oxygen saturated 0.1 M perchloride acid with a sweeping rate of 5 mV/s at successive rotation speed of 100, 400, 900, and 1600 rpm from −0.2- 1V. Stability tests were carried out by voltage scanning from 0.4 -1 V (vs. Ag/AgCl) for 10 000 cycles with a sweeping rate of 100 mv/s in oxygen saturated 0.1 M perchloride acid.

To evaluate the electrochemical performances, electrochemical surface areas (ECSAs) were calculated by measuring the charge collected in the Hupd adsorption/desorption region after double-layer correction and assuming a value of 210 mC/cm2 for the adsorption of a hydrogen monolayer. The number of electrons exchanged in the ORR (n) and the percentage of hydrogen peroxide (% H2O2) can be obtained using the following equations.

$$n = \frac{4I_D}{I_D + \left(\frac{I_R}{N}\right)}$$

$$\%H_2O_2 = 100(4 - n)/2$$

(Where I_D is the disk current, I_R is the ring current and N is the collection efficiency of the RRDE apparatus used in this study which is 0.37 determined using the Fe^{II}/Fe^{III} redox system in a solution containing 1 mM $K_3Fe(CN)_6$ and 0.1 M $NaNO_3$.)

To detailed study the electroactivities of the PtCu/C and Pt/C, the kinetic current is calculated from ORR polarization curves by considering the mass-transport correction using the Levich-Koutecky equation ($\frac{1}{i} = \frac{1}{i_k} + \frac{1}{i_d}$, where i_k is the kinetic current and i_d is the diffusion limiting current) and normalized against to electrochemical surface area and mass of platinum to compare the specific area activity and mass activity.[2]

4.2.5 Single Fuel Cell Test

Membrane electrode assembly were prepared by the methods we described earlier[20]. The electrocatalysts ink were prepared and brushed on the carbon fibre paper (GDL, 5 cm^2) with a loading of 0.4 mg cm^{-2} .For comparison purpose, commercial E-Tek Pt/C and $Pt_{0.5}Cu_1/C$ were chosen, suspended, brushed and used as the cathode electrodes. Pt/C with a loading of 0.2 mg cm^{-2} on carbon fibre paper was used as the anode electrodes. The prepared MEAs were tested using a 850e fuel cell test system (Fuel Cell Technologies, Inc., USA) fed with humidified hydrogen and oxygen respectively. The gas flow was controlled at 0.08 mL min^{-1}. The fuel cell measurements were carried out at 80°C under 15 psi (103.42 kPa) back pressure. The MEAs were activated and electro-dealloyed by the method reported[21]. The polarization curves were recorded using a potential scan method by holding the cell at each potential for 60s in order to get the steady-state current value with a scan rate of 25 mV s^{-1} from 0.95 V to 0.65 V.

4.3 Result and Discussions

4.3.1 Synthesis of Porous Hollow PtCu Nanoparticles

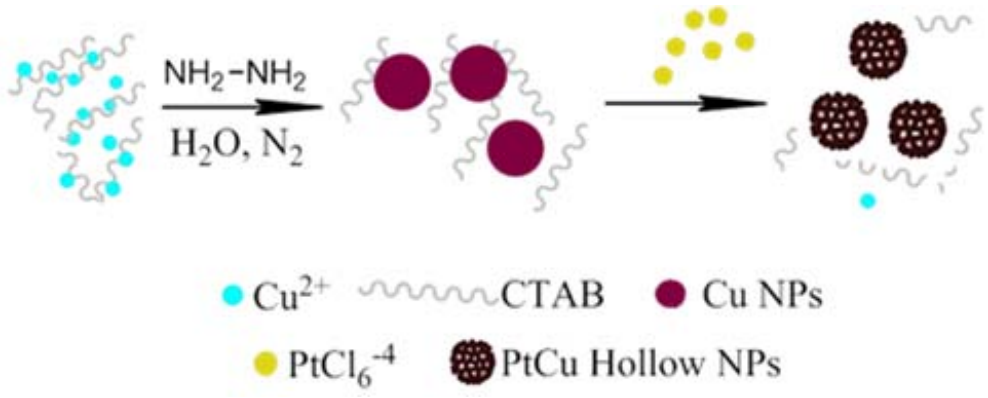

Figure 4.1 Schematic illustration of the formation of porous PtCu hollow NPs

The schematic illustration of the synthesis procedure was depicted in Figure 4.1. In a typical synthesis, copper nanoparticles were firstly synthesized using CTAB as surfactant under inert atmosphere. The chosen of a catholic surfactant would absorb the anodic Pt salts on the surface of copper nanoparticle thereby facilitating the whole process.[8] Once copper nanoparticles were formed, chloroplatinic acid was added into the system under inert environment, the galvanic replacement would take place immediately following the reaction equation shown in $2Cu + PtCl_6^{2-} \rightarrow 2Cu^{2+} + Pt + 6Cl^-$ Equation 4.1, as the standard reduction potential of Cu(II)/Cu (0.34V *vs*. SHE) is much lower than that of $PtCl_6^{2-}/Pt$ pair (0.74V *vs*. SHE), such a large gap on the standard reduction potential would accelerate the reaction mechanism of the sacrifice step.

$$2Cu + PtCl_6^{2-} \rightarrow 2Cu^{2+} + Pt + 6Cl^- \qquad \text{Equation 4.1}$$

4.3.2 UV-Vis Spectroscopy Analysis

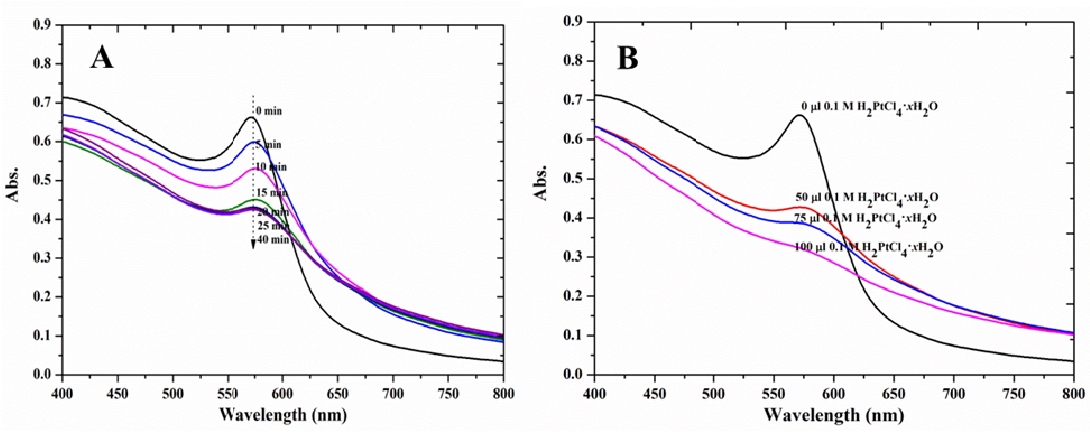

Figure 4.2 (A) UV-Vis spectrums of copper nanoparticles before (0 min) and after begining adding 50 μL 0.1 M $H_2PtCl_6{\cdot}xH_2O$ added for 1 min~ 40 min. (adding rate 1 mL/min, finishing adding after 20 mins); (B) UV-Vis spectrums of copper nanoparticles colloids (0.5 mmol $CuCl_2{\cdot}2H_2O$, 37 mg CTAB, 60 μL hydrazine) and $Pt_{0.5}Cu_1$ nanoparticles (50 μL 0.1 M $H_2PtCl_6{\cdot}xH_2O$ added), $Pt_{0.75}Cu_1$ nanoparticles (75 μ 0.1 M $H_2PtCl_6{\cdot}xH_2O$ added), Pt_1Cu_1 nanoparticles (100 μL 0.1 M $H_2PtCl_6{\cdot}xH_2O$ added)

Ultraviolet–visible (UV-Vis) spectrum was used to in-situ investigate the formation of platinum-copper nanoparticles (Figure 4.2).The strong absorption peak appeared at 572 nm could be ascribed to the excitation of plasma resonances or interband transitions of copper nanoparticles[22]. As could be seen in Figure 4.2a, with the addition of chloroplatinic acid, the density of the peak at 572 nm was gradually decreased reflecting the galvanic reduction of Pt began at copper surface and copper was consumed as sacrificial templates progressively. With more amount of chloroplatinic acid addition, the peak would be lowered and when an amount of 100 μL 0.1 M $H_2PtCl_6{\cdot}xH_2O$ added, the peak around 572 nm was still remaining suggested the existence of copper in the final products.(Figure 4.2b).

4.3.3 Impacts of the Precursors' Molar Ratio on the Structure of the Products

Moreover, we also found that mild reaction process plays a pivotal role in formation of the mesoporous shell of the nanoparticle, as shown in Figure 4.3. At low or mild concentration of Pt precursors (precursors molar ratios of Pt/Cu=0.5/1 or 0.25:1), the shell were much incomplete and constructed with numerous PtCu small grains, while at higher concentration of Pt precursor(precursors molar ratios of Pt/Cu=0.75/1 or 1:1, where the galvanic reaction would occur through a much faster way, a complete and dense shell without any porous features were formed, these comparisons clearly suggested the faster reaction mechanism between the Pt and Cu and mild reaction environment both contributed to the production of mesoporous shells.

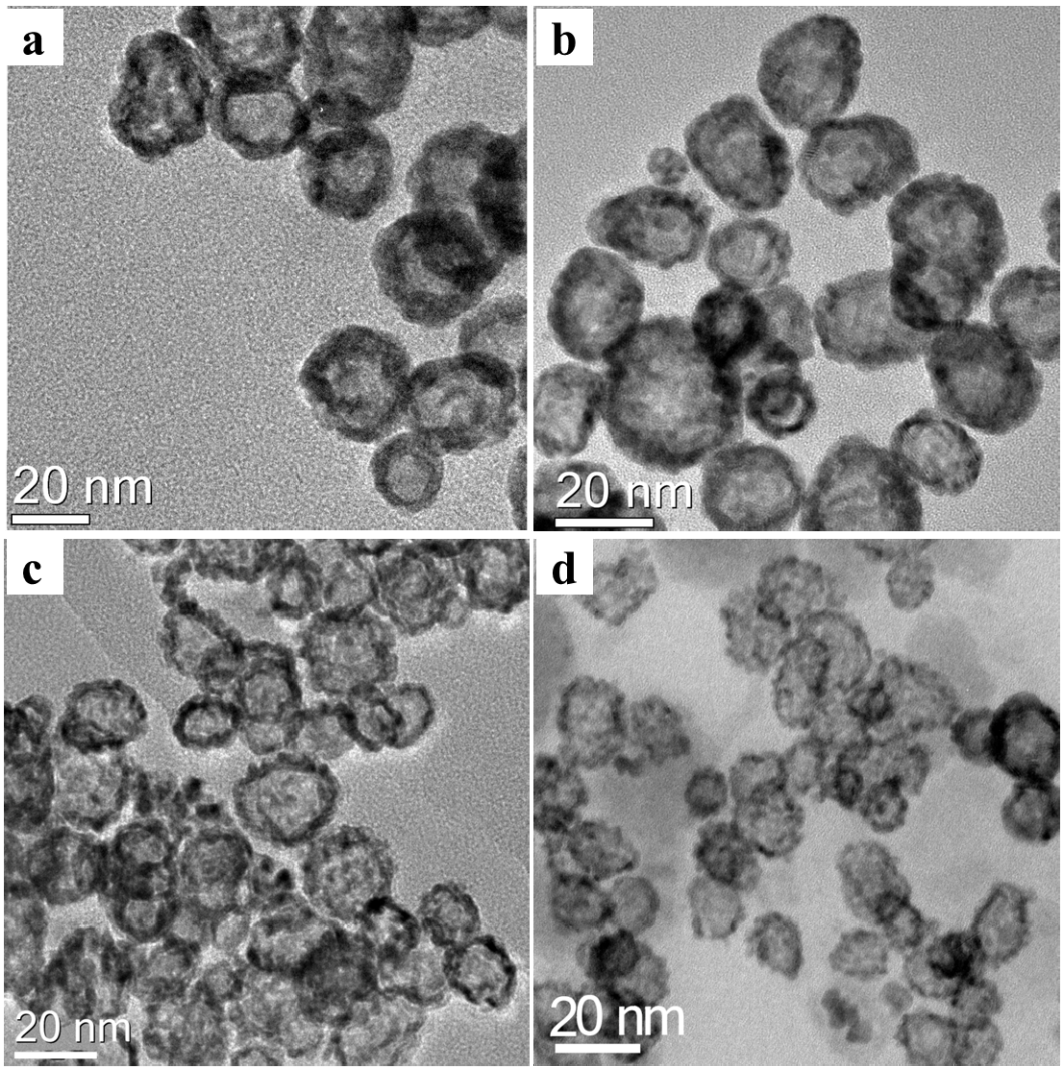

Figure 4.3 The comparison of the structure synthesized from different precursor reation. From a)-d) are the typical TEM images of the Pt_1Cu_1, $Pt_{0.75}Cu_1$, $Pt_{0.5}Cu_1$, $Pt_{0.25}Cu_1$ (the molar ratio of Pt and Cu precursor are 1, 0.75, 0.5, and 0.25 respectively)

4.3.4 Morphology Analysis of the $Pt_{0.5}Cu_1$ Hollow Nanoparticles

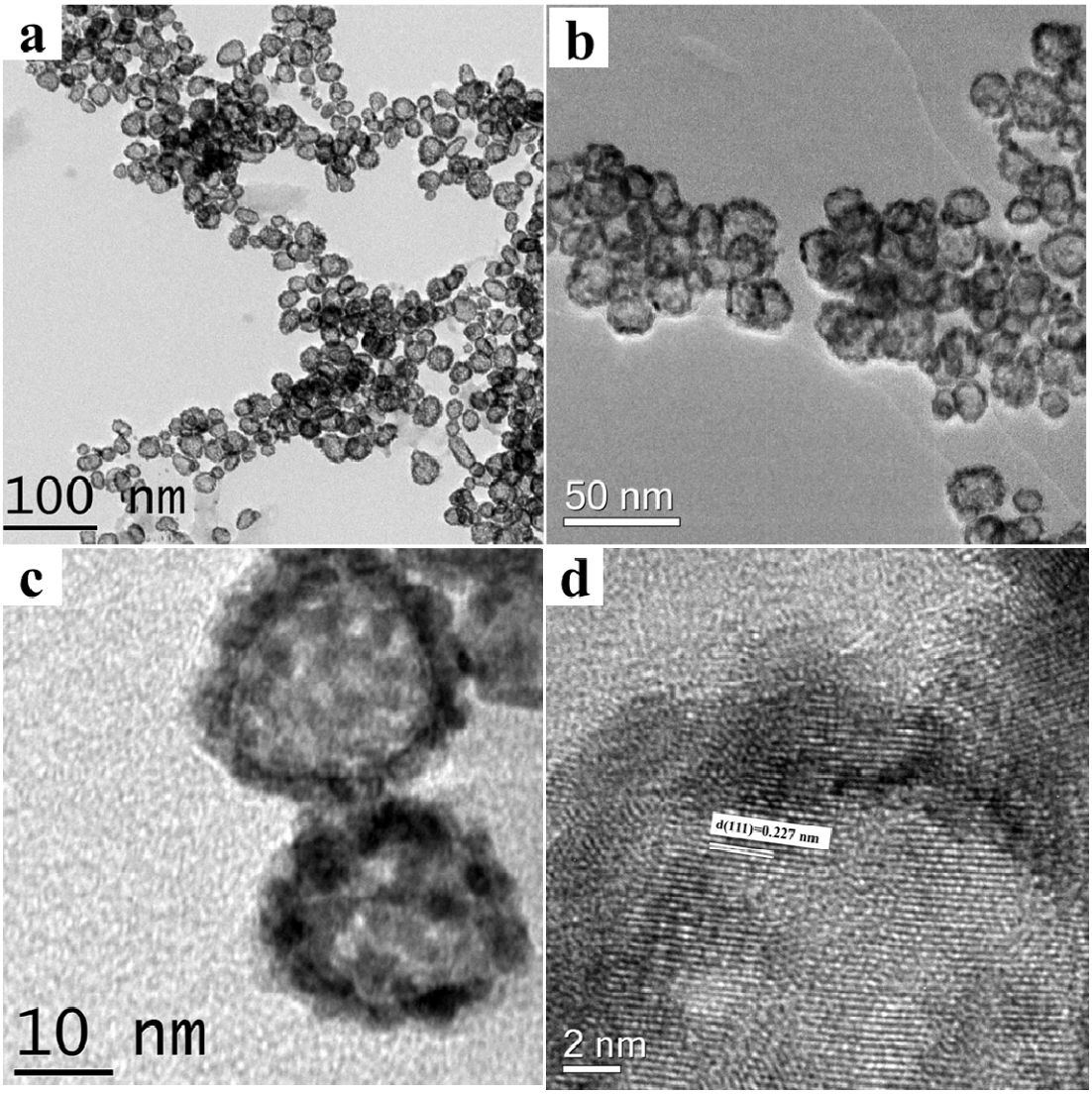

Figure 4.4 Morphology characterisation of the resultant product. Typical (a-c) TEM images and (d) HR-TEM images of the $Pt_{0.5}Cu_1$ hollow nanoparticles.

The mesoporous PtCu hollow nanoparticle synthesized from the precursor ration of 0.5:1 (Cu:Pt) were firstly characterised by the TEM and HRTEM, the corresponding images are shown in Figure 3.2. It could be clearly seen from the TEM images that the

as-synthesised PtCu hollow nanoparticles had an average diameter of about 20–30nm and a shell thickness of 2–3nm. More interestingly, the shells of the hollow nanoparticles were constructed by discontinuous and seamless alloyed PtCu nanoparticles (Figure 3.2c-d), which generated an incomplete and porous shell of the PtCu hollow NPs. This phenomenon, which was not observed using silver[11], selenium[23] as the templates, was also reported when using copper[14] or cobalt[24] as templates. Such a porous structure would benefit oxygen intake and mass transfer thereby facilitate oxygen reduction. The possibilities of formation mechanism of this kind of porous shell structures were generally believed to be caused by the faster reaction kinetics of Pt/Cu, compared with Pt/Ag, Se.[13] Figure 3.2d showed the HR-TEM images of the $Pt_{0.5}Cu_1$ nanoparticle, the lattice fringe was calculated to be approximate 0.227nm indicated the PtCu hollow NPs were alloyed nanostructures.

4.3.5 STEM-EDS Analysis of the $Pt_{0.5}Cu_1$ Hollow Nanoparticles

The STEM-EDS is powerful in qualitatively identifying the structure of the hollow nanoparticle, giving important information on element distribution. showed the STEM-EDS analysis of the $Pt_{0.5}Cu_1$ hollow nanoparticles. The STEM image also confirmed the nanoparticle was hollow shaped with average size around 20-30 nm, besides the particle also showed mesoporous features. EDS line scanning profiles (c-d) further confirmed both Pt and Cu elements were homogenously distributed through the nanoparticle with more copper were detected. While as it should be mentioned, these copper could be easily etched away through acid washing or electrochemical dealloying and this would be discussed later. Also it could been seen the overall element distribution of Pt and Cu were more abundant on the shell revealing the particles were hollow shaped.

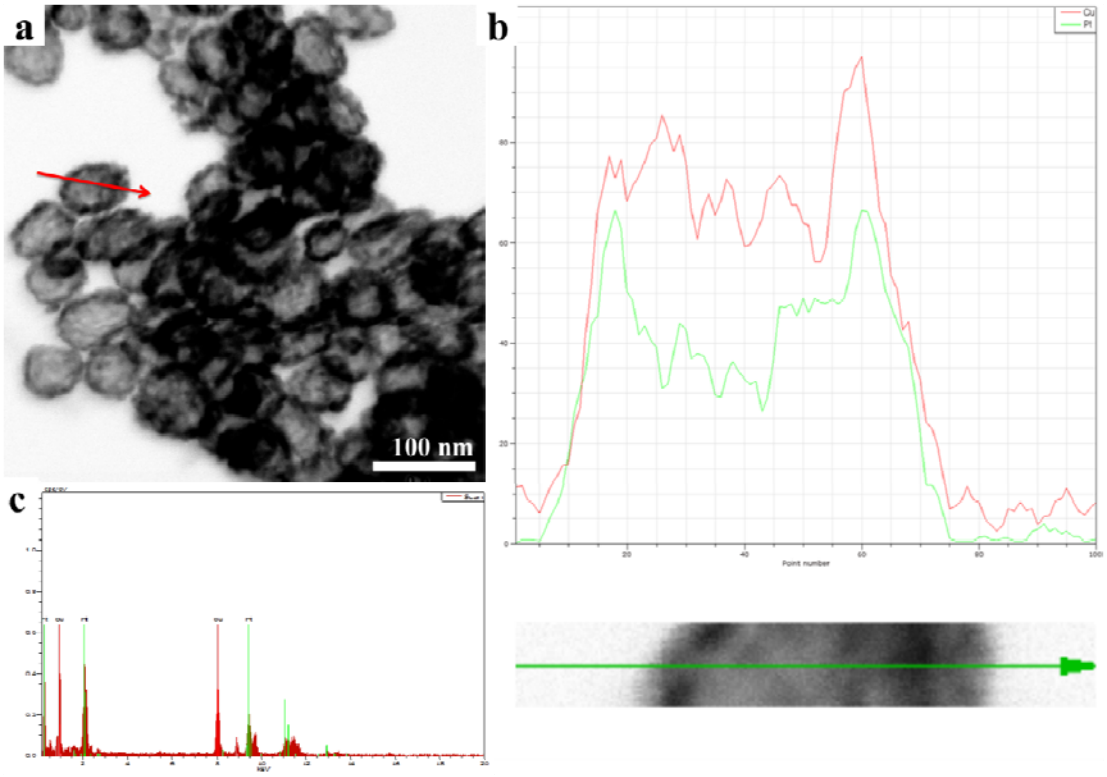

Figure 4.5 STEM-EDS analysis of the as-synthesized $Pt_{0.5}Cu_1$ hollow nanoparticles. a) Typical STEM image, red line indicates where the EDS line scan was performed, b) EDS line scanning profile and c) EDS spectrum of the as-synthesized $Pt_{0.5}Cu_1$ hollow nanoparticles.

4.3.6 X-ray diffraction and ICP-MS Analysis

The XRD pattern would provide useful information on the crystal structures as well as the element composition of the bimetallic nanoparticles while the ICP-MS provides more accurate information of the composition of the element in the hollow nanoparticle.

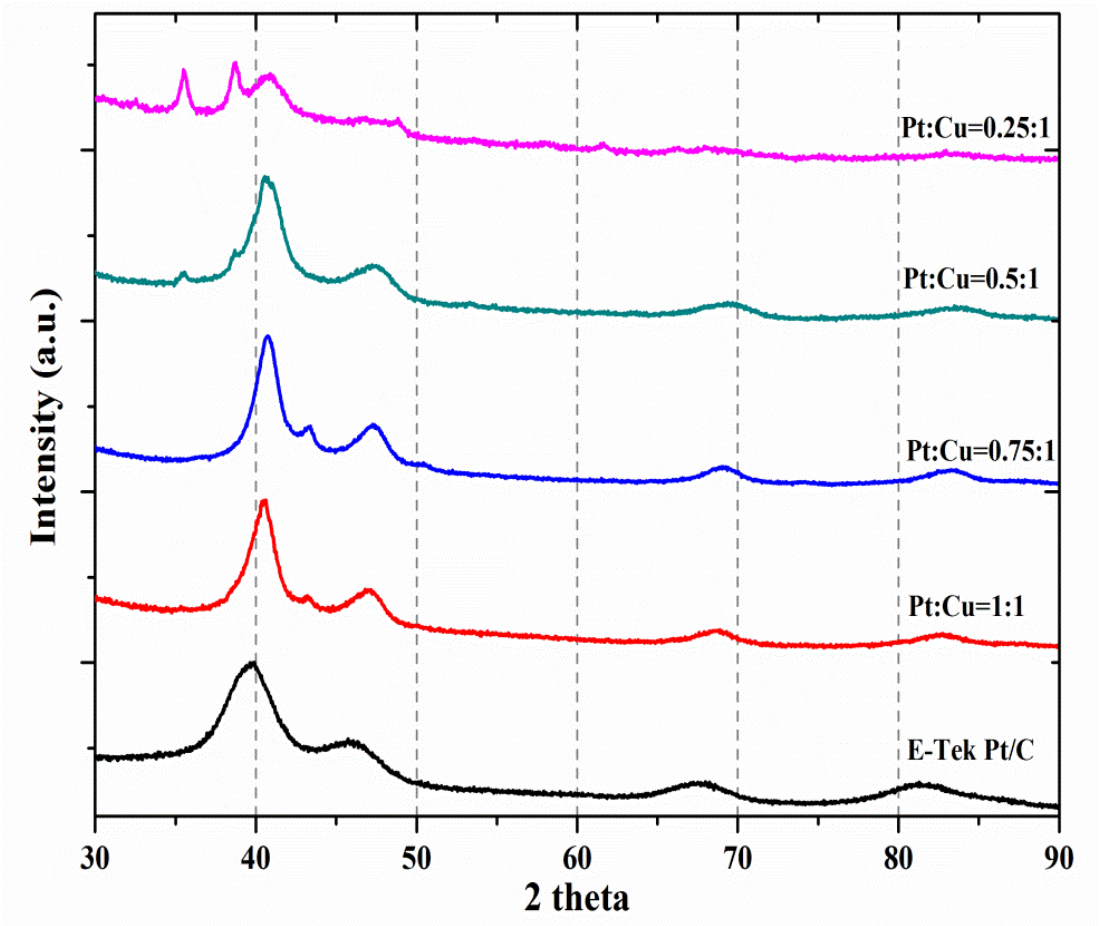

Figure 4.6 XRD patterns of the hollow PtCu/C with various Pt/Cu ratios and the commercial E-Tek Pt/C

As could be seen in Figure 4.6, the four characterised peaks at about 40.7, 47.3, 69.3 and 82.8° (2θ), could be indexed to a face-centred-cubic (*fcc*) structure Pt/Cu alloy (JCPDS 48-1549). Compared with the Pt/C, the shifted peaks of $Pt_{0.5}Cu_1$/C clearly indicated the formation of Pt/Cu alloyed nanostructures. Products with various molar ratios were also examined by XRD (Figure 4.6). In all XRD patterns, the positions of four characterised peaks of PtCu alloyed nanostructures (40.7, 47.3, 69.3 and 82.8° (2θ)) were almost unchanged regardless of the variation of Pt precursor concentrations revealing the fractions of Cu atoms adsorbing in Pt atoms were the same, which is further confirmed by the ICP-MS, as shown in Table 4.1. In addition, as indicated from the UV-Vis spectrum (Figure 4.2), a minor peak at 43.3 indexed to the (111) phase of

fcc Cu, two main peaks of CuO due to the oxidation of the unreacted Cu at 35.5, 38.7° when decreasing the concentration of Pt precursors were shown in the XRD data. The lattice parametres could be calculated from the three major phase ((111), (200) and (220) of PtCu alloyed nanoparticles and the composition of the Cu and Pt in the alloyed PtCu excluding the presence of Cu crystals or CuO crystals could be obtained by Vegard's law[25], which were listed in Table 4.1.

Table 4.1 Metal contents of the synthesized PtCu nanostructures

Reactant Ratio (Pt:Cu)	Analysed from ICP-MS			Derived From XRD			
	Pt (wt%)	Cu (wt%)	Pt/Cu atomic ratio	Lattice Parameter (Åm)	Pt molar fraction	Cu molar fraction	Pt/Cu atomic ratio
1	9.16	2.05	1.46	3.832	0.61	0.39	1.56
0.75	4.21	1.13	1.21	3.830	0.60	0.40	1.50
0.5	2.14	0.95	0.73	3.829	0.59	0.41	1.43
0.25	3.06	4.64	0.22	3.828	0.58	0.42	1.38

The accurate composition of the PtCu nanostructures was also analysed by the ICP-MS. It could be seen that the content of copper increased in all samples indicating copper was remaining in all samples after the sacrificial replacement due to the existence of the reducing agent, which is also in good accordance with the UV-Vis spectrum.

4.3.7 Acid Treatment and Electro-dealloying of the Hollow Nanparticles

As copper or copper oxides were not stable in acidic environment and they showed limited ORR performance in catalysing oxygen in acidic medium, thus copper and copper oxides crystals need to be removed before the measurement of the electrochemical performance of the bimetallic hollow PtCu nanostructure. Fortunately, this could be feasibly done by acid etching or electrochemical etching.

The chemical acid washing was carried out by sonicating the resultant products in pure acetic acid and further reacted for 6 h at 80°C in the air. The XRD of the product after

washing was shown in Figure 4.7. As could be seen in the XRD pattern, the peaks for the PtCu is nearly unchanged after acid washing suggesting copper alloyed in the Pt atoms was stable, while the characteristic peak for the copper oxides was mostly eliminated revealing copper or copper oxides was removed during acid washing.

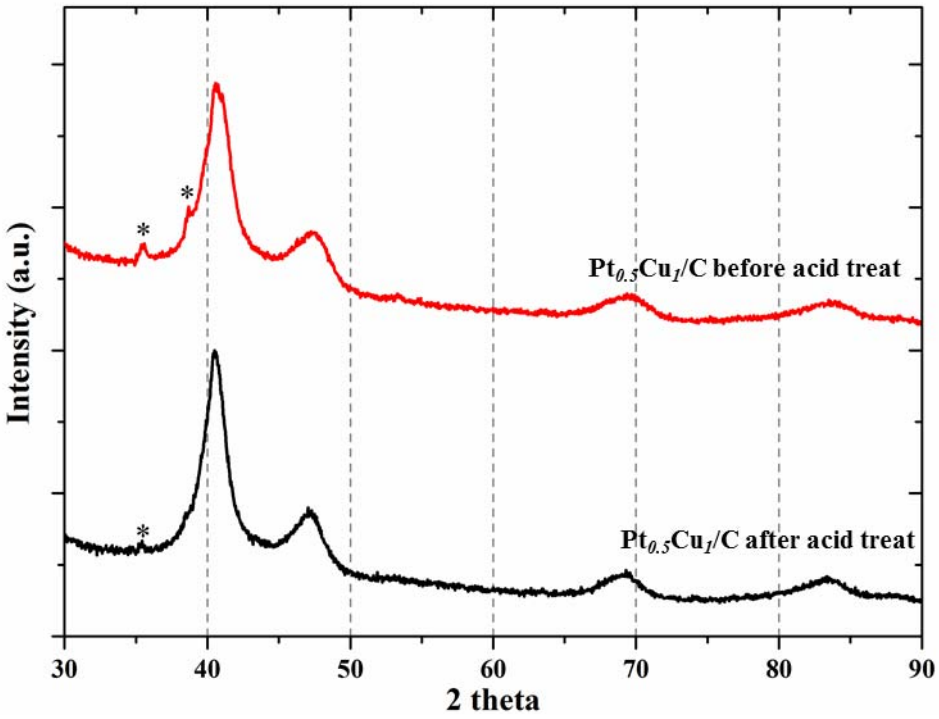

Figure 4.7 XRD patterns of the $Pt_{0.5}Cu_1/C$ before and after acetic acid treatment

We also conduct the EDS analysis to investigate the changes of element distribution after acid washing, which is shown in Figure 4.8, while a Pt abundant shell was constructed after acid washing, such a structure would benefit the ORR process, as the Pt is more stable and efficient in catalysing ORR in acidic environment.

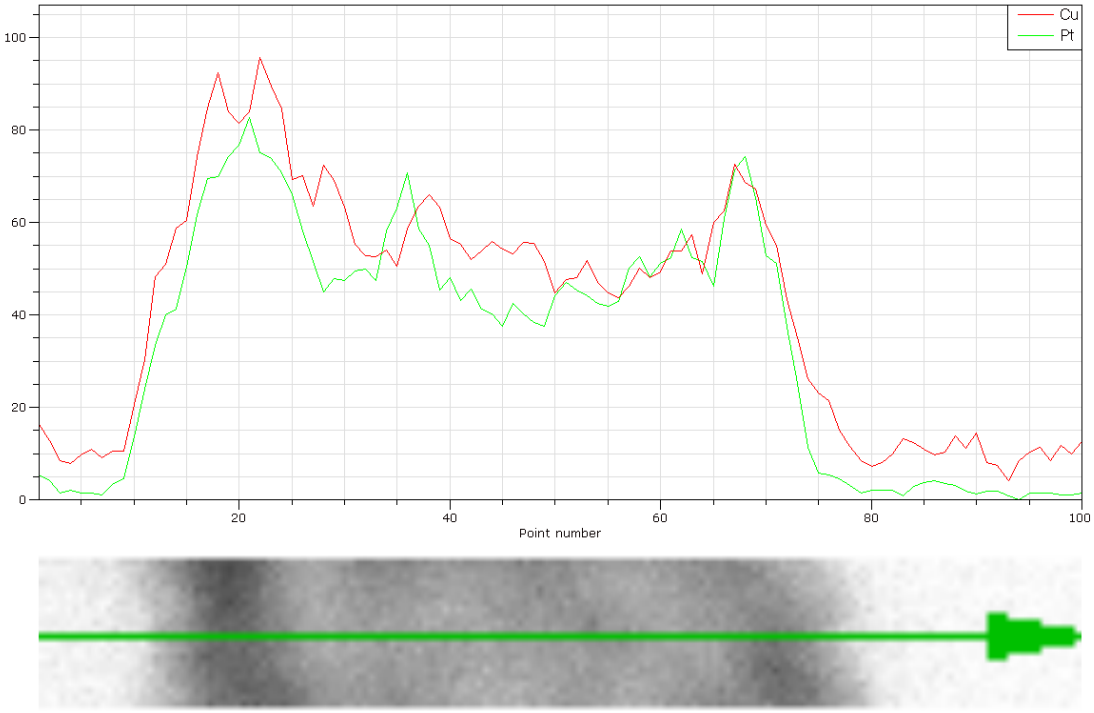

Figure 4.8 STEM-EDS line scanning profile of the $Pt_{0.5}Cu_1/C$ before and after acetic acid treatment

Also the copper or copper oxide could be removed by electrochemical dealloying through cyclic voltammetry (CV) at the potential range of −0.227V to 0.973V (vs. Ag/AgCl) with a scan rate of 100 mv/s for hundred cycles, as shown in Figure 4.9. In the first cycle of the CV, slight bump at ~0.4V was observed which was attributed to dissolution of Cu and the characteristic peak of Pt was not observed suggested the hollow particles was covered with copper species. After 100 cycles, the absence of peak around ~0.4V indicating unalloyed copper were etched away forming a Pt-rich surface and the CVs remained unchanged during the next 100 cycles indicating PtCu nanoparticles were well alloyed and a stable state was reached, which could be used for electrochemistry performance study.

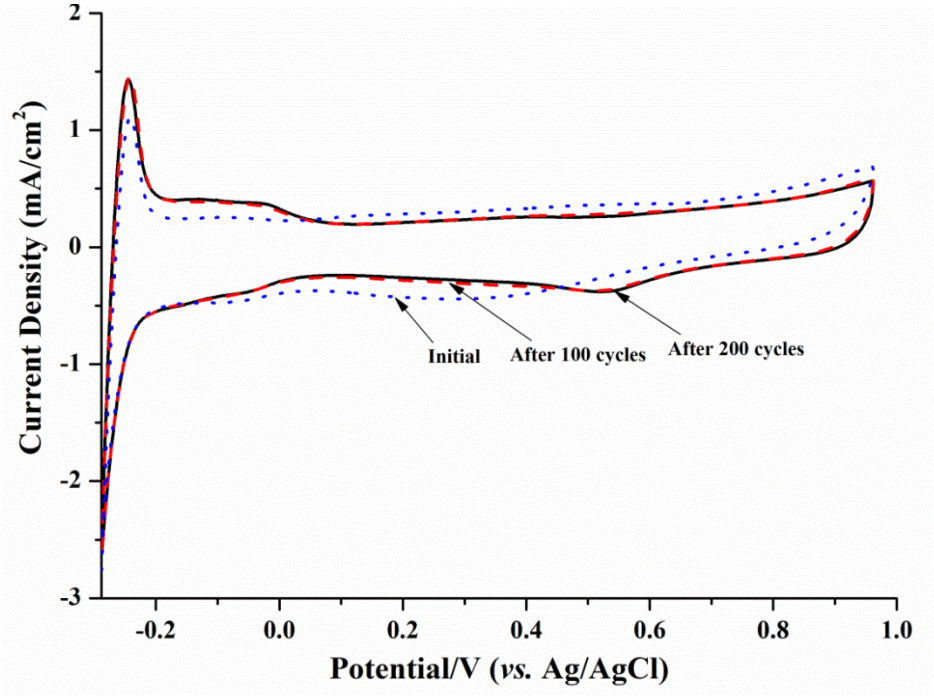

Figure 4.9 CV curves of the $Pt_{0.5}Cu_1/C$ before (initial) and after electrodealloying for 100 cycles and 200 cycles

4.3.8 Thermogravimetric analysis

To minimize nanoparticles aggregation and make a comparison with the commercial E-Tek (20 wt%), the synthesized nanaoparticles were supported with high-surface-area carbon black support (surface area ≈ 200 m^2/g) with a loading amount of 20 wt.%. The thermaogravimetric analysis was carried out in order to obtain the real loading amount of the electrocatalysts and make comparison with the commercial Pt/C (20 wt.% Pt on Vulcan XR72c carbon black). Figure 4.10 showed the TGA curves of $Pt_{0.5}Cu1/C$ calcinated in air atmosphere, it could be seen the loading amount is about 20 wt.%, which is very close the theoretic calculation indicating the efficient loading methods.

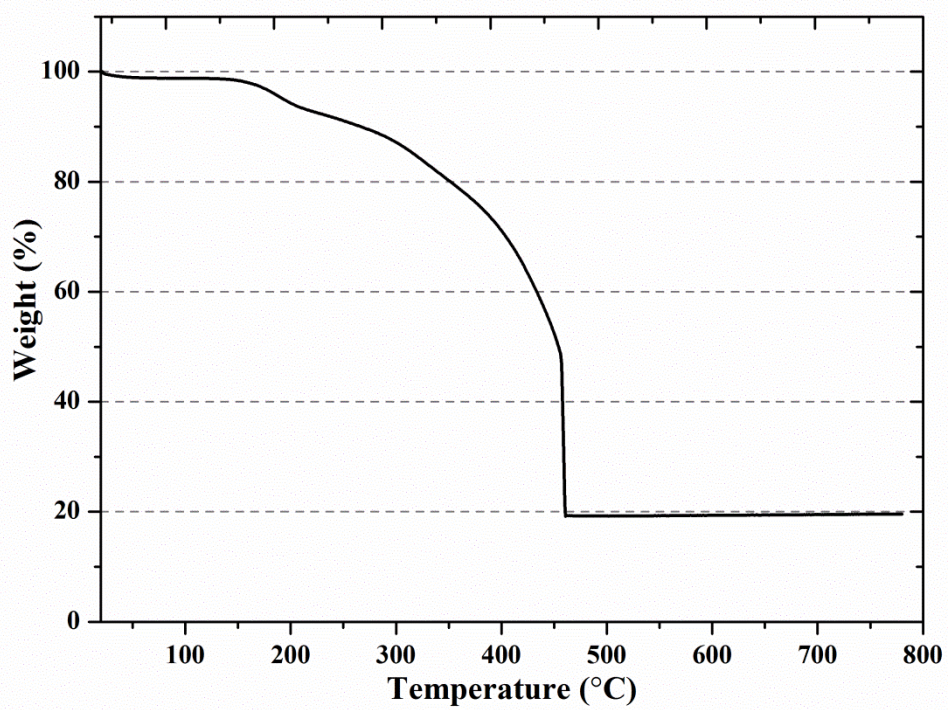

Figure 4.10 TGA curves of the $Pt_{0.5}Cu1/C$ calcinated in air atmosphere

4.3.9 Cyclic Voltammetry Measurement

CV curves were firstly obtained and used for a preliminary study of the electrochemical performance of the hollow nanoparticles. (Figure 4.11) The CVs are consistent with typical characterized CV regimes of Pt: typical hydrogen underpotential adsorption/desorption peaks in the potential range of −0.22 to 0.05 V; a double-layer capacitance region from 0.05 to 0.45 V; and Pt oxidation/reduction peaks in the range between 0.45 and 0.95 V. The electrochemical surface active area (ECSA) was calculated based on the charge transfer in the hydrogen adsopriton/desoprtion region at around −0.22 to 0.05V (vs. Ag/AgCl), subtracting the double layer correction and assuming 0.210 mC cm^{-2} for the adsoprtion of a monolayer of hydrogen on the Pt monolayer surface.[3] The ECSAs calculated are 32 $m^2 g^{-1}_{Pt}$ for $Pt_{0.5}Cu_1/C$ and 62.0 $m^2 g^{-1}_{Pt}$ for Pt/C. The lower ECSA of the $Pt_{0.5}Cu_1/C$ compared with Pt/C could be attributed to the smaller nanoparticle sizes and higher surface Pt concentration [3, 4]. The ECSAs

for other PtCu prepared with different precursor molar ration were also calculated, which were 39.2, 31.0 and 28.8 $m^2 g^{-1}_{Pt}$ for the Pt_1Cu_1, $Pt_{0.75}Cu_1$, $Pt_{0.25}Cu_1$ respectively.

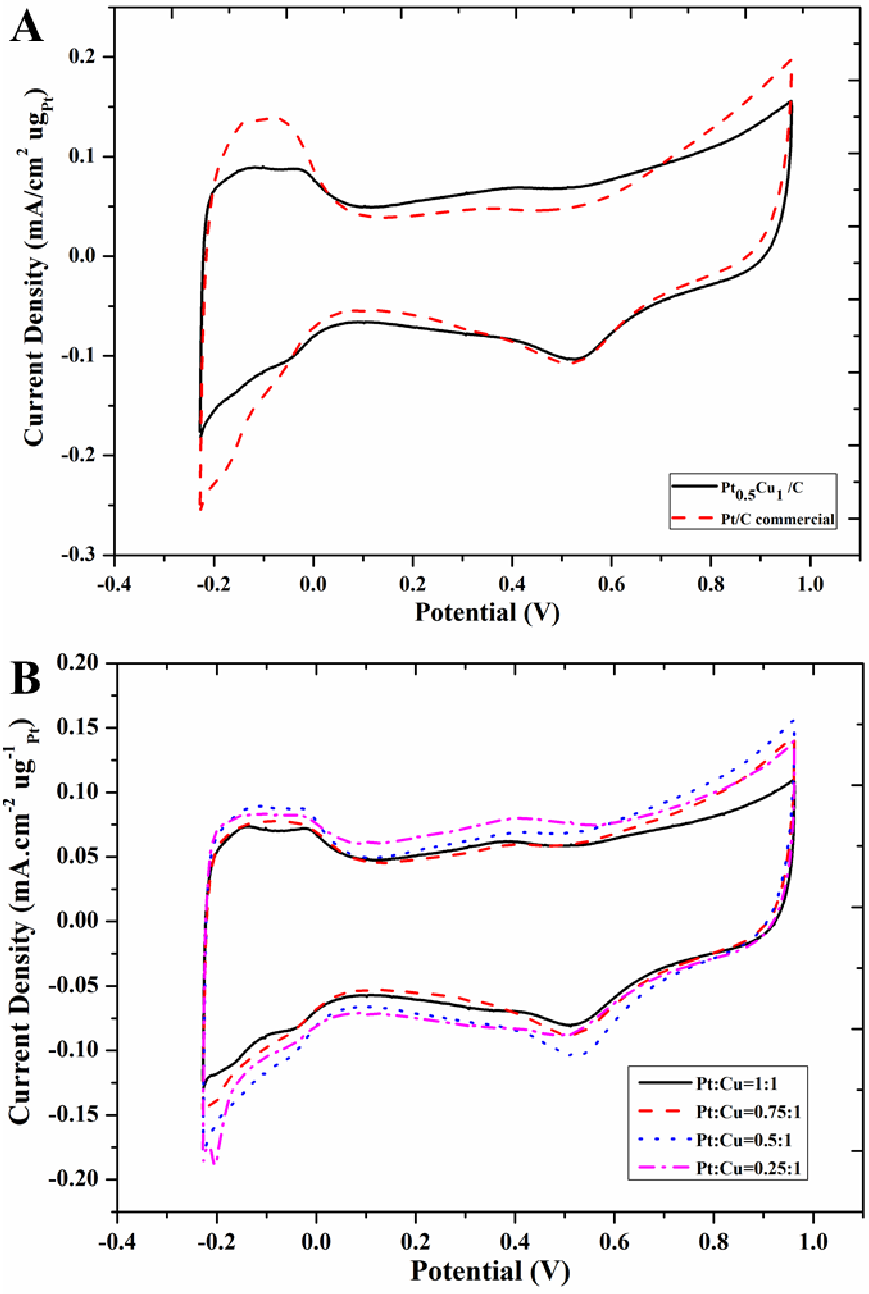

Figure 4.11 CV curves of (A) $Pt_{0.5}Cu_1$/C and Pt/C; (B) PtCu/C hollow nanostructures with various ratios of Pt and Cu precursor

4.3.10 The Oxygen Reduction Reaction Polarisation Curves

The ORR polarisation curves were acquire using the rotating ring disk electrode (RRDE) technique to assess and compare the electrocatalytic performance towards ORR of the PtCu/C which is shown in Figure 4.12. It could be seen the $Pt_{0.5}Cu_1/C$ and $Pt_{0.75}Cu_1/C$ showed similar ORR behaviours which are more efficient that the other two products prepared from precursor ratio of Pt:Cu= 1:1 and 0.25:1 in terms of the onset potential (from which oxygen began to reduce) and half wave potential ($E_{1/2}$). Thus the $Pt_{0.5}Cu_1/C$ was selected to make a comparison between the commercial available Pt/C (20 wt.%, E-Tek), and the ring curves were also obtained to study the production content of hydrogen peroxide during the ORR process of the two electrocatalysts as shown in

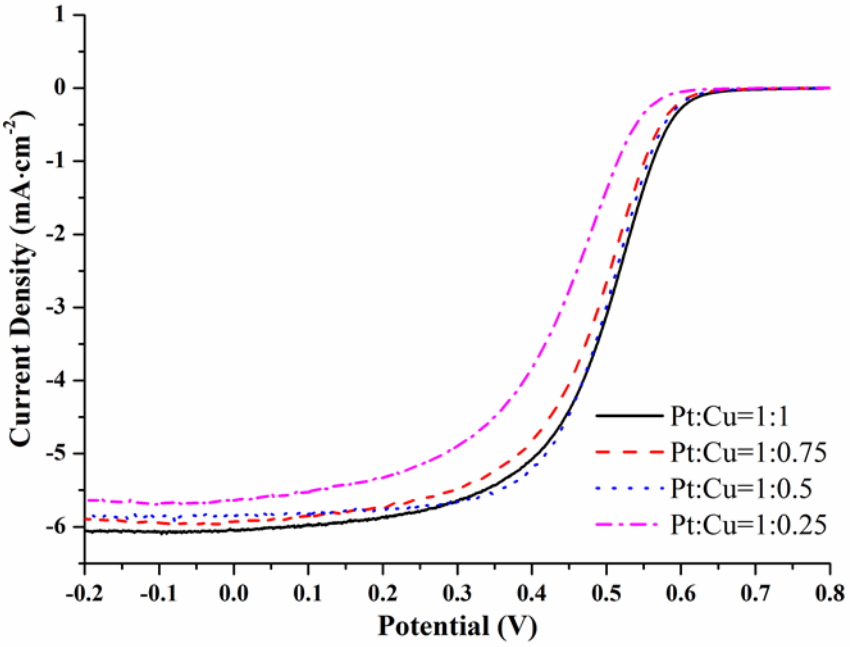

Figure 4.12 Polarisation curves of PtCu hollow nanostructures with various ratios of Pt and Cu precursor using a RRDE technique in oxygen saturated electrolyte (0.1 M $HClO_4$) with a scan rate of 10 mV s^{-1}.

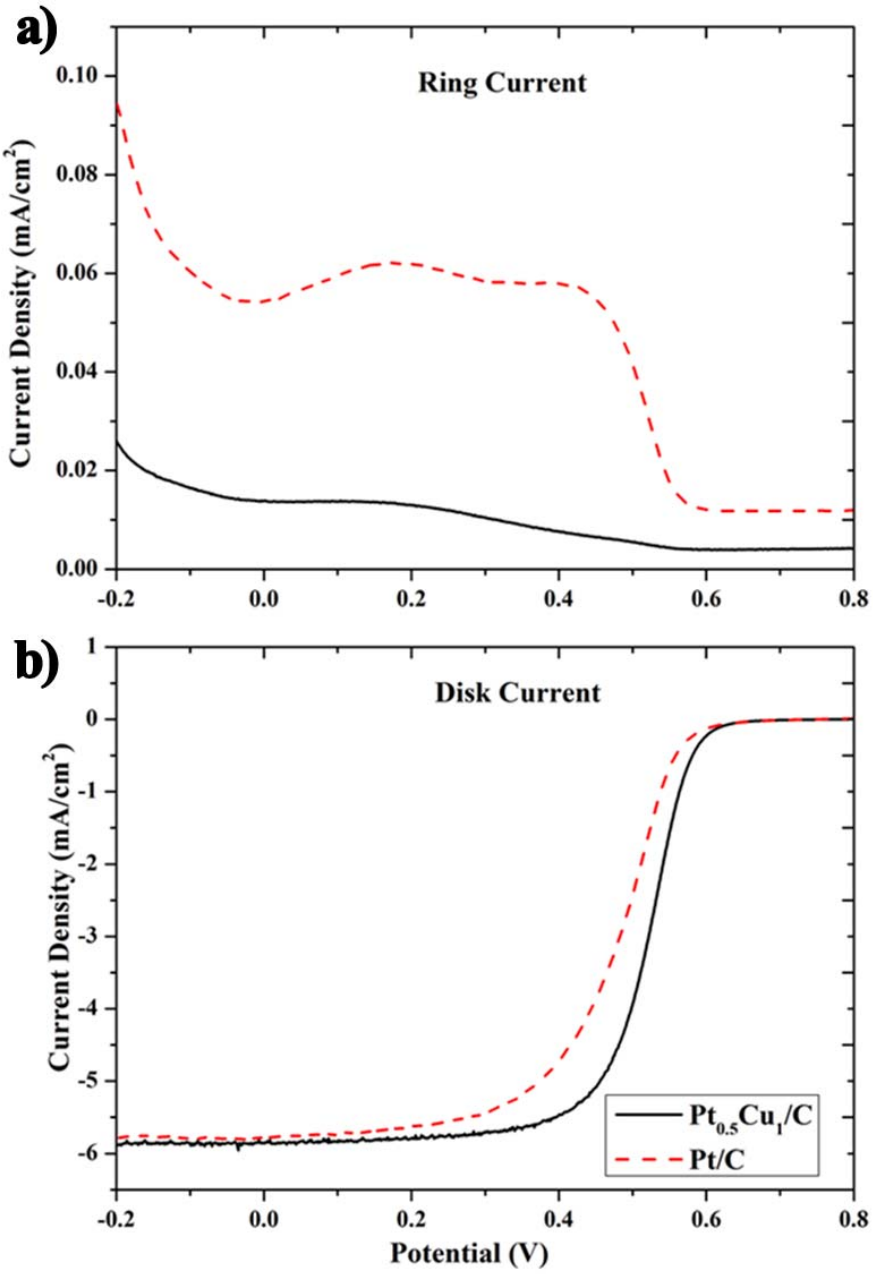

Figure 4.13 (a) Ring and (b) Disk Currents of $Pt_{0.5}Cu_1/C$ and Pt/C in ORR curves obtained using a RRDE technique in oxygen saturated electrolyte (0.1 M $HClO_4$) with a scan rate of 10 mV s^{-1}

As shown in Figure 4.13a and b, the half-wave potential of Pt0.5Cu1/C (0.510V) was positively shifted (30 mV) than that of Pt/C (0.480V) indicating the Pt0.5Cu1/C had a higher electrocatalytic activity towards ORR than that of Pt/C at the same metal loading. The much lower ring current indicated a higher efficiency of Pt0.5Cu1/C towards ORR

with less hydrogen peroxide generated compared with the Pt/C. Besides the electron transfer number calculated based on Error! Reference source not found.a and b was four on Pt0.5Cu1/C indicating that the oxygen reduction proceeded via four-electron pathway, whereas for Pt/C it was 3.29 revealing less efficient compared with the Pt0.5Cu1/C.

For further investigation of electroactivities among the various ratios of as-synthesised PtCu/C and commercial Pt/C catalysts, the specific area activity and mass activity were calculated as described previously[2] (Figure 4.14). Despite the low ECSAs , the PtCu/C showed much enhanced electrocatalytic performance which could be ascribed to the unique hollow alloyed nanostructures of the PtCu/C. In addition, the introduction of a second metal to Pt could also possibly induce the changes of Pt surface geometric features thereby improving the ORR activities[4, 9, 28]. As indicated in the histogram (Figure 4.14), the Pt0.5Cu1/C exhibited best electrocatalytic performances of ~ 3.5 and 7 times higher ORR mass activity and specific area activity than those of commercial E-Tek Pt/C at the potential of 0.510V. We suggested that the higher electrochemical activities of Pt0.5Cu1/C compared with other products may be ascribed to the porous structures which would facilitate the oxygen molecular transfer and enlarge the surface areas to build up more sites for ORR.[12] However as for Pt0.25Cu1/C, the mass of Pt was too low to support efficient oxygen reduction which would possibly cause the inferior performance at this ratio.

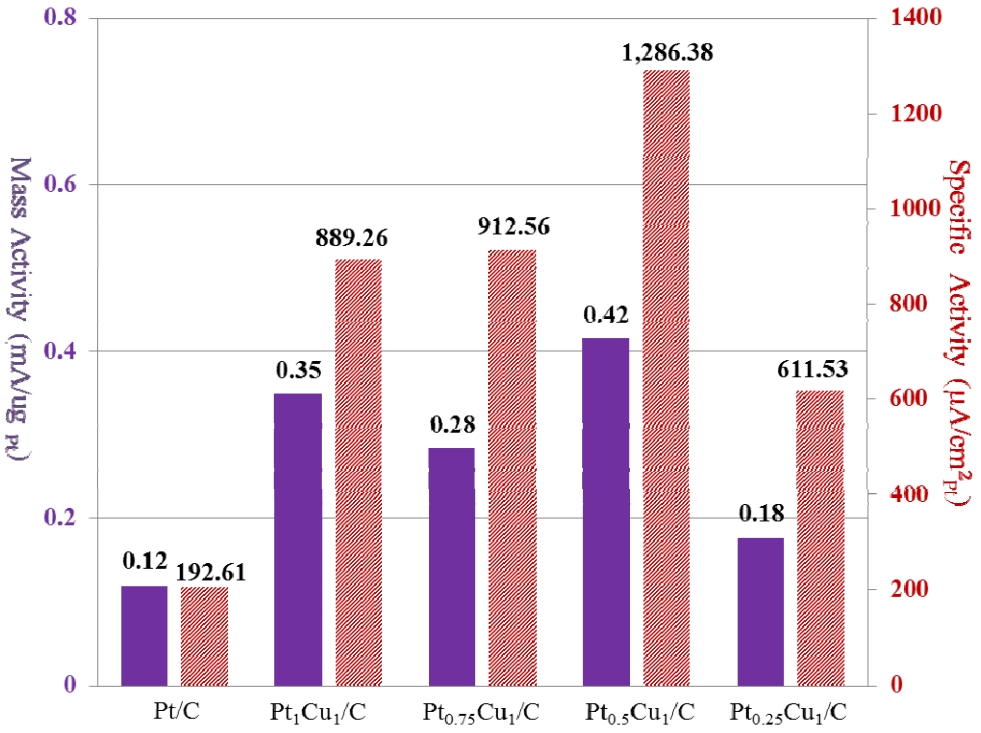

Figure 4.14 Mass activities (solid column) and specific area activities (diagonal pattern filled column) of the hollow PtCu/C with different molar ratios and the E-Tek Pt/C.

4.3.11 Durability Test of the Electrocatalysts

To determine the relative durability of the PtCu catalyst, the ORR activity of a catalyst thin film was measured before and after being subjected to 10,000 voltage cycles from 0.45V to 0.90V (vs Ag/AgCl) in oxygen saturated electrolyte at a rate of 50 mV/s.[26] The polarization curves for ORR before and after 10,000 potential cycles were recorded on Pt0.5Cu1/C and the commercial Pt/C electrocatalysts, as shown in Figure 4.15. No clear degradation changes were observed after 10,000 cycles indicating a significant durability of the Pt0.5Cu1/C, while the E-Tek Pt/C suffered a 70% loss after the same stability tests. Therefore, it suggested that of the Pt0.5Cu1/C could work as much more durable and practicable electrocatalysts for fuel cell.

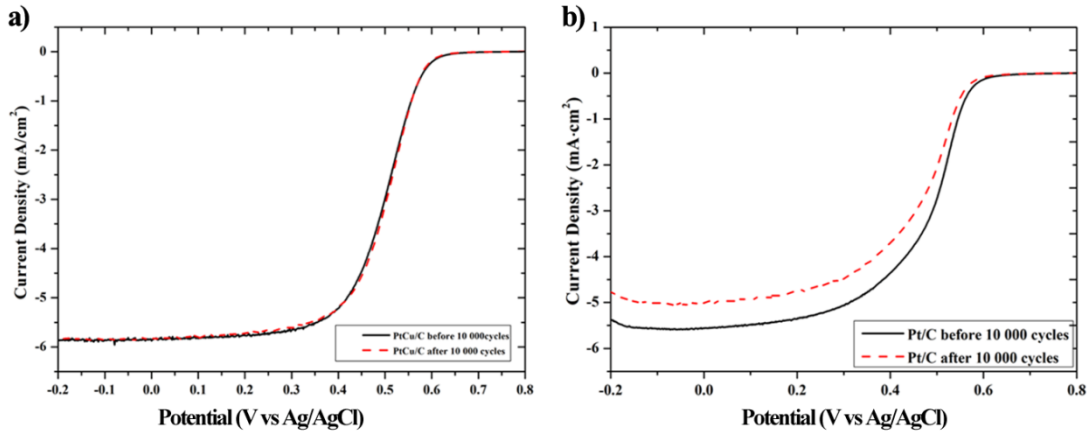

Figure 4.15 The ORR polarisation curves of a) Pt0.5Cu1/C and b) Pt/C before and after 10,000 cycles potential scan

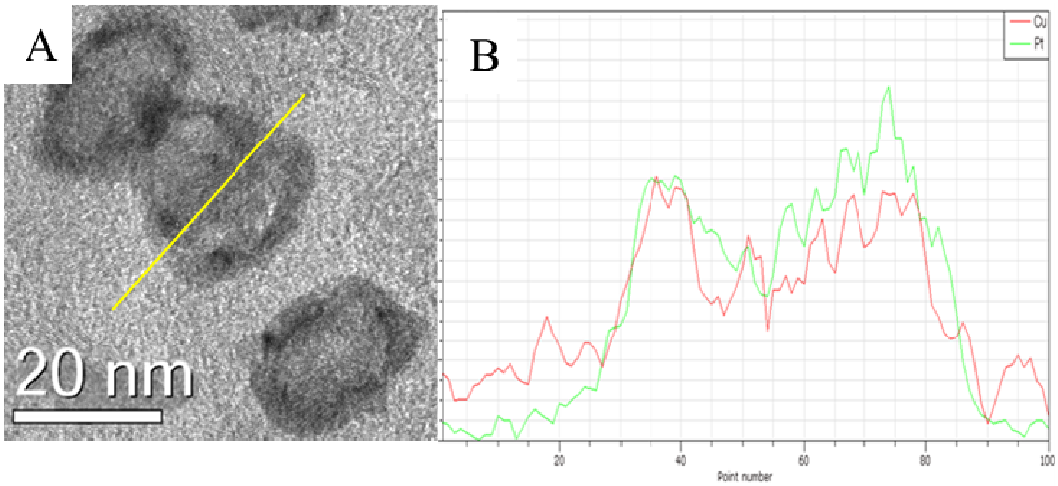

Figure 4.16 A) TEM images; B) EDS line scan profiles of the Pt0.5Cu1/C after durability test

To study the morphology and structural changes during the durability tests, the electrocatalysts was peeled off from the electrocatalysts and characterised with STEM-EDS analysis, as shown in Figure 4.16. TEM of the Pt0.5Cu1/C after durability test revealed the particle sizes were not changed, while EDS analysis showed copper were still remained after dualities test with a minor proportion reduced

4.3.12 Single Proton Exchange Membrane Fuel Cell Test

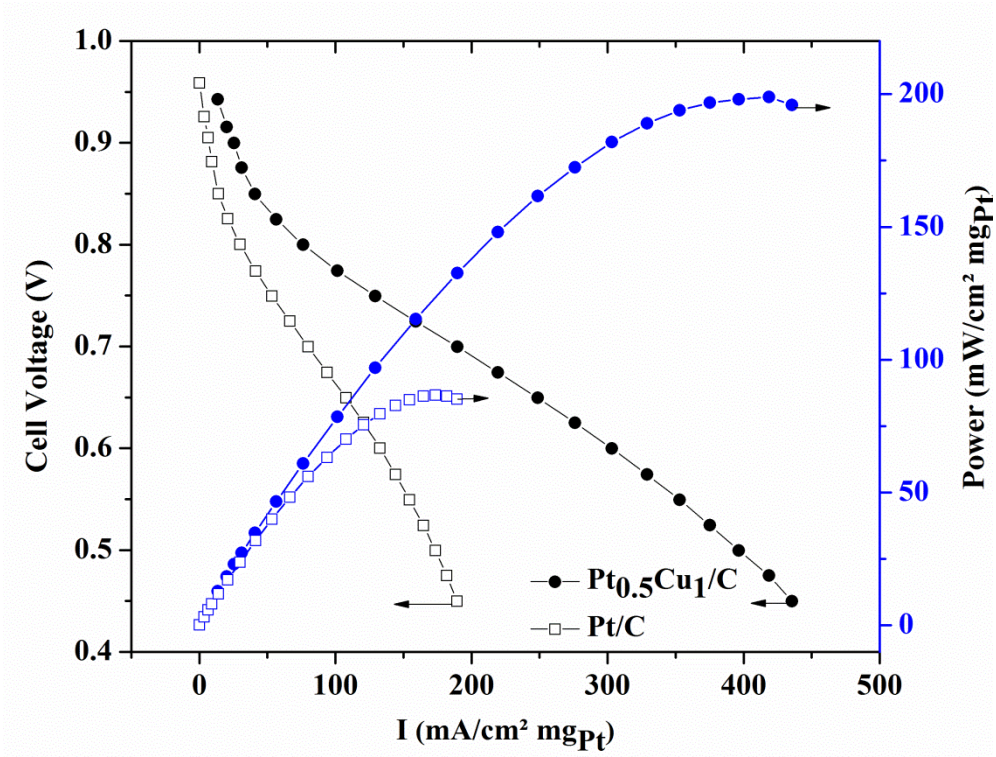

Figure 4.17 Polarisation curves obtained in single fuel cell test using the Pt0.5Cu1/C and Pt/C as cathodes catalysts

The ORR polarisation curves are useful in identifying candidate materials, however to demonstrate the practicable performances of the electrocatalysts, the tests operated under more closely to fuel cell operating conditions are needed[27]. Therefore we conducted single cell tests at last to measure the electrocatalysts performances operated under practicable environment (Figure 4.17). Under identical conditions, the Pt0.5Cu1/C exhibited a much higher electrocatalytic performance in single fuel cell tests, with a current density (248 mA $cm^{-2}mg^{-1}_{Pt}$) 2.3 times larger than that of the Pt/C (107 mA $cm^{-2}mg^{-1}_{Pt}$) at the operating voltage of 0.65V. The maximum power density obtained on the Pt0.5Cu1/C electrocatalysts is 200 mW $cm^{-2}mg^{-1}_{Pt}$, which is about 2.6 times higher than that from the Pt/C electrocatalyst (75 mW $cm^{-2}mg^{-1}_{Pt}$). These

comparisons clearly proved that the as-synthesised porous PtCu hollow NPs could work as the potentially more efficient catalysts under practicable environments.

4.4 Conclusion

In this chapter, we have described a modified galvanic replacement method to synthesize hollow PtCu hollow nanoparticles with mesoporous features, it was found the concentration between the ratios of precursor plays important role in determining the structure of final products. The TEM confirmed the formation of porous hollow shape, the EDS and XRD confirmed the alloyed nature of the nanoparticle consisting of both Pt and Cu elements even Cu or CuO was also detected in the final products, which could be further removed using chemical washing or electrochemical dealloying process producing a Pt rich shell in the catalysts.

Electrochemical tests revealed the mesoporous could work more efficient electrocatalysts compared with the commercial Pt/C with more stable and endurable in the acidic environment. Besides the single fuel cell tests also evidenced the electrocatalysts could work practicable electrocatalysts with much lower cost. The enhanced performance was referred as the change of electronic and geometric structure of Pt due to the introducing Cu into Pt atoms and the mesoporous features which could provide large surface area and ample active sites for oxygen reduction thus facilitating the ORR process.

In addition, we have described the synthesis of Pt-based electrocatalysts with much higher efficiency and stability for PEMFC compared with the commercial Pt/C electrocatalysts in Chapter 3 and 4. Although the synthesis procedures were both based on a modified galvanic replacement method, there are a number of differences between

the Pt-Pd electrocatalysts and Pt-Cu electrocatalysts in terms of their structural composition and the nature of alloying state.

Recently, the ORR in alkaline medium have recently draw considerable research interests because the overpotential of ORR would be greatly decreased and the mechanism of the ORR could be largely facilitated in alkaline medium thus offering wider selection of electrocatalysts. In addition, the development in the anion exchange membrane in recent decades suggests that the performance of anion exchange membrane fuel cell (AEMFC) could reach the same magnitude of that in the PEMFC, therefore it is high attractive to fabricate low-cost, high-efficient electrocatalysts for AEMFC in alkaline medium. With this well-developed acrificial template method in synthesis of Pt-based hollow shaped electrocatalyst for PEMFC, in the next chapter we would demonstrate that the synthesis of non-Pt electrocatalysts to replace the use of Pt through this method. Palladium (Pd), with intrinsic electrocatalytic performance comparable with Pt in alkaline medium, was selected and alloyed with transition metal nickel through the similar procedures. We examine the electrochemical performance of the PtNi hollow nanoparticles in alkaline medium and the PdNi hollow nanoparticles showed improved electrocatalytic ORR performance compared with the Pt/C in alkaline medium.

4.5 References

1. Debe, M.K., Nature, 2012. **486**(7401): p. 43-51.
2. Lim, B., M. Jiang, P.H.C. Camargo, E.C. Cho, J. Tao, X. Lu, Y. Zhu, and Y. Xia, Science, 2009. **324**(5932): p. 1302-1305.
3. Carpenter, M.K., T.E. Moylan, R.S. Kukreja, M.H. Atwan, and M.M. Tessema, Journal of the American Chemical Society, 2012. **134**(20): p. 8535-8542.

4. Kim, J., Y. Lee, and S. Sun, Journal of the American Chemical Society, 2010. **132**(14): p. 4996-4997.

5. Guo, S. and S. Sun, Journal of the American Chemical Society, 2012. **134**(5): p. 2492-2495.

6. Gupta, G., D.A. Slanac, P. Kumar, J.D. Wiggins-Camacho, X. Wang, S. Swinnea, K.L. More, S. Dai, K.J. Stevenson, and K.P. Johnston, Chemistry of Materials, 2009. **21**(19): p. 4515-4526.

7. Yu, Z., J. Zhang, Z. Liu, J.M. Ziegelbauer, H. Xin, I. Dutta, D.A. Muller, and F.T. Wagner, The Journal of Physical Chemistry C, 2012. **116**(37): p. 19877-19885.

8. Vasquez, Y., A.K. Sra, and R.E. Schaak, Journal of the American Chemical Society, 2005. **127**(36): p. 12504-12505.

9. Zhang, J., M.B. Vukmirovic, K. Sasaki, A.U. Nilekar, M. Mavrikakis, and R.R. Adzic, Journal of the American Chemical Society, 2005. **127**(36): p. 12480-12481.

10. Zhang, J., K. Sasaki, E. Sutter, and R.R. Adzic, Science, 2007. **315**(5809): p. 220-222.

11. Zhang, W., J. Yang, and X. Lu, ACS Nano, 2012. **6**(8): p. 7397-7405.

12. Yu, X., D. Wang, Q. Peng, and Y. Li, Chemical Communications, 2011. **47**(28): p. 8094-8096.

13. Xu, C., L. Wang, R. Wang, K. Wang, Y. Zhang, F. Tian, and Y. Ding, Advanced Materials, 2009. **21**(21): p. 2165-2169.

14. Mohl, M., D. Dobo, A. Kukovecz, Z. Konya, K. Kordas, J. Wei, R. Vajtai, and P.M. Ajayan, Journal of Physical Chemistry C, 2011. **115**(19): p. 9403-9409.

15. Xu, C., Y. Liu, J. Wang, H. Geng, and H. Qiu, ACS Applied Materials and Interfaces, 2011. **3**(12): p. 4626-4632.

16. Xu, C., Y. Zhang, L. Wang, L. Xu, X. Bian, H. Ma, and Y. Ding, Chemistry of Materials, 2009. **21**(14): p. 3110-3116.

17. Sun, Y. and Y. Xia, Journal of the American Chemical Society, 2004. **126**(12): p. 3892-3901.

18. Mayers, B., X. Jiang, D. Sunderland, B. Cattle, and Y. Xia, J. Am. Chem. Soc., 2003. **125**: p. 13364-13365.

19. Wu, S.-H. and D.-H. Chen, Journal of Colloid and Interface Science, 2004. **273**(1): p. 165-169.

20. Zhang, W., J. Chen, G.F. Swiegers, Z.-F. Ma, and G.G. Wallace, Nanoscale, 2010. **2**(2): p. 282-286.

21. Mani, P., R. Srivastava, and P. Strasser, The Journal of Physical Chemistry C, 2008. **112**(7): p. 2770-2778.

22. Lisiecki, I., F. Billoudet, and M.P. Pileni, Journal of Physical Chemistry, 1996. **100**(10): p. 4160-4166.

23. Mayers, B., X. Jiang, D. Sunderland, B. Cattle, and Y. Xia, J. Am. Chem. Soc., 2003. **125**(Copyright (C) 2012 American Chemical Society (ACS). All Rights Reserved.): p. 13364-13365.

24. Liang, H.-P., H.-M. Zhang, J.-S. Hu, Y.-G. Guo, L.-J. Wan, and C.-L. Bai, Angewandte Chemie, International Edition, 2004. **43**(12): p. 1540-1543.

25. Liu, Z., S. Koh, C. Yu, and P. Strasser, Journal of The Electrochemical Society, 2007. **154**(11): p. B1192-B1199.

26. Yang, J., X. Chen, X. Yang, and J.Y. Ying, Energy & Environmental Science, 2012. **5**(10): p. 8976-8981.

27. Fernández, J.L., V. Raghuveer, A. Manthiram, and A.J. Bard, Journal of the American Chemical Society, 2005. **127**(38): p. 13100-13101.

Chapter 5

PdNi Hollow Nanoparticles for the Oxygen Reduction Reaction in Anion Exchange Membrane Fuel Cells

5. **CONTENTS**

Chapter 5

5.1 Introduction

We demonstrate the synthesis of Pt based alloyed electrocatalysts with improved catalytic oxygen reduction reaction (ORR) performance in acidic environment and the application of them in the proton exchange membrane fuel cell (PEMFC) in the previous chapters and these Pt based electrocatalysts have shown improved electrocatalytic performance as well as better stabilities in PEMFC. Recently a great efforts have been devoted into the synthesis of non-Pt based electrocatalysts for the ORR in alkaline medium because it has been well documented that the overpotential for the ORR will be significantly reduced in high pH (alkaline) environment, thus offering the possibilities of lower usage and wider selection of electrocatalysts other than platinum to be available for this catalytic reaction.[1, 2]

At the meantime, the anion exchange membrane fuel cell (AEMFC), where the alkaline anion exchange membranes (AAEMs) is used instead of the conventional acidic Nafion® membrane in the proton exchange membrane fuel cell (PEMFC),[3-5] has recently received considerable attraction with the development of AAEMs.[3, 6] The cell design of AEMFC is typical the same with PEMFC except AAEMs were used to only allow anion transfer from the cathode to anode, in specifically, the oxygen in the cathode is reduce to OH^- and crosses through the AAEM to react with H^+ and generate water, this difference between the PEMFC would generate alkaline medium in the cathode of AEMFC thereby offering the opportunities of using the ORR electrocatalysts explored in alkaline medium. Moreover, recently studies have shown that the possibilities of the performance of the AEMFC could reach the same magnitude performance of the PEMFC, and this adds further incentive in developing non-Pt electrocatalysts for the ORR in AEMFC.

Palladium (Pd), with competitive intrinsic electrocatalytic performance in alkaline medium towards the ORR compared to Pt, is less expensive and more abundant and has received considerable attention recently.[2, 7-10] Pd alloyed with transition metals (Pd-TMs), such as Pd-Ni,[11, 12] Pd-Cu,[13-16] Pd-Fe,[2, 17, 18] and Pd-Co,[19] has proven to be an effective way to reduce cost and simultaneously to enhance catalytic performance due to the change of electronic and geometric structure of Pd.[2, 20] Compared with alloying with noble metals such as Pd-Au[7, 21, 22] or Pd-Ag,[1, 20, 23] Pd alloyed with TMs provides a more practical and economical way to produce Pd-based bimetallic electrocatalysts for the ORR in alkaline media.

Previous chapters have well demonstrated the advantage of using hollow nanostructure in catalyzing ORR, including economically viability, higher surface area and catalyst utilization efficiency compared with their filled solid counterparts.[24] The so called sacrificial template protocol (galvanic replacement), which was first well demonstrated by Xia's group[25], has been modified and widely applied to synthesise Pt-based bimetallic hollow nanostructures such as Pt-Pd[26], Pt-Cu[27] in the last chapters with enhanced electrocatalytic performance. In comparison with the development of Pt-bimetallic hollow nanostructures, reports on synthesising Pd-based bimetallic hollow nanostructures have been rare, mainly because the activity and the durability of Pd in the ORR are poor in acidic media.[2] For example, Pd-Ag hollow nanorings were synthesized with good methanol tolerance,[23] while the ORR performance was not improved, mainly because the larger lattice constant of silver would subject the Pd to a tensile strain effect, decreasing the electroactivity of Pd towards the ORR.[28] Pd-Co[29] and Pd-Cu[30] hollow nanostructures were also reported with large particle size (> 50 nm) but their ORR properties were not extensively studied due to the large particle size, which may decrease the active surface

area. Thus, there is still an urgent need to develop Pd-TM bimetallic hollow nanostructures with catalytic oxygen reduction abilities in alkaline media.

In this chapter, with the well-developed method in the previous chapter, we present novel hollow PdNi nanostructures synthesized via a modified galvanic process using Ni nanoparticles as sacrificial templates in aqueous solution. Electrochemical testing to investigate the ORR effects showed that the as-synthesized PdNi had an outstandingly high mass activity of 588.97 mA g^{-1}_{Pd}, which is 3.9 times higher than that of Pt/C, when the precursor ratio of Pd:Ni was 1:1 (denoted as Pd_1Ni_1 in this report) at −0.114 V (vs. Ag/AgCl). Together with single H_2/O_2 fuel cell testing, it is evidenced that Pd_1Ni_1/C could serve as an efficient and durable AEMFC electrocatalyst in a practical working device.

5.2 Experimental

5.2.1 Reagents

Nickel(II) chloride hexahydrate ($NiCl_2 \cdot 6H_2O$), palladium(II) chloride ($PdCl_2$), sodium citrate (99%), and sodium borohydride ($NaBH_4$, 99.99%) were purchased from Sigma-Aldrich. Carbon black (CB, Vulcan XC-72 R) was provided by the Cabot Corporation. All glassware and PTFE-coated magnetic stir bars were cleaned with *aqua regia*, followed by copious rinsing with distilled water before drying in an oven.

5.2.2 Synthesis

Ni nanoparticles were synthesized using the borohydride reduction method. Briefly, 0.02 mmol $NiCl_2 \cdot 6H_2O$ and 29.4 mg sodium citrate were added to 40 ml distilled water. After deoxygenating with nitrogen for 15 min, 2 ml freshly prepared $NaBH_4$ (7.5 mg) was injected into the solution by syringe. The colour of the solution immediately turned

dark yellow after the addition of $NaBH_4$, indicating the formation of Ni nanoparticles. After a few minutes, 0.02 mmol H_2PdCl_4 in 40 ml deoxygenated water was added dropwise into the Ni particle/colloid at a rate of 1 ml min^{-1} and allowed to react for another 2 hours. The synthesized PdNi nanoparticles were supported on carbon black (CB, Vulcan XC-72 R, Cabot Corp.) with a loading of 20 mass%, achieved by mixing the above colloids with acid treated CB. A solid sample was obtained by filtration. Before filtration, an aliquot of sodium hydroxide was added with stirring for another 2 hours, and then the products were filtered and rinsed with water several times to remove the residual impurities in the catalysts, and then dried at 80°C overnight. This sample was denoted as Pd_1Ni_1/C. To determine the optimized molar ratio of Pd:Ni, PdNi/C catalysts with various precursor mole ratios of Pd to Ni, 3:1, 2:1, 1:1, and 0.5:1, were synthesized. The corresponding samples were denoted as Pd_3Ni_1/C, Pd_2Ni_1/C, Pd_1Ni_1/C, and $Pd_{0.5}Ni_1/C$ respectively

5.2.3 Physical Characterisation

Low magnification TEM images were collected with a JEOL JEM-2100F transmission electron microscope (TEM). High resolution (HR)-TEM images, scanning transmission electron microscope (STEM) images, and probe-corrected energy dispersive spectroscopy (EDS) line scans were collected in high-angle annular dark-field imaging (HAADF)-STEM mode, using a JEOL-JEM 2200FS TEM operated at 200 kV. Samples for TEM were prepared by dropping one drop of the cleaned nanoparticles in ethanol dispersion on a copper grid (200 mesh). The powder X-ray diffraction (XRD) patterns were collected using a Bruker D8-Advance X-ray powder diffractometer with Cu Kα radiation (λ = 1.5406 Å). X-ray photoelectron spectroscopy (XPS) spectra were collected using a Thermo Scientific K-Alpha instrument. Metal contents of the products

were determined using energy dispersive spectroscopy (EDS, Bruker) in SEM (JEOL-7500FA) and inductively coupled plasma – mass spectrometry (ICP-MS 7500CS, Agilent Technologies).

5.2.4 Electrochemical measurements

Electrochemical measurements were performed using a glassy carbon rotating ring disk electrode (RRDE, Pine Research Instrumentation, disk area=0.2475 cm^2) connected to a CHI 720c potentiostat (CHI instrument) in a standard three-electrode cell with a Pt mess as the counter electrode and a 3 M KCl saturated Ag/AgCl electrode as the reference electrode. An electrochemical cell (Pine Instrument) was filled with about 100 ml 0.1M KOH and covered with a Teflon cap. The eletrocatalysts ink was prepared by dispersing the electrocatalysts in 5% Nifion/H_2O/isopropanol (m/m/m/=0.5/10/50) to reach a 1mg/ml dispersion with an ultrasonicator (Brandson). 30 μL of the ink was dropped on the RRDE electrode and let it air-dry for 2 hours before the electrochemical tests.

The cyclic voltammetry (CV) traces were recorded in N_2-saturated KOH(aq) (0.1 mol L^{-1}) solution with a sweep rate of 50 mV s^{-1}. The ORR polarization curves were recorded using a linear sweep voltammetry (LSV) technique in oxygen saturated electrolyte with a sweep rate of 10 mV s^{-1} at various rotation speeds of 100, 400, 900, and 1600 rpm from 0.1 to -0.8 V. Stability tests were carried out by the chronoamperometry technique at the potential of -0.2 V and with rotation at 1600 rpm in oxygen-saturated electrolyte for 8000 seconds.

To evaluate the electrochemical performances, electrochemical surface areas (ECSAs) were calculated by measuring the charge The electrochemical surface active area (ECSA) was calculated based on the charge transfer in the metal reduction region at around -0.25 (vs. Ag/AgCl), subtracting the double layer correction and assuming 0.405

mC cm^{-2} for the reduction of a monolayer of PdO on the catalyst surface and 0.210 mC cm^{-2} for the reduction of a monolayer of PtO.[2]

In order to obtain the kinetics of the ORR, ORR polarization curves were collected at various rotation speeds, and corresponding Koutecky-Levich (K-L) plots were drafted from the ORR polarization curves at different potentials. The number of electrons involved per O_2-molecule reduction can be determined using the Koutecky-Levich (K-L) equation

$$j = 1/j_k + 1/B\omega^{0.5};$$

$$[B = 0.2n\mathrm{F}(D_{O2})^{2/3}(v)^{-1/6}C_{O2}]$$

where, j_k is the kinetic current, ω is the electrode rotation rate, n is the transferred electron number, F is the Faraday constant (F = 96485 C mol^{-1}), D_{O2} is the diffusion coefficient of O_2 = 1.9×10^{-5} cm^2 s^{-1}, v is the kinetic viscosity (0.01 cm^2 s^{-1}), and C_{O2} is the bulk concentration of O_2 (1.2×10^{-6} mol cm^{-3}). The constant 0.2 is adopted when the rotation speed is expressed in rpm.

5.2.5 Single Fuel Cell Test

The anion-exchange membranes used were electron-beam-grafted EFTE membranes (graft co-polymerised) using vinylbenzyl chloride and functionalised using trimethylamine (University of Surrey);[5] the membrane used was of type S80, with membrane thickness ≈ 80 μm (thickness depends on hydration level) and ion exchange capacity IEC ≈ 1.3 meq g^{-1}. The anodes and cathodes were prepared as described previously.[5] In brief, the electrocatalyst ink with ca. 10 mass%. PTFE as binder were firstly sprayed on the gas diffusion layers (GDLs, 5cm^2) to a loading of 0.4 mg cm^{-2} and were then spray-treated with poly(vinybenzyl chloride) dissolved in ethyl acetate. The prepared GDLs were subsequently immersed in undiluted *N, N, N', N'-*

tetramethylhexane-1,6-diamine (TMEDA) for 24 hours and then washed thoroughly with water. The Pt/C was used as the electrocatalysts for anodes. For comparison purpose, the commercial E-Tek Pt/C and the Pd_1Ni_1/C were chosen and used as catalysts for cathodes. Before single fuel cell testing, the AAEMs and GDL electrodes were immersed in KOH(aq) (1 mol L^{-1}) solution for 1 hour to give alkaline anion-exchange materials (OH^- conducting polymer electrolyte and cross-linked ionomer). The membrane electrode assemblies (MEAs) were preparing by sandwiching the anode GDLs and the AAEMs and tested using an 850e fuel cell test system (Fuel Cell Technologies, Inc., USA) fed with humidified hydrogen and oxygen. The gas flow was controlled at 0.08 ml min^{-1}. The fuel cell measurements were carried out at 60°C under 15 psi (103 kPa) back pressure. The polarization curves were recorded using a potential scan method by holding the cell at each potential for 30 s in order to obtain the steady-state current value with a scan rate of 25 mV s^{-1} from 0.90 V to 0.25 V.

5.3 Result and Discussions

5.3.1 Synthesis of Porous Hollow PdNi Nanoparticles

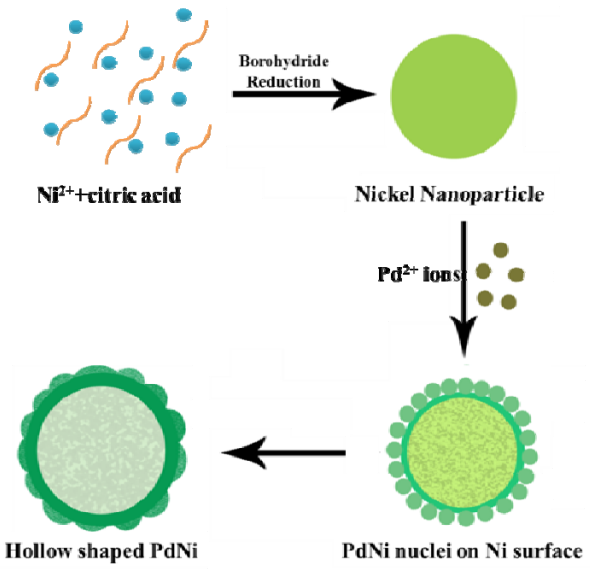

Figure 5.1 Schematic illustration of the formation of PdNi hollow NPs

The schematic illustration of the synthesis procedure was depicted in Figure 4.1, which is quite similar to the mechanism proposed in our previous work.[27]. In a typical synthesis, nickel nanoparticles were firstly synthesized using citric acid as surfactant and sodium borohydride as reducing agent under inert atmosphere. As the standard reduction potential of Ni(II)/Ni (-0.257 V vs. standard hydrogen electrode (SHE)) is lower than that of the $PdCl_4^{2-}$ /Pd couple (0.59 V vs. SHE), once dihydrogen tetrachloropalladate(II) solution is added the galvanic replacement will occur immediately following the reaction equation shown in Equation 5.1. In this process, Ni nanoparticles serve as the template and are gradually consumed by Pd salts, thereby forming hollow cores. The Pd(II) ions will be co-reduced with a certain amount of Ni(II) (leached away during the previous process) and to be deposited on the surface of the Ni nanoparticles and form PdNi alloy shells.

$$2Ni + PdCl_4^{2-} \rightarrow 2Ni^{2+} + Pd + 4Cl^- \qquad \text{Equation 5.1}$$

5.3.2 Morphology of the Synthesized PdNi Hollow Nanoparticless with Various Precursor Ratio

Impacts of the precursors' molar ratio on the morphology of the nanoparticles were carefully examined, as shown in Figure 5.2. When the precursor ratio Pd/Ni is $\geq$ 3, the hollow feature can barely be observed due to the relatively thick shells of the nanoparticles (> 10 nm, Figure 5.2(A)). The shell thickness decreases, and the particle size slightly increases, with reduction of the Pd proportion. As a consequence, well-defined hollow shapes gradually appear. When the ratio of Pd/Ni is 0.5 in the precursor, some smaller nanoparticles with sizes of about 15 nm are also produced (Figure 5.2(D)), which may be because the Pd ions were insufficient to consume all the Ni nanoparticles to form hollow shapes in the solution, causing the thus produced nanoparticles to be

partially solid. This was evidenced by the single Ni peak on the XRD patterns, which would be discussed later. The shell porosity was also changed when the ratio in the precursors was varied; with less Pd, the shell tended to be more porous.

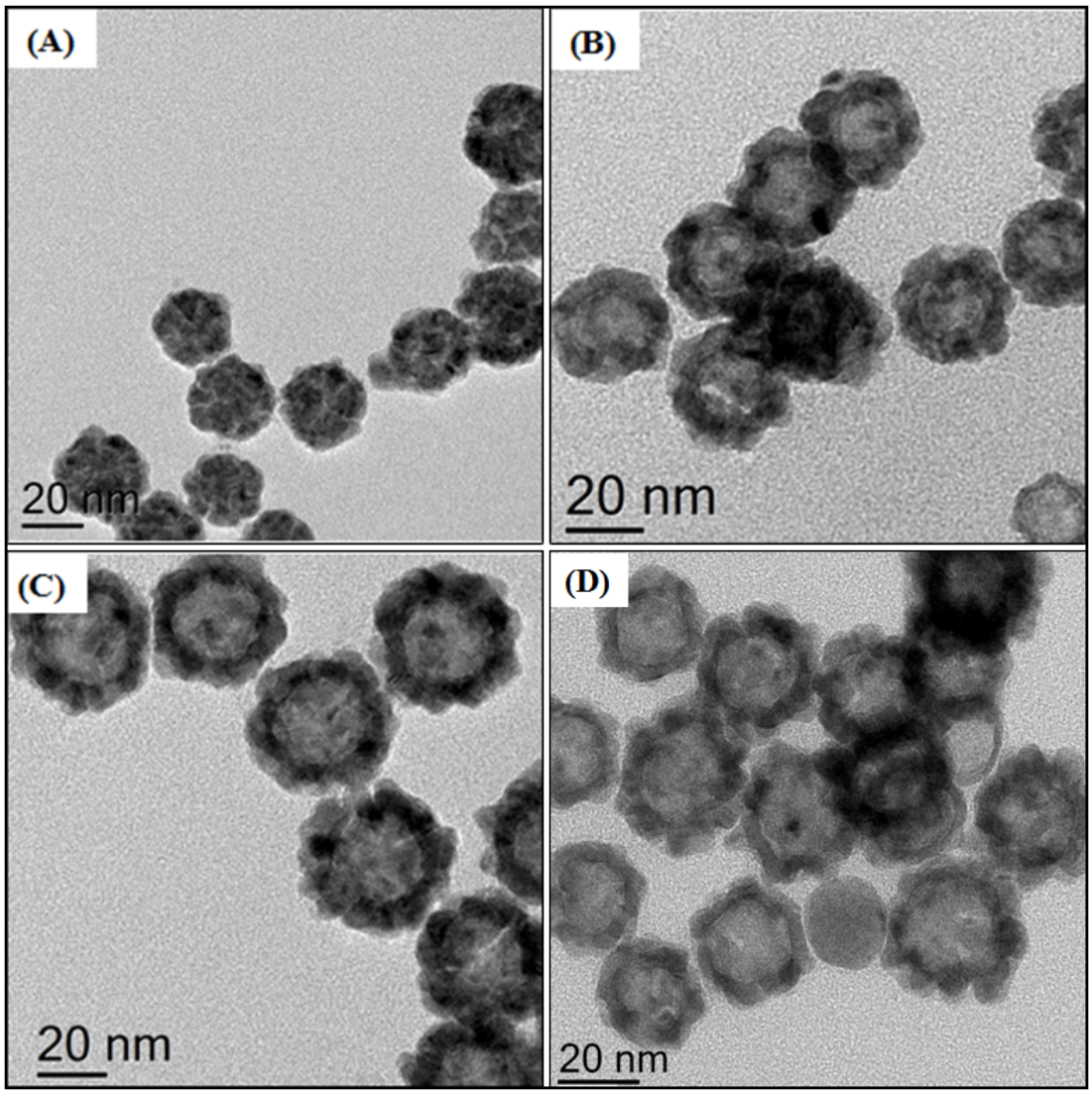

Figure 5.2 Typical TEM images of PdNi hollow nanoparticles with different Pd/Ni precursors ratios; the molar ratios of Pd/Ni are (A) 3:1, (B) 2:1, (C) 1:1, (D) 0.5:1

5.3.3 Crystal Structure Analysis

XRD was employed to analyse the crystal structures of the hollow PdNi particles, as shown in Figure 5.3. The diffraction peaks indicated that the structure could be indexed using a face-centred-cubic (*fcc*) lattice, with (111), (200), (220), and (311) crystal planes

forming the facets. In comparison to the pure Pd/C (JCPDS 89-4897), the four characteristic peaks of PdNi/C are noticeably shifted toward higher diffraction angles, suggesting the formation of Pd/Ni alloyed nanostructures. Moreover, a single pure Pd peak was not detected, indicating that all the Pd is in the alloyed state.

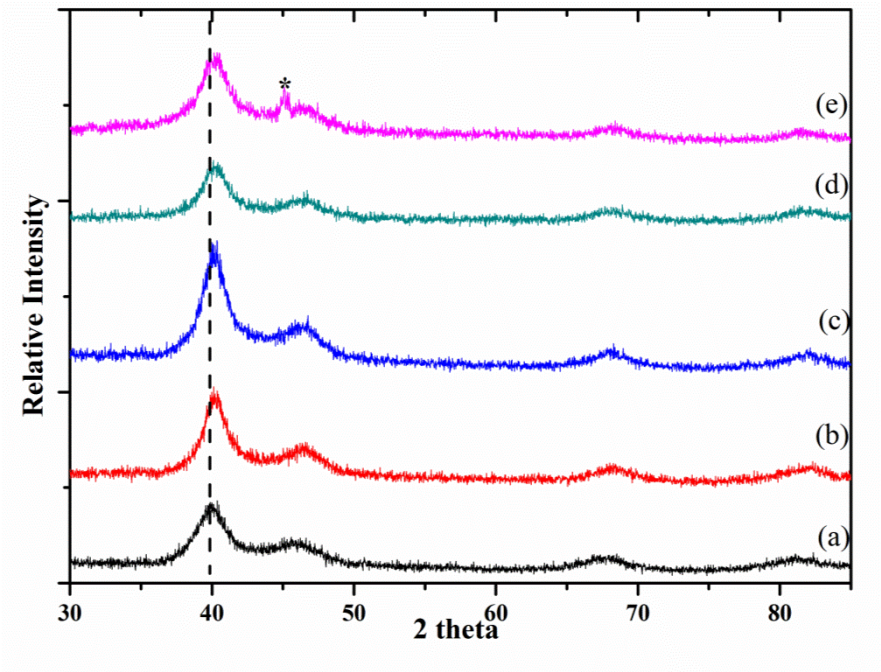

Figure 5.3 XRD patterns of the synthesized nanoparticles: (a) "homemade" Pd/C, (b-e) PtNi hollow nanoparticles with various Pt/Ni products: (b) to (e) $Pd_{0.5}Ni_1$/C Pd_1Ni_1/C, Pd_2Ni_1/C, and Pd_3Ni_1/C.

Products with various mole ratios were also examined by XRD. The positions of the four characteristic peaks of the PdNi alloyed nanostructures (40.7°, 47.3°, 69.3°, and 82.8° (2θ)) are almost unchanged, regardless of variation in the Pd precursor concentration, revealing that the fractions of Ni atoms alloyed with Pd atoms were the same (~ 22%, Table 5.1). A single Ni peak (marked with the star symbol) which could be assigned to the (111) planes of the face-centered-cubic (fcc) nickel (JCPDS No. 04-0850) is detected when the precursor ratio of Pd to Ni is decreased to 0.5:1, revealing that some Ni still remains unconsumed in the final products.

5.3.4 Metal Contents Analysis

The metal composition of the final products was determined through using the ICP-MS and also calculated from the result of the XRD using the Vegard's Law by calculating the lattice parameters of the major three phase of the PdNi alloy and the results were shown in Table 5.1. As could been seen, the final Pd/Ni ratios in the products are mostly around 3.0-3.7:1, decreasing as the molar ratio of Pd to Ni decreases in the precursor. When the Pd/Ni precursor ratio was 0.5:1, the results derived from XRD show that the Pd/Ni molar ratio is 2.89 in the alloyed PdNi nanoparticles, excluding the presence of Ni nanocrystals. When considering the existence of unconsumed Ni, the ICP-MS shows a more accurate ratio of Pd:Ni, which is about 0.53.

Table 5.1. Summary of metal contents derived from ICP-MS and XRD.

Precursors	**Derived from ICP-MS**	**Derived from XRD***		
Pd/Ni mole ratio		Lattice Constant (Å)	Pd mole fraction	Pd/Ni mole ratio
3	3.44	3.812	78.92	3.74
2	3.32	3.802	76.22	3.20
1	3.06	3.798	75.13	3.04
0.5	0.53	3.795	74.32	2.89

*

The lattice parameters were the average lattice spacings calculated from the three major reflections ((111), (200), and (220)) of the alloyed nanoparticles; the Pd molar fraction were obtained assuming Vegard’s law.

5.3.5 Electrochemcial Catalytic ORR Performance of Synthesized

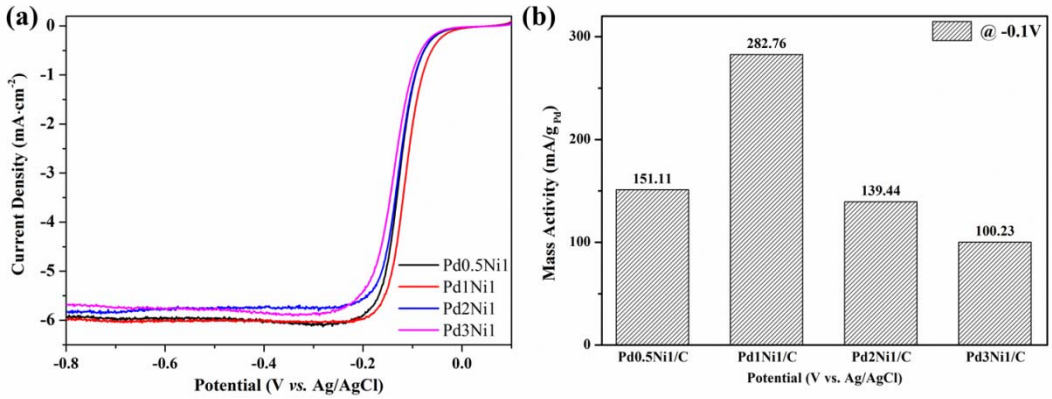

Figure 5.4 (a) ORR polarization curves and (b) Mass activities of the synthesized PdNi hollow nanoparticles with different precursor molar ratio at –0.1V.

To qualify the electroactivities of the PdNi/C ssynthesized with different precursor molar ratio, the solid state ORR polarisation curves and the kinetic mass current density were obtained. (Figure 5.4) The onset potential and half-wave potential of the Pd_1Ni_1/C (synthesized from the precursor molar ratio of Pd/Ni=1/1) is obviously positive than other three products synthesized from different precursor molar ratios indicating the Pd_1Ni_1/C had a higher ORR catalytic activity than the other three products.(Figure 5.4a) The mass activity also revealed the similar trends on the ORR activities of the various products, the mass activity the Pd_1Ni_1/C is 282.76 mA g^{-1}_{Pd}, which is significantly higher than those of the other products activities (151.11, 139.44, and 100.23 mA g^{-1}_{Pd} for $Pd_{0.5}Ni_1/C$, Pd_2Ni_1/C, and Pd_3Ni_1/C respectively at −0.1 V (vs. Ag/AgCl)). The enhanced ORR activity of the Pd_1Ni_1/C can be ascribed to the optimized hollow structures with porous shells of Pd_1Ni_1nanoparticles compared with the other three products.[2] Thus in this chapter, the Pd_1Ni_1 nanoparticles was further characterized in detail and made comparisons with the commercial E-Tek Pt/C and homemade Pd/C electrocatalysts to study the differences of the electrocatalytic ORR abilities.

5.3.6 Morphology Analysis of the Pd_1Ni_1 Nanoparticles

Morphologies of the Pd_1Ni_1 nanoparticles thus produced were examined by TEM (Figure 4.2a and b). It is clear that the nanoparticles are mostly well dispersed, with the shell color much darker than the inside core, suggesting hollow-featured nanostructures. The average diameter of the hollow spheres is ca. 30 nm, and the shell thickness of 5-7 nm. Another feature of the hollow nanoparticles is that their shells are constructed from numerous discontinuous grains (crystalline alloy particles (Figure 4.2c) with an average size of 3-5 nm, which indicates that the shells are incomplete and porous. This mechanism could be explained by the faster reaction kinetics of Pd/Ni, as proposed in our previous report.[27] The selected area electron diffraction (SAED) pattern (inseted, Figure 4.2b)) indicates that the nanoparticles are polycrystalline nanocrystals with a face-centred-cubic (*fcc*) structure. The *d*-spacing of lattice fringes determined from the HR-TEM images (Figure 4.2d) is 0.216 nm, corresponding to the (111) planes of the PdNi alloy nanostructure.

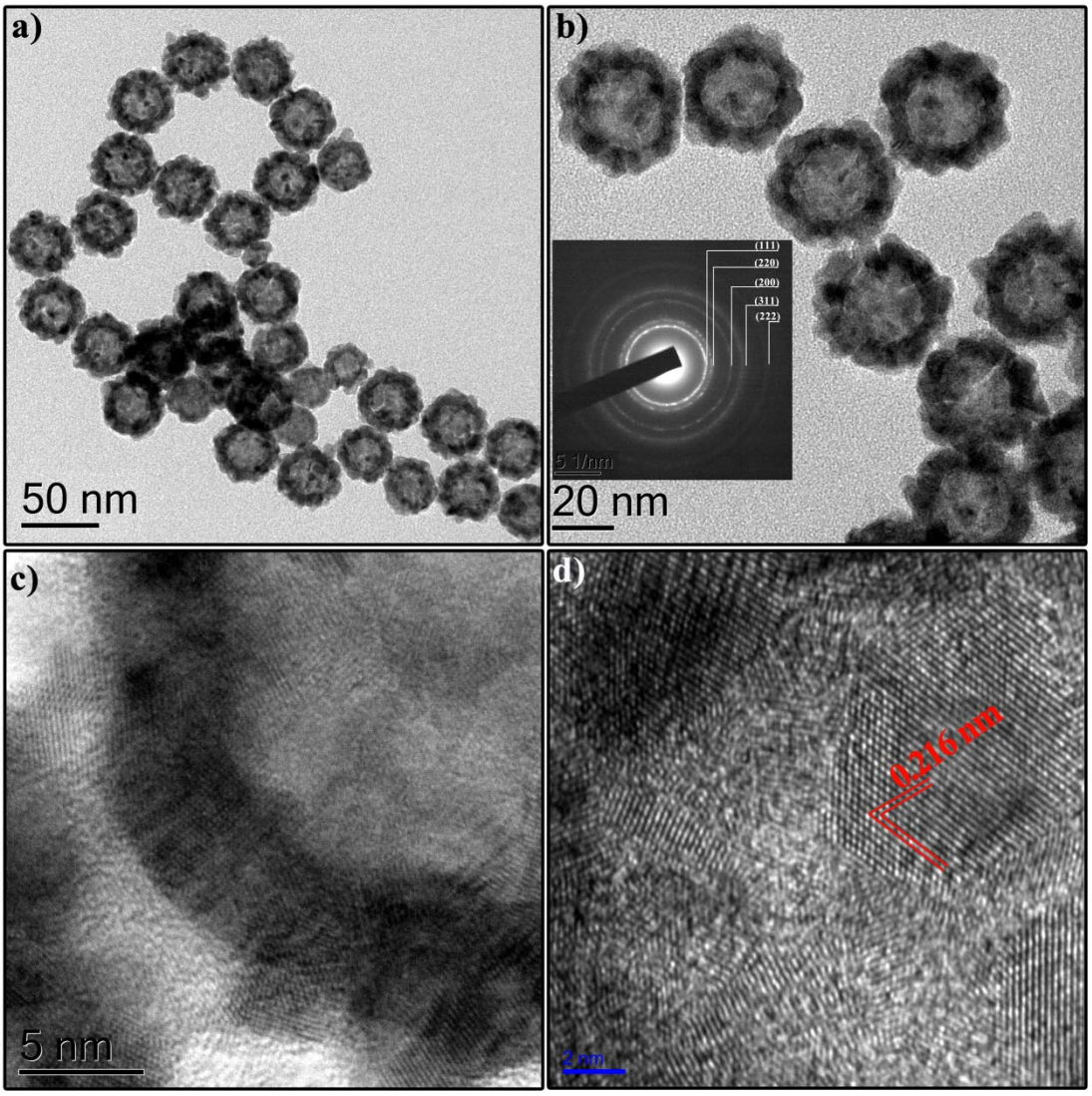

Figure 5.5 (a) low magnification TEM image and (b) high magnification TEM image of the Pd_1Ni_1 hollow nanoparticles, inset: corresponding SAED pattern ; (c) representative high resolution (HR) TEM image d) Ultra high resolution (UHR) TEM images showing with lattice spacing of the hollow Pd_1Ni_1 nanoparticles.

5.3.7 Element Analysis of the Pd_1Ni_1 Nanoparticles

The high-angle annular dark-field imaging (HAADF)-STEM image of the Pd_1Ni_1 hollow nanparticles (Figure 5.6 a) further confirmed the as synthesized nanoparticle are hollow shaped with uniform size about 25 nm. The probe-corrected HAADF-STEM EDS line scan analysis (Figure 5.6 b) was further used to determine the elemental

distribution within the nanoparticles. As is shown, Pd and Ni are both distributed through the particles, with more Pd aggregated on the shell. In addition, more of the elements were detected on the shell than in the core, reflecting the formation of a hollow shape.

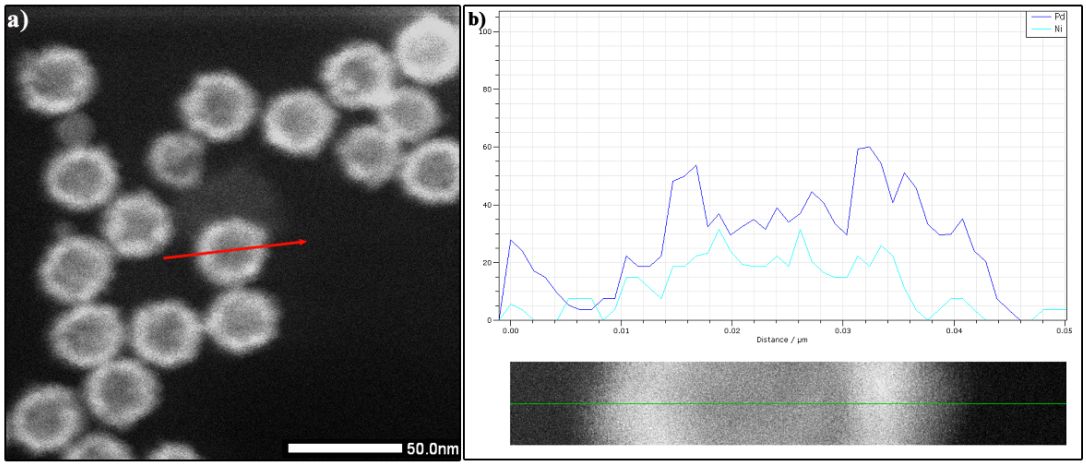

Figure 5.6 a) High-angle annular dark-field imaging (HAADF)-STEM image of the Pd_1Ni_1 hollow nanparticles and b) Probe corrected EDS line scan profile of the Pd_1Ni_1 nanoparticle indicated in a).

5.3.8 X-ray Photoelectron Spectroscopy Analysis of the Pd_1Ni_1 Nanoparticles

X-ray Photoelectron Spectroscopy (XPS) was employed to acquire important information on the composition as well as the electronic state of the metals component in the nanoparticles (Figure 5.7). It could be seen all the element were presenting in the XPS spectra except Ni, which is possibly due to the Ni was under the skin of Pd. Considering XPS is a surface sensitive technique, it was understanding that nickel was not detected using the XPS analysis. The narrowed XPS was employed to investigate the electronic environment of Pd in the hollow Pd_1Ni_1 nanoparticles (Figure 5.7b). The two peaks around the binding energies of 341 and 336.5 eV are assigned to the Pd $3d_{3/2}$ (high-energy band) and $3d_{5/2}$ (low-energy band), reveal that Pd is metallic Pd(0) in the

alloyed nanostructures.[31] When compared to data for pure Pd/C, the binding energy is lowered by ca. 0.8 eV , clearly showing the changes in the electronic structure of Pd, possibly due to the charge transfer between Ni and Pd in the alloyed shell.[12]

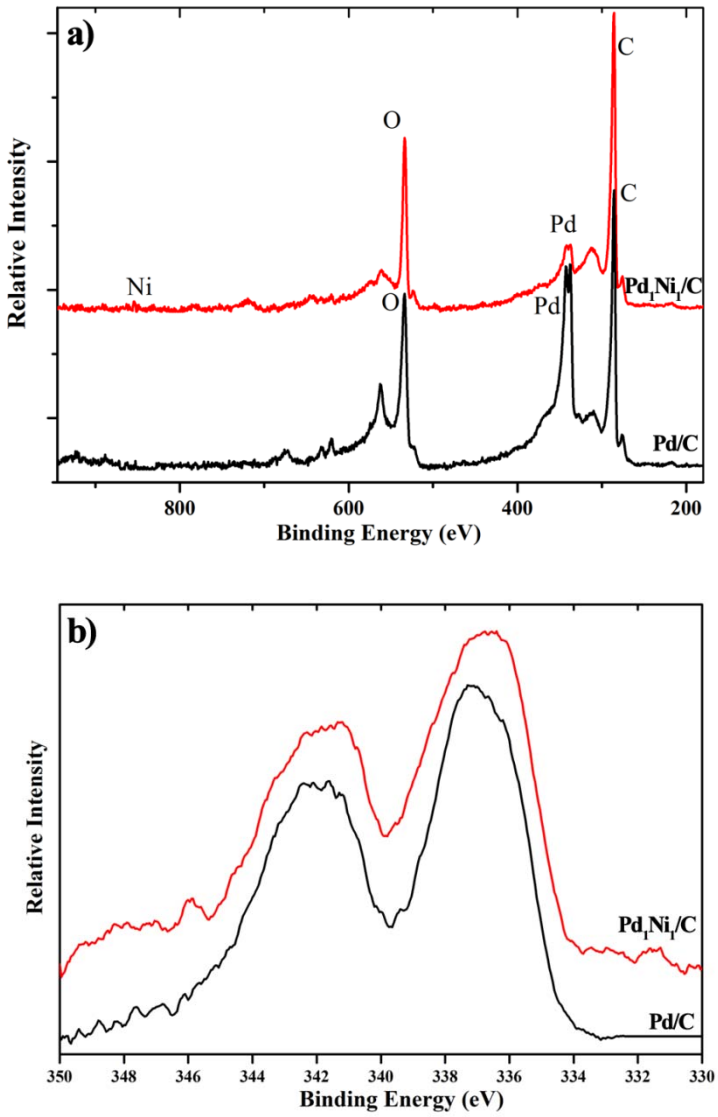

Figure 5.7 a) XPS spectra and b) Narrowed scan of Pd 3d of Pd_1Ni_1/C and "homemade" Pd/C

5.3.9 Cyclic Voltammetry Measurement

CV traces were obtained and used for a preliminary study of the electrochemical properties of the synthesized Pd_1Ni_1/C, Pd/C, and E-Tek Pt/C (Figure 5.8).The CVs are consistent with typical characterized CV regimes of Pd or Pt: typical hydrogen

underpotential adsorption/desorption peaks in the potential range of -0.9 to -0.6 V; a double-layer capacitance region from -0.6 to -0.4 V; and metal oxidation/reduction peaks in the range between -0.3 and 0.1 V. The electrochemical surface active area (ECSA) was calculated based on the charge transfer in the metal reduction region at around – 0.25 (vs. Ag/AgCl), subtracting the double layer correction and assuming 0.405 mC cm^{-2} for the reduction of a monolayer of PdO on the catalyst surface and 0.210 mC cm^{-2} for the reduction of a monolayer of PtO.[2] The ECSAs are 48.1 and 44.5 $m^2g^{-1}_{Pd}$ for Pd_1Ni_1/C and Pd/C, and 59.7 $m^2g^{-1}_{Pd}$ for Pt/C. Although the particle size of Pd_1Ni_1/C is much larger than that for Pd/C, it still shows a slightly higher ECSA than that of the Pd/C, mainly because of its hollow and porous characteristics.

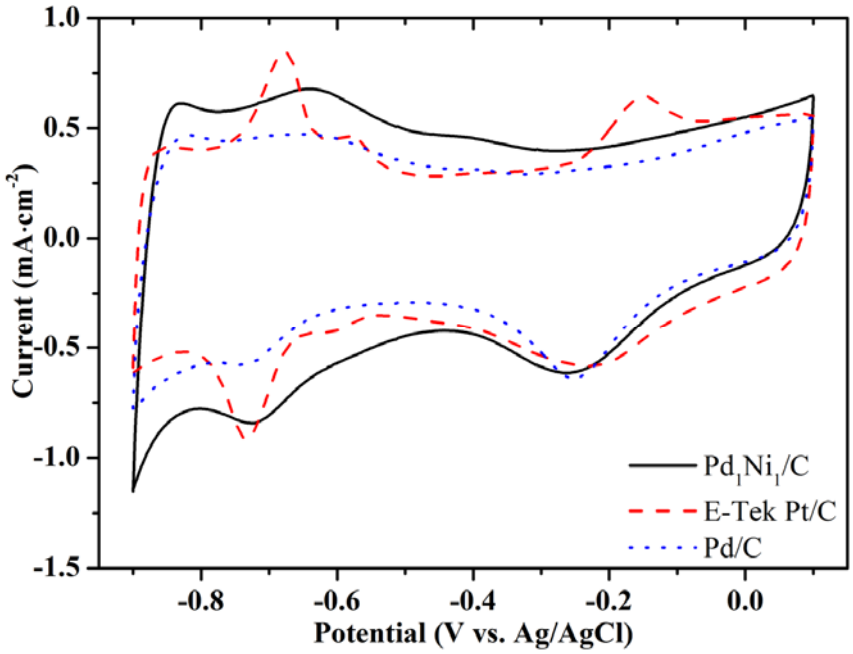

Figure 5.8 CVtraces of the Pd_1Ni_1/C, home-made Pd/C, and commercial E-Tek Pt/C.

5.3.10 Performance of Electrocatalytic Oxygen Reduction Reaction

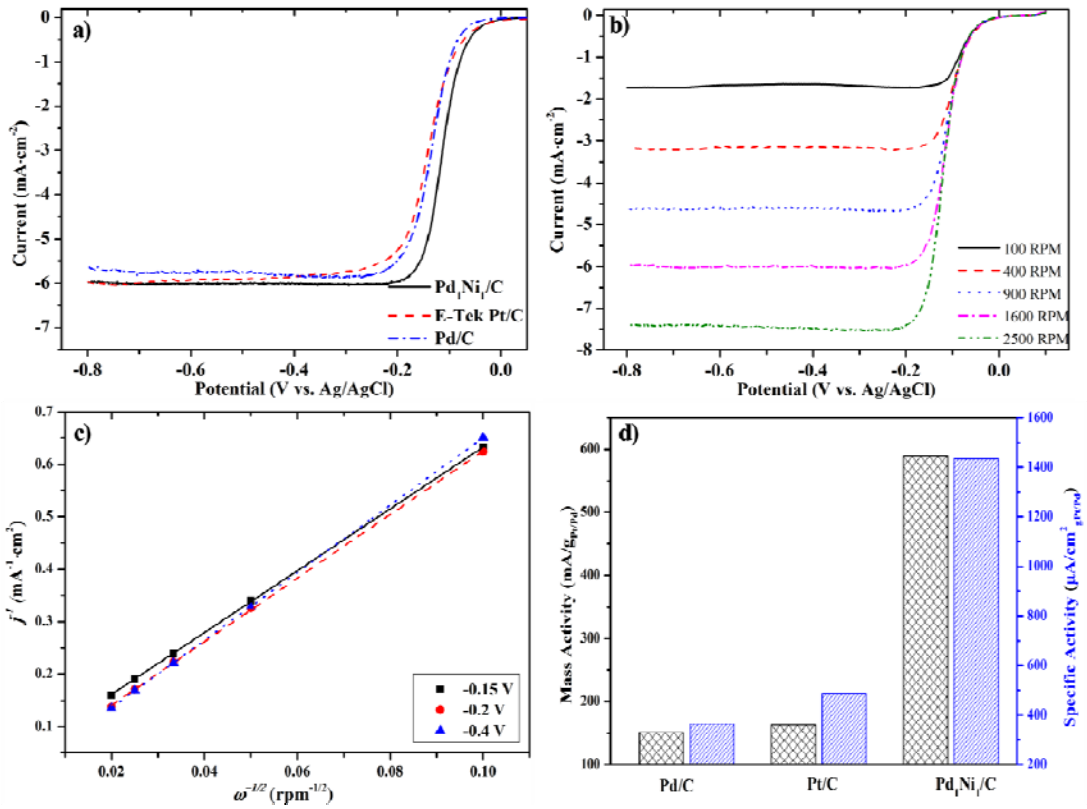

Figure 5.9 a) ORR polarization curves of the Pd_1Ni_1/C, home-made Pd/C, and commercial E-Tek Pt/C. (b) ORR polarization curves of the Pd_1Ni_1/C at various rotation rates. (c) K-L plots derived from the ORR curves of the Pd_1Ni_1/C at different potentials. (d) Mass activities and specific activities of the Pd1Ni1/C, Pd/C, and E-Tek Pt/C at -0.1 V.

The thin film rotating-disk electrode (TF-RDE) technique was used to study the ORR activities and kinetics at the Pd_1Ni_1/C, Pd/C, and commercial Pt/C electrodes. Figure 5.9a shows the ORR polarization curves of these catalysts obtained at a rotation speed of 1600 rpm. All the polarization curves display a well-defined diffusion-limiting current region from –0.8 V - –0.2 V and a mixed kinetic-diffusion control region from 0.05V - –0.2 V. The half-wave potential of the Pd_1Ni_1/C for the ORR is –0.114 V (RSD=1%), which is slightly higher than that of Pt/C (–0.117 V, RSD=1%) and much

more positive than that of Pd/C (–0.135 V, RSD=1%), indicating the hollow shaped Pd_1Ni_1 nanoparticles feature a significant enhancement in the electrocatalytic ORR in an alkaline medium compared with Pd/C or commercial Pt/C.

In order to obtain the kinetics of the ORR, ORR polarization curves were collected at various rotation speeds (Figure 5.9b) and corresponding Koutecky-Levich (K-L) plots (Figure 5.9c) were drafted from the ORR polarization curves at different potentials. The number of electrons involved per O_2-molecule reduction can be determined using the Koutecky-Levich (K-L) equation

$$j = 1/j_k + 1/B\omega^{0.5};$$

$$[B = 0.2n\mathrm{F}(D_{O2})^{2/3}(v)^{-1/6}C_{O2}]$$

where, j_k is the kinetic current, ω is the electrode rotation rate, n is the transferred electron number, F is the Faraday constant (F = 96485 C mol^{-1}), D_{O2} is the diffusion coefficient of O_2 = 1.9×10^{-5} cm^2 s^{-1}, v is the kinetic viscosity (0.01 cm^2 s^{-1}), and C_{O2} is the bulk concentration of O_2 (1.2×10^{-6} mol cm^{-3}). The constant 0.2 is adopted when the rotation speed is expressed in rpm. The transferred electron number was calculated to be 4.20 – 4.40 at around –0.15 - –0.4 V, revealing that the ORR from 0.15 - –0.4 V is dominated by a four-electron (4e) pathway and that O_2 is reduced to OH^- during the reaction.

To study the electroactivities of the PdNi/C, Pd/C, and Pt/C in detail, the kinetic current has been calculated from the ORR polarization curves by considering the mass-transport correction using the Levich-Koutecky equation ($1/i = 1/i_k + 1/i_d$, where i_k is the kinetic current and i_d is the diffusion limited current), which is normalized against and then normalized to the mass and specific area of Pd or Pt to compare the mass activities and specific area activities of the catalysts. The mass activity and the specific area activity of the Pd_1Ni_1/C is 588.97 mA g^{-1}_{Pd} and 1434 μA cm^{-2}, which is

3.89 and 3.92 times higher than those of Pt/C or Pd/C, respectively, indicating the significant improvement of ORR catalytic activity for the hollow Pd_1Ni_1. Comparing with Pt/C (151.3 mA g^{-1}_{Pd}) or Pd/C (162.96 mA g^{-1}_{Pd}), we infer that the enhanced ORR activity of the PdNi/C can be ascribed to the unique hollow alloyed structures with porous shells of nanoparticles. Moreover, the changes in the surface electronic features through the introduction of a second metal to Pd would also contribute to the increased activity.[2]

5.3.11 Poison Resistance Ability Test

The selectivity to methanol of the catalysts is a key factor in the real application for fuel cells, because the relative small methanol molecular would cross through the membrane and react with the catalysts in the cathodes causing poor ORR performance and further reducing the cell efficiency.[23] To this end, the selectivity of Pd_1Ni_1/C, E-Tek Pt/C and Pd/C were compared through chronoamperometric measurements at the rotating speed of 1600 rpm at − 0.3 V with introduction of methanol at 200s as displayed in Figure 5.10. A stable current was observed for both catalysts revealing the ORR performance of them were comparative. However, after the addition of methanol, a distinct change on current was observed for the Pt/C and Pd/C catalyst indicating methanol oxidation occurred, i.e., the selectivity of the Pd/C or Pt/C was poor. In contrast, for Pd_1Ni_1/C, the current remained nearly unchanged after the addition of methanol reflecting its superior selectivity and better methanol tolerance.

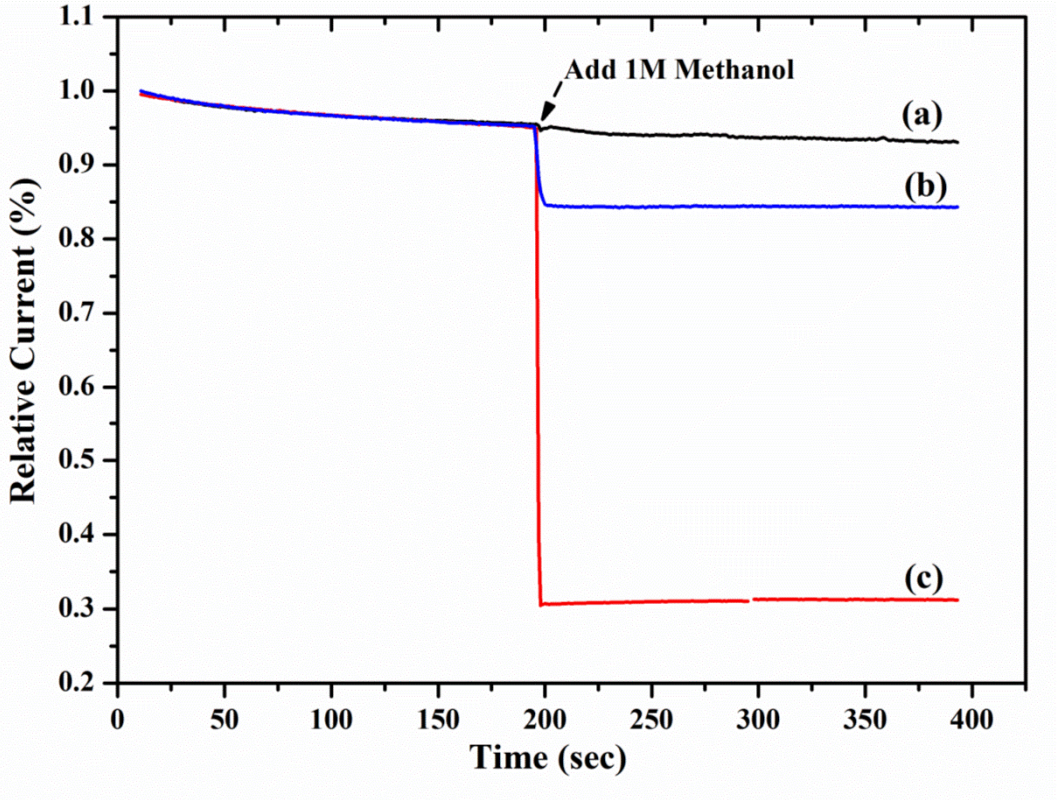

Figure 5.10 Chronoamperometric responses of the electrocatalysts a) Pd_1Ni_1/C, b) Pd/C and c) E-Tek Pt/C at – 0.2 V with rotation rate of 1600 rpm. ORR curves and chronoamperometric responses were measured in O_2-saturated KOH(aq) (0.1 mol L^{-1}) solution with a scan rate of 10 mV s^{-1} with the addition of methanol at 200 s

5.3.12 Stability Tests

A chronoamperometric study was conducted to determine the durability of the catalyst for the ORR (Figure 5.11). During the long (~ 8000 s) ORR test at -0.2 V, a 5% current loss for the hollow shaped Pd_1Ni_1/C was observed. In contrast, for Pd/C or commercial Pt/C, the current losses under identical conditions are more than 10%. These results clearly indicate the hollow PdNi/C is much more stable than the commercial Pt/C or Pd/C in terms of the catalytic activities of oxygen.

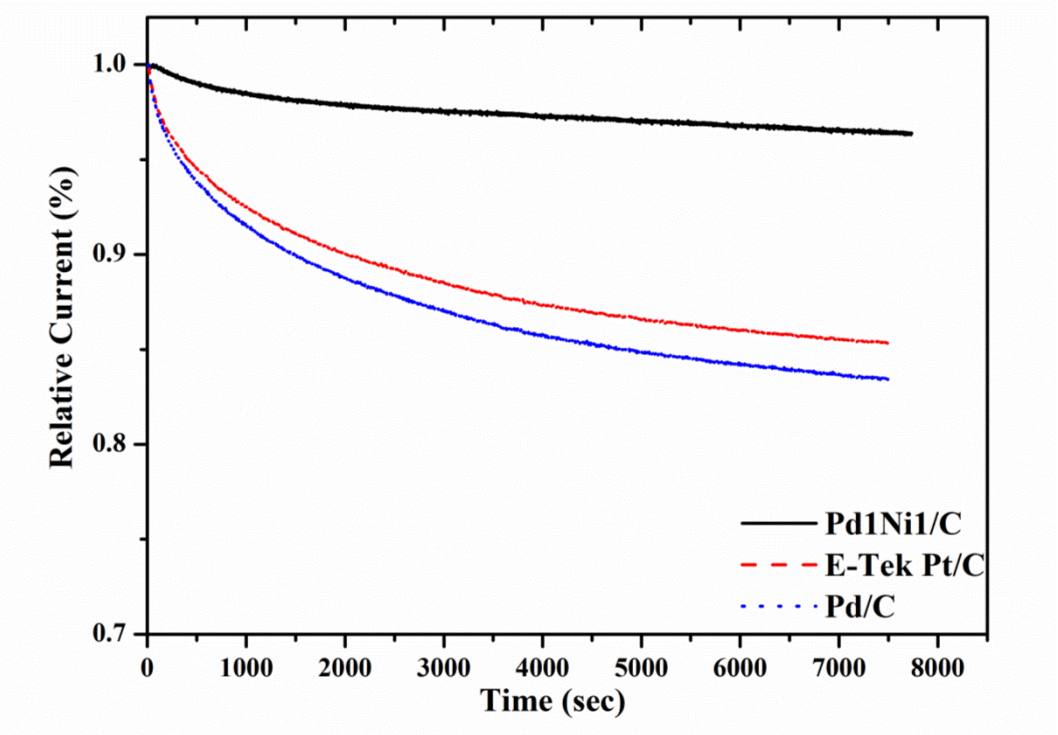

Figure 5.11 Chronoamperometric responses of the electrocatalysts at -0.2 V with rotation rate of 1600 rpm. ORR curves and chronoamperometric responses were measured in O_2-saturated KOH(aq) (0.1 mol L^{-1}) solution with a scan rate of 10 mV s^{-1}

5.3.13 Single Anion Exchange Membrane Fuel Cell Test

The TF-RDE technique is useful for identifying candidate materials but tests operated under conditions that are much closer to fuel cell operating conditions are necessary to demonstrate the practical performances of the electrocatalysts,. Anion exchange membrane fuel cell tests as described previously[5] were carried out in order to evaluate the performance of the catalysts in a practical environment. Figure 5.12 shows the polarization curves and power density curves of AEMFC tests with commercial E-Tek Pt/C and Pd_1Ni_1/C cathode catalysts, respectively. The peak power density obtained with the commercial E-Tek Pt/C electrocatalysts is 92 mW cm^{-2} at the loading of 0.4 mg cm^{-2}, which is compatible to the previous results.[5] Under the same testing conditions, the hollow Pd_1Ni_1/C electrode exhibits much higher power density and current density

than those with Pt/C. The peak power density of the hollow Pd_1Ni_1/C electrode obtained at 0.4 V is 150 mW cm^{-2}, which is more than 1.7 times higher than that with the commercial Pt/C (90 mW/cm^2). In addition, at 0.4V the current density of the hollow Pd_1Ni_1/C is 375 mA cm^{-2}, which is 1.5 times larger than that of the Pt/C at the same voltage (current then 240 mA cm^{-2}). These results, which are consistent with the RDE results (Figure 5.9a), provide clear evidence to suggest that the Pd_1Ni_1/C electrocatalysts have the potential to perform as more promising and efficient electrocatalysts in alkaline membrane fuel cells (a working, real environment) when compared with state-of-the-art commercial Pt/C electrocatalyst.

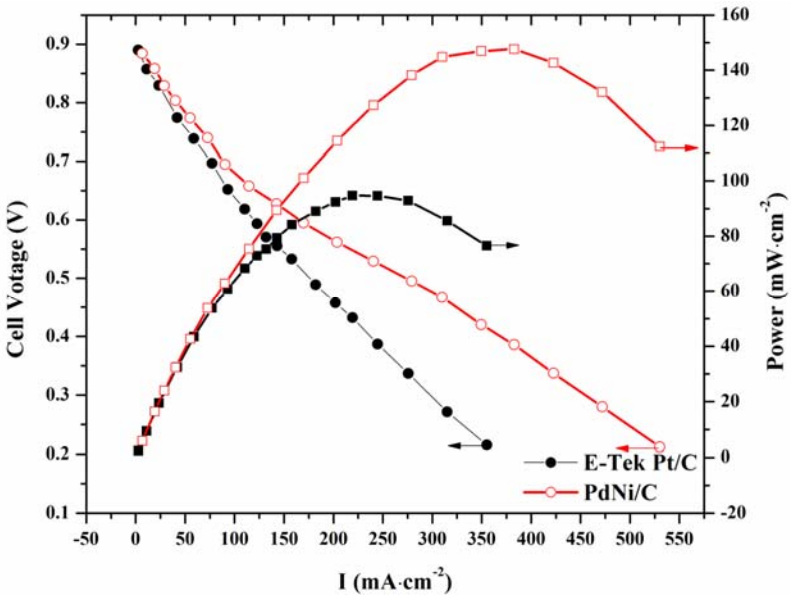

Figure 5.12 AEMFC polarization curves (round symbols) and power density curves (square symbols) of a single cell test using E-Tek Pt/C (filled symbols) and PdNi/C (hollow symbols) as cathode catalysts with a loading amount of 0.4 mg cm^{-2}. Operating conditions: cell temperature 60°C, humidifier temperatures 60°C for both H_2 and O_2, flow rate 0.08 L min^{-1}, and back pressure 15 psi for both H_2 and O_2

5.4 Conclusion

In this chapter, with the method we have developed in synthesized hollow PtCu which was described in last chapter, we continuously use the modified galvanic replacement method synthesizing the hollow PdNi hollow nanoparticles with porous features, it was also found the concentration between the ratios of precursor plays important role in determining the structure of final products. The TEM confirmed the formation of porous hollow shape, the EDS and XRD confirmed the alloyed nature of the nanoparticle consisting of both Pd and Ni elements. The XPS results give further evidence in the change of electronic structure of Pd owing to the introducting of Ni into the Pd atoms, which may cause the enhancement of the catalysts' performance.

Electrochemical tests revealed the hollow PdNi nanparticles could work more efficient electrocatalysts compared with the commercial Pt/C or Pd/C with more stable and selective in the basic environment for the AEMFC. At last the single fuel cell tests also evidenced the electrocatalysts could work practicable electrocatalysts with much lower cost. The enhanced performance was ascribed to the change of electronic and geometric structure of Pd due to the introducing Ni into Pd atoms and the hollow features of the electrocatalysts which could provide large surface area and ample active sites for oxygen reduction thus facilitating the ORR process.

To further reduce the cost of the ORR catalysts, the synthesis of noble-metal free electrocatalysts with comparable electrocatalytic activities, better methanol tolerance and longer stability has been devoted into many efforts in recent decades. The heteroatoms doped carbon has been recognised as one of the most promising electrocatalysts for the ORR as they offer comparable electrocatalytic performance, low cost and much better stability compared with the commercial Pt/C. In the later chapters of this study, we will demonstrate the synthesis of non-noble metal based

electrocatalysts using nitrogen doped graphene or using transition metal oxides, cobalt oxides as catalytic sites and explore their applications in the catalytic ORR in alkaline medium. Initial research on these non-noble metal electrocatalysts involves the synthesis of nanostructured porous nitrogen doped graphene with well controlled nitrogen doping level and configuration, which is derived from the vapour phase polymerisation of PPy on graphene aerogel following by heat treatment and the synthesized nitrogen doped crumpled graphene showed comparable electrocatalytic ORR performance compared with the commercial Pt/C. Further, to improve the catalytic performance of the nitrogen doped graphene, we incorporated cobalt /cobalt metal oxides onto the doped graphene aerogel through a facial hydrothermal synthesis method and the electrochemical results showed the as-synthesized cobalt /cobalt oxides based electrocatalysts showed improved electrocatalytic ORR performance compared with the pure nitrogen doped graphene aerogel and with similar electrocatalytic performance with the Pt/C.

5.5 References

1. Sekol, R.C., X. Li, P. Cohen, G. Doubek, M. Carmo, and A.D. Taylor, Applied Catalysis, B: Environmental, 2013. **138–139**(0): p. 285-293.
2. Zhang, Z., K.L. More, K. Sun, Z. Wu, and W. Li, Chemistry of Materials, 2011. **23**(6): p. 1570-1577.
3. Gu, S., R. Cai, T. Luo, Z. Chen, M. Sun, Y. Liu, G. He, and Y. Yan, Angewandte Chemie, International Edition, 2009. **48**(35): p. 6499-6502.
4. Varcoe, J.R., R.C.T. Slade, and E. Lam How Yee, Chemical Communications (Cambridge, United Kingdom), 2006. **0**(13): p. 1428-1429.

5. Varcoe, J.R. and R.C.T. Slade, Electrochemistry Communications, 2006. **8**(5): p. 839-843.

6. Deavin, O.I., S. Murphy, A.L. Ong, S.D. Poynton, R. Zeng, H. Herman, and J.R. Varcoe, Energy & Environmental Science, 2012. **5**(9): p. 8584-8597.

7. Shim, J.H., J. Kim, C. Lee, and Y. Lee, Chem. Mater., 2011. **23**: p. 4694-4700.

8. Sun, W., A. Hsu, and R. Chen, Journal of Power Sources, 2011. **196**(10): p. 4491-4498.

9. Koenigsmann, C., A.C. Santulli, E. Sutter, and S.S. Wong, ACS Nano, 2011. **5**(9): p. 7471-7487.

10. Halder, A., S. Patra, B. Viswanath, N. Munichandraiah, and N. Ravishankar, Nanoscale, 2011. **3**(Copyright (C) 2012 American Chemical Society (ACS). All Rights Reserved.): p. 725-730.

11. Lee, K., S.W. Kang, S.U. Lee, K.H. Park, Y.W. Lee, and S.W. Han, ACS Applied Materials & Interfaces, 2012. **4**(8): p. 4208-4214.

12. Chen, L., H. Guo, T. Fujita, A. Hirata, W. Zhang, A. Inoue, and M. Chen, Advanced Functional Materials, 2011. **21**(22): p. 4364-4370.

13. Zhang, L., F. Hou, and Y. Tan, Chemical Communications (Cambridge, United Kingdom), 2012. **48**(57): p. 7152-7154.

14. Caixia, X., Z. Yan, X. Liqiang, B. Xiufang, M. Houyi, and D. Yi, Chemistry of Materials, 2009. **21**(14): p. 3110-3116.

15. Fouda-Onana, F., S. Bah, and O. Savadogo, Journal of Electroanalytical Chemistry, 2009. **636**(1-2): p. 1-9.

16. Shih, Z.-Y., C.-W. Wang, G. Xu, and H.-T. Chang, Journal of Materials Chemistry A, 2013. **1**(15): p. 4773-4778.

17. Neergat, M., V. Gunasekar, and R. Rahul, Journal of Electroanalytical Chemistry, 2011. **658**(1-2): p. 25-32.

18. Shao, M.-H., K. Sasaki, and R.R. Adzic, Journal of the American Chemical Society, 2006. **128**(11): p. 3526-3527.

19. Fernández, J.L., V. Raghuveer, A. Manthiram, and A.J. Bard, Journal of the American Chemical Society, 2005. **127**(38): p. 13100-13101.

20. Slanac, D.A., W.G. Hardin, K.P. Johnston, and K.J. Stevenson, Journal of the American Chemical Society, 2012. **134**(23): p. 9812-9819.

21. Kim, J.-H., W.W. Bryan, H.-W. Chung, C.Y. Park, A.J. Jacobson, and T.R. Lee, ACS Applied Materials & Interfaces, 2009. **1**(5): p. 1063-1069.

22. Koenigsmann, C., E. Sutter, R.R. Adzic, and S.S. Wong, Journal of Physical Chemistry C, 2012. **116**(29): p. 15297-15306.

23. Liu, M., Y. Lu, and W. Chen, Advanced Functional Materials, 2013. **23**(10): p. 1289-1296.

24. Xu, C., L. Wang, R. Wang, K. Wang, Y. Zhang, F. Tian, and Y. Ding, Advanced Materials, 2009. **21**(21): p. 2165-2169.

25. Sun, Y. and Y. Xia, Journal of the American Chemical Society, 2004. **126**(12): p. 3892-3901.

26. Zhang, W., M. Wang, J. Chen, T. Romeo, A.T. Harris, and A.I. Minett, Electrochemistry Communications, 2013. **34**(0): p. 73-76.

27. Wang, M., W. Zhang, J. Wang, A. Minett, V. Lo, H. Liu, and J. Chen, Journal of Materials Chemistry A, 2013. **1**(7): p. 2391-2394.

28. Yang, J., X. Chen, X. Yang, and J.Y. Ying, Energy & Environmental Science, 2012. **5**(10): p. 8976-8981.

29. Li, H., Z. Zhu, J. Liu, S. Xie, and H. Li, Journal of Materials Chemistry, 2010. **20**(21): p. 4366-4370.

30. Yang, L., C.-G. Hu, J.-L. Wang, Z.-X. Yang, Y.-M. Guo, Z.-Y. Bai, and K. Wang, Chem. Commun. , 2011. **47**(30): p. 8581-8583.

31. Zhu, L.D., T.S. Zhao, J.B. Xu, and Z.X. Liang, Journal of Power Sources, 2009. **187**(1): p. 80-84.

Chapter 6

Nitrogen Doped Crumpled Graphene Derived from Vapor Phase Deposition of PPy on Graphene Aerogel as Efficient Oxygen Reduction Reaction Electrocatalysts

6. **CONTENTS**

Chapter 6

6.1 Introduction

Previous chapter has shown PdNi hollow nanoparticle could work as the improved electrocatalytic oxygen reduction reaction (ORR) electrocatalysts, while to further reduce the cost of the electrocatalysts, synthesis of non-noble metal based electrocatalysts has become a necessarily in the real-world application. Recent advances in synthesis of heteroatoms (nitrogen,[1, 2] boron,[3-5] sulfur,[6-9] phosphorus,[10, 11] etc.) doped graphene suggested that the doped carbon could be used to replace the high-cost platinum (Pt) as efficient and "poison"-resistant electrocatalysts for the oxygen reduction reaction (ORR), which is recognized as a kinetically limited step in fuel cells and metal-air batteries due to the sluggish reaction mechanism.[12, 13] The chemically converted graphene[14-16], owing to the ease of preparation and processing, has been extensively used for doping through chemical vapor deposition,[17] thermal annealing with nitrogen-contained precursors at high temperatures[2, 5, 6, 9, 18-20], hydrothermal reactions at relatively low temperatures[8, 12, 21, 22] or nitrogen plasma treatment.[23, 24] During the doping of foreign atoms, the alternation of the spin density and charge distribution on carbon could effectively improve the chemical and electronic properties of pristine graphene sheets thus producing enhanced performance electrocatalysts for the ORR.[5, 6, 22, 25] However, the chemically derived graphene sheets are vulnerable to stack and aggregate during the reduction or drying processes due to the strong van der waals and hydrogen bonding between water molecular and graphene sheets[26, 27]. This irreversible stack would decrease the specific surface area, cause the losses of active sites and further hamper uniform doping thereby compromising the overall properties of the electrocatalysts.[16, 18, 26-39]

In light of this, the integration of the plane sheets into designed 3D graphene macroscopic structures becomes a key process in further widening the application of

graphene for practical electrochemical devices because the resulted 3D structures could prevent the flat sheets from largely aggregating, providing them with large surface areas and ample active sites for electrocatalytic reactions.[16, 18, 26-38] The graphene hydrogel (GH)/aerogel (GA), synthesized *via* a feasible self-assembly hydrothermal method, represents a novel class of 3D macroporous graphene architectures with good mechanical properties.[19, 21, 33, 34, 40] As was dicussed by Shi. et.al, at high temperature (above 180 °C), the self-assemble of graphene hydrogel was possibly driven by stacking interactions of graphene sheets and during the hydrothermal process, the noncovalent cross-links of the graphene sheets were partly dissociated through the parallel sliding between graphene sheets, leading to the substantial decrease in viscosity of the graphene oxide and thereby forming GH. [32] The 3D interconnected macropores could offer more active sites, multiple electron and ion transport pathways and easy access to the oxygen and electrolyte thus minimizing the ions and electrons transfer resistance between bulk electrode and electrolyte.[8, 19, 21, 32, 34, 40-43] These features clearly suggest that graphene hydrogel or aerogel as a macroporous 3D nanostructure aerogel could be perfectly qualified as candidates for the ORR upon doping.

Despite many notable achievements in producing doped graphene 3D nanostructures, [2, 19, 21, 44] there are still certain issues need to be addressed, ranging from the doping process to the post-treatment process. For instance, the high temperature thermal annealing GA with nitrogen source would also unexpectedly cause the stack of graphene sheets in the GA due to the remaining π-π interactions and H-bonds between graphene sheets[32] thus further hampering uniform doping.[17-19] While in-situ hydrothermal reaction doping during the formation of graphene hydrogels proposes a strategy for uniform doping, the nitrogen configuration, which is crucial in

determining catalysts performance, is beyond control.[8, 21, 22] Moreover, these doped 3D monolithic graphene aerogels would be inevitably sonicated and re-dispersed for preparing oxygen reduction electrodes or membranes electrodes assemblies (MEAs) of fuel cells or metal-air batteries[1, 7, 13, 45, 46], at this time the 3D monolithic porous structures would usually be demolished and the dispersed flat sheets in the Nafion® dispersion would easily aggregate when drying on the electrodes which would again decrease the specific surface areas and activated sites of the electrocatalysts.

In this chapter, we demonstrate a two-step synthesis of nitrogen doped crumpled graphene (NCG) first evolved from hydrothermal synthesizing GH and then followed by vapor phase deposition of PPy film on the GA sheets and then introduce the nitrogen species into graphene lattice *via* thermal annealing. The vapor phase polymerization (VPP) is a well-established method in our group to produce inherent conducting polymer films with high conductivities, uniformities at the nanoscale on certain substrates.[47] The uniform PPy coating would effectively inhibit stacking during heat treatment and thus facilitate uniform doping. Besides the crumpled sheets could be produced in the graphene aerogel during the doping process, which makes this architecture as attracting electrocatalysts for preparing oxygen reduction electrodes or MEAs because the micro-3D crumpled feature could be well maintained during post treatment. The electrocatalytic performance towards ORR of the NCG was carefully examined in alkaline medium, showing comparable electrocatalytic activities with Pt/C but with better methanol tolerance and longer durability. At last, we conduct anion exchange membrane fuel cell (AEMFC) tests to acquire the real performance of our catalysts in a practicable environment. To our best knowledge, this is the first AEMFC test using metal-free doped carbon materials as cathodes catalysts. At the same loading level with the commercial Pt/C (10 wt. % Pt on Vulcan XC-72, E-Tek), our catalysts

show a max power output of 63 mW cm^{-2}, reaching 83 % of the max power density of E-Tek Pt/C (76 mW cm^{-2}) suggesting its comparable performance with the Pt/C in practicable environment This result would provide important information on the real performance of the metal-free catalysts and therefore benefit the research in metal-free electrocatalysts for the ORR.

6.2 Experimental

6.2.1 Reagents

Graphite (325 mesh, Sigma), Sulphuric acid (H_2SO_4, concentrated, Ajax Finechem), phosphoric acid (70%, H_3PO_4, Ajax Finechem), Potassium permanganate ($KMnO_4$, Sigma), hydrogen peroxide (H_2O_2, Sigma), Hydrochloric Acid (33%, HCl, Ajax Finechem), L-ascorbic acid (L-AA, Sigma), Iron (III) p-toluenesulfonate (FeToS, Sigma) , butanol (Sigma), Pyrrole (distilled, Sigma), Urea (Sigma)

6.2.2 Synthesis

Synthesis of Graphene Oxide (GO): GO was prepared from natural graphite flakes (Sigma) using a modified Hummers method, which was described elsewhere.[14, 48] In a typical synthesis, a 9:1 mixture of concentrated H_2SO_4/H_3PO_4 (360:40 mL) was added to a mixture of graphite flakes (3.0 g, 1 wt equiv) and $KMnO_4$ (18.0 g, 6 wt equiv), producinga slight exotherm to 35-40 °C. The reaction was then heated to 50 °C and stirred for 12 h. The reaction was cooled to rt and poured onto ice (400 mL) with 30% H_2O_2 (10 mL). The obtained yellow bright solution was centrifuged (4000 rpm for 4 h), and the supernatant was decanted away. The remaining solid material was then washed in diluted HCl acid and water for 2 times. At last, the solid materials in water was dialysis for 2 weeks with changing water frequently for before use.

Synthesis of Graphene hydrogels (GHs) and Graphene alcogels(GAs): GHs was synthesized by reduction of GO with L-ascorbic acid at mild temperature.[40] In a typical procedure, a 20 mL GO (4 mg mL^{-1}) with 320 mg L^{-1} ascorbic acid solution were mixed and sonicated for 10 min before placing in a water bath at 70 °C for 4 hours. After reduction, GHs were carefully taken out and purified by distilled water for one week. To synthesize GAs, the GHs were directly freeze-dried overnight.

Synthesis of Polypyrrole coated graphene aerogels (PPy-GAs) and NCGs: In order to deposit Iron (III) p-toluenesulfonate (FeToS) (dissolved in butanol(Sigma)), GHs were firstly converted to alcogels by exchanging with ethanol for several times. The synthesized alcogels were soaked into 20 wt. % FeToS butanol solutions for 20 hours, after that alcogels were dried in a conventional oven at 100 °C for 30 minutes to prepare FeToS films on the graphene aerogel sheets. To synthesize PPy-GA, these GAs were placed in sealed flasks saturated with pyrrole (distilled, Sigma) monomer for 1 hour in an oven at 60 °C to polymerized polypyrrole on the GFs sheets. After vapor phase polymerization, the PPy-GAs were washed with copious amount of ethanol and water several times to completely removed unreacted oxidizing agent, pyrrole and butanol. Freeze-drying was used to dehyrate PPy-GA to maxium maintain the 3D structure of PPy-GA. To convert PPy-GAs to NCGs, the purified PPy-GAs were annealed at required temperature for 2 hours with a heating rate of 10 °C /min under the protection of argon (400 sccm).

Synthesis of nitrogen doped graphene aerogel (NGA): The GH was directly submerged into urea water solution with a concentration of 2 mol L^{-1} for 24 hours and then dehydrated with freeze drying without any washing. Then the aerogel was annealled at required temperature as the manner above

6.2.3 Physical Characterisation

SEM images were obtained using a JEOL-7500FA. TEM images, High resolution (HR)-TEM images were collected with a JEOL JEM-2100F transmission electron microscope operated at 80 kV. Scanning transmission electron microscopy (STEM) images and Energy dispersive X-Ray spectrum (EDS) mapping analysis were acquired with a JEOL JEM-ARM200F operated at 80 kV. Samples for TEM, EDS, STEM were prepared by dropping one drop of the catalysts ethanol dispersion on a holy carbon film coated copper grid (200 mesh). Ethanol dispersion was prepared from sonication using a probe sonicator (Brandson S-250D) operated at 50 % aptitude for 1 hour The fourier transform infrared (FTIR) Spectrum were collecting using a Shimadzu FTIR Prestige-21 instrument. The The powder X-ray diffraction (XRD) patterns were collected using a GMC MMA X-ray powder diffractometer with Cu Kα radiation (λ = 1.5418 Å). X-ray photoelectron spectroscopy (XPS) spectra were collected using a Thermo Scientific K-Alpha instrument. Raman spectrums were acquired with a Raman JY HR800 Spectrometer with the excitation laser of 632.18 nm.

6.2.4 Electrochemical Measurements

Electrochemical measurements were performed using the thin film rotating-disk electrode (TF-RDE) technique, as reported elsewhere.[49] The electrocatalysts ink was prepared by dispersing the electrocatalysts in Nafion/H_2O/isopropanol (m/m/m = 0.05/10/50) to obtain a 2 mg ml^{-1} dispersion via a probe sonicator (Brandson S-250D). The thin film electrode was prepared through placing 60 μL of the catalyst ink on a glassy carbon rotating ring disk electrode (RRDE, 0.2475 cm^2, Pine Research Instrumentation). The electrode was then connected to a CHI 720c bipotentiostat (CH Instruments) in a standard three-electrode cell with a Pt-mesh counter electrode and a

KNO_3(aq) saturated (10 wt.%) Ag/AgCl reference. Unless otherwise specified, all the potentials are against Ag/AgCl as reference potential.

The cyclic voltammetry (CV) traces were recorded in N_2 saturated KOH (0.1 mol L^{-1}) solution with a sweep rate of 50 mV s^{-1}. The ORR polarization curves were recorded using a linear sweep voltammetry (LSV) technique in oxygen saturated electrolyte with a sweep rate of 10 mV s^{-1} at various rotation speeds of 100, 400, 900, and 1600 rpm from 0.1 to − 0.8 V. Koutecky-Levich (K-L) plots were drafted from the ORR polarization curves at different potentials. Ohmic drop caused by system resistentce was compensated using atomatic mode within the CHI software.[50] The number of electrons involved per O_2-molecule reduction can be determined using the Koutecky-Levich (K-L) equation

$$j = 1/j_k + 1/B\omega^{0.5};$$

$$[B = 0.2n\mathrm{F}(D_{O2})^{2/3}(v)^{-1/6}C_{O2}]$$

where, j_k is the kinetic current, ω is the electrode rotation rate, n is the transferred electron number, F is the Faraday constant (F = 96485 C mol^{-1}), D_{O2} is the diffusion coefficient of O_2 = 1.9×10^{-5} cm^2 s^{-1}, v is the kinetic viscosity (0.01 cm^2 s^{-1}), and C_{O2} is the bulk concentration of O_2 (1.2×10^{-6} mol cm^{-3}).

Methanol tolerant were carried out through a chronoamperometry technique at the potential of − 0.3 V and with rotation at 1600 rpm with subsquently introducing of oxygen and methanol (0.5 M) at set time. Stability tests were carried out by the chronoamperometry technique at the potential of − 0.3 V with rotation spped at 1600 rpm in oxygen-saturated electrolyte up to 15000 seconds

6.2.5 Single Fuel Cell Test

The anion-exchange membranes used were (graft co-polymerised) using vinylbenzyl chloride and functionalised using trimethylamine (University of Surrey);[51] the membrane used was of type S80, with membrane thickness ≈ 80 μm (thickness depends on hydration level) and ion exchange capacity IEC ≈ 1.3 meq g^{-1}. The anodes and cathodes were prepared as described previously.[51] In brief, the electrocatalyst ink prepared with ca. 15 wt.% poly(vinybenzyl chloride) dissolved in ethyl acetate were sprayed on the gas diffusion layers (GDLs, 5cm^2) to a loading of 0.4 mg cm^{-2} and were subsequently immersed in undiluted *N, N, N', N'*-tetramethylhexane-1,6-diamine (TMEDA) for 24 hours and then washed thoroughly with water. The Pt/C was used as the electrocatalysts for anodes at a loding level of 0.2 mg_{Pt} cm^{-2}. For comparison purpose, the commercial E-Tek Pt/C with Pt loading about 10 wt. % and 20 wt. % and the NCG-1000 were chosen and used as catalysts for cathodes. Before single fuel cell testing, the AAEMs and GDL electrodes were submeged into KOH(aq) (1 M) solution for 1 hour to give alkaline anion-exchange materials (OH^- conducting polymer electrolyte and cross-linked ionomer). The membrane electrode assemblies (MEAs) were preparing by sandwiching the anode GDLs and the AAEMs and tested using an 850e fuel cell test system (Fuel Cell Technologies, Inc., USA) fed with humidified hydrogen and oxygen (RH=80%) at temperature of 55 °C. The gas flow was controlled at 0.17 ml min^{-1}. The cell temperature were maintained at 60°C and the back pressure is 15 psi (103 kPa). The steady-state polarization curves were recorded using a current scan method by holding the cell at each point for 60 s with a scan rate of 10 dec/pt from 0 A to 2 A.

6.3 Result and Discussions

6.3.1 Synthesis

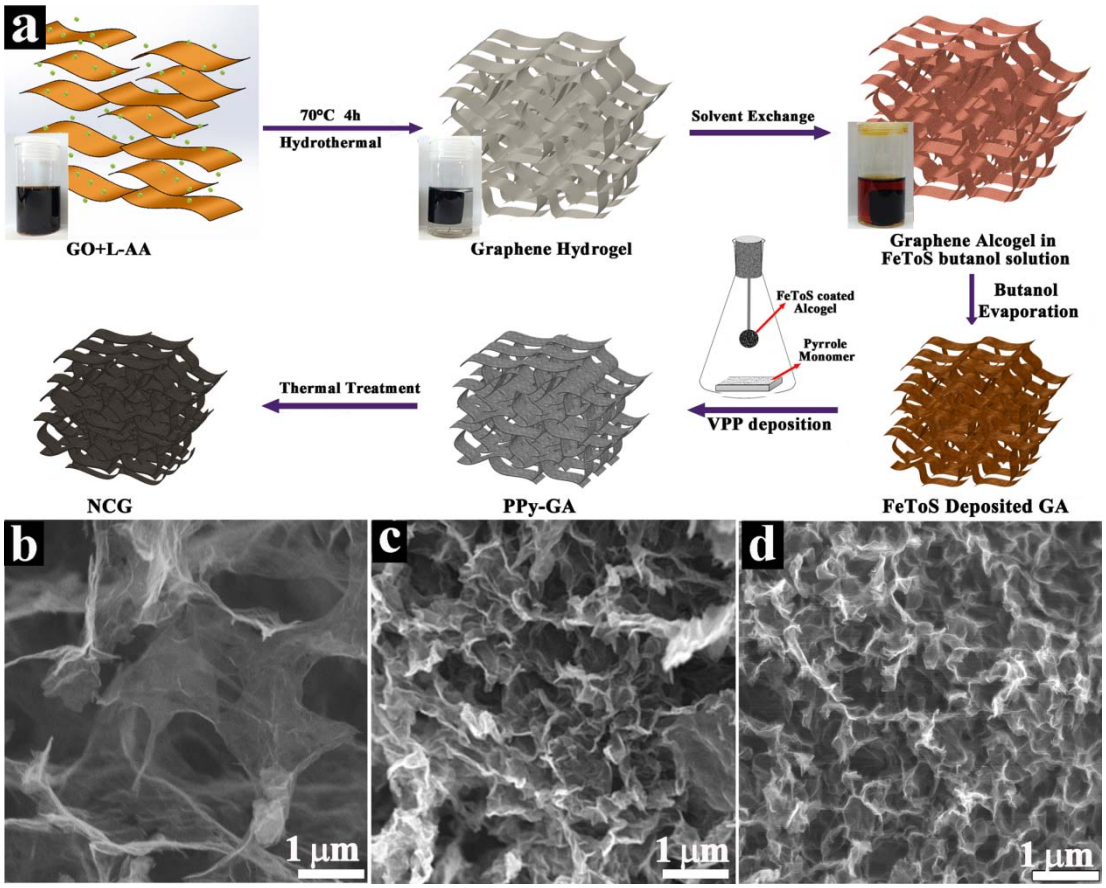

Figure 6.1 (a) schematically illustration of synthetic process of NCG based on a vapor phase polymerization method on graphene hydrogel and (b-d) SEM images collected during the preparation process to show a comparison between the (b) GA, (c) PPy-GA and (d) NCG-1000.

The fabrication process for NCG was depicted in Figure 6.1a. In a typical synthesis, the GH with was firstly produced and submerged in ethanol and butanol subsequently to exchange FeToS butanol solution in the alcogel. In the following step, the alcogel was cut into desired shape (Figure 1a (II)) for better deposition and was directly annealed at 100 °C for 0.5 hour to deposit the FeToS films on the graphene sheets, at such high evaporating rate, a uniform deposition would be formed without any observed

crystallization.[52]During deposition, the graphene gel would be shrunk because of the capillary force through butanol evaporation thereby crumpling the sheets in graphene alcogel. VPP was then carried out to grow PPy films on the alcogel (PPy-GA) by placing the FeToS film deposited alcogel in pyrrole vapor for 1 hour. To convert into the NCG, The PPy-GA was finally annealed at a set of temperatures after carefully washing, at this step the coated PPy would be eventually decomposed providing nitrogen source evolving into the graphene lattice.

The morphology and structure transformation associating with the fabrication process between the pure GA, PPy-GA and NCG was studied by scanning electron microscopy (SEM) as shown in Figure 6.1 b-d. Compared with the GA (Figure 6.1b), the pore sizes of the PPy-GA become much smaller and the sheets were more wrinkled which were possibly arisen from the shrinkage of the gel during butanol evaporation. More obviously (Figure 6.1c), it could be seen the graphene sheets become thicker and not transparent indicating the deposition of PPy, which was very uniform across all the sheets. After heat treatment, the 3D porous structure was well maintained and the sheets of the NCG were featured with abundant crumpled wrinkles (Figure 6.1d) due to the VPP process and heat treatment.

6.3.2 Characterization of PPy-GA

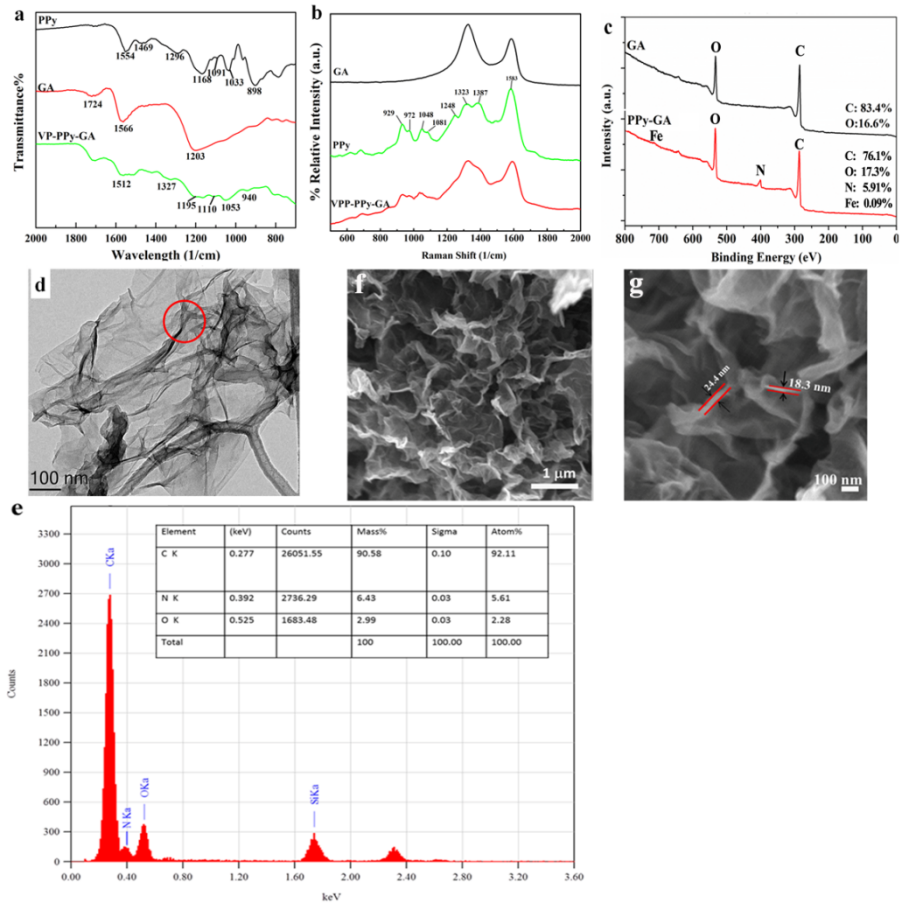

Figure 6.2 (a) Fourier transform infrared (FTIR) Spectrum, (b) Raman spectrum , (c) X-Ray photoelectron Spectroscopy (XPS) spectrum of the vapor phase polymerized polypyrrole coated graphene aerogel (PPy-GA), graphene aerogel (GA) and polypyrrole (PPy). (d) TEM images of the PPy-GA, (e) Energy dispersive X-Ray spectrum (EDS) of the PPy-GA, the region selected for EDS is on (d), inserted table: element percent calculation analysis. (f-g) High-Mag SEM images of the PPy-GA

The PPy-GA was also characterized with the Fourier transform infrared spectroscopy (FTIR, Figure 6.2a), which also indicated the existence of PPy. The characteristic peaks of PPy could be clearly identified. Peaks located at 1554 and 1469 cm^{-1} could be assigned to the stretching vibrations of pyrrole rings, peaks at 1296 and 1033 cm^{-1} are attributed to the C-N stretching vibration and C-H deformation vibration, the peaks

1168 and 898 are relating to the doping state of PPy.[53] For the GA, the 1724 cm^{-1} were carbonyl C=O stretching vibration, the C=C and C-OH stretching vibration were located at 1566 cm^{-1} and 1203 cm^{-1} respectively. It could be obviously seen that after VPP, the characteristic peaks of PPy were realized even with somewhat shift which may be ascribed to the H-bonds and π-π interconnections between PPy and GA. The Raman spectra (Figure 6.2b) further confirmed the observation on FTIR. For the sample GA, two typical bands indexed at 1324 and 1586 cm^{-1}, which were attributed to the well-documented D and G bands of reduced GO.[54] For instance, after VPP, the characteristic peaks of PPy which were around 929, 972, 1048, 1081, 1248, 1313, 1386 and 1583 cm^{-1} were observed indicating the PPy was coated on GA.[55] The relatively broad peak of D-band and small up-shifted G-band on VPP-PPy-GA suggesting the interaction between the PPy and GA was covalently coordinated.[55] Figure 6.2c showed the XPS spectra before VPP and after VPP, nitrogen was detected after VPP clearly indicated the existence of N species, further confirmation on the high-resolution N1s spectrum (Figure 6.4) indicated the N was originated from PPy and thus convinced the existence of PPy after VPP.

Figure 6.2d-e showed the TEM and TEM-EDS spectrum of the PPy-GA. A heavily wrinkled nanostructure with some layer were folded together were identified in the PPy-GA. It could been see from the TEM images that no observed PPy particles were seen indicating the thin and uniform of coating. The EDS was carried out to determine the nitrogen on the sample, it could be found a content of 5.61 at% was detected which agreed well with the previous XPS results. Figure 6.2f-g showed the SEM images of the PPy-GA, it could be seen that the transparency of the graphene sheets were lost and the sheets were covered with PPy, and the width of the PPy were measured about 20nm.

6.3.3 Thermal Treatment Temperature Impacts on Nitrogen Doping Content

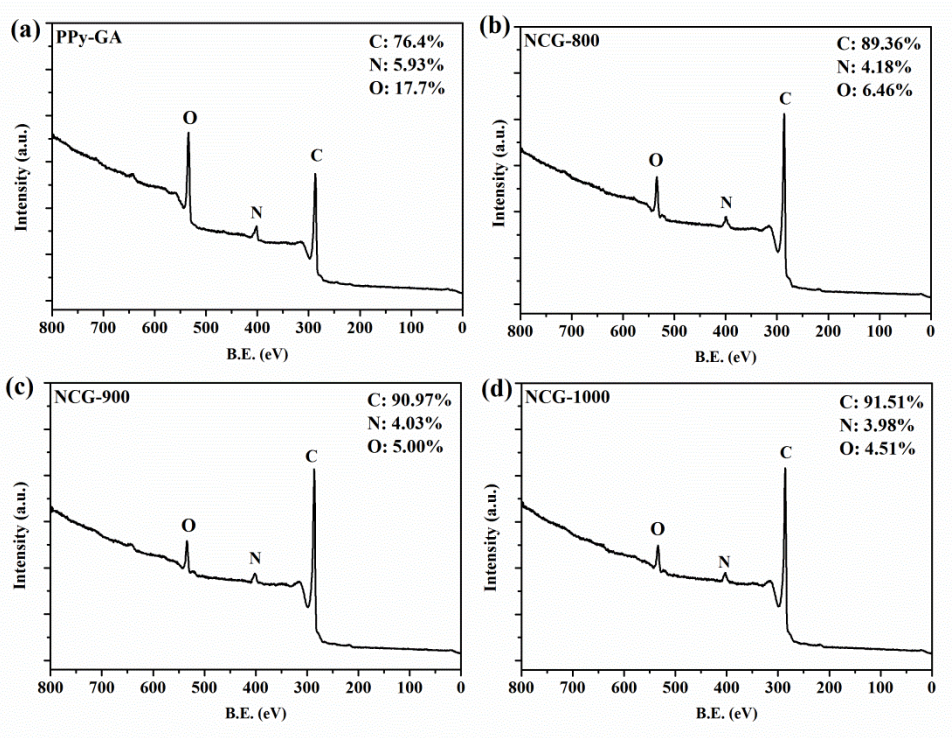

Figure 6.3 XPS spectrum of the a) PPy-GA and b-d) NCG annealed at a set of temperatures from 800-1000°C

Nitrogen doping level could be well controlled by varying the annealing temperatures. Generally, the nitrogen doping content is around 4 at. % decreasing with the increase of temperatures. Figure 6.3 showed the trend of nitrogen content as a function of annealing temperature. From the initial 5.66 at. % N on PPy-GA, the nitrogen was decreased to about 4.18, 4.03 and 3.98 at. % when annealed at 800, 900 and 1000 °C, indicating the nitrogen content loss during the increasing temperature, which might be because instability of nitrogen atoms in graphene lattice and the difficulties in forming C-N bonds at higher temperatures.[22] It could also be seen that the content of O was also decreased during the increase of temperature indicating the higher temperature would further reduce graphene.[9]

6.3.4 Thermal Treatment Temperature Impacts on Nitrogen Configuration

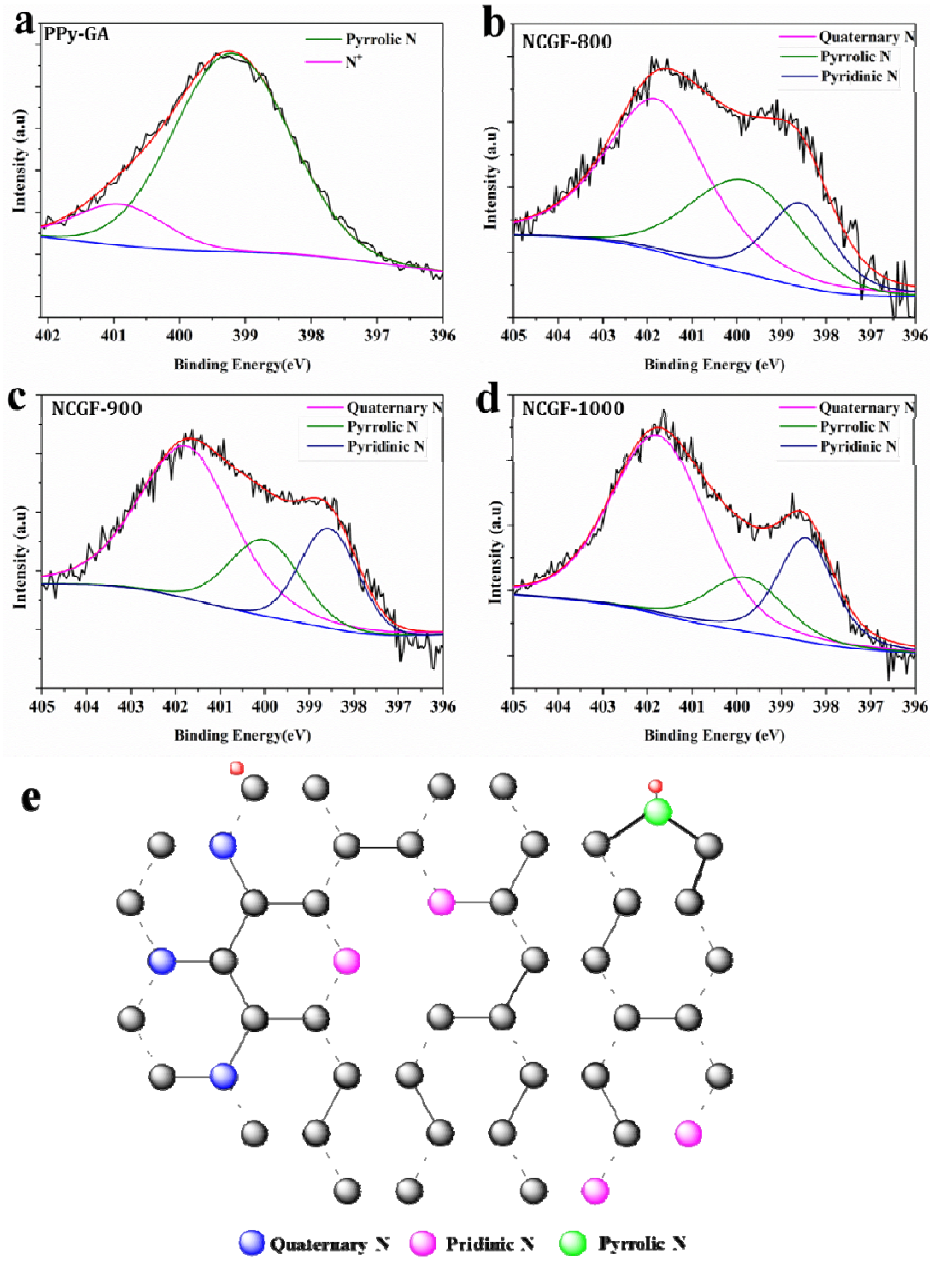

Figure 6.4 Peak analysis of high resolution N 1s XPS spectrum of a) PPy-GA and b-d) NCG annealed at a set of temperatures from 800-1000°C; e) Schematic representation of N-doped graphene (grey balls for carbon atoms, colour balls for nitrogen atoms, different types of nitrogen were as shown, a possible defect structure is shown in the middle of the ball-stick model)

Nitrogen configuration could also be well regulated through varying the annealed temperatures, which was analysed by peak fitting of the high resolution N1s spectrum as seen in Figure 6.4. Generally, for the NCG samples the N1s peak could be fitted into three separated peaks, quaternary N (BE= 401.2 ± 0.1 eV), pyrrolic N (BE=399.4 ± 0.1 eV) and pyrindic N (BE=398.4 ± 0.1 eV). For the PPy-GA, two peaks could be separated, pyrrolic N (BE=399.4 ± 0.1 eV) and positively charged N (BE= 401.2 eV) which were characteristic N peaks of PPy.[56] The nitrogen configuration were calculated and listed in Table 6.1. It could be seen from the table with the increase of temperature the pyrrolic N was decreased and the quaternary and pyridinic N was largely increased, possibly because the pyrrolic N was not stable at high temperature.[17].

Table 6.1 Nitrogen configuration derived from peak analysis of N 1s XPS spectrum of a) PPy-GA and b-d) NCG annealed at a set of temperatures from 800-1000°C

Samples	Nitrogen Configuration		
	Quaternary%	Pyrrolic%	Pyridinic%
VP-PPy-GA	-	85.67	14.33
NCG-800	52.57	28.52	18.92
NCG-900	59.42	20.13	20.46
NCG-1000	62.41	15.08	22.52

6.3.5 Thermal Treatment Temperature Impacts on the ORR Performance

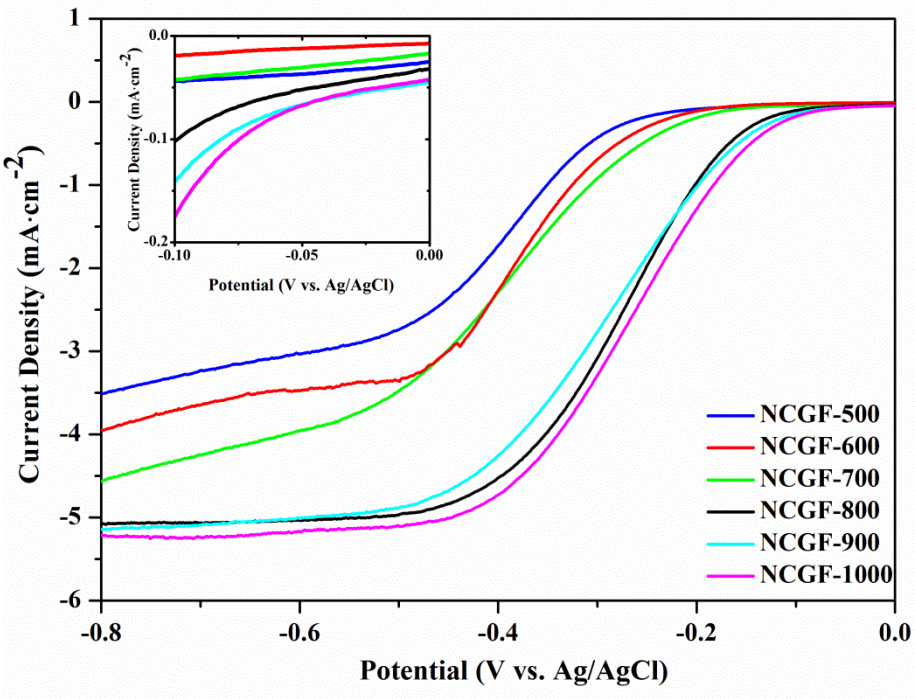

Figure 6.5 Steady-state Linear sweep voltammetry (LSV) curves of the NCG annealing at different temperatures from 500 - 1000 °C at the rotating speed of 1600 rpm in O_2 saturated electrolyte with a sweep rate of 10 mV s^{-1}, the insert is the highlight of potential regime from −0.1V to 0V.. Electrolyte is 0.1 M KOH

Figure 6.5 shows the ORR performance of the catalysts as a function of the annealing temperature, it could be seen the ORR performance was largely enhanced when annealing to above 800 °C when may be ascribed to the nitrogen configuration changed to be dominated by quaternary and pyridinic N.[17] From 800 – 1000 °C the ORR performance was slightly increased, it is clear that the NCG-1000 had the highest onset potential, half-wave potential ($E_{1/2}$) and diffusion limiting current among these samples (Table 6.2). Combined with the results that with the increase of temperature, quaternary N and pyridinic N become dominate in the graphene lattice, it is reasonable to believe that the quaternary N and pyridinic N rather than the pyrrolic N serve as catalytically active sites for the ORR, which is in good accordance with previous reports.[17]

Table 6.2 Electrochemical Performance Comparison of the onset potential (V, *vs.* Ag/AgCl), the $E_{1/2}$(V, *vs*. Ag/AgCl) and the current density at −0.8 V($mA \cdot cm^{-2}$) potential the NCG Synthesized at Different Annealing Temperature

Samples / Performance	NCG-500	NCG-600	NCG-700	NCG-800	NCG-900	NCG-1000
Onset Potential	−0.232	−0.208	−0.157	−0.059	−0.055	−0.045
$E_{1/2}$ Potential	−0.385	−0.373	−0.381	−0.299	−0.285	−0.273
Current Density (−0.8V)	−3.512	−3.94	−4.56	−5.08	−5.12	−5.22

Therefore, in this chapter, NCG-1000 was chosen for further characterisation unless otherwise specified. Pure GA without the VPP process annealed at 1000 °C, denoted as GA-1000 and GA annealed at 1000 °C with a commonly used nitrogen source-urea, denoted as NGA-1000 was produced as control experiments to investigate the structural differences due to the VPP process and study the impacts on electrochemical properties due to different nitrogen doping methods.

6.3.6 XPS Analysis of the NCG-1000, NGA-1000 and GA-1000

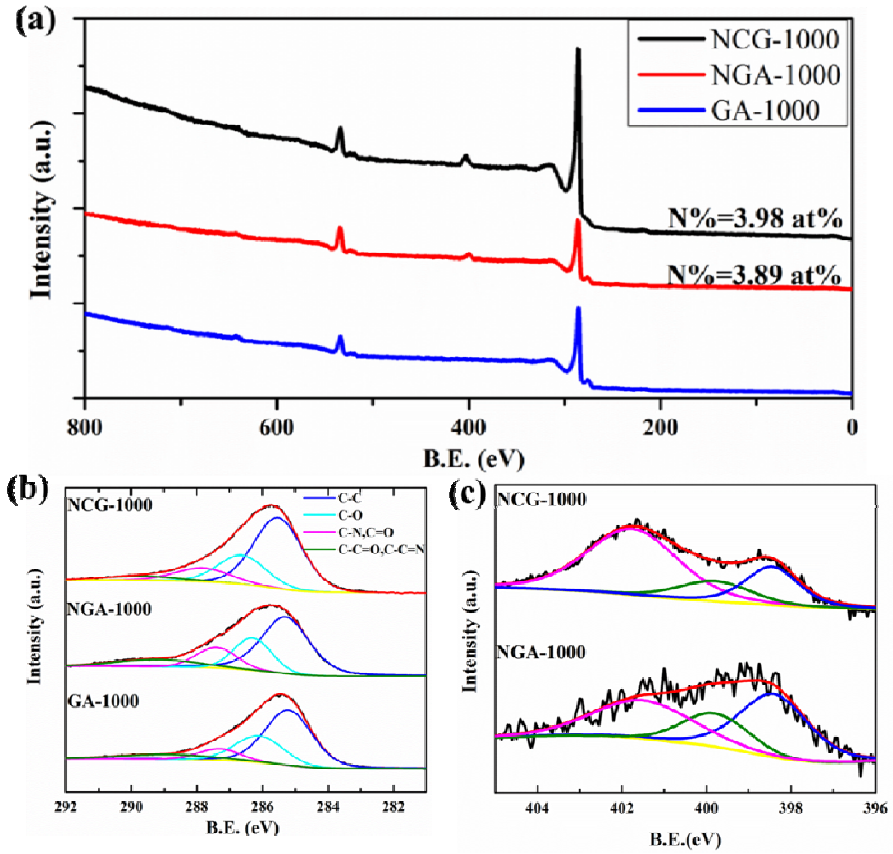

Figure 6.6 (a) XPS spectrum, (b-c) high resolution scan of (b) C1s and (c) N1s of the NCG-1000, NGA-1000 and GA-1000

The nature of doping was studied by X-ray photoelectron spectroscopy (XPS, Figure 6.6). Nitrogen content was almost similar for the NCG-1000 and NGA-1000, with about 4 at. % of nitrogen are incorporated into the graphene sheets. While compared with the initial 5.91 at.% N in the PPy-GA, the doping level for the NCG-1000 was significant efficient than the NGA-1000 and many reports,[1, 3, 6, 18, 23] the relatively high doping level was possibly because of the strong bindings between the PPy and graphene sheets which may be useful in converting nitrogen atoms into graphene lattice through cyclization or rearrangement during heat treatment. The high-resolution C 1s could be assigned into several spectral peaks: C-C at 284.8 eV, C-O at 285.9 eV, C=O or C-N at

287.1 eV and C-C=O at 289.0 eV, compared with the GA-1000, the peak at 287.1 eV of NCG-1000 and NGA-1000 was increased indicating the nitrogen was doped into the graphene lattice (Figure 6.6).[23] The nitrogen configuration was investigated by the high-resolution N 1s spectrum, as could be fitted to three peaks of pyridinic N (398.4 eV), pyrrolic N (399.5 eV) and quaternary N (401.5 eV) [3, 21, 23]. Nitrogen atoms for the NCG-1000 and NGA-1000 were rearranged through heat treatment from pyrrolic N to quaternary N and pyridinic N possible because the pyrrolic N were not stable at high temperature,[17] while such rearrangement is beneficial for the electrocatalysts as the quaternary and pyridinic N are more active in catalysing the ORR than the pyrrolic N as aforementioned. In addition, for the NGA-1000, the content of pyridinic N is more than that of the quaternary N which may be caused by the different nitrogen precursors.

6.3.7 Structural Analysis on GA-1000, NGA-1000 and NCG-1000

It's worthwhile to note that all of the three electrocatalysts (GA-1000, NGA-1000 and NCG-1000) maintained with porous 3D structure after heat treatment (Figure 6.7a-c), however, for practicable applications, electrocatalysts need to be dispersed *via* sonication in order to apply these electrocatalysts on membrane electrodes or other electrodes. After deposition, the NCG-1000 still exhibits a highly porous structure (Figure 6.7d). In contrast, the 3D macrostructure of the GA-1000 and NGA-1000 were demolished, and most of the sheets were flat and stacked on the membrane electrode (Figure 6.7e-f). These observations clearly suggest that the synthesized NCG-1000 manifest unique crumpled micro-3D nanostructure and this porous feature could be well maintained during post-processing. Therefore it is expected that the NCG-1000 would be an ideal candidate for the ORR because of the ample O_2 and ion transfer channels, as well as the greater number of active sites on ORR electrodes and this unique crumpled

feature of the NCG-1000 was further characterized in detail in order to fully understand of its structural and nitrogen doping information.

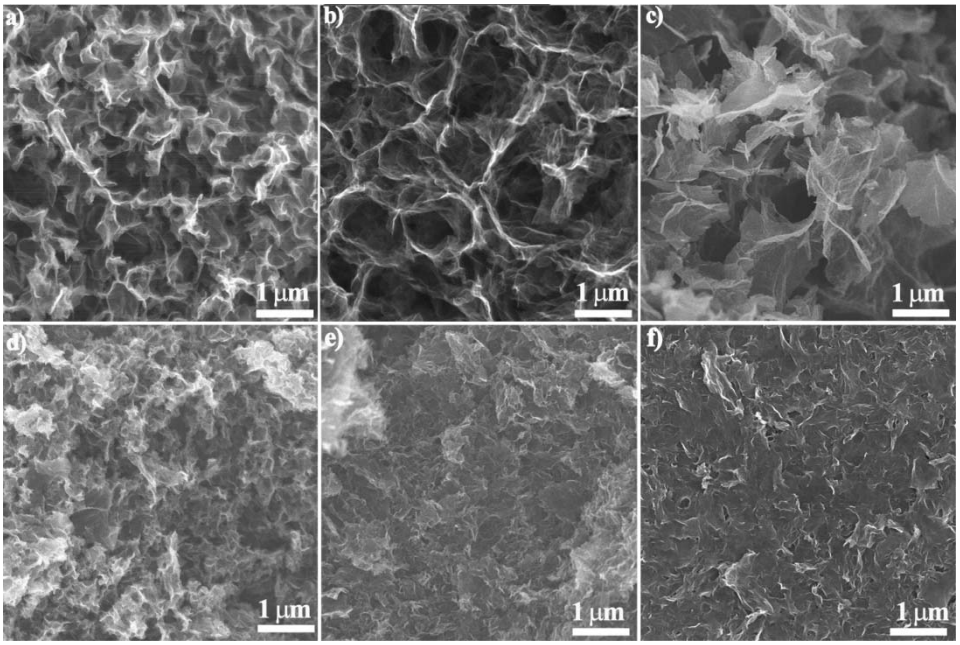

Figure 6.7 (a-c) SEM images of (a) NCG-1000, (b) GA-1000 and (c) NGA-1000. (d-f) SEM images of the catalysts layer deposited on the gas diffusion layer with (d) NCG-1000, (e) GA-1000 and (f) NGA-1000 as electrocatalysts

6.3.8 SEM and TEM Analysis of the NCG-1000

SEM images confirmed a micro-3D structure composed with crumpled folded graphene sheets was produced in the NCG-1000 (Fig. 2a). TEM also displays that the porous structure of NCG-1000 is constructed with numerous curves and wrinkles (Fig. 2b) and these wrinkled features were further investigated by high resolution TEM (HRTEM) as shown in Fig. 2c. Typical graphite crystalline structure could be seen on the sheets edges, indicating that the sheets in the NCG-1000 were somewhat stacked during the formation of GA and the heat treatments, while on the wrinkles, no visible graphite crystalline structures could be detected, implying these wrinkles were caused by crumpling of graphene sheets rather than stacking of graphene.[18, 29]

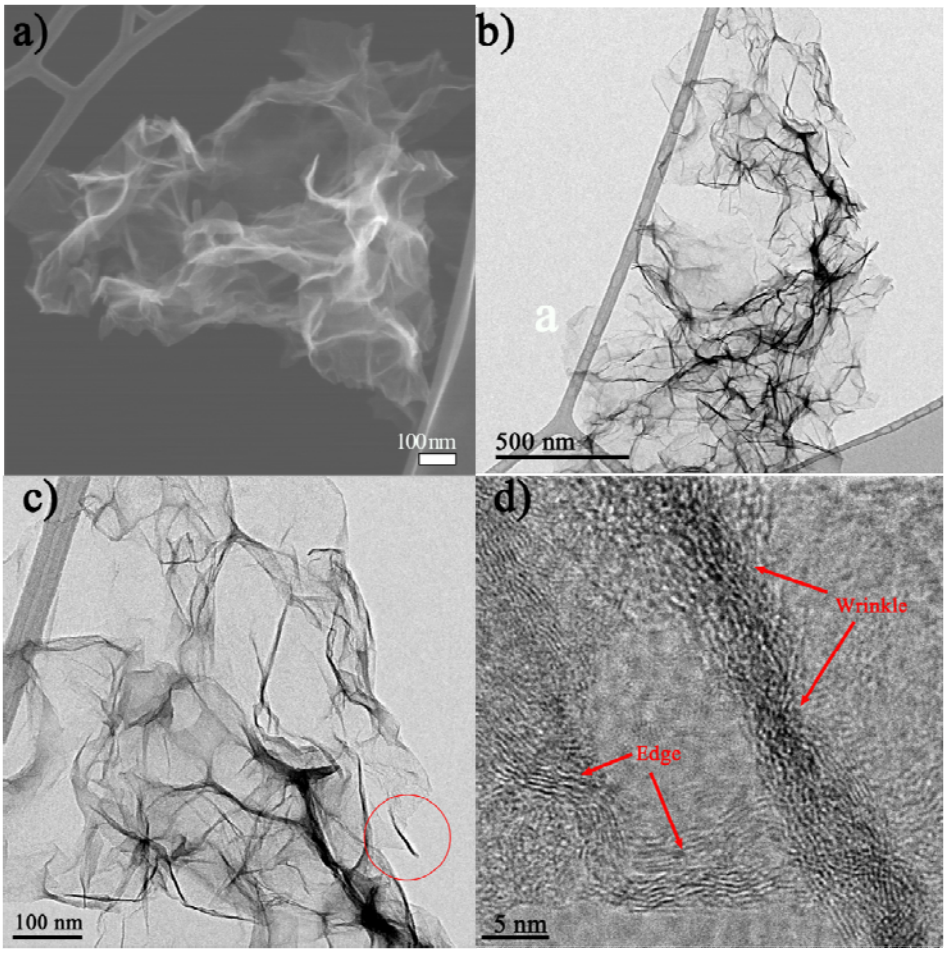

Figure 6.8**.** Characterisations of the NCG-1000. a) SEM images, b-c) TEM images, d) HR-TEM images.

6.3.9 STEM and EDS Mapping Analysis of the NCG-1000

Figure 6.9 shows scanning transmission electron microscope (STEM) image of the NCG-1000, which again confirmed the porous 3D crumpled sheets as discussed above. The uniformity of nitrogen doping was evidenced by energy-dispersive X-ray spectroscopy (EDS) mapping analysis, as is shown in Figure 6.9b-d. A homogenous nitrogen doping was realized in the element mapping suggesting the effectiveness in producing uniform doping through this method.

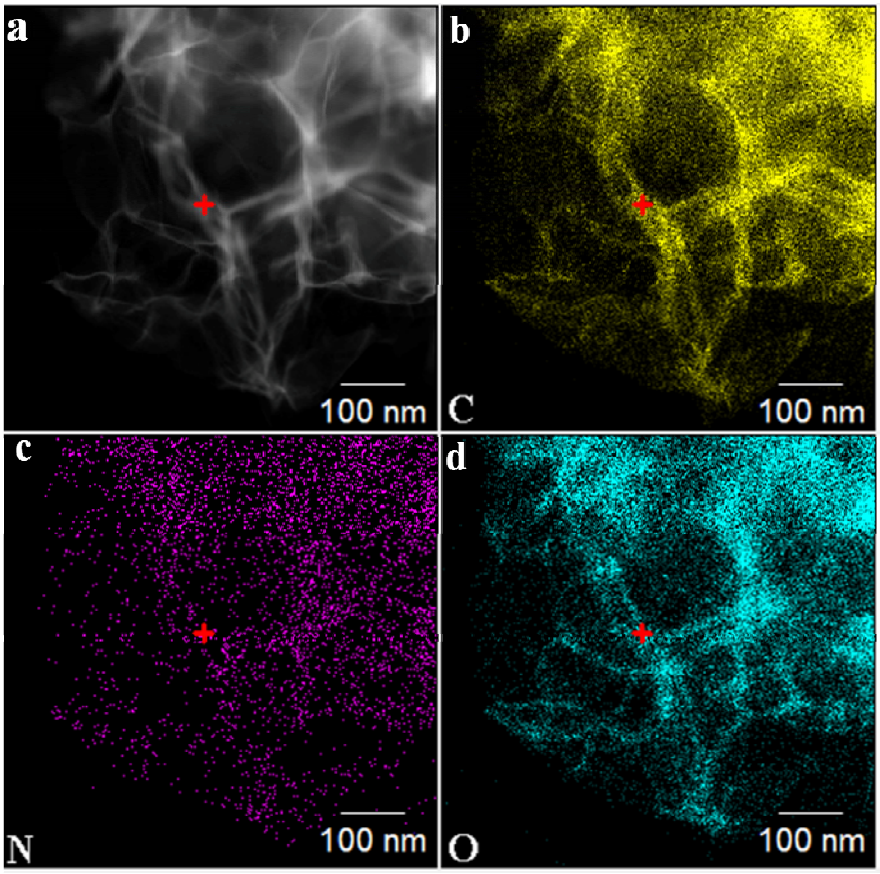

Figure 6.9 a) Scanning transmission electron microscopy (STEM), (b-c) EDS element mapping analysis (b) carbon, (c) oxygen and d) nitrogen of the NCG-1000

6.3.10 Cyclic Voltammetry Measurement

Cyclic voltammetry (CV) curves were obtained and used for a preliminary study of the electrocatalytic oxygen reduction properties of the synthesized electrocatalysts NCG-1000 at a scan rate of 50 mV s^{-1} (Figure 6.10). As shown in Figure 6.10, a quasi-rectangular featureless voltammetric currents within the potential range of −0.9 to 0.1 V were observed for NCG-1000 in the N_2-saturated solution, as a result of the typical supercapacitance effect on porous carbon materials.[1, 6] In contrast, when the electrolyte was saturated with O_2, a well-defined ORR peak centered at −0.31 V with a current density of −2.9 mA cm^{-2} was detected, the onset potential (the potential at which oxygen began to be reduced) was at about −0.05 V, which was comparable with the

Pt/C (−0.01 V). In comparison with the NGA-1000, which showed an onset potential of −0.12V, the higher onset potential of the NCG-1000 suggested the determining role of nitrogen configuration as well as the porous structures on the electrocatalytic performance of the electrocatalysts, which also indicated the advantages of this method in producing well-controlled nitrogen doping crumpled graphene

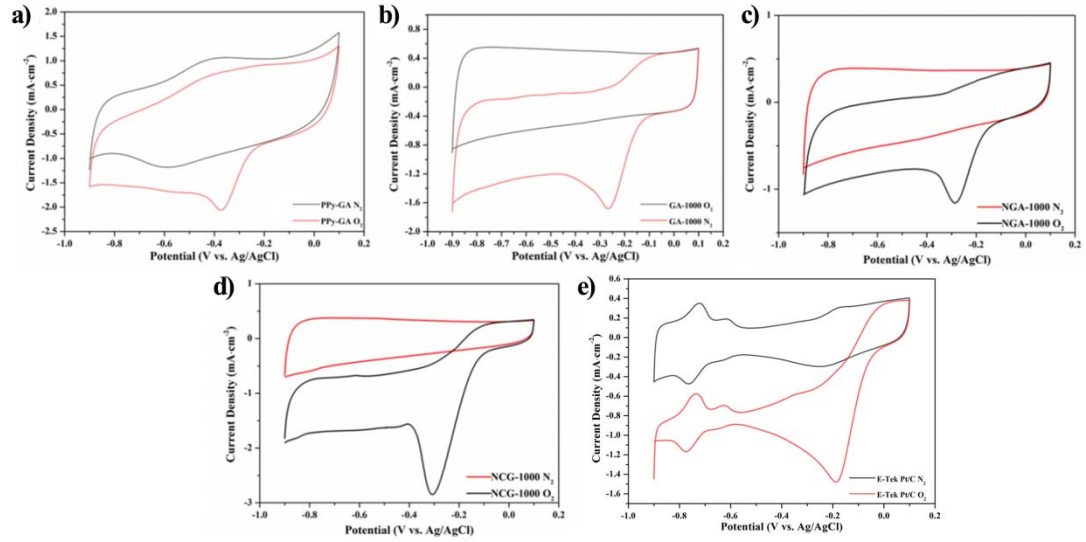

Figure 6.10 Comparison of the electrochemical catalytic performance of the synthesized electrocatalysts. CV curves of the (a) PPy-GA, (b) GA-1000, (c)NGA-1000, (d) NCG-1000, and (e) the commercial available E-Tek Pt/C catalysts in N_2 (solid line) and O_2 (dash line) saturated electrolyte with a scan rate of 50 mV s^{-1}.

6.3.11 ORR Polarisation Curves

To gain insight into the ORR activities and kinetics of the electrocatalysts, the steady state ORR polarization curves of the E-Tek Pt/C, PPy-GA, GA-1000, NGA-1000 and NCG-1000 electrocatalysts were obtained (Figure 6.11a). To be used as efficient electrocatalysts for ORR, the diffusion current limit is a crucial parameter to qualify catalysts' performance; a well-defined current limiting plateau reveals a higher and more stable performance of the electrocatalysts.[57, 58] The curves on GA-1000 and

PPy-GA showed a slow current increase and no current plateau revealing their poor performance towards the ORR. In contrast, a well-defined diffusion-limiting current region from −0.6 V to −0.35 V and a mixed kinetic-diffusion control region from −0.08V to −0.35 V were observed on the NCG-1000, which is very similar to the behavior of the Pt/C indicating its comparable activity toward ORR compared with the commercial Pt/C. As a comparison, the NGA-1000 displayed a similar plateau but with a much lower diffusion limiting current density possibly owing to high resistance between the bulk electrode and electrolyte due to the lack of sufficient ion and mass transfer channels on the electrodes. To qualify the ORR activity of the electrocatalysts, the half-wave potential ($E_{1/2}$), at which the current is a half of the limiting current is calculated, for the NCG-1000, the $E_{1/2}$ is −0.223 V, which is about 30 mV lower than that of Pt/C (−0.193 V) and much more positive than that of GA-1000 (−0.295 V) and PPy-GA (−0.351 V). The above comparisons clearly indicated the crumpled porous NCG-1000 manifested significant improvement in electro-catalyzing O_2 in alkaline medium compared with GA-1000, PPy-GA or NGA-1000 suggesting this doping method could effectively increase the electrocatalytic performance of the catalysts due to the well-organized nitrogen configuration and the well maintained porous structure during post treatment process.

In order to obtain the kinetics of the ORR, steady state ORR polarization curves were also collected at various rotation speeds and corresponding Koutecky-Levich (K-L) plots were drafted from the ORR polarization curves at different potentials (See Experimental for details). The plots of all samples shows good linearity and noticeably, the NCG-1000 showed a much higher ORR current, which was close to that of the commercial Pt/C and significantly higher than those of GA-1000, PPy-GA and NGA-1000 at all rotation speeds; which was a further indication of the outstanding ORR

catalytic performance on the crumpled doped graphene as compared with other three carbon materials. The electron-transfer numbers (n) and the kinetic limiting current (J_k) of all the samples at −0.5 V were calculated according to the slopes of the linear fitted K-L plots on the basis of the K-L equation (Figure 6.11b-c). The NCG-1000 exhibited a much higher electron transfer number as well as the kinetic limiting current over the GA-1000, PPy-GA, NGA-1000. In comparison with the E-Tek Pt/C, the J_k for the NCG-1000 was even much higher than that of the Pt/C at and was comparable or even higher than recently reported doped graphene,[5, 6, 17, 19] suggesting the unique superiority of this method in producing high efficient metal-free electrocatalyst for the ORR by controllable varying the nitrogen configuration and the generation of enduring porous structure. The electron transfer number and kinetic limiting current was also calculated at various potential (Figure 6.11d), general increasing n value were seen as the potential become more negative, while for the NCG-1000, the n value is about 3.8 at most potentials suggesting a smooth and efficient process of the oxygen reduction.

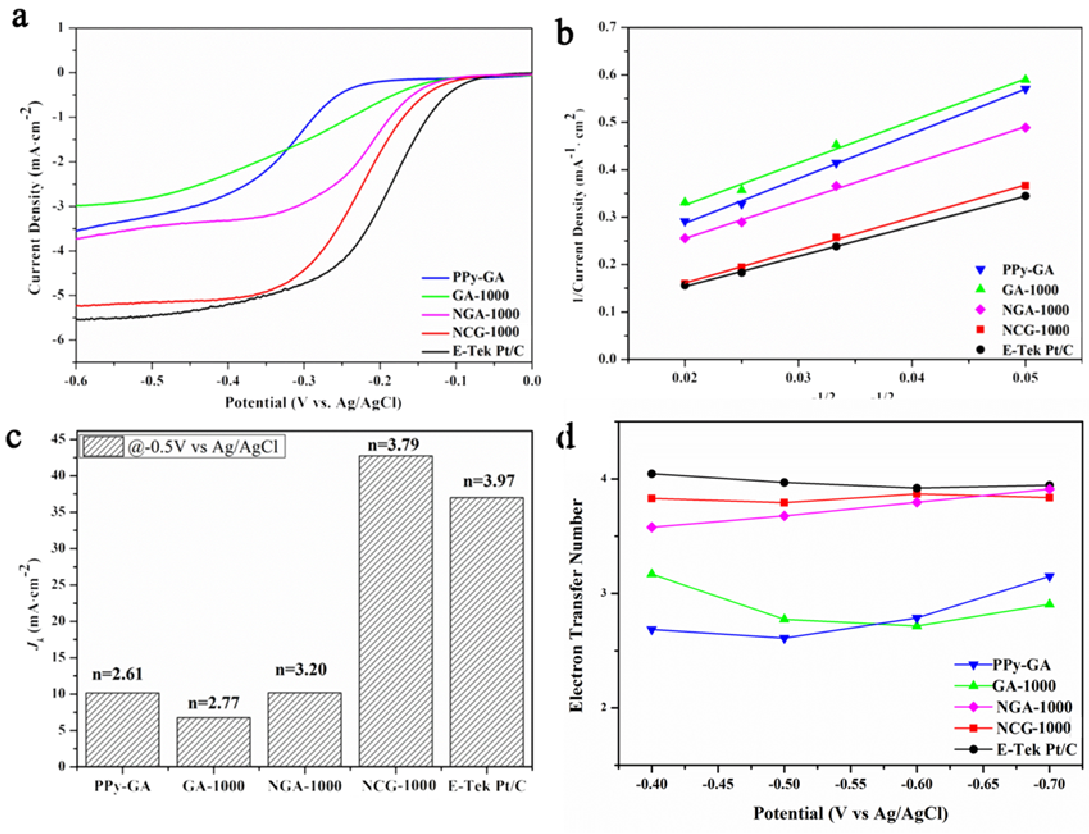

Figure 6.11 a) Steady-state Linear sweep voltammetry (LSV) curves at a rotating speed of 1600 rpm in O_2 saturated electrolyte with a sweep rate of 10 mV s^{-1}. b) Koutecky-Levich plots of the electrocatalysts at the potential of −0.5 V. c) The kinetic limiting current density (J_k) and the corresponding electron transfer number of various samples. d) The electron transfer number of various catalysts at −0.4V to −0.7V. Catalyst loading is 0.242 mg cm^{-2}. The electrolyte is 0.1 M KOH solution

6.3.12 Methanol Resistance and Durability Test

The selectivity to methanol of the catalysts is a key factor in the real application for fuel cells, because the relative small methanol molecular would cross through the membrane and react with the catalysts in the cathodes causing poor ORR performance and further reducing the cell efficiency.[59] To this end, the selectivity of NCG-1000, NGA-1000 and commercial Pt/C were compared through chronoamperometric measurements at the

rotating speed of 1600 rpm at −0.3 V with subsequently introduction of oxygen and methanol as displayed in Figure 6.12a. The introduction of oxygen led to significant increase in the current density and a stable current was reached for all the catalysts revealing the ORR performance of them were comparative. However, after the addition of methanol, a distinct change on current was observed for the Pt/C catalyst indicating methanol oxidation occurred, i.e., the selectivity of the Pt/C was poor. In contrast, for NCG-1000 or the NGA-1000, the current remained nearly unchanged after the addition of methanol reflecting its superior selectivity and better methanol tolerance due to the nature of carbon doped materials.[5, 20]

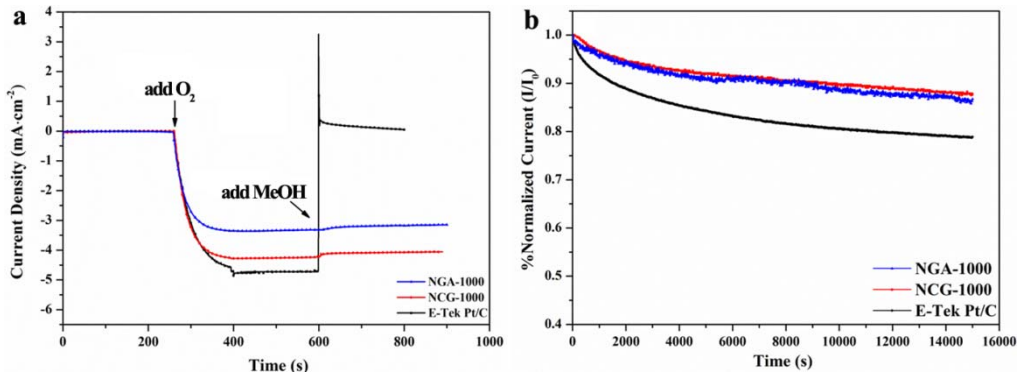

Figure 6.12 Chronoamperometric responses at −0.3 V of the NCG and E-Tek Pt/C at the rotation speed of 1600 rpm a) with oxygen and methanol (1 M) added at about 260 s and 700 s respectively, b) in O_2 saturated electrolyte up to 15000 seconds inserted: (the current density of the E-Tek Pt/C and NCG-1000 before and after Chronoamperometric tests at −0.3V.

The durability of these catalysts was also assessed by the chronoamperometric technique at −0.3V (*vs.* Ag/AgCl) (Fig. 4b).[5, 6] During the long term testing (up to 15000 s), a similar current loss was observed for the NCG-1000 and NGA-1000 suggesting their durability were almost the same, whereas for the commercial Pt/C, a

dramatic current loss was observed, indicating that the NCG-1000 had superior advantages over the commercial Pt/C when used as long-term running electrocatalysts.

6.3.13 Single Anion Exchange Membrane Fuel Cell Test

The anion exchange membrane fuel cell tests (AEMFC) was finally conducted in order to obtain the real performance of the catalysts in practical environment. To our best knowledge, the testing of metal-free nitrogen doped materials in a real anion membrane single cell was rarely mentioned,[1-6, 9, 13, 17, 19] possibly because of the lack of the anion exchange membrane and anion exchange ionomer and the relative poor ORR activities of the non-metal carbon electrocatalysts compared with the metal-nitrogen-carbon electrocatalysts[60, 61] or noble catalysts.[62] The configuration of AEMFC is very similar to that of proton exchange membrane fuel cell (PEMFC) except the membrane was changed from Nafion to anion exchanged membrane, in this case, an electron-beam-grafted EFTE membranes provided by University of Surrey[51, 63] were selected an used.

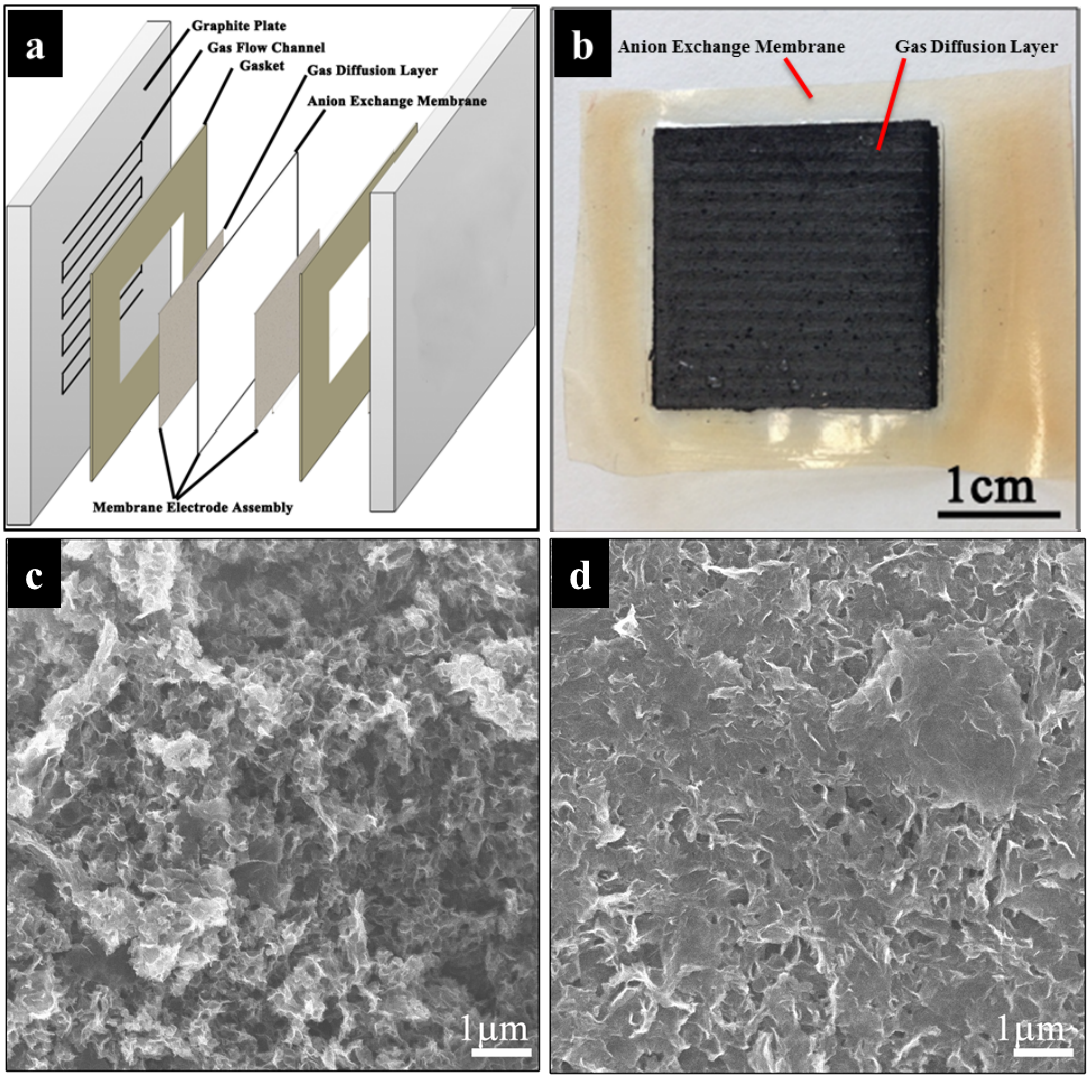

Figure 6.13(a) Schematic illustration of anion exchange membrane fuel cell (AEMFC) assembly. (b) Digital photo of the membrane electrode assembly (MEA) using anion exchange membrane. c, d) SEM image of the c) NCG-1000 and d) NGA-1000 on the gas diffusion layer after single fuel cell test

Figure 6.13c-d showed the SEM image of the NGA-1000 and NCG-1000 on the gas diffusion layer (GDL) after single cell test, it could been seen the porous structure was well maintained on the GDL for the NCG-1000, however in contrast (Figure 6.13c), the porous structure of NGA-1000 were mostly demolished and most sheets were relatively flat with some area stacking together on the GDL due to the post-process for preparing the MEA. This is another indication of the unique advantage of this VPP method in

preparing microporous crumpled graphene sheets which would benefit the mass transport in a real fuel cell system and this was further evidenced by the polarization curves of the single cell on these two catalysts, as shown in Figure 6.14.

Figure 6.14 showed the polarization curves and power density curves of a single cell test using E-Tek Pt/C, NGA-1000 and NCG-1000 as cathode catalysts with a catalysts. It could been seen at low current density area (< 50 mA cm^{-2}), the polarization curves for the NCG-1000 and NGA-1000 were almost the same, however as the potential lowered, the NCG-1000 delivers a much higher current than the NGA-1000, owing the open and porous structure on the electrode, which could facilitate oxygen and ion transport thereby enhancing the performance. This comparison again suggested the significance of the porous structure in producing high performance ORR catalysts in real fuel cell. Further comparisons were made against the commercial E-Tek Pt/C, at the same loading level (2 mg cm^{-2}), at practicable operating potential (~0.6 V)[61], the current density for the NCG-1000 was about 60 mA cm^{-2}, which is about 63% of the E-Tek Pt/C (95 mA cm^{-2}) and the max power density for the NCG-1000 was about 63 mW cm^{-2}, reaching 83 % of the max power density of E-Tek Pt/C (76 mW cm^{-2}). These comparisons clearly indicated the power output of the NCG-1000 was comparable with that of the Pt/C, revealing it could work as efficient metal-free electrocatalysts under practicable working conditions

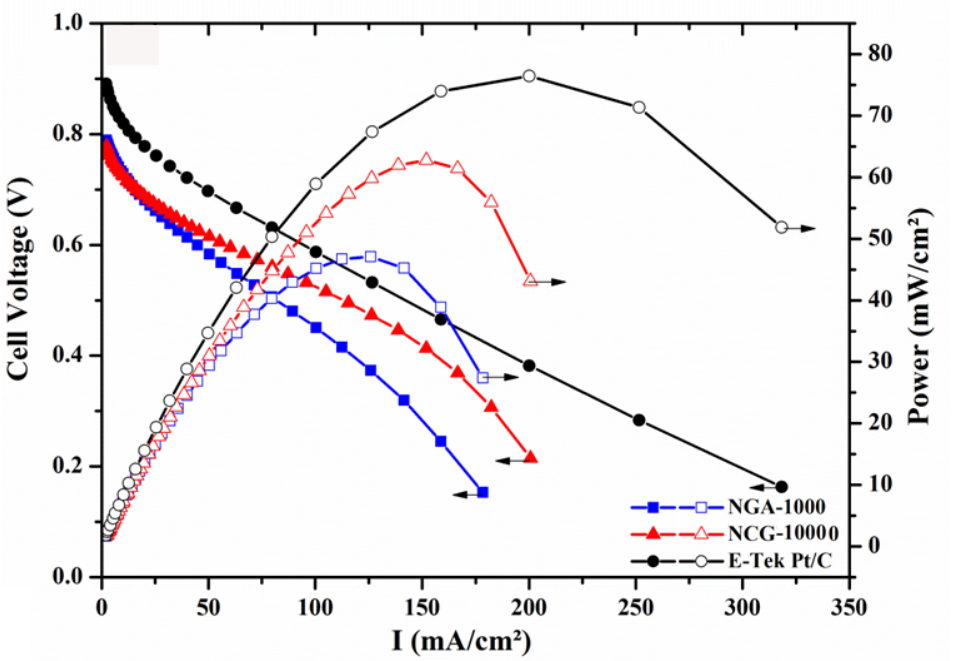

Figure 6.14 AEMFC polarization curves and power density curves of a single cell test using E-Tek Pt/C, NGA-1000 and NCG-1000 as cathode catalysts with a catalysts loading amount of 2 mg cm^{-2}. Operating conditions: cell temperature 60°C, humidifier temperatures 55°C for both H_2 and O_2, flow rate 0.18 L min^{-1}, and cell back pressure is about 15 psi

6.4 Conclusion

In summary, we have demonstrated that the uniform nitrogen doped 3D crumpled graphene could be produced *via* the vapor phase deposition of PPy coated on GA in this report. The micro-3D crumpled porous nanostructure, which could be well-maintained after post processing in preparing ORR electrodes or membrane electrodes, enables the catalysts high surface area and more active sites thus featuring the electrocatalyst with excellent catalytic performance towards the ORR with better methanol tolerance and longer durability. Besides the AEMFC tests firstly convinced these metal-free nitrogen doped carbon materials could work as comparable efficient catalysts under real operation condition thus giving further confidence in developing metal-free catalysts for

the next generation fuel cells. This work will help further understand of the mechanism of nitrogen doping on ORR electrocatalytic performance and would benefit the development in preparing conducting polymer graphene composites and metal-free doping graphene catalysts in the application for the electrocatalysis, energy storage devices and energy conversion systems.

Since it was aware that the electrocatalytic performance of the pure nitrogen doped graphene showed promising catalytic results towards the ORR in alkaline medium, we further incorporated cobalt oxide with the form of core shell nanostructures onto the nitrogen doped graphene aerogel to further increase the ORR performance. Cobalt oxides have been reported with excellent catalytic performance when they were coupled with nitrogen carbon due to the synergistic effects among the nitrogen doped carbon and metal oxides and the formation of carbon-metal-nitrogen bonds. Such an electrocatalysts would greatly improve the ORR performance compared with the pure nitrogen doped graphene or metal oxides, while the metal oxides is non-electrical conductive which would hamper electron transfer among the metal oxides thereby limiting the overall performance of the electrocatalysts. In the next chapter, we will demonstrate the core shell nanostructured cobalt/ cobalt oxides anchored on the nitrogen doped graphene supports, which was synthesized from a facile hydrothermal method, could largely decrease the electron transfer resistance between metal oxides thus improving the electrocatalytic performance of the electrocatalyst.

6.5 References

1. Parvez, K., S. Yang, Y. Hernandez, A. Winter, A. Turchanin, X. Feng, and K. Müllen, ACS Nano, 2012. **6**(11): p. 9541-9550.

2. Liang, J., Y. Zheng, J. Chen, J. Liu, D. Hulicova-Jurcakova, M. Jaroniec, and S.Z. Qiao, Angewandte Chemie, International Edition, 2012. **51**(16): p. 3892-3896.

3. Zheng, Y., Y. Jiao, L. Ge, M. Jaroniec, and S.Z. Qiao, Angewandte Chemie, International Edition, 2013. **52**(11): p. 3110-3116.

4. Zhu, J., C. He, Y. Li, S. Kang, and P.K. Shen, Journal of Materials Chemistry A, 2013. **1**(46): p. 14700-14705.

5. Wang, S., L. Zhang, Z. Xia, A. Roy, D.W. Chang, J.B. Baek, and L. Dai, Angewandte Chemie, International Edition, 2012. **51**(17): p. 4209-4212.

6. Liang, J., Y. Jiao, M. Jaroniec, and S.Z. Qiao, Angewandte Chemie, International Edition, 2012. **51**(46): p. 11496-11500.

7. Liu, Q., J. Jin, and J. Zhang, ACS Applied Materials & Interfaces, 2013. **5**(11): p. 5002-5008.

8. Su, Y., Y. Zhang, X. Zhuang, S. Li, D. Wu, F. Zhang, and X. Feng, Carbon, 2013. **62**: p. 296-301.

9. Xu, J., G. Dong, C. Jin, M. Huang, and L. Guan, ChemSusChem, 2013. **6**(3): p. 493-499.

10. Zhang, C., N. Mahmood, H. Yin, F. Liu, and Y. Hou, Advanced Materials, 2013. **25**(35): p. 4932-4937.

11. Latorre-Sánchez, M., A. Primo, and H. García, Angewandte Chemie, International Edition, 2013. **52**(45): p. 11813-11816.

12. Liang, Y., Y. Li, H. Wang, J. Zhou, J. Wang, T. Regier, and H. Dai, Nature Materials, 2011. **10**(10): p. 780-786.

13. Gong, K., F. Du, Z. Xia, M. Durstock, and L. Dai, Science, 2009. **323**(5915): p. 760-764.

14. Hummers, W.S. and R.E. Offeman, Journal of the American Chemical Society, 1958. **80**(6): p. 1339-1339.

15. Chen, Z., W. Ren, L. Gao, B. Liu, S. Pei, and H.-M. Cheng, Nature Materials, 2011. **10**(6): p. 424-428.

16. Bai, H., C. Li, and G. Shi, Advanced Materials, 2011. **23**(9): p. 1089-1115.

17. Yang, S., L. Zhi, K. Tang, X. Feng, J. Maier, and K. Muellen, Advanced Functional Materials, 2012. **22**: p. 3634-3640.

18. Wen, Z., X. Wang, S. Mao, Z. Bo, H. Kim, S. Cui, G. Lu, X. Feng, and J. Chen, Advanced Materials, 2012. **24**(Copyright (C) 2013 American Chemical Society (ACS). All Rights Reserved.): p. 5610-5616.

19. Wu, Z.-S., S. Yang, Y. Sun, K. Parvez, X. Feng, and K. Müllen, Journal of the American Chemical Society, 2012. **134**(22): p. 9082-9085.

20. Silva, R., D. Voiry, M. Chhowalla, and T. Asefa, Journal of the American Chemical Society, 2013. **135**(21): p. 7823-7826.

21. Wu, Z.S., A. Winter, L. Chen, Y. Sun, A. Turchanin, X. Feng, and K. Müllen, Advanced Materials, 2012. **24**(37): p. 5130-5135.

22. Wang, H., M. Xie, L. Thia, A. Fisher, and X. Wang, Journal of Physical Chemistry Letters, 2013. **5**(1): p. 119-125.

23. Wang, Y., Y. Shao, D.W. Matson, J. Li, and Y. Lin, ACS Nano, 2010. **4**(4): p. 1790-1798.

24. Moon, J., J. An, U. Sim, S.-P. Cho, J.H. Kang, C. Chung, J.-H. Seo, J. Lee, K.T. Nam, and B.H. Hong, Advanced Materials, 2014: p. 3501-3505.

25. Zhang, L. and Z. Xia, Journal of Physical Chemistry C, 2011. **115**(22): p. 11170-11176.

26. Lee, J.H., N. Park, B.G. Kim, D.S. Jung, K. Im, J. Hur, and J.W. Choi, ACS Nano, 2013. **7**(10): p. 9366–9374.

27. Mao, S., Z. Wen, H. Kim, G. Lu, P. Hurley, and J. Chen, ACS Nano, 2012. **6**(Copyright (C) 2013 American Chemical Society (ACS). All Rights Reserved.): p. 7505-7513.

28. Luo, J., H.D. Jang, and J. Huang, ACS Nano, 2013. **7**(Copyright (C) 2013 American Chemical Society (ACS). All Rights Reserved.): p. 1464-1471.

29. Ma, X., M.R. Zachariah, and C.D. Zangmeister, Nano Letters, 2012. **12**(Copyright (C) 2013 American Chemical Society (ACS). All Rights Reserved.): p. 486-489.

30. Tao, Y., X. Xie, W. Lv, D.-M. Tang, D. Kong, Z. Huang, H. Nishihara, T. Ishii, B. Li, D. Golberg, F. Kang, T. Kyotani, and Q.-H. Yang, Sci. Rep., 2013. **3**.

31. Xu, Y., Z. Lin, X. Huang, Y. Liu, Y. Huang, and X. Duan, ACS Nano, 2013. **7**(5): p. 4042-4049.

32. Xu, Y., K. Sheng, C. Li, and G. Shi, ACS Nano, 2010. **4**(7): p. 4324-4330.

33. Xu, Y., Q. Wu, Y. Sun, H. Bai, and G. Shi, ACS Nano, 2010. **4**(12): p. 7358-7362.

34. Hu, H., Z. Zhao, W. Wan, Y. Gogotsi, and J. Qiu, Advanced Materials, 2013. **25**(15): p. 2219-2223.

35. Niu, Z., J. Chen, H.H. Hng, J. Ma, and X. Chen, Advanced Materials, 2012. **24**(30): p. 4144-4150.

36. Chen, J., K. Sheng, P. Luo, C. Li, and G. Shi, Advanced Materials, 2012. **24**(33): p. 4569-4573.

37. Lee, S.H., H.W. Kim, J.O. Hwang, W.J. Lee, J. Kwon, C.W. Bielawski, R.S. Ruoff, and S.O. Kim, Angewandte Chemie, International Edition, 2010. **49**(52): p. 10084-10088.

38. Yoon, Y., K. Lee, C. Baik, H. Yoo, M. Min, Y. Park, S.M. Lee, and H. Lee, Advanced Materials, 2013. **25**(32): p. 4437-4444.

39. Compton, O.C., S. Kim, C. Pierre, J.M. Torkelson, and S.B.T. Nguyen, Advanced Materials 2010. **22**(Copyright (C) 2013 American Chemical Society (ACS). All Rights Reserved.): p. 4759-4763.

40. Zhang, X., Z. Sui, B. Xu, S. Yue, Y. Luo, W. Zhan, and B. Liu, Journal of Materials Chemistry, 2011. **21**(Copyright (C) 2013 American Chemical Society (ACS). All Rights Reserved.): p. 6494-6497.

41. Chen, W. and L. Yan, Nanoscale, 2011. **3**(Copyright (C) 2013 American Chemical Society (ACS). All Rights Reserved.): p. 3132-3137.

42. Ren, L., K.S. Hui, and K.N. Hui, J. Mater. Chem. A, 2013. **1**(Copyright (C) 2013 American Chemical Society (ACS). All Rights Reserved.): p. 5689-5694.

43. Chen, L., X. Wang, X. Zhang, and H. Zhang, Journal of Materials Chemistry, 2012. **22**(Copyright (C) 2013 American Chemical Society (ACS). All Rights Reserved.): p. 22090-22096.

44. Yin, H., C. Zhang, F. Liu, and Y. Hou, Advanced Functional Materials, 2014. **24**(20): p. 2930-2937.

45. Lim, B., M. Jiang, P.H.C. Camargo, E.C. Cho, J. Tao, X. Lu, Y. Zhu, and Y. Xia, Science, 2009. **324**(5932): p. 1302-1305.

46. Wu, G., K.L. More, C.M. Johnston, and P. Zelenay, Science, 2011. **332**(6028): p. 443-447.

47. Winther-Jensen, B., J. Chen, K. West, and G. Wallace, Macromolecules, 2004. **37**(16): p. 5930-5935.

48. Marcano, D.C., D.V. Kosynkin, J.M. Berlin, A. Sinitskii, Z. Sun, A. Slesarev, L.B. Alemany, W. Lu, and J.M. Tour, ACS Nano, 2010. **4**(8): p. 4806-4814.

49. Paulus, U.A., T.J. Schmidt, H.A. Gasteiger, and R.J. Behm, Journal of Electroanalytical Chemistry, 2001. **495**(2): p. 134-145.

50. van der Vliet, D., D.S. Strmcnik, C. Wang, V.R. Stamenkovic, N.M. Markovic, and M.T.M. Koper, Journal of Electroanalytical Chemistry, 2010. **647**(1): p. 29-34.

51. Varcoe, J.R. and R.C.T. Slade, Electrochemistry Communications, 2006. **8**(5): p. 839-843.

52. Chen, J., J.Z. Wang, A.I. Minett, Y. Liu, C. Lynam, H. Liu, and G.G. Wallace, Energy & Environmental Science, 2009. **2**(4): p. 393-396.

53. Gong, F., X. Xu, G. Zhou, and Z.-S. Wang, Physical Chemistry Chemical Physics, 2013. **15**(2): p. 546-552.

54. Zhao, Y., J. Liu, Y. Hu, H. Cheng, C. Hu, C. Jiang, L. Jiang, A. Cao, and L. Qu, Advanced Materials, 2013. **25**(4): p. 591-595.

55. Zhang, J. and X.S. Zhao, The Journal of Physical Chemistry C, 2012. **116**(9): p. 5420-5426.

56. Cen, L., K.G. Neoh, and E.T. Kang, Langmuir, 2002. **18**(22): p. 8633-8640.

57. Guo, S., S. Zhang, L. Wu, and S. Sun, Angewandte Chemie, International Edition, 2012. **51**(47): p. 11770-11773.

58. Shim, J.H., J. Kim, C. Lee, and Y. Lee, Chem. Mater., 2011. **23**: p. 4694-4700.

59. Liu, M., Y. Lu, and W. Chen, Advanced Functional Materials, 2013. **23**(10): p. 1289-1296.

60. Li, X., B.N. Popov, T. Kawahara, and H. Yanagi, Journal of Power Sources, 2011. **196**(4): p. 1717-1722.

61. He, Q., Q. Li, S. Khene, X. Ren, F.E. López-Suárez, D. Lozano-Castelló, A. Bueno-López, and G. Wu, Journal of Physical Chemistry C, 2013. **117**(17): p. 8697-8707.

62. Wang, M., W. Zhang, J.-Z. Wang, D. Wexler, S.D. Poynton, R.C.T. Slade, H. Kun-Liu, B. Winther-Jenson, R. Kerr, D. Shi, and J. Chen, ACS Applied Materials & Interfaces, 2013. **5**(23): p. 12708-12715.

63. Varcoe, J.R., R.C.T. Slade, and E. Lam How Yee, Chemical Communications (Cambridge, United Kingdom), 2006. **0**(13): p. 1428-1429.

Chapter 7

Core shell Co/CoO Anchored on 3D Nitrogen doped Graphene Aerogel as an Enhanced Electrocatalyst for the Oxygen Reduction Reaction in Alkaline Medium

7. CONTENTS

7.1 Introduction

Fuel cells (FCs) are believed to be the promising energy conversion systems to satisfy today's increasing energy demand because of their high specific power density and low environment impact.[1] The cathodic oxygen reduction reaction (ORR) is considered to be the kinetically decisive step for the power conversion efficiency of FCs because of its sluggish reaction mechanism and high overpotential.[1, 2] As a commonly used and effective electrocatalyst, platinum (Pt, in the form of Pt nanoparticles supported on carbon), is impeded from large-scale commercialisation because of its high cost, limited stability, and poor "poison" resistance.[1-3] Therefore, numerous efforts have been devoted in discovering novel electrocatalysts for the ORR with high efficiency, low cost and environmentally friendliness. Previous chapter has shown the nitrogen doped crumpled graphene could work as a comparable electrocatalyst with the Pt/C in alkaline medium, while recent studies in the synthesis of transition metal-oxides coupled with carbon supports materials have suggested that these transition metal oxides supported on graphene sheets could be used as substitutes for the ORR with improved electrocatalytic performance.[1, 4, 5] Apart from the low cost and abundance, these compounds are advantageous for affording comparable catalytic efficiency, good poison resistance and longer durability.[1, 4-7] Moreover promisingly, when nitrogen doped graphene were used as carbon supports, owing to the unique charge transfer between graphene-metal interface[8] and the "synergistic effects" between nitrogen, carbon and transition metal atoms, the electrocatalytic activities of the electrocatalysts towards the ORR could be largely promoted.[1, 4-7, 9]

Despite these notable achievements, most of used graphene supports which are produced from chemical exfoliation method owing to the ease of preparation,[1-4, 8-12],

are vulnerable to stack and aggregate during the reduction or drying processes due to the strong van der Waals and hydrogen bonding between water molecular and graphene sheets. This irreversible stack would decrease the specific surface area, cause the losses of active sites and further hamper mass transfer thereby compromising the overall properties of the electrocatalysts.[13-16] In addition, since the transition metal oxides were not electrical conductive, one would also question that whether the relatively lower conductivity would possibly increase the electrical resistance and inhibit the electron transfer thereby limiting the catalytic performance of the electrocatalysts.[7, 17] In light of these issues, exploring simple approaches in producing high-specific area nitrogen doped graphene support and minimizing the resistance between transition metal oxides have become necessary in further improving the electrocatalytic performance of this kind of electrocatalysts.

We herein report the facial and surfactant-free synthesis of novel Co/CoO core shell nanostructure supported on nitrogen doped GA (denoted as Co/CoO-NGA) and explore it as an efficient electrocatalyst for the ORR. The substitute of the core of metal oxides with pure metal would greatly increase electric conductivity and facilitate the electron transfer of the nanoparticle. [8, 18, 19] In addition, different from the traditional method based on the complex wet chemistry method by controlled growth the shells on the pre-synthesized metal nanoparticles using surfactant, which has low capacities in massive production,[8, 20] our synthetic procedure provides a much more simple and economically feasible way in large-scale synthesis of core shell nanostructures. Moreover, the designed 3D macroscopic structures of nitrogen doped graphene aerogel could effectively prevent the flat sheets from largely aggregating when drying and reducing, offering more active sites, multiple electron and ion transport pathways and easy access to the oxygen and electrolyte thus improving the electrocatalytic

performance of the electrocatalyst.[5, 21-25] The electrocatalyst shows comparable ORR catalytic activities with the commercial Pt/C catalysts (20 wt.% Pt on Vulcan XC-72), but with much better stability and excellent methanol tolerance leading to a promising electrocatalyst for the ORR. To our best knowledge, some of cobalt oxides and graphene aerogel composites were reported,[17, 26, 27] however the core-shell structures of cobalt oxides and the doping of nitrogen into graphene aerogel were not mentioned in these literatures.

7.2 Experimental

7.2.1 Reagents

Graphite (325 mesh, Sigma), Sulphuric acid (H_2SO_4, concentrated, Ajax Finechem), phosphoric acid (70%, H_3PO_4, Ajax Finechem), Potassium permanganate ($KMnO_4$, Sigma), hydrogen peroxide (H_2O_2, Sigma), Hydrochloric Acid (33%, HCl, Ajax Finechem),Cobalt Nitrate Hexahydrate ($Co(NO_{3)2}\,6H_2O$), Urea (Sigma)

7.2.2 Synthesis

Synthesis of Graphene Oxide (GO): GO was prepared from natural graphite flakes (Sigma) using a modified Hummers method, which was described elsewhere.[12, 28] In a typical synthesis, a 9:1 mixture of concentrated H_2SO_4/H_3PO_4 (360:40 mL) was added to a mixture of graphite flakes (3.0 g, 1 wt equiv) and $KMnO_4$ (18.0 g, 6 wt equiv), producinga slight exotherm to 35-40 °C. The reaction was then heated to 50 °C and stirred for 12 h. The reaction was cooled to rt and poured onto ice (400 mL) with 30% H_2O_2 (10 mL). The obtained yellow bright solution was centrifuged (4000 rpm for 4 h), and the supernatant was decanted away. The remaining solid material was then washed

in diluted HCl acid and water for 2 times. At last, the solid materials in water was dialysis for 2 weeks with changing water frequently for before use.

Synthesis of nitrogen doped graphene aerogels (NGA) : In a typical synthesis, 15 ml of 2 mg mL^{-1} well dispersed GO were mixed with 1 g urea and put into an autoclave at 170°C for 15 h to produce N doped graphene hydrogel. After reaction, the hydrogel were taken out with a tweezer and directly freezed using liquid nitrogen and dehyrated with a freeze-dryer for 12 h. After freeze-drying the NGA was annealled at required temperature.

Synthesis of Co/CoO core shell supported on nitrogen doped graphene aerogel (Co/CoO-NGA): The procedure is similar to the synthesis of NGA except 53.8 mg $Co(NO)_3 \cdot 6H_2O$ was added before hydrothermal process. After freeze-drying the mixed aerogel was anealled at 800°C under argon.

Synthesis of CoO supported on nitrogen doped graphene aerogel (CoO-NGA): The synthesis is the same as Co/CoO-NGA except the mixed aerogel was anealed at 400 °C.

7.2.3 Physical Characterisation

SEM images were obtained using a JEOL-7500FA. TEM images, High resolution (HR)-TEM images were collected with a JEOL JEM-2100F transmission electron microscope operated at 80 kV. Scanning transmission electron microscopy (STEM) images and Energy dispersive X-Ray spectrum (EDS) mapping analysis were acquired with a JEOL JEM-ARM200F operated at 80 kV. Samples for TEM, EDS, STEM were prepared by dropping one drop of the catalysts ethanol dispersion on a holy carbon film coated copper grid (200 mesh). Ethanol dispersion was prepared from sonication using a probe sonicator (Brandson S-250D) operated at 50 % aptitude for 1 hour. The The powder X-ray diffraction (XRD) patterns were collected using a GMC MMA X-ray powder

diffractometer with Cu Kα radiation (λ = 1.5418 Å). X-ray photoelectron spectroscopy (XPS) spectra were collected using a Thermo Scientific K-Alpha instrument. Raman spectrums were acquired with a Raman JY HR800 Spectrometer with the excitation laser of 632.18 nm.

7.2.4 Electrochemical measurements

Electrochemical measurements were performed using the thin film rotating-disk electrode (TF-RDE) technique, as reported elsewhere.[29] The electrocatalysts ink was prepared by dispersing the electrocatalysts in Nafion/H_2O/isopropanol (m/m/m = 0.05/10/50) to obtain a 2 mg ml^{-1} dispersion via a probe sonicator (Brandson S-250D). The thin film electrode was prepared through placing 60 μL of the catalyst ink on a glassy carbon rotating ring disk electrode (RRDE, 0.2457 cm^2, Pine Research Instrumentation). The electrode was then connected to a CHI 720c bipotentiostat (CH Instruments) in a standard three-electrode cell with a Pt-mesh counter electrode and a KNO_3(aq) saturated (10 wt.%) Ag/AgCl reference. Unless otherwise specified, all the potentials are against Ag/AgCl as reference potential.

The cyclic voltammetry (CV) traces were recorded in N_2 saturated KOH (0.1 mol L^{-1}) solution with a sweep rate of 50 mV s^{-1}. The ORR polarization curves were recorded using a linear sweep voltammetry (LSV) technique in oxygen saturated electrolyte with a sweep rate of 10 mV s^{-1} at various rotation speeds of 100, 400, 900, and 1600 rpm from 0.1 to − 0.8 V. Koutecky-Levich (K-L) plots were drafted from the ORR polarization curves at different potentials. Ohmic drop caused by system resistentce was compensated using atomatic mode within the CHI software.[30] The number of electrons involved per O_2-molecule reduction can be determined using the Koutecky-Levich (K-L) equation

$$j = 1/j_k + 1/B\omega^{0.5};$$

$$[B = 0.2n\mathrm{F}(D_{O2})^{2/3}(v)^{-1/6}C_{O2}]$$

where, j_k is the kinetic current, ω is the electrode rotation rate, n is the transferred electron number, F is the Faraday constant (F = 96485 C mol^{-1}), D_{O2} is the diffusion coefficient of O_2 = 1.9×10^{-5} cm^2 s^{-1}, v is the kinetic viscosity (0.01 cm^2 s^{-1}), and C_{O2} is the bulk concentration of O_2 (1.2×10^{-6} mol cm^{-3}).

Methanol tolerant were carried out through a chronoamperometry technique at the potential of − 0.3 V and with rotation at 1600 rpm with subsquently introducing of oxygen and methanol (0.5 M) at set time. Stability tests were carried out by the chronoamperometry technique at the potential of − 0.3 V with rotation spped at 1600 rpm in oxygen-saturated electrolyte up to 15000 seconds

7.2.5 Single Fuel Cell Test

The anion-exchange membranes used were (graft co-polymerised) using vinylbenzyl chloride and functionalised using trimethylamine (University of Surrey);[31] the membrane used was of type S80, with membrane thickness ≈ 80 μm (thickness depends on hydration level) and ion exchange capacity IEC ≈ 1.3 meq g^{-1}. The anodes and cathodes were prepared as described previously.[31] In brief, the electrocatalyst ink prepared with ca. 15 wt.% poly(vinybenzyl chloride) dissolved in ethyl acetate were sprayed on the gas diffusion layers (GDLs, $5cm^2$) to a loading of 0.4 mg cm^{-2} and were subsequently immersed in undiluted *N, N, N', N'*-tetramethylhexane-1,6-diamine (TMEDA) for 24 hours and then washed thoroughly with water. The Pt/C was used as the electrocatalysts for anodes at a loading level of 0.2 mg_{Pt} cm^{-2}. For comparison purpose, the commercial E-Tek Pt/C with Pt loading about 20 wt. % and the Co/CoO-NGA were chosen and used as catalysts for cathodes. Before single fuel cell testing, the

AAEMs and GDL electrodes were submeged into KOH(aq) (1 M) solution for 1 hour to give alkaline anion-exchange materials (OH^- conducting polymer electrolyte and cross-linked ionomer). The membrane electrode assemblies (MEAs) were preparing by sandwiching the anode GDLs and the AAEMs and tested using an 850e fuel cell test system (Fuel Cell Technologies, Inc., USA) fed with humidified hydrogen and oxygen (RH=100%) at temperature of 50 °C. The gas flow was controlled at 0.20 $L \cdot min^{-1}$. The cell temperature was maintained at 50°C without back pressure. The steady-state polarization curves were recorded using a current scan method by holding the cell at each point for 60 s with a scan rate of 10 dec/pt from 0 A to about 2 A.

7.3 Result and Discussions

7.3.1 Synthesis

The fabrication process for Co/CoO-NGA was depicted in Figure 6.1. In a typical synthesis, graphene oxide, cobalt nitrate hexahydrate and urea were firstly dispersed in water to form a stable aqueous suspension (Figure 6.1a). Subsequently, these ternary components were hydrothermally assembled at 170 °C for 15 h to produce a graphene based 3D hydrogel. (Figure 6.1b). In this step, the cobalt-urea complex would be localized on graphene sheets and nitrogen species would simultaneously be incorporating into graphene lattice. At last the hydrogel was directly dehydrated through lyophilization to maintain the 3D structure of graphene and annealed at 800 °C for 2 h under argon. In this way the cobalt-urea complex would be eventually converted into metallic cobalt and decomposed nitrogen species in the complex would also doping into the graphene lattice at high temperature. When exposed to air at ambient atmosphere, the top surface of Co would be oxidized forming Co/CoO core shell nanostructures (Figure 6.1c). The mechanism for formation of metallic cobalt is similar as previously

reported.[32] To make a comparison, nitrogen doped graphene aerogel (NGA), CoO supported on nitrogen doped graphene aerogel (CoO-NGA) were also synthesized accordingly (See Experimental for details).

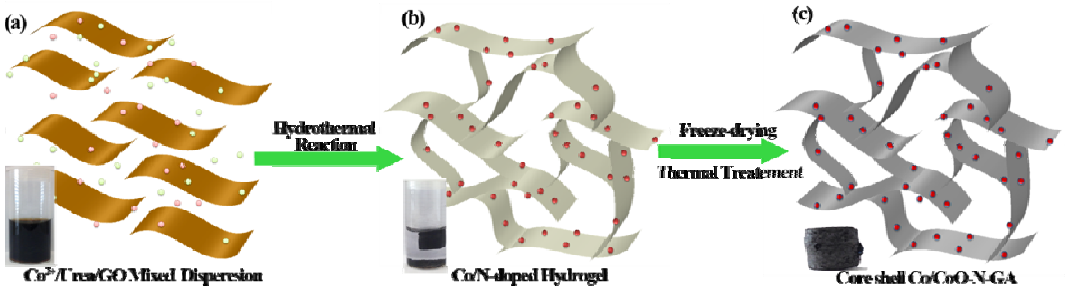

Figure 7.1 Schematic illustration of the fabrication process for Co/CoO-NGA based on a hydrothermal method.

7.3.2 Structural Analysis

The synthesized products associating with different annealing temperature were firstly examined using XRD in order to acquire the crystallization differences during the annealing process, which is shown in Figure 7.2. Obviously, after hydrothermal process, the intermediates of cobalt-urea complex were obtained [33]. No virtual crystal changes could be observed when the annealing temperature was below 400 °C, indicating the Co-urea complex was thermal stabile below 400 °C. Further increase of annealing temperature will lead the formation of cobalt oxides indicating the decomposed of the Co-urea complex, as reported with many other literatures.[6, 9] When the annealing temperature was further increased, metallic cobalt could be produced. The temperatures was finally set to 800 °C to completely reduce the Co^{2+} and when the metallic cobalt was exposed to air, the CoO was produced on the shell of the cobalt forming a protecting oxidation layer to prevent further oxidation. It was observed further increase the annealing temperature lead no changes on the XRD pattern while the nitrogen doping content would be decreased thus a temperature of 800 °C is chosen as the

optimized temperature and used in this study. Besides, it is worthwhile to note even metallic cobalt could not be formed in the ammonium reducing environment at 800 °C, [7] the successful synthesis of cobalt metallic in this experiment could be ascribed to the formation of cobalt-urea organic complex intermediates, which would facilitate the crystallization of cobalt metal by producing a regional reducing environment when decomposing at high temperatures.[32]

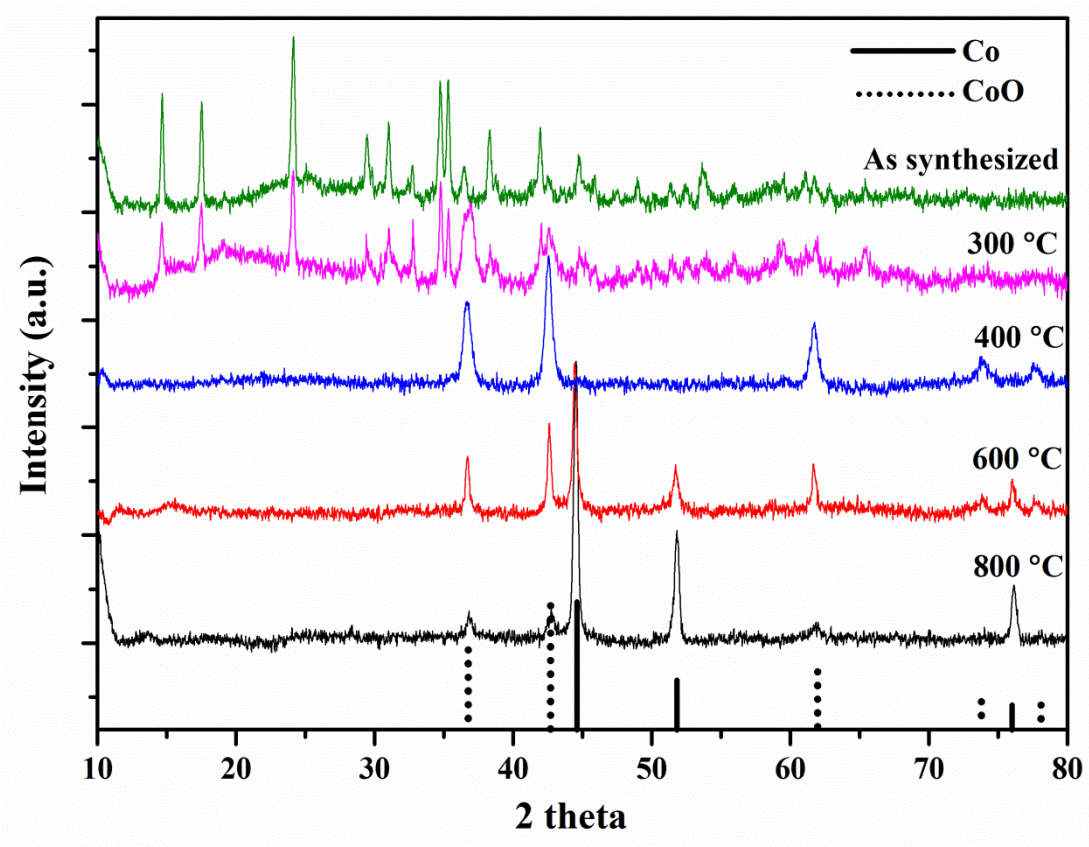

Figure 7.2 XRD patterns of the products synthesized with different annealing temperatures

7.3.3 Morphology Analysis

The morphologies and structure of the synthesized products were characterized with the SEM as shown in Figure 7.3. A 3D interconnected macroporous graphene structure, as a supporting materials could be clearly discerned in Figure 7.3a, the pore size of the

graphene aerogel are around tens micrometers. The graphene sheets in the GA are transparent and relatively thin indicating the integration of 3D graphene could effectively inhibited graphene sheets from stacking. (Figure 7.3b). Then the graphene sheets were detailed investigated through high-mag SEM (Figure 7.3c-d). A notably homogenously decoration of metal oxides nanoparticles with the size arranging from 20-30 nm was realized in this experiment. The uniformly decoration of cobalt based nanoparticles on graphene of this robust strategy could be possibly originated from the addition of urea forming the cobalt-urea organic complex, which could in-situ regulate the pH and stabilize the growth of nanoparticles.[34] Interestingly, the nanoparticles were grown on both sides of graphene sheets and even some of them were encapsulated within the graphene layer, and this unique structure has been reported to enhance interaction between metal oxide nanoparticle and graphene support and to suppress the dissolution of the nanoparticle during electrochemical process thereby improving the catalytic performance and stability the electrocatalysts.[5]

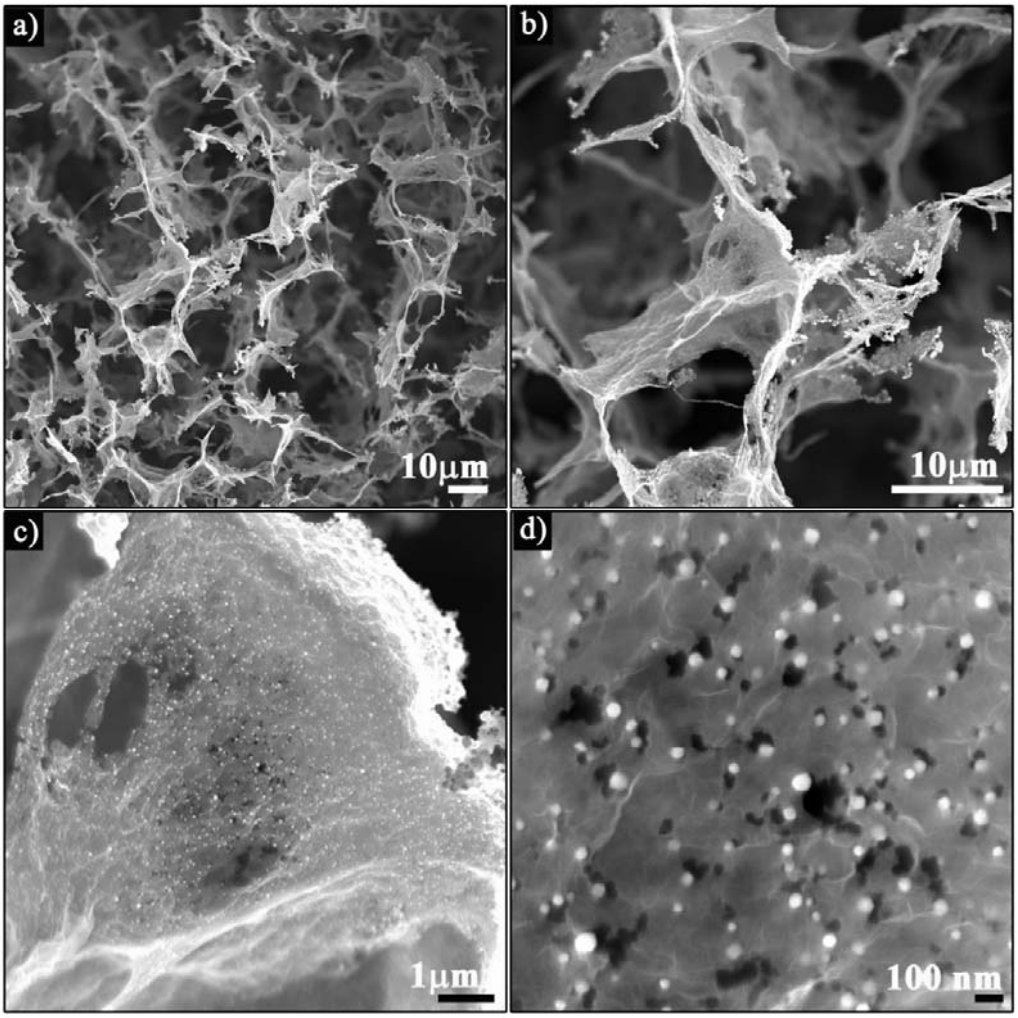

Figure 7.3 Morphologies analysis: a-d) typical SEM images of the synthesized Co/CoO-NGA.

7.3.4 TEM Analysis

To gain insight into the structural information of the Co/CoO-NGA, TEM analysis was conducted. The high angle annular dark field (HAADF)-scanning transmission electron microscopy (STEM) and transmission electron microscopy (TEM, Figure 7.4 a-b) confirmed the observation on the SEM images with homogeneously nanoparticles decorated on the porous graphene structure were identified. The structure was further investigated by the HR TEM images showing distinct core shell structures of the cobalt-cobalt oxide nanoparticles, the shell thickness were calculated to be around 2-3 nm

(Figure 7.4d), besides it could be seen lattice pattern could be well discerned suggesting the core and shell of the nanoparticles were both well crystallized. More interestingly, the three types of subunits, NG, CoO and Co were highly integrated together, suggesting the strong chemical bonding between them which would benefit electron and charge transfer among the active sites thus facilitating the ORR process and increasing the electrocatalytic perfomance.

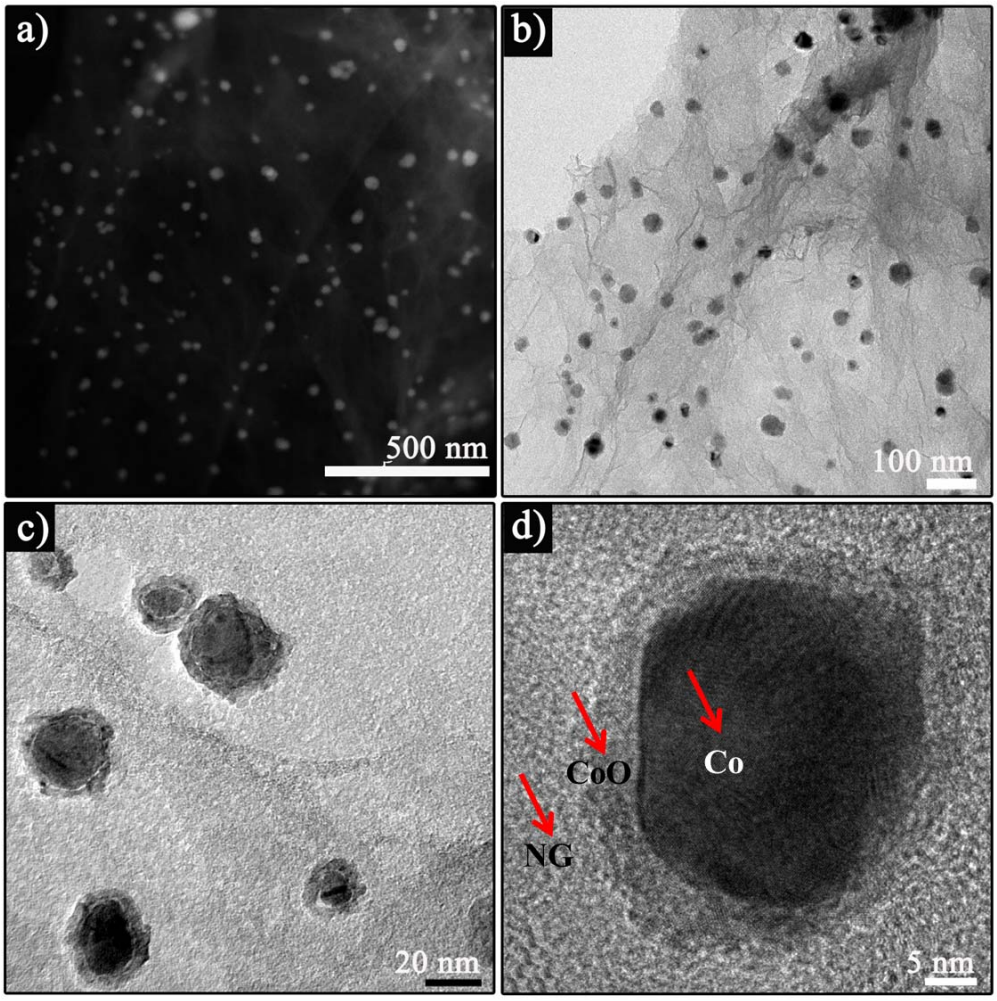

Figure 7.4 a) High angle annular dark field (HAADF)-scanning transmission electron microscopy (STEM), b) TEM and c-d) high resolution (HR)-TEM images of the synthesized Co/CoO-NGA.

7.3.5 STEM and EDS analysis

The high-mag STEM associating with the EDS mapping analysis was conducted in order to acquire the element distribution among the samples and is shown in Figure 7.5. The high-mag STEM images also indicated the structure differences on the shell and core of the nanoparticles revealing a core/shell structure. The element mapping evidenced the existence of C, N, Co, O in the products and suggested that nitrogen was uniformly doped into the graphene lattice. The element analysis on cobalt and oxygen revealed the intensity of oxygen is much high around the shell of the cobalt nanoparticle, which is due to the formation of CoO shell on the Co core thus confirming the successful synthesis of a Co/CoO core shell nanostructure on nitrogen graphene sheets.

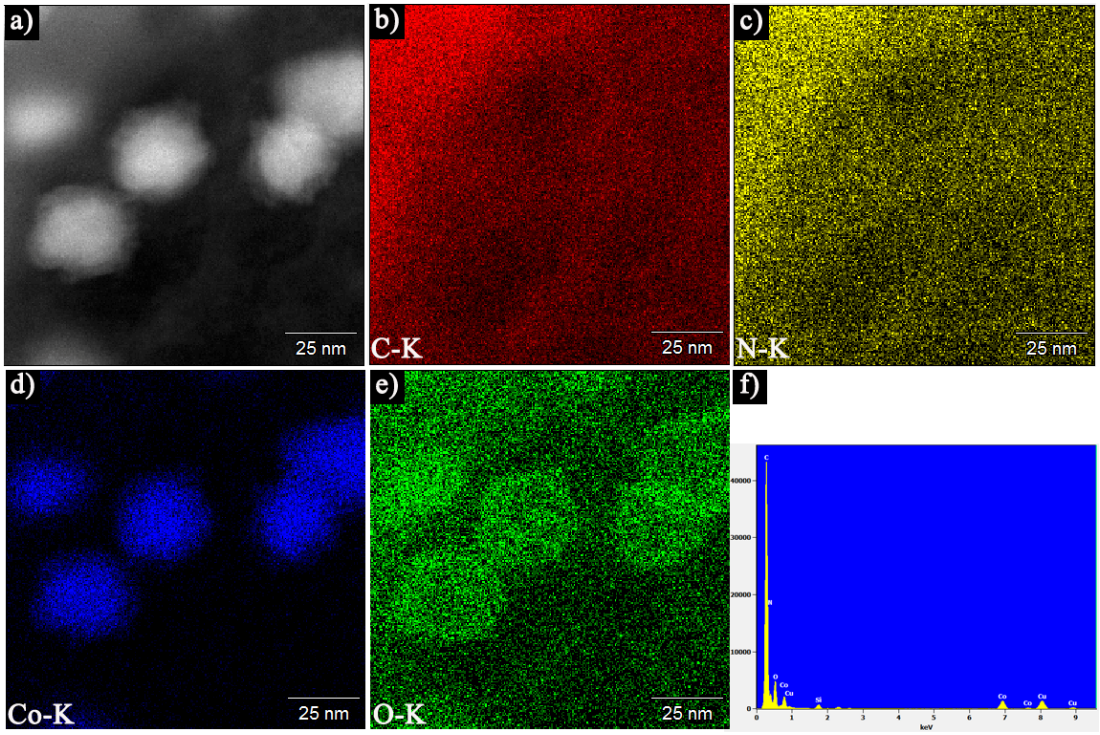

Figure 7.5 (a) High-mag STEM images, (b-e) the corresponding element mapping analysis of the (b) carbon, (c) nitrogen, (d) cobalt, (e) oxygen and (f) EDS spectrum of the Co/CoO-NGA. (Note Cu and Si were detected from the TEM grid)

7.3.6 XPS Analysis

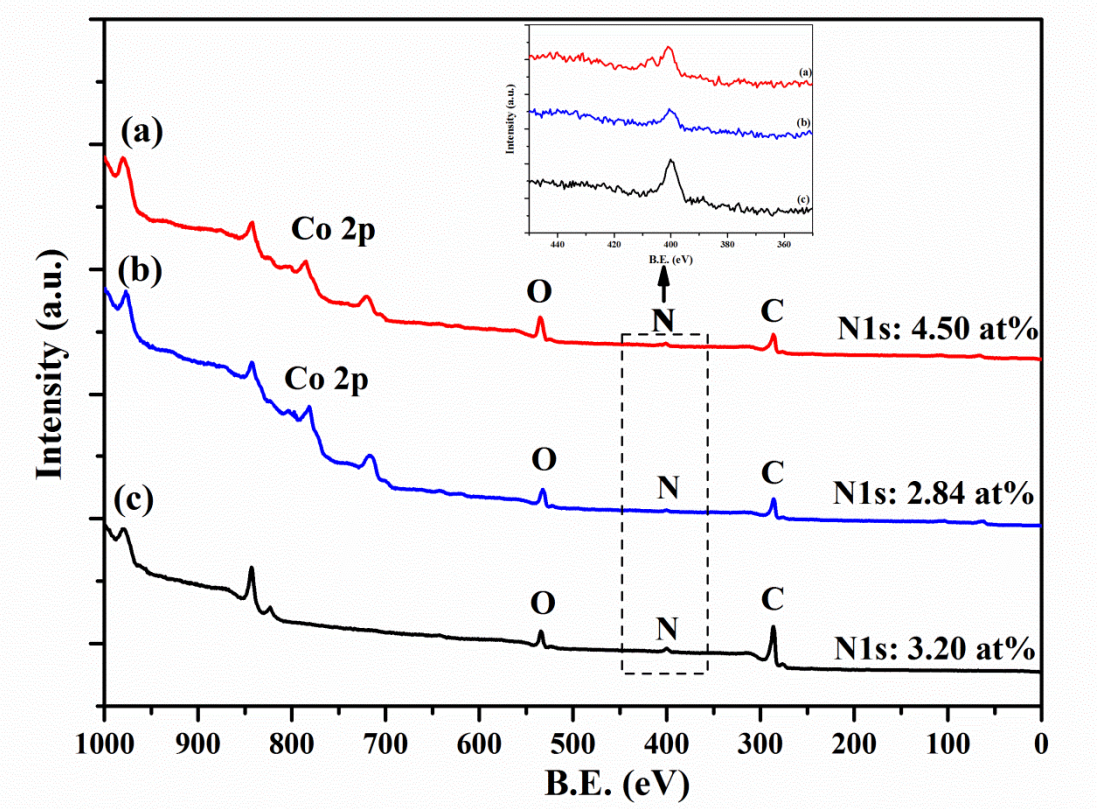

Figure 7.6 XPS spectrum of (a) CoO-NGA, (b) Co/CoO-NGA and (c) NGA. Insert is the highlight of nitrogen region.

The XPS was also employed to investigate the element presence and state in the electrocatalysts as is shown in Figure 7.6. Based on the results, N was detected in all the three samples indicating nitrogen could be doped into graphene lattice when using urea as precursor in a hydrothermal process following by heat treatment. While for different samples, the nitrogen content is slightly different, for the Co/CoO-NGA, only 2.8 at% N is detected, while for the CoO-NGA and NGA, 4.5 at% and 3.2 at% N were discovered respectively. The differences in N content is possibly because of the annealing temperature and chemical state of nitrogen precursors.

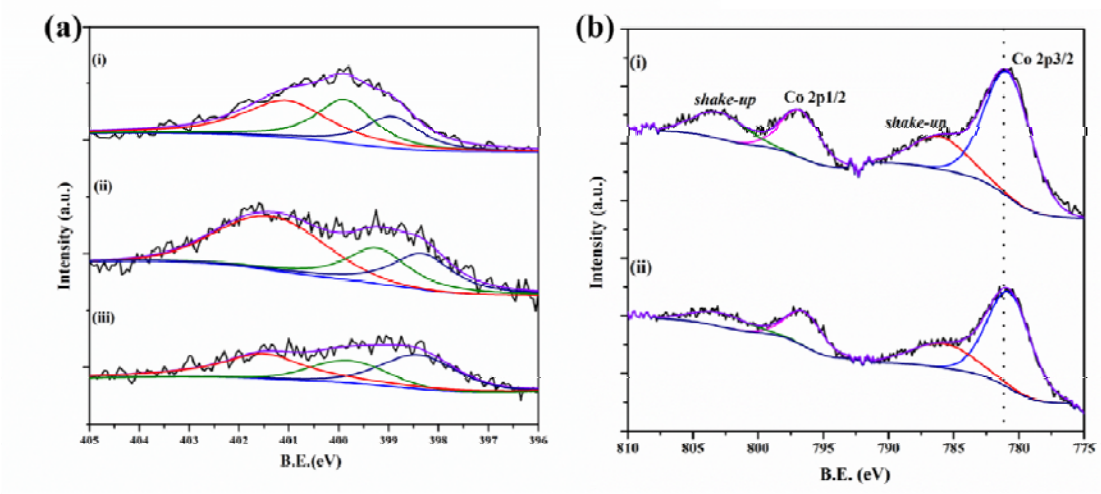

Figure 7.7 High resolution (a) N1s and (b) Co 2p XPS spectrum of the (i) CoO-NGA, (ii) Co/CoO-NGA and (iii) NGA.

To further investigate nitrogen configuration, high resolution XPS spectrum of N were obtained and fitted into three peaks of pyridinic N (≈398.5 eV), pyrrolic N (≈399.8 eV) and quaternary N (≈401.5 eV) [35] as shown in Figure 7.7a. In the CoO-NGA, the content of the pyrrolic N is slightly higher than the other two. While with the increase temperature (from 400 – 800 °C), owing to their different thermal stability[36], the quaternary N become dominant in the N configuration and the content of pyrrolic N were largely reduced in the samples of the Co/CoO-NGA and NGA. While such a rearrangement is beneficial for the oxygen reduction reaction as evidenced by many reports that, the quaternary and pyridinic N are more active in catalysing the ORR than the pyrrolic N[36]. The high resolution XPS spectrum of Co was also acquired and fitted in order to study the electronic state of Co, as shown in Figure 7.7b. It could be seen that, the Co 2p spectrum were spin-orbit split into $2p_{1/2}$ and $2p_{3/2}$ components and were all fitted, and both component qualitatively contain the same chemical information. Broad peaks around 786.3 eV were found in the Co $2p_{3/2}$, which could be ascribed to the shake-up satellite of the cobalt ions, indicating the metal oxides is cobalt (II) oxides.[37] Besides, as no observed metallic Co were observed in the spectrum, it is reasonably to

believe all Co were covered with oxides layer. In addition, compared with the CoO-NGA, the peaks of the Co2p for the Co/CoO-NGA were slightly up-shifted about 0.5 eV, which may be caused by the Co metallic core suggesting their strong electronic interactions.

7.3.7 CV Analysis

Cyclic voltammetry (CV) curves were obtained and used for a preliminary study of the electrocatalytic oxygen reduction properties of the synthesized electrocatalysts NCG-1000 at a scan rate of 50 mV s^{-1} (Figure 7.8). As shown in Figure 7.8, a quasi-rectangular featureless voltammetric currents within the potential range of −0.9 to 0.1 V were observed for all the three carbon based electrocatalysts, CoO-NGA, Co/CoO-NGA and NGA in the N_2-saturated solution, as a result of the typical supercapacitance effect on porous carbon materials.[3, 38] In contrast, when the electrolyte was saturated with O_2, a well-defined ORR peak centered at −0.25 V with a current density of −3.3 mA cm^{-2} was detected, the onset potential (the potential at which oxygen began to be reduced) was at about −0.03 V, which was comparable with the Pt/C (−0.01 V) and significantly higher than those of the CoO-NGA (−0.13V) and NGA (−0.13V) suggesting that the incorporation of metallic Co core could significantly increase the electrocatalytic activities of the electrocatalysts by largely increasing the electron and charge transfer around the nanoparticles on the nitrogen doped graphene sheets.. In comparison with the commercial E-Tek Pt/C, the Co/CoO-NGA showed a much higher ORR current peak density (Figure 7.8) suggested the determining role of porous graphene support on the electrocatalytic performance of the electrocatalysts in facilitating mass and ion transfer.

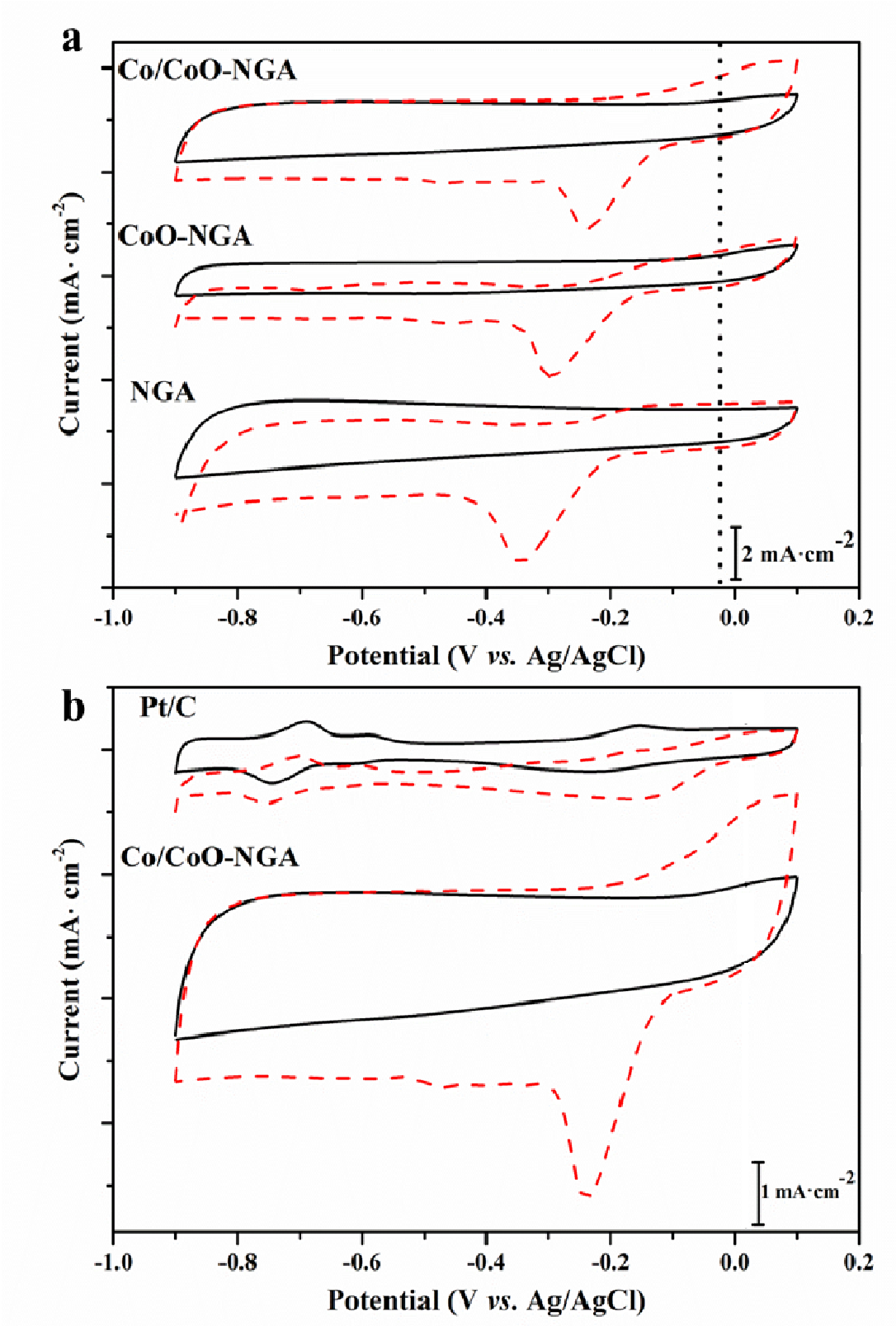

Figure 7.8 Comparison of the electrochemical catalytic performance of the synthesized Co/CoO-NGA, CoO-NGA, NGA and the commercial available E-Tek Pt/C catalysts: (a-b) CV curves of the Co/CoO-NGA, CoO-NGA, NGA and the Pt/C electrocatalysts in

N_2 (solid line) and O_2 (dash line) saturated electrolyte with a scan rate of 50 mV s^{-1}; the black dash line indicated the onset potential of the NCG-1000.

7.3.8 The ORR Performance Analysis

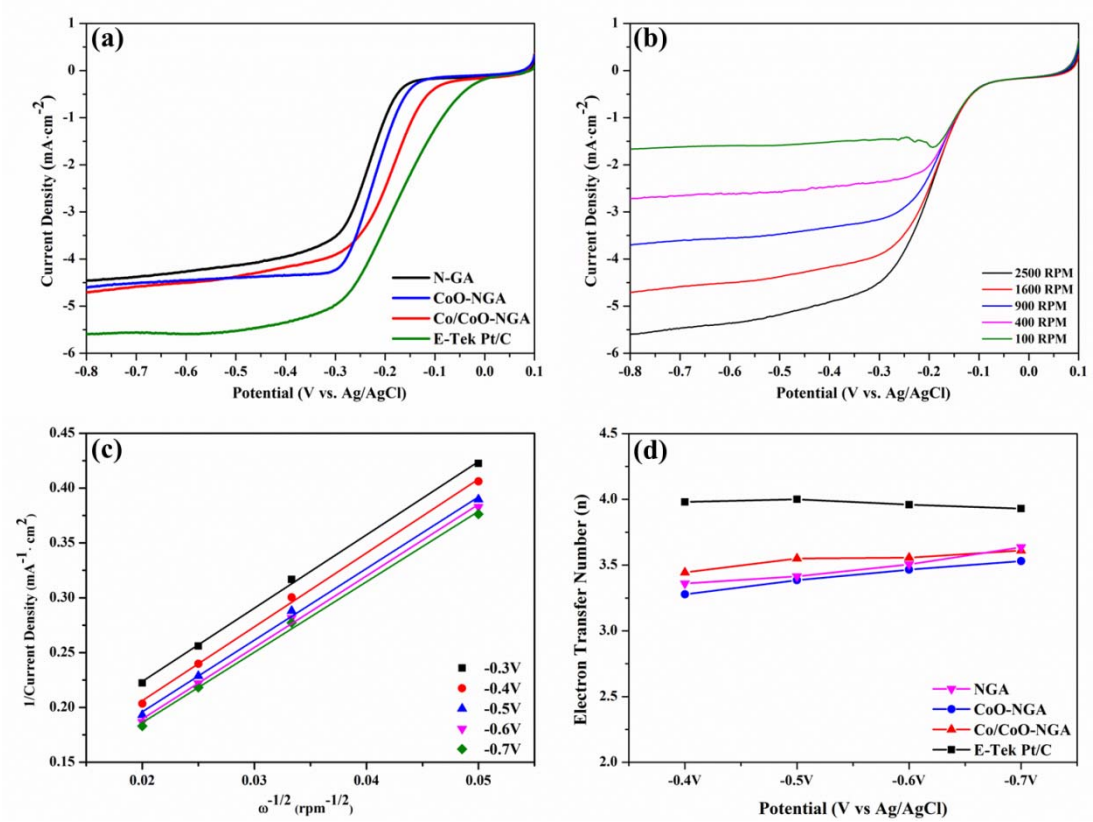

Figure 7.9 Electrochemical Characterisation of the electrocatalysts: (a) Steady-state Linear sweep voltammetry (LSV) curves at a rotating speed of 1600 rpm in O_2 saturated electrolyte with a sweep rate of 10 mV s^{-1} of the Co/CoO-NGA, CoO-NGA, NGA and Pt/C, (b) Rotating ring disk electrode (RRDE) curves of the Co/CoO-NGA recorded at various rotating speed from 2500 rpm to 100 rpm, (c) Corresponding Koutecky-Levich plots of the electrocatalysts at the potential of −0.5 V derived from (b) and (d) electron transfer numbers of the Co/CoO-NGA, CoO-NGA, NGA and the Pt/C at different potentials. Catalyst loading is 0.242 mg cm^{-2}. The electrolyte is 0.1 M KOH solution.

To gain insight into the ORR activities and kinetics of the electrocatalysts, the steady state ORR polarization curves of the Co/CoO-NGA, CoO-NGA, NGA and Pt/C were

obtained using a linear sweep voltammetry (LSV) technique with a sweep rate of 10 mV s^{-1} (Figure 7.9a). To qualify catalysts' performance, the half-wave potential ($E_{1/2}$), at which the current is a half of the limiting current is calculated, for the Co/CoO-NGA, the $E_{1/2}$ is −0.189V, which is very closed to that of the Pt/C (−0.170V) and much higher than those of CoO-NGA (−0.219V) and NGA(−0.254V) indicating the Co/CoO-NGA had comparable ORR electrocatalytic performance compared with the Pt/C and much higher ORR catalytic activities over the other two samples.

In order to obtain the kinetics of the ORR, steady state ORR polarization curves were also collected at various rotation speeds and corresponding Koutecky-Levich (K-L) plots were drafted from the ORR polarization curves at different potentials (Figure 7.9 b-c). Generally, the diffusing limiting current density was increased with the increase of rotating speed and the K-L plots of the Co/CoO-NGA shows good linearity. The electron-transfer numbers (n) were thereafter calculated at various potentials and showed in Figure 7.9d, general increasing n value were seen as the potential become more negative, while for the Co/CoO-NGA, the n value is slightly higher than the other two samples suggesting oxygen is reduced through a more efficient way than the other two again possibly owing to the unique core-shell structure which may be beneficial in accelerating the electron and charge transfer around the regional area around the metal oxides nanoparticles.

7.3.9 Poison Resistance Test

The selectivity to methanol of the catalysts is a key factor in the real application for fuel cells, because the relative small methanol molecular would cross through the membrane and react with the catalysts in the cathodes causing poor ORR performance and further reducing the cell efficiency.[39] To this end, the selectivity of Co/CoO-NGA and

commercial Pt/C were compared through chronoamperometric measurements at the rotating speed of 1600 rpm at −0.3 V with subsequently introduction of oxygen and methanol as displayed in Figure 7.10. The introduction of oxygen led to significant increase in the current density and a stable current was reached for both catalysts revealing the ORR performance of them were comparative. However, after the addition of methanol, a distinct change on current was observed for the Pt/C catalyst indicating methanol oxidation occurred, i.e., the selectivity of the Pt/C was poor. In contrast, for Co/CoO-NGA, the current remained nearly unchanged after the addition of methanol reflecting its superior selectivity and full methanol tolerance. These comparisons suggest the Co/CoO-NGA could be qualified as better electrocatalysts compared with the commercial Pt/C in the application for the direct methanol fuel cell (DMFC).

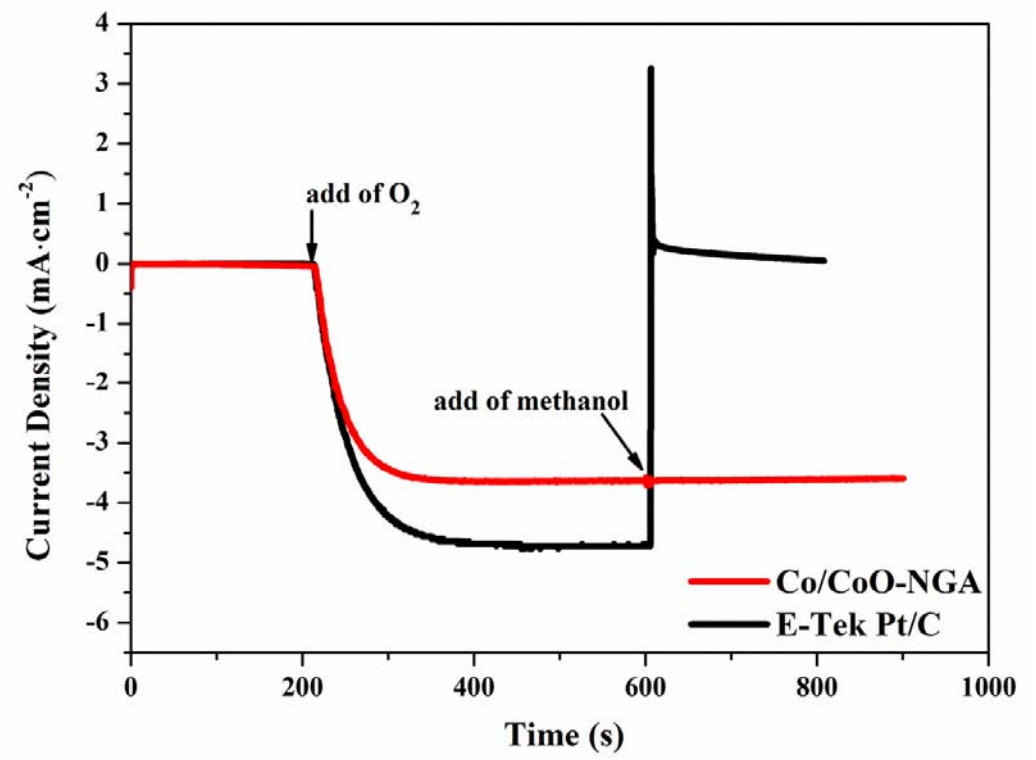

Figure 7.10 Chronoamperometric responses at −0.3 V of the Co/CoO-NGA and E-Tek Pt/C at the rotation speed of 1600 rpm a) with oxygen and methanol (1 M) added at about 260 s and 600 s respectively. The electrolyte is 0.1 M KOH.

7.3.10 Durability Tests

The durability of the Co/CoO-NGA was also assessed by the chronoamperometric technique under the same conditions with the methanol tests (Figure 7.11). During the long term (up to 13000 s), only 2% of the current loss was observed for the Co/CoO-NGA, whereas for the commercial Pt/C the current loss was calculated to be about 22%. These comparisons clearly indicated that the Co/CoO-NGA had ultra-long stability than the commercial Pt/C, revealing its superior potential capacities as long-term running catalysts.

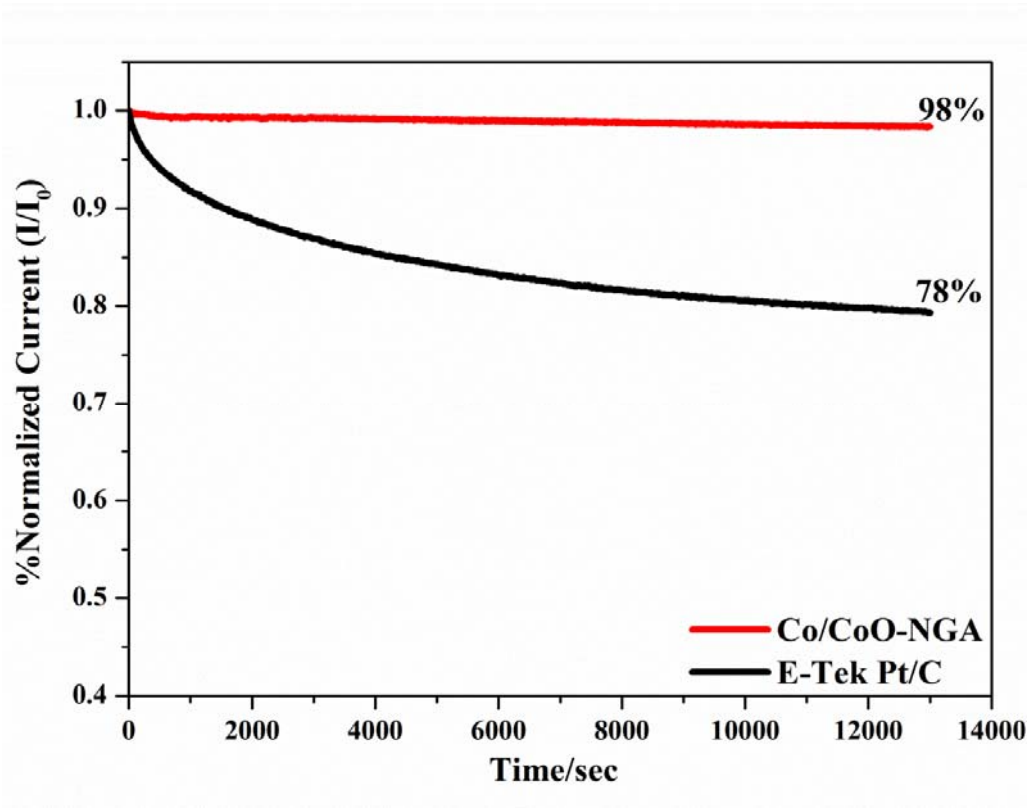

Figure 7.11 Chronoamperometric responses at −0.3 V of the Co/CoO-NGA and E-Tek Pt/C in O2 saturated electrolyte up to 13000 seconds

7.3.11 Single Anion Exchange Membrane Fuel Cell Tests

The AEMFC test was finally conducted in order to acquire the practical performance of the Co/CoO-NGA in a real-world fuel cell application (Figure 7.12a). To our surprise,

under identical testing conditions, the Co/CoO-NGA electrocatalyst shows a much similar catalytic behaviour compared with the commercial Pt/C. At the practicable operating potential (≈ 0.6V), the Co/CoO-NGA electrocatalyst delivered a current density of 127 mA·cm^{-2}, which reached about 78% of the Pt/C (162 mA·cm^{-2}, Figure 7.12b). Additionally, the max power output of Co/CoO-NGA was 110 mW·cm^{-2}, which was over 90% of the Pt/C (120 mW·cm^{-2}, Figure 7.12b). These comparisons clearly indicated the Co/CoO-NGA had the similar electrocatalytic performance with the commercial Pt/C under real world applications suggesting it could work as low cost ORR electrocatalysts under practical operating conditions.

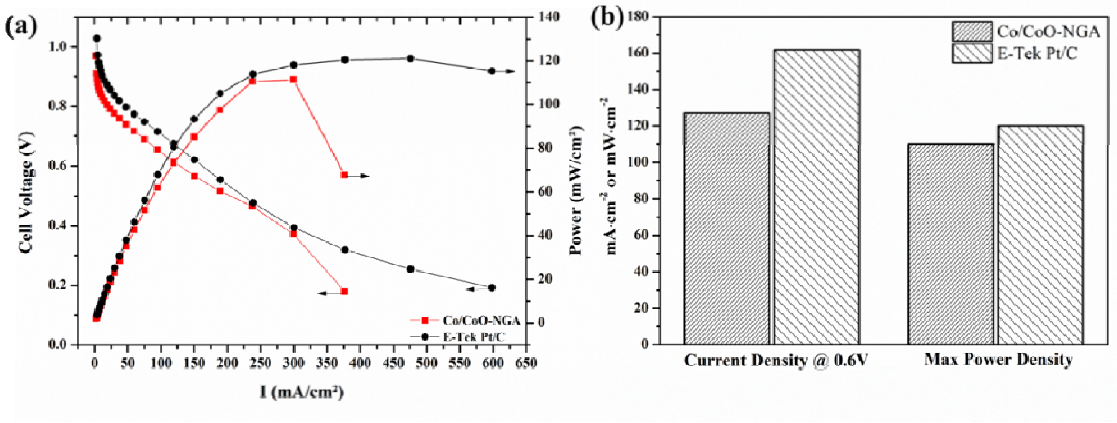

Figure 7.12 (a) Polarization curves of the anion exchange membrane single fuel cell test using Co/CoO-NGA and E-Tek Pt/C as cathode electrocatalysts respectively. The electrocatalyst loading amount is 0.2 mg/cm-2. (b) Comparisons of current density at 0.6 V and max power density derived from the results of the single fuel cell test.

7.4 Conclusion

In summary, we have demonstrate a facile method in fabricating core-shell cobalt /cobalt oxide nanostructure using 3D nitrogen doped grapheneas supporting materials (Co/CoO-NGA) without adding any surfactants. The Co/CoO-NGA was explored as an electrocatalysts for the oxygen reduction reaction in alkaline medium, showing

excellent ORR catalytic performance, superior methanol tolerance and strong durability. The superb electrocatalytic performance in ORR were attributed to the excellent electron and charge transfer properties of the unique core shell structures and the robust 3D structure of the supporting materials and the synergistic enhancement from the nitrogen-metal-carbon interactions in the electrocatalysts. We anticipate this synthetic method could be further employed into other transition-metal core shell nanostructure synthesis and would be beneficial in developing low-cost, economical feasible and environmental friendly electrocatalysts for the next-generation alkaline fuel cells.

7.5 References

1. Liang, Y., Y. Li, H. Wang, J. Zhou, J. Wang, T. Regier, and H. Dai, Nature Materials, 2011. **10**(10): p. 780-786.
2. Chen, S., J. Duan, W. Han, and S.Z. Qiao, Chemical Communications (Cambridge, United Kingdom), 2014. **50**: p. 207-209.
3. Liang, J., Y. Jiao, M. Jaroniec, and S.Z. Qiao, Angewandte Chemie, International Edition, 2012. **51**(46): p. 11496-11500.
4. Zhang, G., B.Y. Xia, X. Wang, and X.W. Lou, Advanced Materials, 2013: p. 2408-2412.
5. Wu, Z.-S., S. Yang, Y. Sun, K. Parvez, X. Feng, and K. Müllen, Journal of the American Chemical Society, 2012. **134**(22): p. 9082-9085.
6. Liang, Y., Y. Li, H. Wang, and H. Dai, Journal of the American Chemical Society, 2013. **135**(6): p. 2013-2036.
7. Liang, Y., H. Wang, P. Diao, W. Chang, G. Hong, Y. Li, M. Gong, L. Xie, J. Zhou, J. Wang, T.Z. Regier, F. Wei, and H. Dai, Journal of the American Chemical Society, 2012. **134**(38): p. 15849-15857.

8. Guo, S., S. Zhang, L. Wu, and S. Sun, Angewandte Chemie, International Edition, 2012. **51**(47): p. 11770-11773.

9. Mao, S., Z. Wen, T. Huang, Y. Hou, and J. Chen, Energy and Environmental Science, 2014. **7**(2): p. 609-616.

10. Liu, Q., J. Jin, and J. Zhang, ACS Applied Materials & Interfaces, 2013. **5**(11): p. 5002-5008.

11. Gao, M.R., X. Cao, Q. Gao, Y.F. Xu, Y.R. Zheng, J. Jiang, and S.H. Yu, ACS Nano, 2014. **8**(4): p. 3970-3978.

12. Hummers, W.S. and R.E. Offeman, Journal of the American Chemical Society, 1958. **80**(6): p. 1339-1339.

13. Luo, J., H.D. Jang, and J. Huang, ACS Nano, 2013. **7**(Copyright (C) 2013 American Chemical Society (ACS). All Rights Reserved.): p. 1464-1471.

14. Wen, Z., X. Wang, S. Mao, Z. Bo, H. Kim, S. Cui, G. Lu, X. Feng, and J. Chen, Advanced Materials, 2012. **24**(Copyright (C) 2013 American Chemical Society (ACS). All Rights Reserved.): p. 5610-5616.

15. Xu, Y., Z. Lin, X. Huang, Y. Liu, Y. Huang, and X. Duan, ACS Nano, 2013. **7**(5): p. 4042-4049.

16. Niu, Z., J. Chen, H.H. Hng, J. Ma, and X. Chen, Advanced Materials, 2012. **24**(30): p. 4144-4150.

17. Zheng, B., J. Wang, F.-B. Wang, and X.-H. Xia, Journal of Materials Chemistry A, 2014. **2**(24): p. 9079-9084.

18. Zhuang, Z., W. Sheng, and Y. Yan, Advanced Materials, 2014. **26**(23): p. 3950-3955.

19. Luo, J., L. Wang, D. Mott, P.N. Njoki, Y. Lin, T. He, Z. Xu, B.N. Wanjana, I.I.S. Lim, and C.-J. Zhong, Advanced Materials, 2008. **20**(24): p. 4342-4347.

20. Yin, H., C. Zhang, F. Liu, and Y. Hou, Advanced Functional Materials, 2014. **24**(20): p. 2930-2937.

21. Xu, Y., K. Sheng, C. Li, and G. Shi, ACS Nano, 2010. **4**(7): p. 4324-4330.

22. Hu, H., Z. Zhao, W. Wan, Y. Gogotsi, and J. Qiu, Advanced Materials, 2013. **25**(15): p. 2219-2223.

23. Wu, Z.S., A. Winter, L. Chen, Y. Sun, A. Turchanin, X. Feng, and K. Müllen, Advanced Materials, 2012. **24**(37): p. 5130-5135.

24. Ren, L., K.S. Hui, and K.N. Hui, J. Mater. Chem. A, 2013. **1**(Copyright (C) 2013 American Chemical Society (ACS). All Rights Reserved.): p. 5689-5694.

25. Chen, W. and L. Yan, Nanoscale, 2011. **3**(Copyright (C) 2013 American Chemical Society (ACS). All Rights Reserved.): p. 3132-3137.

26. Zhang, M., Y. Wang, and M. Jia, Electrochimica Acta, 2014. **129**: p. 425-432.

27. Yuan, J., J. Zhu, H. Bi, X. Meng, S. Liang, L. Zhang, and X. Wang, Physical Chemistry Chemical Physics, 2013. **15**(31): p. 12940-12945.

28. Marcano, D.C., D.V. Kosynkin, J.M. Berlin, A. Sinitskii, Z. Sun, A. Slesarev, L.B. Alemany, W. Lu, and J.M. Tour, ACS Nano, 2010. **4**(8): p. 4806-4814.

29. Paulus, U.A., T.J. Schmidt, H.A. Gasteiger, and R.J. Behm, Journal of Electroanalytical Chemistry, 2001. **495**(2): p. 134-145.

30. van der Vliet, D., D.S. Strmcnik, C. Wang, V.R. Stamenkovic, N.M. Markovic, and M.T.M. Koper, Journal of Electroanalytical Chemistry, 2010. **647**(1): p. 29-34.

31. Varcoe, J.R. and R.C.T. Slade, Electrochemistry Communications, 2006. **8**(5): p. 839-843.

32. Querejeta-Fernández, A., M. Parras, A. Varela, F. del Monte, M. García-Hernández, and J.M. González-Calbet, Chemistry of Materials, 2010. **22**(24): p. 6529-6541.

33. Wang, B., T. Zhu, H.B. Wu, R. Xu, J.S. Chen, and X.W. Lou, Nanoscale, 2012. **4**(6): p. 2145-2149.

34. Fang, B., N.K. Chaudhari, M.-S. Kim, J.H. Kim, and J.-S. Yu, Journal of the American Chemical Society, 2009. **131**(42): p. 15330-15338.

35. Wang, Y., Y. Shao, D.W. Matson, J. Li, and Y. Lin, ACS Nano, 2010. **4**(4): p. 1790-1798.

36. Yang, S., L. Zhi, K. Tang, X. Feng, J. Maier, and K. Muellen, Advanced Functional Materials, 2012. **22**: p. 3634-3640.

37. Yang, J., H. Liu, W.N. Martens, and R.L. Frost, The Journal of Physical Chemistry C, 2009. **114**(1): p. 111-119.

38. Parvez, K., S. Yang, Y. Hernandez, A. Winter, A. Turchanin, X. Feng, and K. Müllen, ACS Nano, 2012. **6**(11): p. 9541-9550.

39. Liu, M., Y. Lu, and W. Chen, Advanced Functional Materials, 2013. **23**(10): p. 1289-1296

Chapter 8

Conclusion and Outlook

8. **CONTENTS**

Chapter 8

8.1 General Conclusion

As have been addressed in this thesis, the oxygen reduction reaction (ORR) is a kinetically limited step in fuel cells (FCs), and the electrocatalysts for the ORR play a pivotal role in determining the performance and energy conversion efficiency of FCs. Platinum (Pt) is considered as the most efficient electrocatalyst for the ORR, however, it is impeded from large-scale commercialisation due to its high cost, low "poison" resistance, and poor stability. Therefore, in recent decades, numerous efforts have been devoted to exploring novel electrocatalysts with low cost, high efficiency and environmental friendliness. In this study, focusing on developing low-cost catalysts for fuel cells, we first explored the novel Pt-based electrocatalysts for the proton exchange membrane fuel cell (PEMFC) through alloying Pt with a second metal (Pd, Cu) to reduce the cost. The as-synthesized materials were well characterised by electrochemical tests showing improved ORR performance compared with Pt/C in acidic medium.

In addition, with the development of anion exchange membranes (AEM) in anion exchange membrane fuel cells (AEMFC), which is an analogue of the PEMFC using anion exchange polymer membrane as electrolyte, there is an emerging demand for electrocatalysts for the AEMFC with lower cost. In addition, there is awareness that the replacement of proton exchange membranes with anion exchange membranes could substantially increase the kinetics of the ORR, thus offering more choice of electrocatalysts. Therefore, the following chapters are devoted to the development of non-Pt based electrocatalysts, including Pd-based electrocatalyst, nitrogen-doped graphene, cobalt/cobalt oxide core/shell nanostructures integrated on nitrogen-doped

graphene, and their ORR performance has been well characterised within alkaline medium.

8.1.1 Electrocatalysts for the Oxygen Reduction Reaction in the PEMFC

It has already been well documented that alloying Pt with other metals, such as Pd, Cu, Ni, etc., could greatly reduce the cost, and at the same time, increase the catalytic efficiency of Pt. It is still an ongoing challenge, however, to develop facile approaches to fabricating high-surface-area Pt-based electrocatalysts for better utilisation of the Pt and to further increase the catalytic efficiency of the Pt-based electrocatalyst. Based on the author's research, hollow-shaped Pt-based nanostructures, consisting of Pt-Pd, and Pt-Cu, have shown great enhancement in the catalytic performance towards the ORR, which was attributed to the unique hollow shaped porous structure and to the changes of in the geometric effect and electronic effect on Pt when alloying with a second metal. It is also found the compositions of Pt/Pd and Pt/Cu are very important for determining the final structure and the electrocatalytic performance of the synthesized electrocatalysts. Both of these two electrocatalysts were well examined with single PEMFC tests, where the catalysts indeed showed improved performance compared with the commercially available Pt/C electrocatalyst.

8.1.2 Electrocatalysts for the Oxygen Reduction Reaction in the AEMFC

The kinetics of the ORR in alkaline medium could be largely increased, thus offering a wider selection of electrocatalysts. In addition, recent advances in the development of alkaline anion exchange membranes (AAEMs) has also added considerable incentives to explore new electrocatalysts in alkaline medium, because the performance of AEMFCs has been demonstrated to approach that of the analogous, conventional acidic Nafion® proton exchange membrane fuel cell (PEMFC). From this perspective, a series

of electrocatalysts, including PdNi hollow nanoparticles, nitrogen-doped crumpled graphene sheets, and core-shell cobalt/cobalt oxide integrated on nitrogen-doped graphene aerogel, have been developed with improved or comparable performance compared with Pt/C. These non-Pt based electrocatalysts, with much lower cost compared with Pt/C, have also shown better "poison" resistance and better durability. The author also performed single AEMFC tests with the three electrocatalysts to fully investigate the electrochemical performance of the electrocatalysts under real practicable application, and the results revealed that these materials could indeed work as low-cost and efficient ORR electrocatalysts for the AEMFC.

8.2 Outlook

Although the synthesized electrocatalysts (Pt based, Pd-based, N-doped carbon based) have shown remarkable electrocatalytic performance towards the ORR, the efficiency of the electrocatalysts as well as the feasibility of the synthetic method need further improvements. In addition, much more efficient, low-cost electrocatalysts are urgently needed in the near future in order to meet the requirements for the commercialisation of fuel cells. Therefore, future work should focus on the development of non-noble-metal-based electrocatalysts for the ORR in alkaline medium and may possibly also focus on the following aspects: (i) the development of transition metals coordinated with nitrogen-doped carbon materials with mesoporous features to increase the efficiency of the ORR catalytic performance; (ii) the development of mixed transition metal oxides coupled with nitrogen-doped carbon materials to further increase the efficiency; (iii) the development of other nitrogen-doped carbon materials such as graphene ribbons and the exploration of new doping methods to fabricate efficient ORR catalysts; and (iv) the

development of cost-effective synthesis procedures for other heteroatom-doped or co-doped carbon materials.

APPENDICES

PUBLICATION

- **Wang, M**.; Wang, J.; Hou, Y.; Shi, D.; Wexler, D.; Poynton, S. D.; Slade, R. C. T.; Zhang, W.; Liu, H.; Chen, J., N-Doped Crumpled Graphene Derived from Vapor Phase Deposition of PPy on Graphene Aerogel as an Efficient Oxygen Reduction Reaction Electrocatalyst. ***ACS Appl. Mater. Interfaces*** 2015;7(13):7066-7072
- **Wang, M**.; Zhang, W.; Wang, J.-Z.; Wexler, D.; Poynton, S. D.; Slade, R. C. T.; Kun-Liu, H.; Winther-Jenson, B.; Kerr, R.; Shi, D.; Chen, J., PdNi Hollow Nanoparticles for Improved Electrocatalytic Oxygen Reduction in Alkaline Environments***. ACS Appl. Mater. Interfaces*** 2013, 5 (23), 12708-12715;
- **Wang, M**.; Zhang, W.; Wang, J.; Minett, A.; Lo, V.; Liu, H.; Chen, J., Mesoporous hollow PtCu nanoparticles for electrocatalytic oxygen reduction reaction. ***J. Mater. Chem. A*** 2013, 1 (7), 2391-2394;
- Zhang, W.; **Wang, M**.; Chen, J.; Romeo, T.; Harris, A. T.; Minett, A. I., Localized growth of Pt on Pd as a bimetallic electrocatalyst with enhanced catalytic activity and durability for proton exchange membrane fuel cell. ***Electrochem. Commun***. 2013, 34, 73-76;
- Wang, M.; Huang, J.; **Wang, M**.; Zhang, D.; Zhang, W.; Li, W.; Chen, J., Co3O4 nanorods decorated reduced graphene oxide composite for oxygen reduction reaction in alkaline electrolyte. ***Electrochem. Commun***. 2013, 34, 299-303;
- Wang, M.; Huang, J.; **Wang, M**.; Zhang, D.; Chen, J., Electrochemical

nonenzymatic sensor based on CoO decorated reduced graphene oxide for the simultaneous determination of carbofuran and carbaryl in fruits and vegetables. ***Food Chem***. 2014, 151, 191-197

- Shu, K.; Wang, C.; **Wang, M**.; Zhao, C.; Wallace, G., Graphene Cryogel Paper with Enhanced Mechanical Strength for High Performance Lithium Battery**. *J. Mater. Chem. A*** 2014, 2, 1325-1331;
- Wang, M.-Y.; Shen, T.; **Wang, M**.; Zhang, D.-E.; Tong, Z.-w.; Chen, J., One-pot synthesis of α-Fe2O3 nanoparticles-decorated reduced graphene oxide for efficient nonenzymatic H_2O_2 biosensor. ***Sensors and Actuators B: Chemical*** 2014, 190 (0), 645-650.
- **Wang, M.**, Wang, J. Z., Chen, J., et al; Co/CoO core shell nanostructure anchored on nitrogen doped graphene aerogel as bifunctional electrocatalysts for both oxygen reduction reaction and evolution reactions, In preparation.

CONFERENCE PRESENTATION

- 2014 *GrapChina Conference, Ningbo China*
  N-Doped Crumpled Graphene Derived from Vapor Phase Deposition of PPy on Graphene Aerogel as Efficient Oxygen Reduction Reaction Electrocatalysts (Oral Presentation)
- 2014 *5th Australia-China Symposium for Materials Science, Wollongong, Australia,*
  Co/CoO anchored on nitrogen doped graphene aerogel as bifunctional electrocatalysts for oxygen reduction and evolution reactions (Poster)
- 2014 *9th Annual International Electromaterials Science Symposium*, *Wollongong, Australia*
  Bimetallic hollow nanostructures for the oxygen reduction reaction (Poster)
- 2013 8*th Annual International Electromaterials Science Symposium,*

Wollongong, Australia

Mesoporous bimetallic PtCu nanoparticles for the oxygen reduction reaction (Poster)